Layer-by-layer Deposition of Silicon Phthalocyanines-based Organic Photovoltaics

BY

Marie Faure

A THESIS
SUBMITTED TO THE UNIVERSITY OF OTTAWA
IN PARTIAL FULFILMENT OF THE REQUIREMENTS FOR THE
DOCTORATE OF PHILOSOPHY DEGREE
IN CHEMICAL ENGINEERING

DEPARTMENT OF CHEMICAL AND BIOLOGICAL ENGINEERING
FACULTY OF ENGINEERING
UNIVERSITY OF OTTAWA

Abstract

With the need for the development of renewable sources of energy, organic photovoltaic (OPV) has been attracting researchers' interest for the past decades. This solar technology utilizes carbon-based semiconductors instead of conventional inorganic materials which enables inexpensive, lightweight and flexible roll-to-roll fabrication of large area solar panels with a very short energy payback time. Device efficiencies have rapidly increased to above 18% within the last few years, becoming competitive with solar technologies available on the market. However, research has been focused on the maximization of efficiencies at all cost leading to synthetically challenging materials and processes with negligible commercial scalability. In this thesis, silicon phthalocyanines (SiPcs), synthetically facile molecules most known for their extensive use as dyes and pigments in the industry, were employed as low-cost and scalable active materials for OPV devices. We also report the use of layer-by-layer deposition of the donor and acceptor layer providing a more scalable process compared to the conventional blended heterojunction morphology. Different SiPc derivatives, both soluble and non-soluble, were used as acceptors, paired with different donor polymers (P3HT, PCDTBT, and PBDB-T) and integrated into hybrid evaporation-solution and all-solution layer-by-layer OPV devices. Significant device engineering and optimization was performed through the investigation of several processing conditions such as solvent choice, spin-speed, concentration and annealing temperature/time. In particular, all-solution processed SiPc-based bilayer OPV devices achieved *PCE*s above 3% with *Voc* above 1 V, which was similar to performances of corresponding BHJ OPVs. SiPc derivatives also demonstrated their ability to act as electron transport layers in perovskite solar cells. These results further establish the potential of SiPc derivatives as active materials in different solar technologies, while promoting the use of the bilayer structure in OPV devices.

Abstrait

Le besoin de nouvelles sources d’énergie renouvelables ne faisant qu’augmenter, les cellules photovoltaïques organiques (OPV) ont stimulées l’intérêt des chercheurs cette dernière décennie. Cette technologie solaire utilise des semi-conducteurs à base de carbone au lieu de semi-conducteurs inorganiques conventionnels. Cela facilite la fabrication de modules solaires larges peu coûteux, légers et flexibles via des procédures rouleau à rouleau, et avec un délai d’amortissement énergétique moindre. L’efficacité des cellules a rapidement dépassée les 18% ces dernières années, les rendant compétitives avec les autres technologies solaires disponibles sur le marché. Cependant, la recherche s’est focalisée sur la maximisation des efficacités à tout prix ce qui a conduit au développement de matériaux complexes à synthétiser et à des procédés de fabrication difficilement transposables à l’échelle commerciale. Dans cette thèse, les phthalocyanines de silicium (SiPcs), des molécules connues pour leur simplicité synthétique et leur utilisation extensive comme colorants et pigments dans l’industrie, ont été utilisées comme matériaux actifs bon marché et transposables à l’échelle industrielle dans des modules OPV. L’utilisation d’un procédé de déposition couche par couche des films donneur et accepteur, une technique davantage transposable à plus grande échelle comparativement à la configuration conventionnelle BHJ, est aussi rapportée. Plusieurs dérivés SiPc, solubles et insolubles, ont été utilisés comme accepteurs et couplés avec différents polymères donneurs (P3HT, PCDTBT, et PBDB-T). Ils ont été intégrés dans des modules OPV préparés via procédé couche par couche hybride évaporation-solution ou bien entièrement solution. D’importants travaux de fabrication et d’optimisation des modules ont été réalisés à travers l’étude de différentes conditions expérimentales comportant le choix des solvants, des vitesses de rotation, des concentrations et des temps et températures de recuit. En particulier, les modules OPV bicouches à base de SiPc fabriqués via procédé solution ont atteint un *PCE* supérieur à 3% avec un *Voc* supérieur à 1 V, des résultats similaires à leurs homologues BHJ. Les dérivés SiPc ont aussi prouvé leur capacité à se comporter comme des couches transporteuses d’électrons dans des cellules solaires perovskites. Ces résultats renforcent le potentiel des dérivés SiPc comme matériaux actifs pour diverses technologies solaires, tout en encourageant l’emploi de la structure bicouche pour les modules OPV.

Acknowledgements

The fulfillment of my projects would not have been possible without the help of many people. First, I would like to thank Dr. Benoît Lessard for giving me the opportunity to join his research group at the University of Ottawa. Thank you for everything you taught me, your guidance, the opportunities of collaboration abroad, and your understanding and listening ears during these great but intense years. I am confident that the group will continue its successful growth.

I would like to thank the staff of the Department of Chemical and Biological Engineering at the University of Ottawa for their administrative and technical support, especially Franco Ziroldo and James Macdermid for their help with the design and machining of components for the lab. I would also like to thank Frantz Célestin for handling our shipping so well.

I would like to thank my colleagues of the Lessard Research Group (LRG) for the support and positive research environment they provided during these years. Special thanks to Trevor Grant that trained me to organic photovoltaic when I started. I'd also like to thank him for the synthesis of many semiconductors I used in my projects, and for all the brainstorming and scientifical exchanges we had. Special thanks to Dr. Nicole Rice for providing a great lab management and support, and for taking care of the AFM characterizations. Finally, special thanks to Dr. Chloé Dindault for her emotional and collaborative support in the lab during my last year.

I would like to express my heartfelt gratitude to my parents, Yvan Faure and Joséphine Clapet, to my grandmother, Yvette Faure, and to my friends, Vida Gabriel, Landry Ngembo, Katia Chelouah, Ikram Kharroubi, for their unfailing love and encouragement. Special note of gratitude to my boyfriend, Tom Migné, for his daily love, support, cheering and understanding, despite the long distance.

Table of Contents

List of Figures

List of Tables

List of Key Abbreviations

Ag: Silver

AFM: Atomic force microscopy

BCP: Bathucoproine

BHJ: Bulk heterojunction

CuPc: Copper phthalocyanine

C_{60}: Fullerene

E_g: Band gap

EQE: External quantum efficiency

ETL: Electron transport layer

FF: Fill factor

HOMO: Highest occupied molecular orbital

HTL: Hole transport layer

ITIC: 3,9-bis(2-methylene-(3-(1,1-dicyanomethylene)-indanone))-5,5,11,11-tetrakis(4-hexylphenyl)-dithieno[2,3-d:2’,3’-d’]-s-indaceno[1,2-b:5,6-b’]dithiophene

ITO: Indium tin oxide

J-V: Current density-voltage

Jsc: Short-circuit current

LbL: Layer-by-layer

L_D: Exciton diffusion length

LUMO: Lowest occupied molecular orbital

MPc: Metal phthalocyanine

NFA: Non fullerene acceptors

NIR: Near infrared

OLED: Organic light emitting diodes

OPV: Organic photovoltaic

OTFT: Organic thin film transistor

PBDB-T: Poly[(2,6-(4,8-bis(5-(2-ethylhexyl)thiophen-2-yl)benzo[1,2-b:4,5-b′]dithiophene)-co-(1,3-di(5-thiophene-2-yl)-5,7-bis(2-ethylhexyl)benzo[1,2-c:4,5-c′]dithiophene-4,8-dione)]

Pc: Phthalocyanine

$PC_{61}BM$: Phenyl-C61-butyric acid methyl ester

PCDTBT: Poly[N-90-heptadecanyl-2,7-carbazole-alt-5,5-(40,70-di-2-thienyl-20,10,30-benzothiadiazole)]

PCE: Power conversion efficiency
PEDOT:PSS: Poly(3,4-ethylenedioxythiophene):poly(styrene sulfonate)
PHJ: Planar heterojunction
PM-HJ: Planar-mixed heterojunction
PSCs: Perovskite solar cells
PTB7: Poly([4,8-bis[(2-ethylhexyl)oxy]benzo[1,2-b:4,5-b']dithiophene-2,6-diyl][3-fluoro-2-[(2-ethylhexyl)carbonyl]thieno[3,4-b]thiophenediyl])
PTQ10: Poly[(thiophene)-alt-(6,7-difluoro-2-(2-hexyldecyloxy)quinoxaline)]
PVD: Physical vapour deposition
P3HT: Poly(3-hexylthiophene)
SiPc: Silicon phthalocyanine
Voc: Open circuit voltage
Y6: 2,2'-((2Z,2'Z)-((12,13-bis(2-ethylhexyl)-3,9-diundecyl-12,13-dihydro-[1,2,5]thiadiazolo[3,4-e]thieno[2",3”:4’,5']thieno[2',3':4,5]pyrrolo[3,2-g]thieno[2',3':4,5]thieno[3,2-b]indole-2,10-diyl)bis(methanylylidene))bis(5,6-difluoro-3-oxo-2,3-dihydro-1H-indene-2,1-diylidene))dimalononitrile
ZnPc: Zinc phthalocyanine
(246F)$_2$-SiPc: Bis(2,4,6-trifluorophenoxy) SiPc
(345F)$_2$-SiPc: Bis(3,4,5-trifluorophenoxy) SiPc
(3BS)$_2$-SiPc: Bis(tri-n-butylsilyl oxide) silicon phthalocyanine

Chapter 1: Introduction

1.1. Introduction to OPV

As the global population continues to increase, the demand for clean and sustainable energy is ever pressing. Thus, a major need for low-cost renewable energy sources is ever pressing. Solar irradiation remains as one of the renewable sources of energy with the most potential, which could produce roughly 2800 times the actual world yearly energetic demand if we could harvest the solar radiation that hits the Earth surface.[1],[2] Solar energy can be harnessed through two methods: 1) solar thermal, where heat from the sun is converted to energy and 2) through solar photovoltaic (PV) that converts photons directly into electricity and which is of interest for this thesis. However, only a small fraction of the global energy supply is deriving from PV technologies, but their ability to compete with fossil fuels and address global greenhouse gas emissions forecast a boosted development in the years to come.[3]

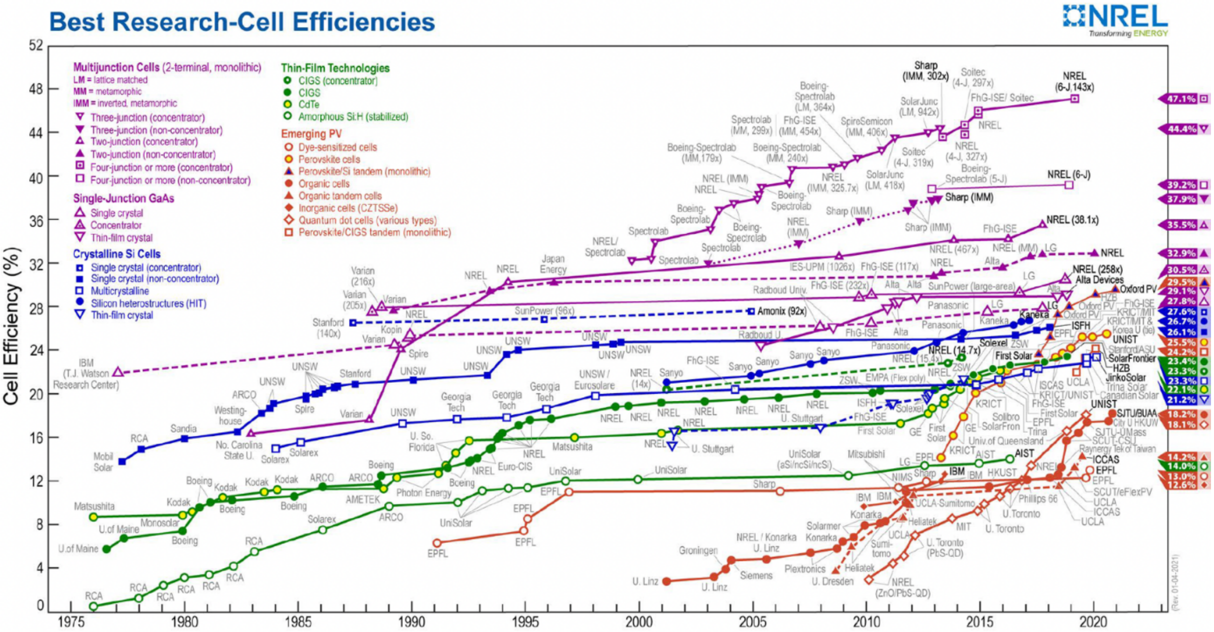

Figure 1.1. Record research solar cell efficiencies summarized by the National Renewable Energy Laboratory as of early 2021.

PV technologies are divided in several categories whose best performances are tracked by the National Renewable Energy Laboratory (USA) (**Figure 1.1**). The first PV generation emerged in 1954 and is known as inorganic crystalline silicon (c-Si) technologies.[4] PV c-Si modules are leading at present with >90% of the market due to silicon availability, cell stability, high cell efficiencies surpassing 26%, and constant reduction of production cost.[5] Second generation encompasses inorganic thin-film technologies such as copper indium gallium selenide (CIGS), cadmium telluride (CdTe), amorphous Si (a-Si), and gallium arsenide (GaAs), providing device performances of roughly 23%.[6] CIGS advantage over c-Si was that devices were significantly thinner, however, with the decrease of c-Si modules prices, along with the scarcity of tellurium and indium, and toxicity of cadmium, CIGS have fallen out of favour. The third PV generation includes dye-sensitized solar cells (DSSCs), perovskite solar cells (PSCs), organic photovoltaics (OPVs), and quantum-dot photovoltaics (QDPVs). They are based on dye coated TiO_2 nanoparticles, organic carbon-based semiconductors, hybrid organic-inorganic tin or lead halide materials and inorganic particles such as PbS in the active layer, respectively, and the materials themselves can be processed by solution providing opportunity for low-cost manufacturing compared to c-Si. A rapid growth of performances was observed, especially for PSCs whose efficiency is now reaching 25.5% for single-junction and above 29% for tandem with Si.[7] However, some major challenges remain such as the use of detrimental lead core in the perovskite crystal structure, and a lack of reproducibility of modules.[8]

OPVs based on organic materials have inherent advantages over other emerging technologies. First, most of them have a high molar absorptivity making them effective at absorbing photons and facilitating thin films solar cells with active layers thickness in the order of only 100-200 nm.[9] Secondly, organic materials have a potential lower manufacturing cost compared to ultrapure silicon due to the low temperature processing conditions. Moreover, unlike lead-based materials used in PSCs and QDPVs, they are generally non-toxic. Their absorption spectra is also highly tunable which enables devices with targeted absorption, colour, and transparency. Organic semiconductors can be soluble in a solvent which means they can be deposited by already well implemented printing techniques such as ink jet printing or spray coating enabling low cost, large area, roll-to-roll fabrication of devices. Finally, organic semiconductors are inherently malleable, such as polymers, and can therefore be integrated onto flexible and stretchable substrates. Hence, OPVs represent an inexpensive, lightweight, flexible pathway with a low energy payback time on the order of months.[10] Efficiencies have increased from bellow 3% in the year 2000 to above 18% within the last few years (**Figure 1.1**), which demonstrates incredible growth. OPVs have also the potential to serve decentralized niche solar applications where other technologies could be impracticable, such as roll-up devices, portable electronics, semi-transparent window covers, electronic textiles or greenhouse agriculture.[11-14] Some companies such as Armor (France), Heliatek (Germany), Merck (Germany), InfinityPV (Denmark) and others have already launched OPVs-based products such as portable/deployable chargers (**Figure 1.2A**) or integrated OPVs on different infrastructure surfaces such as glass windows (**Figure 1.2B**) or membranes tents (**Figure 1.2C**). Therefore, even though record values remain below other technologies, the quick and steady increase of the organic cells yield as well as its potential applications have set OPVs as one of the next generation solar cells alongside c-Si or PSCs.

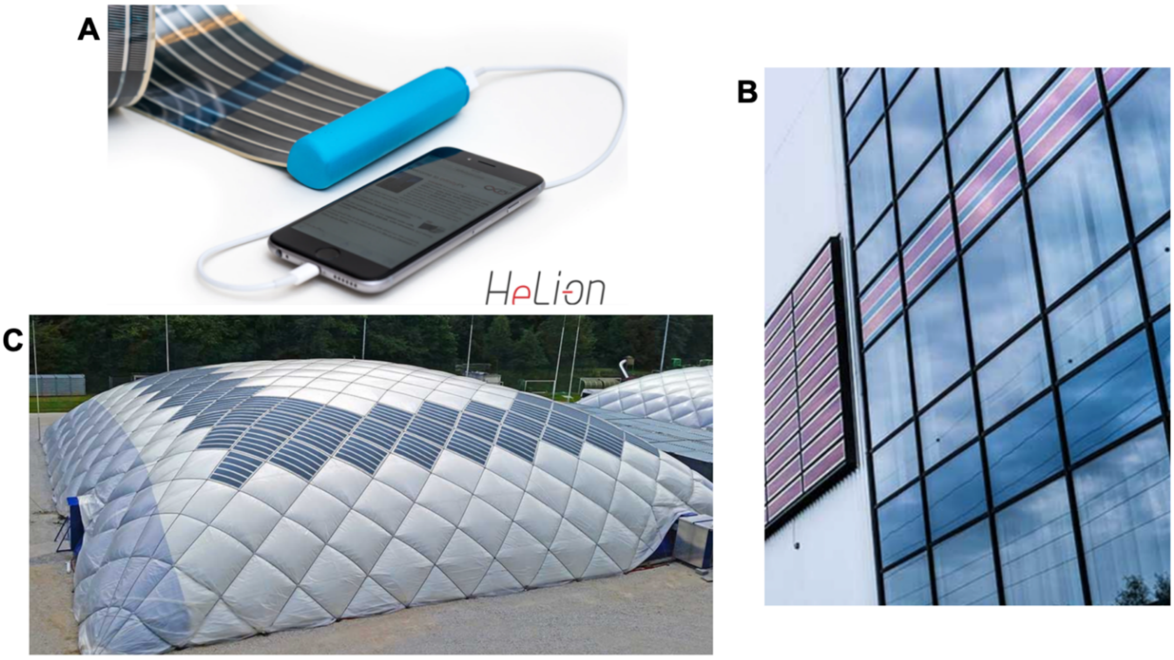

Figure 1.2. Examples of OPV modules application: (A) portable charger from InfinityPV (B) PV-integrated glass windows from Heliatek (C) PV-integrated air inflated hall from Heliatek.

1.2. OPV Devices Structure and Fabrication

The operating principles of OPVs is similar to that of inorganic c-Si. The light is absorbed by the active materials that generates a pair of excited electrons (e^-) and electrons holes (h^+) charge carriers. The carriers have to be separated in order to be collected at their respective electrodes and to supply current to an external circuit. In conventional c-Si solar cells the generated e^-/h^+ pairs have a very low binding energy, on the order of 0.015 eV, due to the high dielectric constant of silicon leading to instantaneous charge separation into free carriers at room temperature. These free charge carriers can then be transported and harvested using a simple silicon p^+/n^- doped junction. In OPVs, when light is absorbed in an organic material, a strongly bound e^-/h^+ pair is generated. This pair is called an exciton, and has a binding energy on the order of 0.3-1.0 eV.[15] Consequently, an additional driving force is required for the exciton dissociation to prevent charge recombination and the loss of the current. This is the major limitation of first generation OPVs based on single organic materials.

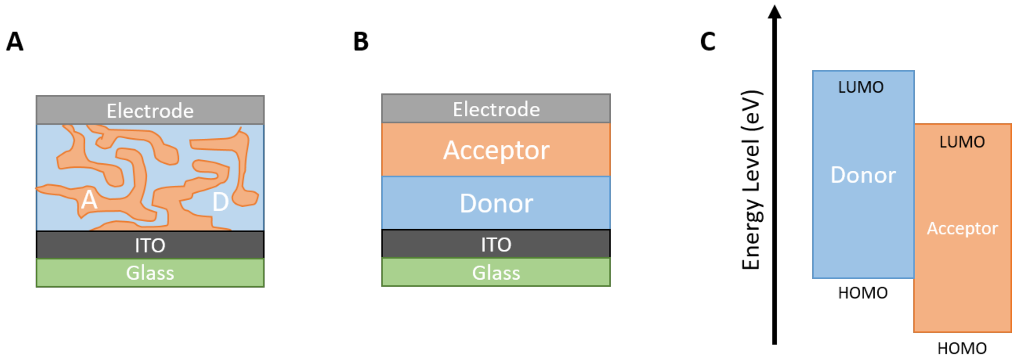

Figure 1.3. Side view of (A) a BHJ interpenetrating network and (B) a PHJ bilayer donor/acceptor device. (C) Representative energy offset between an acceptor and a donor material.

C. W. Tang was the first to break the 1% efficiency barrier in 1986 by introducing a planar heterojunction (PHJ) (**Figure 1.3B**) OPV comprised of two organic materials forming a bilayer.[16] A perylene carboxylic derivative with a high electron affinity (electron acceptor), and copper phthalocyanine (CuPc) with a low electron affinity (electron donor) facilitated the separation of the e^-/h^+ pairs into free carriers at the interface between the donor and acceptor materials. The offset between the materials energy levels, defined as the highest occupied molecular orbital (HOMO) and the lowest unoccupied molecular orbital (LUMO), is what provided a local driving force to dissociate the charge carriers (**Figure 1.3C**). A second breakthrough by Heeger et al. consisted in the blending of the donor with the acceptor into an interpenetrating network, which was called a bulk heterojunction (BHJ) (**Figure 1.3A**).[17] A film consisting of an intermixed conjugated polymer donor, poly(2-methoxy-5-(2'-ethyl-hexyloxy)-1,4-phenylene vinylene) (MEH-PPV), with a fullerene small molecule acceptor, phenyl-C_{61}-butyric acid methyl ester ($PC_{61}BM$), enabled improved exciton separation due to the increased interfacial area between the donor and acceptor domains. The use of a donor/acceptor pair is detrimental to efficient charge dissociation and is presently employed in the majority of modern devices, and these PHJ and BHJ configurations are the most commonly used.

Fabrication of both PHJ and BHJ OPV devices consists of the sequential deposition of multiple layers onto a transparent substrate, either plastic or glass. The subsequent layers can be deposited using a combination of different solution and/or physical vapour deposition (PVD) techniques. Many organic materials such as polymers can be solubilized by organic solvents and can therefore be solution-processed. For lab scale devices, spin coating is commonly used, while large area devices can be processed via mature printing techniques such as blade coating, ink jet printing or spray coating for scale up. This would be more favorable for a low-cost continuous industrial process such as roll-to-roll printing. However, care must be taken during the fabrication of the stack to prevent the destruction of the subsequent layers. Morphology of the thin film will highly depend on the chemical structure of the active materials, but not only. Experimental parameters such as the choice of solvent, the use of co-solvents, solvent additives, the concentration, donor/acceptor mass ratio, drying-time, post anneal thermal treatments, will help improve the thin film characteristics such as crystallinity, coverage, thickness roughness or blend morphology.[18]

Another method used for the fabrication of OPVs consists of thermally evaporating an insoluble small organic molecule as a subsequent layer. This route is inherently orthogonal and suppresses the potential risk for sequential layers degrading the previous layer. PVD can be used to easily control the thickness of the thin films through control of the deposition rate. Morphology (such as crystallinity) of material thin films will depend on the deposition rate, the substrate temperature, and anneal treatments, among other parameters.[19],[20] Nonetheless, thermal evaporation requires high vacuum and bears the drawbacks of high capital and operating costs.[21]

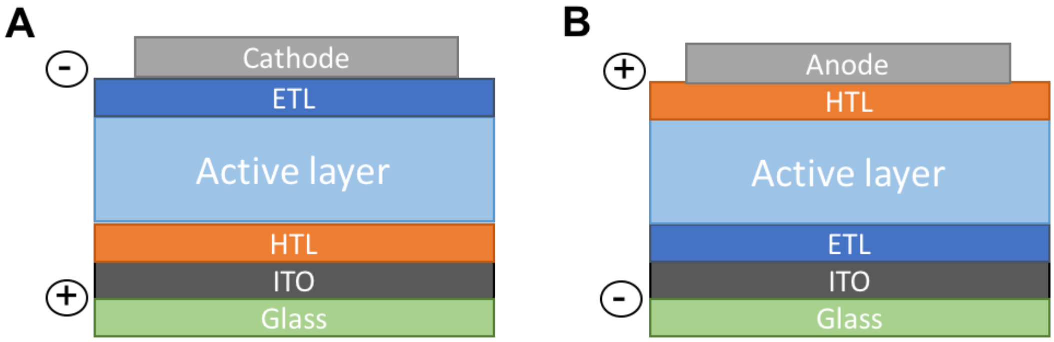

Figure 1.4. (A) Direct OPV device architecture. (B) Indirect OPV device architecture.

Commonly, an OPV device is made of a transparent back electrode, a top metal electrode, and the active layer is sandwiched between an electron transport layer (ETL) and a hole transport layer (HTL) (**Figure 1.4**). These additional charge transport layers help extracting the charges and limit recombination while acting as a buffer to prevent the electrode diffusion in the active layer.[22] The order of the thin films used in the OPV stack is based on the direction of charge transport within the device. The direction is determined by the bias applied by the electrodes material, electrons and holes being drawn towards the lower and higher work function electrode, respectively. The two architectures (direction of stacks) are called direct (**Figure 1.4A**) and indirect (**Figure 1.4B**). Independent of the architecture, indium tin oxide

(ITO) is the standard material used as the transparent electrode. Direct device architectures generally use poly(3,4-ethylenedioxythiophene):poly(styrene sulfonate) (PEDOT:PSS) as the HTL and bathucoproine (BCP) as the ETL, while the indirect devices use zinc oxide (ZnO) as the ETL and molybdenum(VI) oxide (MoO_3) as the HTL. The standard top electrode is silver (Ag) but many other materials have been investigated.[22]

1.3. OPV Devices Working Principle

The conversion of light into current in an OPV is a four steps process (**Figure 1.5**). Each step is crucial and must be completed in succession to efficiently generate current. Increasing the efficiency of any step will result in an increase in the overall device's efficiency.

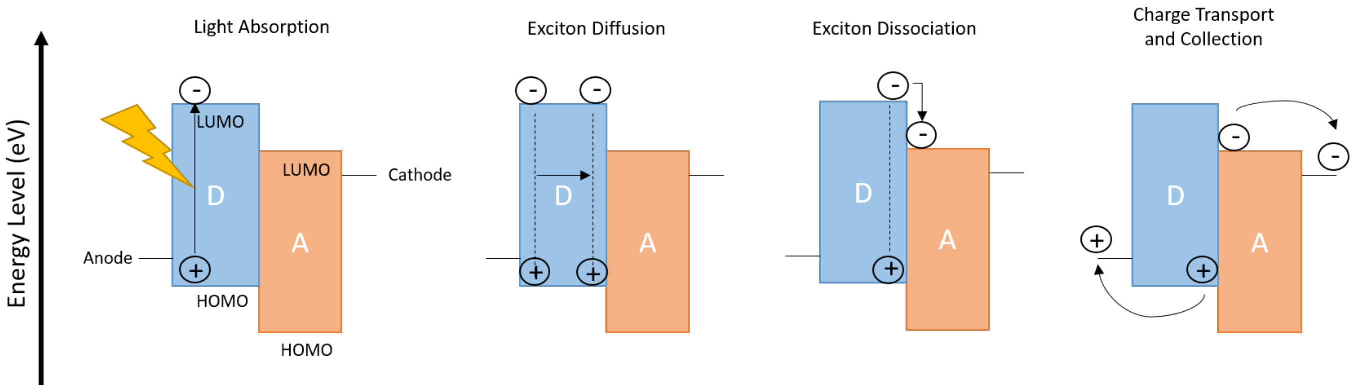

Figure 1.5. The 4 steps for photocurrent generation in an OPV device: (1) Light absorption (2) Exciton diffusion (3) Exciton separation (4) Charge transport and collection. Coloured areas represent the material band gap.

Light Absorption and Exciton Formation

An organic material is defined by its HOMO and its LUMO which are representing its valence and conductance bands respectively. The difference in energy between these two energy levels is called the band gap (E_g). The band gap is highly dependent on the level of conjugation of the semiconducting material chemical structure. If the degree of conjugation is increased, the energy difference between the HOMO and the LUMO decreases, reducing the band gap value. The band gap value is also dependant on other factors, such as the presence of hetero atoms or specific functional groups.[23] Photons with greater energy than the band gap will be absorbed and will promote an electron from the HOMO to the LUMO, leaving a positive electron hole behind and creating an exciton. Factors affecting the number of photons the organic material can absorb are the active layer thickness, the absorption spectrum, as well as its molar absorptivity.[24] Therefore, this enable the tuning of the absorption range or colour of devices depending on the desired application. Molecular structure is therefore often modified as a way to tune the absorption of the thin layer either targeting a broad absorption spectrum covering a large portion of the solar spectrum or a specific absorption of desired wavelength.

Exciton Diffusion

For the exciton to dissociate into free charge carriers, it must diffuse to the donor/acceptor interface. However, excitons have a very short lifetime on the order of 1-10 ns and therefore can only diffuse short distances prior to recombination. Therefore, an exciton has a diffusion length (L_D) typically on the order of 5-15 nm in most organic materials, before recombination occurs.[25] If this exciton is not generated close to the donor/acceptor interface, it will recombine before being able to separate into free electron and hole carriers. Interfacial surface area available between the donor and the acceptor is thus a crucial parameter and must be maximized: the greater the interfacial area, the greater the chance for exciton dissociation. Excitons can hop from molecule to molecule via either non-radiative Forster or Dexter energy transfer. Forster energy transfer involves dipole-dipole interactions between the donor and the acceptor requiring an important spectral overlap, while Dexter energy transfer involves an exchange of electrons which can only happen between immediate neighbours.[26] The distance the excitons can travel (L_D) is a function of the material structure and of the film crystallinity. Increased grain size and ordering in the crystal stack facilitate a diffusion on a longer distance due to reduced grain boundaries that can act as charge traps and induce excitons quenching.[27] Therefore, film morphology and degree of crystallinity and phase separation are crucial factors which need to be controlled through thin film processing in hopes to attain high performing devices.

Exciton Dissociation

The exciton dissociation is provided by the energetic driving force between the donor and acceptor, which is defined by the difference in HOMO and LUMO energy levels of the respective active materials. For example, when an exciton is generated in the donor material, electrons will travel from the donor LUMO energy level to the acceptor LUMO energy level. When an exciton is generated in the acceptor material, holes will be transported from the acceptor HOMO energy level to the donor HOMO energy level. For the separation to be favourable, it was commonly believed that the energy difference should have been greater than the exciton binding energy, typically 0.3 eV.[15] This led to a general typical rules for high performances OPVs [28]:

$$\left|E_{LUMO,A} - E_{LUMO,D}\right| > 0.3\ eV \text{ and } \left|E_{HOMO,A} - E_{HOMO,D}\right| > 0.3\ eV$$

However, it was recently proven that devices not following this rule were still capable of producing high efficiencies.[29],[30] As a matter of fact, other factors such as entropy, charge delocalisation, energetic disorder or hot transfer states seem to also play an important role.[31],[32]

Charge Transport and Collection

To facilitate charge extraction, free carriers must travel from the donor/acceptor interfaces to their respective electrodes. The work functions difference between the two electrodes is providing a built-in electric field capable of attracting electrons and holes to the cathode and anode, respectively. Charge carriers transport also depends on the materials electrons and holes mobilities.[33] Charge transport mobilities, which is different for each organic material and not the same for both types of carriers, should be balanced to avoid charge accumulation. In other words, the electron transport mobility in the acceptor molecule would be similar and preferably equivalent to the hole transport mobility of the donor material to reach effective separation of both types of carriers. Morphology and purity of the donor/acceptor materials also play a crucial role. While the carriers travel to respective electrodes they can recombine at the electrodes or with charge traps in the active layer. Introducing charge extracting layers between the active layer and the electrodes can help reduce the band offset between the donor and acceptor energy levels and the electrodes work function, decreasing the potential for charge recombination at the electrodes.[34] Moreover ensuring an unhindered path through each of the material to the respective electrodes, will prevent charges trapping in isolated donor/acceptor region. Charges that successfully reach the electrodes are then extracted leading to a current.

1.4. OPV Devices Characterisation

To determine the characteristic parameters of an OPV, the evolution of the current (I) with the voltage (V) applied to the cell terminals is measured under illumination. The standard within the photovoltaic community is to use an intensity of 100 mW.cm^{-2} and an air mass 1.5 (AM1.5) spectrum, corresponding to the solar spectrum when the sun is at an angle of approximately 48 °C from the horizon. This is providing an average of the yearly solar spectrum at mid-latitude regions, giving a realistic expected efficiency of devices.[35] As the photocurrent generated is dependent on the device area, current density – voltage (J-V) curves (**Figure 1.6**) are commonly reported to allow comparison between different areas.

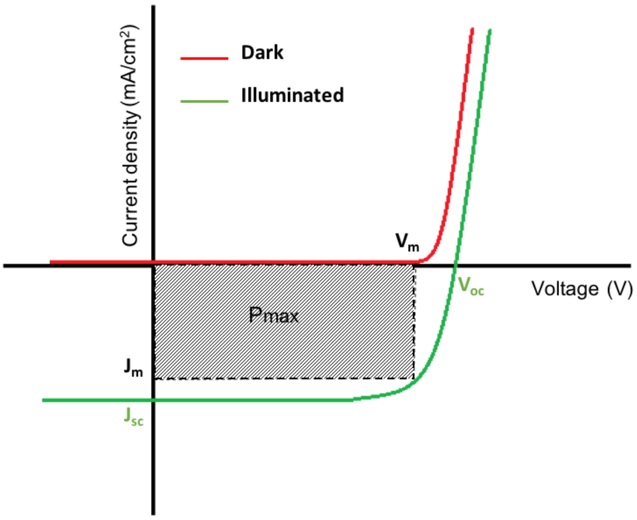

Figure 1.6. Typical J-V characteristic for an OPV in the dark (red line) and illuminated (green line).

Under dark conditions, the solar cell behaves like an ideal diode and is characterized using following the Shockley equation:

$$I = I_0\left(\exp\left(\frac{qV}{nkT}\right) - 1\right)$$

where I is the current flow, I_0 is the reverse bias current, q is the elementary charge, V is the voltage across the device, n is an ideality factor typically between 1 and 2, k is the Boltzmann constant, and T is the absolute temperature of the device. Under illumination, a photocurrent I_L is generated, and the equation becomes:

$$I = I_0\left(\exp\left(\frac{qV}{nkT}\right) - 1\right) - I_L$$

The J-V curve provides information on the power conversion efficiency (*PCE*) which is defined as the ratio of the maximum power generated by the device to the power of the incident light, per unit area and can be calculated using the following equation:

$$PCE = \frac{P_{max}}{P_{inc}} = \frac{Jsc \times Voc \times FF}{P_{inc}}$$

Where, P_{inc} is the incident light intensity in mW.cm^{-2}. *Jsc* is the short circuit current density in mA.cm^{-2}. *Jsc* is the current density generated by the OPV when the voltage applied is zero (V = 0 V), corresponding to the y-intercept of the J-V curve. The *Jsc* is representative of how many photons were absorbed and successfully converted into free charge carriers and can be increased by improving the efficiency of any of the four steps described above. The *Jsc* is correlated the organic material absorbance, mobility, and morphology.[36] The *Voc* is the open circuit voltage in V. It is the maximum voltage across the device when no current is flowing (J = 0), corresponding to the x-intercept of the J-V curve. This value is correlated to the energy difference between the HOMO level of the donor and the LUMO level of the acceptor. It is also dependant on the donor/acceptor interfacial area or the recombination losses.[37] The fill factor (*FF*) is a unitless ideality factor defined as the ratio of the theoretical maximum power output of the device to the actual power that that is defined by:

$$FF = \frac{J_m \times V_m}{Jsc \times Voc}$$

where J_m and V_m are the current and voltage at the maximum power point of the OPV, respectively. The theoretical maximum power output *Jsc* x *Voc* can be visually represented by a rectangle area that can fit within the surface area of the curve, thus, the *FF* can be seen as a measure of the "squareness" of the device characteristic. It is highly dependent on the quality of the donor/acceptor and organic material/electrode interface areas, representative of charge recombination and contact resistance.[38] However, the Shockley equation is for an ideal cell. For a cell comprising of several layers, other parameters need to be taken into account and can be extracted from the J-V curve. R_s is the series resistance in Ω.cm^2 and corresponds to resistances between each layer. R_s can be measured from the slope of the J-V curve at the *Voc* point and should be at a minimum. R_{sh} is the shunt resistance, in Ω.cm^2, and represents different short-circuits within the device. R_{sh} can be measured from the slope of the J-V curve at the *Jsc* point and should be maximized.

1.5. The Current Status of OPV Devices

OPV device most often employ conjugated donor polymers and small molecule-based acceptors in BHJ systems where materials are blended in a solvent, forming a random interpenetrating network and maximizing interfacial area. However, OPV devices based on all-polymer[39] or all-small molecule[40] active layers are still an active area of research. The most widely studied pair is poly(3-hexylthiophene) (P3HT) polymer with a PC$_{61}$BM fullerene small molecule.[41] It is usually used as a baseline in literature with a *PCE* ranging between 2 and 5%, a *Voc* average of 0.6 V, a *Jsc* average of 9 mA.cm^{-2}, and a *FF* average of 0.6.[42] P3HT became popular as a donor in part due to its ease of synthesis and purification, along with a strong affinity for self-assembly, a strong absorption in the visible region around 660 nm, and a high hole mobility. Yet, its relatively high band gap around 2 eV is problematic due to its limited absorption in the NIR region, which limits *PCE*s. Thus, further development was aimed to synthesize narrower band gap polymers to better complement fullerenes absorption that mostly covers the UV region, and increase the solar spectrum absorption overlap towards the NIR range. This was achieved by the design of “push-pull” donor-acceptor (D-A) polymers consisting of an electron rich and an electron poor unit within the backbone, facilitating fine tuning of properties such as HOMO/LUMO levels. When paired with fullerene derivatives, most push-pull polymers outperformed P3HT-based devices. Famous examples include poly[N-90-heptadecanyl-2,7-carbazole-alt-5,5-(40,70-di-2-thienyl-20,10,30-benzothiadiazole)] (PCDTBT, **Figure 1.7**) and poly([4,8-bis[(2-ethylhexyl)oxy]benzo[1,2-b:4,5-b']dithiophene-2,6-diyl][3-fluoro-2-[(2-ethylhexyl)carbonyl]thieno[3,4-b]thiophenediyl]) (PTB7, **Figure 1.7**) derivatives with E_g ranging from 1.6 to 1.9 eV, and *PCE*s ranging from 7% to above 10%.[43-45]

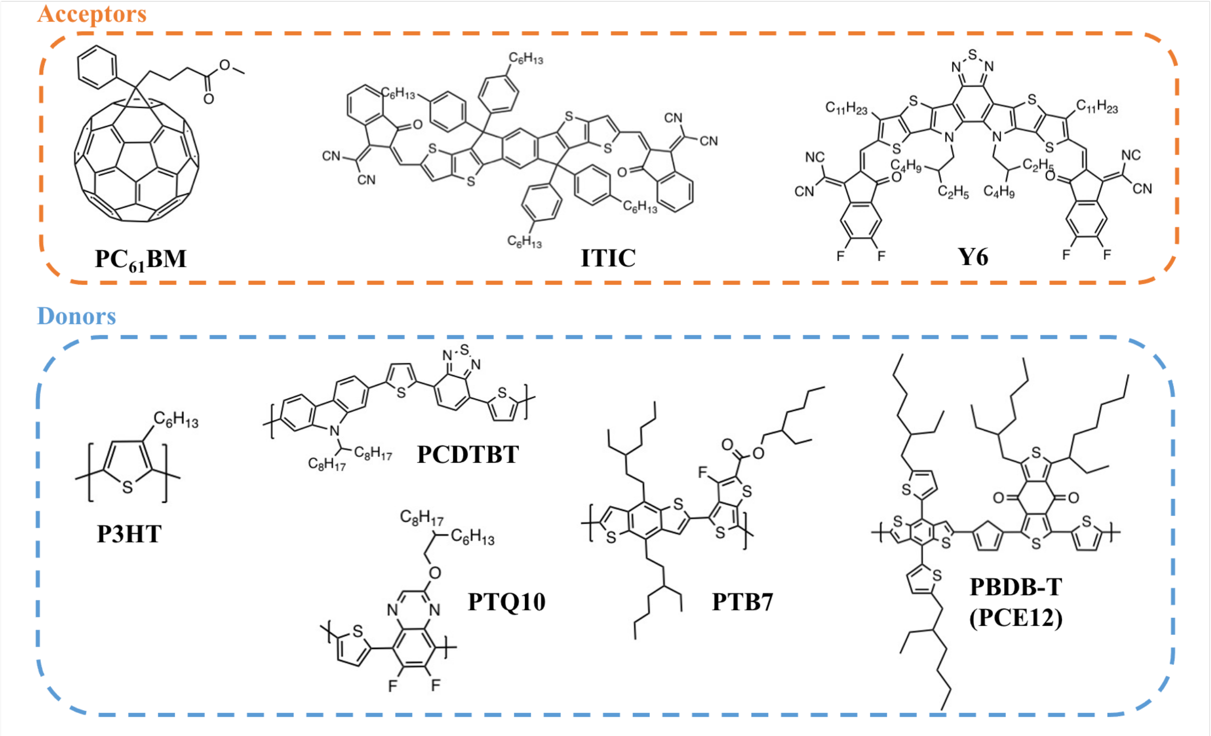

Figure 1.7. Chemical structure of common donor and acceptor materials found in literature.

Initial interests in fullerene derivatives came from their high electron affinity and their ability to form good domain sizes with donor polymers, however, their weak absorption in the Vis/NIR regions and their deep LUMO levels limits the resulting device *Voc* and *Jsc*.[46] Moreover, their rigid and ordered structure induce a poor tunability window, along with an expensive synthesis and a tendency to aggregate. For these reasons, alternatives known as non-fullerene acceptors (NFAs) small molecules based on “push-pull” architecture started to gain popularity. With expanded absorption into the NIR region these new NFAs enabled the development of wider band gap polymers with significant improvements in devices performances. The most common strategy to achieve low band gaps NFAs is to use an acceptor-donor-acceptor (A-D-A) architecture where two electron-poor units are bounded to a core electron-rich unit.

Zhan et al synthetized one of the first NFA based on these A-D-A fused-rings, ITIC (E_g = 1.59 eV, **Figure 1.7**), using an indacenodithiophene electron-rich core unit and 2-(3-oxo-2,3-dihydroinden-1-ylidene)malononitrile electron-poor end units.[47] When paired with D-A copolymer wide band gap donor, poly[(thiophene)-alt-(6,7-difluoro-2-(2-hexyldecyloxy)quinoxaline)] (PTQ10, E_g = 1.92 eV, **Figure 1.7**), it delivered devices with a *Voc* above 1 V and *PCE*s above 12%.[48],[49] The A-D-A structure proved to promote intermolecular charge transfers and strong absorption in the 500-780 nm wavelength range of the solar spectrum, improving electron mobilities and *Jsc* values. Other ITIC derivatives with methyl (ITIC-M), chlorine (ITIC-Cl) or fluorine (ITIC-F) substituents have also been explored, but more recently a top performing NFA called Y6 (E_g = 1.33 eV, **Figure 1.7**) was developed by replacing the core by a dithienothiophen[3.2-b]-pyrrolobenzothiadiazole donor unit. When Y6 was blended with D-A donor polymers, such as W1 (E_g = 2.16 eV) or poly[(2,6-(4,8-bis(5-(2-ethylhexyl)thiophen-2-yl)benzo[1,2-b:4,5-b′]dithiophene)-co-(1,3-di(5-thiophene-2-yl)-5,7-bis(2-ethylhexyl)benzo[1,2-c:4,5-c′]dithiophene-4,8-dione)] (PBDB-T) derivatives (E_g ~ 1.8-1.9 eV, **Figure 1.7**), *PCE*s >16% were reached due to increased light harvesting in the visible and NIR regions.[50-52] This extended solar absorption was achieved through engineering of the NFA core while lateral groups and side chains were introduced to promote intermolecular interactions and solubility. Recently, Y6 was paired with a new D-A copolymer donor, D18 (E_g = 1.98 eV), leading to an OPV *PCE*, of 18.2%, with a *Voc* of 0.86 V, a *Jsc* of 27.7 mA.cm^{-2}, and a *FF* of 0.77.[53] A new *PCE* record > 18.6% brake a month ago with a ternary blend involving a Y6 derivative.[54]

1.6. On the Way to OPV Commercialization

1.6.1. Current OPV Issues and Challenges

Now that OPV modules performances are becoming competitive in regards to other commercially available solar technologies, other major factors that have been put aside until now, such as scalability and cost, have to be addressed. A major drawback of the OPV field is that its been exclusively focusing on the maximization of *PCE*s leading using complex non-scalable active materials and non-scalable processing methods. A perfect example is that the synthesis of the current NFA OPV champion, Y6, requires 15 low-yielding steps and multiple column chromatography purification steps suggesting it has negligible scale up potential. The cost of OPV modules for an industrial scenario have been shown to largely rely on the active materials production cost, which itself has been closely related to the number of synthetic steps.[55],[56] Further suggesting active materials such as Y6 are likely to never make it on the OPV market. Lately, this issue has been identified by several researchers, and a shift towards more industrial relevant materials is being developed.[57] A few examples that can be cited are NFAs based on perylene diimide (PDI), a common dye used in the industry, or PTQ10, a donor polymer that involves only simple thiophene and quinoxaline units, that both produced impressive *PCE*s close or above 10%.[29],[49] However, the development of inexpensive scalable donor/acceptor pairs for commercially and industrially viable OPV modules is still a challenge today. Another issue is the use of fabrication methods that are not scalable as well. Therefore, the drastic change in the processing technique, along with inhomogeneities and variable film quality upon upscaling makes it still difficult for large-area modules to catch up with "hero" lab-scale cells.[58] Again, top performances in labs are often obtained with small area (< 0.1 cm^2) devices and with thin films deposited by spin coating using the BHJ configuration. Device performance is closely related to the active layer nanoscale morphology, and the use of BHJ introduces a level of randomness in the film formation which increases the complexity of engineering a high performing device.[59] The optimal BHJ morphology that is obtained via spin coating is often kinetically trapped and therefore when moving towards more scalable techniques such as blade coating, which have slower drying times, more optimization is required.[60],[61] Another challenge with the BHJ morphology is that predicting the final morphology as a function of processing conditions is very challenging. The resulting BHJ morphology can also forms separate domains, with no path for charges to reach their respective electrodes leading to inevitable recombination and losses in device efficiencies.[62] Further losses can emerge from the random repartition of materials as well, as donor domains can aggregate against the cathode and acceptor domains against the anode. Bimolecular recombination in blends and surface recombination at the electrode interfaces, are often amplified as the devices area increases, which can be detrimental to device performance.[63] Therefore, establishing scalable lab processes will facilitate rapid active materials assessment while providing easier transition to larger areas modules with high efficiency retainment.

1.6.2. A Dye based NFA Alternative: Silicon Phthalocyanines

Many dyes have been integrated into OPVs, such as rylene imides,[64] squaraines,[65] cyanines,[66] indigos,[67],[68] boron dipyrromethene (BODIPY),[69],[70] and porphyrins[71], (**Figure 1.8**) with *PCE*s approaching 10% in some cases. In addition to being relatively inexpensive, these dyes have a high molecular versatility, along with good chemical and thermal stability, and a strong tunable absorption in the visible and/or NIR regions of the solar spectrum. Therefore, dyes turn out to be ideal candidates for efficient and large-scale OPV modules.

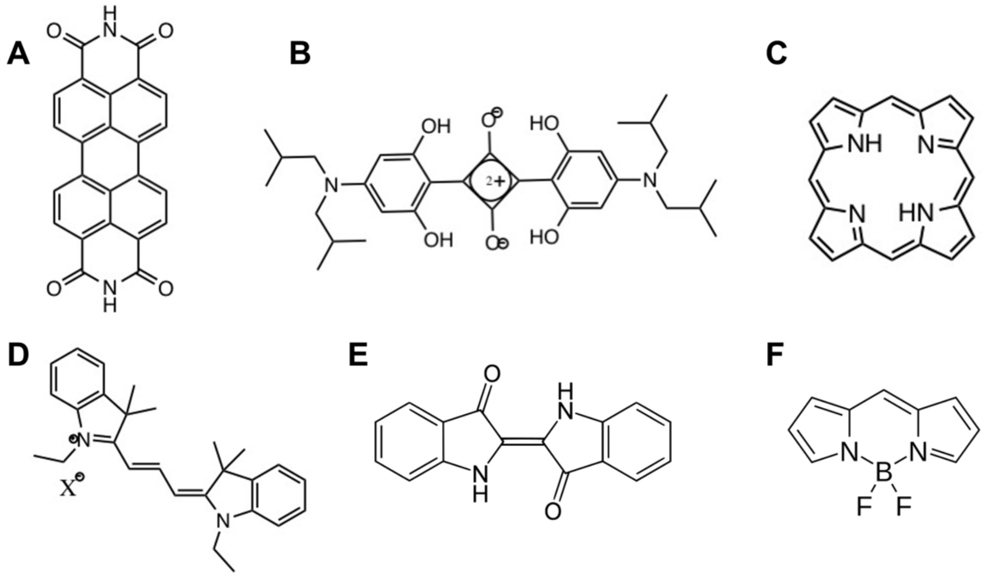

Figure 1.8. Example of chemical structures of (A) rylene imide, (B) squaraine, (C) porphyrin, (D) cyanine, (E) indigo, and (F) BODIPY dyes.

In this thesis, metal containing phthalocyanines (MPcs) are of particular interest. MPcs are molecules from the porphyrin family forming planar aromatic macrocycles consisting of four bound isoindoline groups linked to a central metal atom (**Figure 1.9**). Thanks to their extensive chemical and thermal stability, combined to their low production cost, they have been broadly used as dyes and pigments in industry and are currently produced on a ton basis each year.[72-75] Their characteristic blue/green colour originates from their conjugated macrocyclic structure, which provides strong NIR absorption, and a large area for delocalized pi electrons. MPcs have a high chemical diversity through their possible complexation with over 70 different elements and functionalization both in peripheral and axial positions (**Figure 1.9B**). These chemical handles facilitate the tuning of the resulting material properties necessary such as the band gap and HOMO/LUMO levels, solubility and solid state interactions, all critical for a wide range of emerging applications.[76],[77] They also have a high molar extinction coefficient and favorable molecular stacking, providing relatively high charge transport properties. MPcs have been employed as the active material in organic thin film transistor (OTFTs),[78] organic light emitting diodes (OLEDs),[79] in several solar technologies including DSSCs,[80] OPVs,[81] and perovskites,[82] but also as catalysts,[83] as additives for lubricants,[84] or as sensitizers in photodynamic therapy of oncological diseases[85].

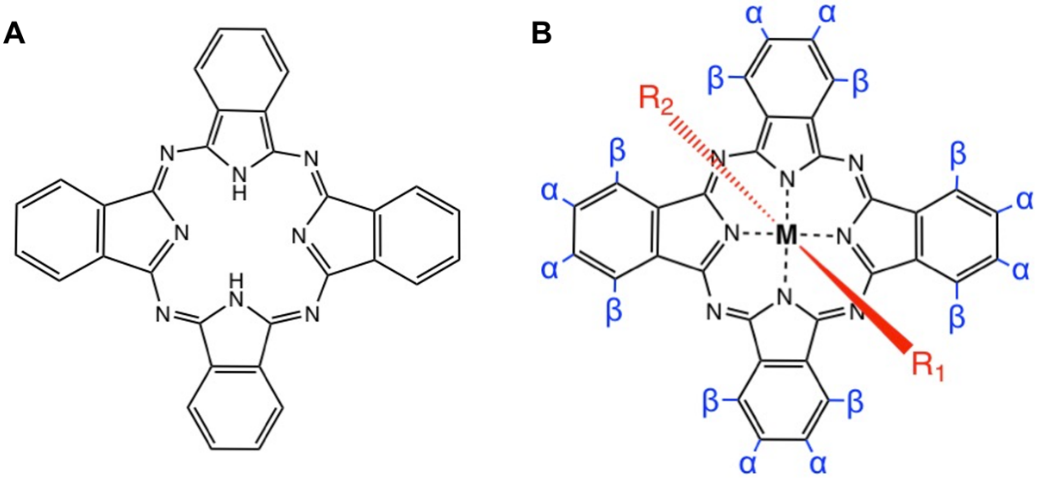

Figure 1.9. (A) Metal-free phthalocyanine, and (B) general structure for a MPc substituted with a metal atom center, and functionalized in peripheral (blue) and axial (red) positions.

The first reported bilayer OPV device was using an MPc material, and since then, the most studied MPcs are CuPc or zinc phthalocyanine (ZnPc).[86] However, Pcs usually have a poor solubility in most common organic solvents, and these compounds require chemical functionalization to become soluble. Examples of soluble CuPc and ZnPc derivatives have been reported with the addition of different peripheral substituents, such as thioalkanes,[87] trifluoroethoxy,[88] tert-butyl,[89] polyoxyethylene,[90] or sulfonic acid tetrasodium salt[91]. The incorporation of soluble CuPc and ZnPc derivatives in either blend or bilayer devices have led to OPVs with *PCE*s <1%. CuPc and ZnPc have been mainly studied as a donor layer deposited through thermal evaporation with insoluble C_{60} fullerene acceptor derivatives ; these resulting planar hetero junction (PHJ) OPVs were characterized by a *PCE*s ranging from 1% to 5%.[92-99] Recently, our group has explore the use of tetravalent Pcs such as silicon phthalocyanines (SiPc) due to their axial groups which can easily be functionalized. SiPcs are simply obtained from the formation of silicon phthalocyanine dichloride (Cl_2-SiPc) through the 1-step reaction of diiminoisoindoline with silicon tetrachloride in quinoline followed by purification by train sublimation (**Figure 1.10**).[100],[101] The incorporation of axial functional groups can provide additional solubility, and can enable the engineering of the solid state molecular stacking providing further devices optimization.[102],[103]

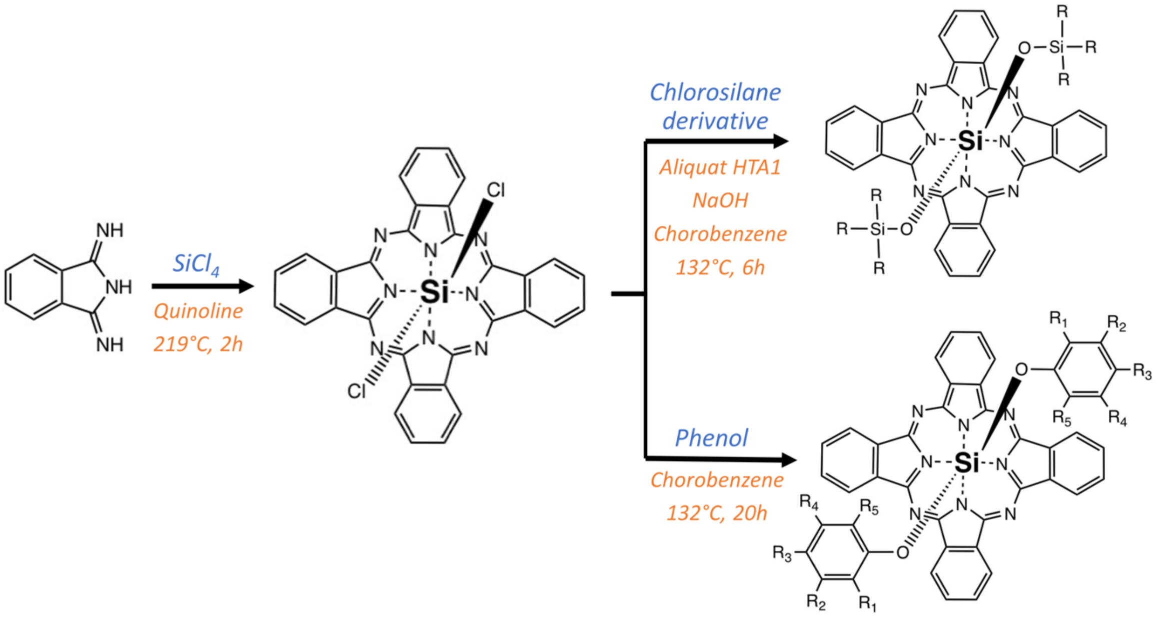

Figure 1.10. Synthetic route for SiPc derivatives reported in literature.[102]

The first modern integration of SiPc in OPV devices was reported by Honda *et. al.* in 2009.[104] The authors performed a series of studies to assess the potential of bis(tri-nhexylsilyl oxide) silicon phthalocyanine ((3HS)$_2$-SiPc, **Figure 1.11A**) as a ternary additive in P3HT:PC$_{61}$BM BHJ modules, a SiPc derivative which was first synthetized by Wheeler *et. al.* in 1984.[101] They found that the introduction of <10 wt% (3HS)$_2$-SiPc induced a 50% increase in *Jsc* and improved the overall *PCE* by 20% thanks to increased EQE contribution from P3HT:PC$_{61}$BM, and an additional EQE contribution from (3HS)$_2$-SiPc in the 650-700 nm wavelength range. The presence of bulky axial groups reduced the tendency of aggregation and phase separation, helping to maintain an optimal BHJ morphology and performance. Moreover, (3HS)$_2$-SiPc was shown to preferably migrate to the P3HT/PC$_{61}$BM interfaces, improving charge transfer and charge collection thanks to its intermediate energy levels between the donor and acceptor, and further increasing the *Jsc*.[105-107] Several studies followed, further demonstrating the potential of these SiPcs derivatives as ternary additives in BHJ devices. In 2014, Lessard et. al. observed that (3HS)$_2$-SiPc had a unique high driving force for crystallization compared to other metal substituted Pcs, and hypothesized that it facilitated the charge transfer and increased performances.[108] The Lessard research group published a follow-up study where Dang *et. al.* investigated the variation of the alkyl chain length substituent and its impact on the properties by synthetizing bis(tri-n-butylsilyl oxide) silicon phthalocyanine ((3BS)$_2$-SiPc) (**Figure 1.11B**) and bis(tri-n-isopropylsilyl oxide) silicon phthalocyanine ((3TS)$_2$-SiPc).[109] The use of these derivatives as ternary additives in P3HT:PC$_{61}$BM BHJ as well resulted in a 10% increase in *Jsc* compared to the use of $(3HS)_2$-SiPc. While they showed a similar trend for high crystallization, XRD results revealed that shorter alkyl chains were potentially forming smaller crystalline domains allowing better dispersion at the donor/acceptor interface. By synthetizing 6 more alkyl derivatives, we demonstrated that devices performances could be further improved by matching the SiPc additive solubility to that of the polymer donor.[110] The Lessard group also investigated another SiPc derivative with crosslinking groups, bis(6-azidohexanoate)silicon phthalocyanine ($(HxN_3)_2$-SiPc) (**Figure 1.11D**).[111] In P3HT:PC_{61}BM blends, it simultaneously increased the *PCE* by additional photocurrent generation in the NIR region, while stabilizing the active layer morphology with a 97% *PCE* retention after thermal ageing at 150 °C for 23 h compared to 47% for baseline devices by reducing fullerene aggregation. Honda et. al. investigated a silicon naphthalocyanine (SiNc) based ternary additive as well functionalised with tri-n-hexylsilyl axial substituents and similarly achieved an extended EQE contribution around 750-800 nm and an improved *Jsc* for P3HT:PC_{61}BM and P3HT:N2200 blend devices.[112],[113] In addition to these benefits, Lim et. al. showed that functionalisation of SiNc with tert-butyl axial substituents allowed higher dye concentration in P3HT:PC_{61}BM blends thanks to reduced aggregation.[114] This further increased the ternary additive contribution to absorption and photocurrent generation, and a *PCE* of 4.5% was achieved. More recently, Ke et. al. reported a series of pyrene-substituted SiNcs and SiPcs with different lengths of alkyl chain spacer that were incorporated as ternary and quaternary additives.[115],[116] P3HT:SiPc:PC_{61}BM systems yielded to a 20% and 50% increase of the *Jsc* and *PCE* respectively, with a *PCE* value above 4%.

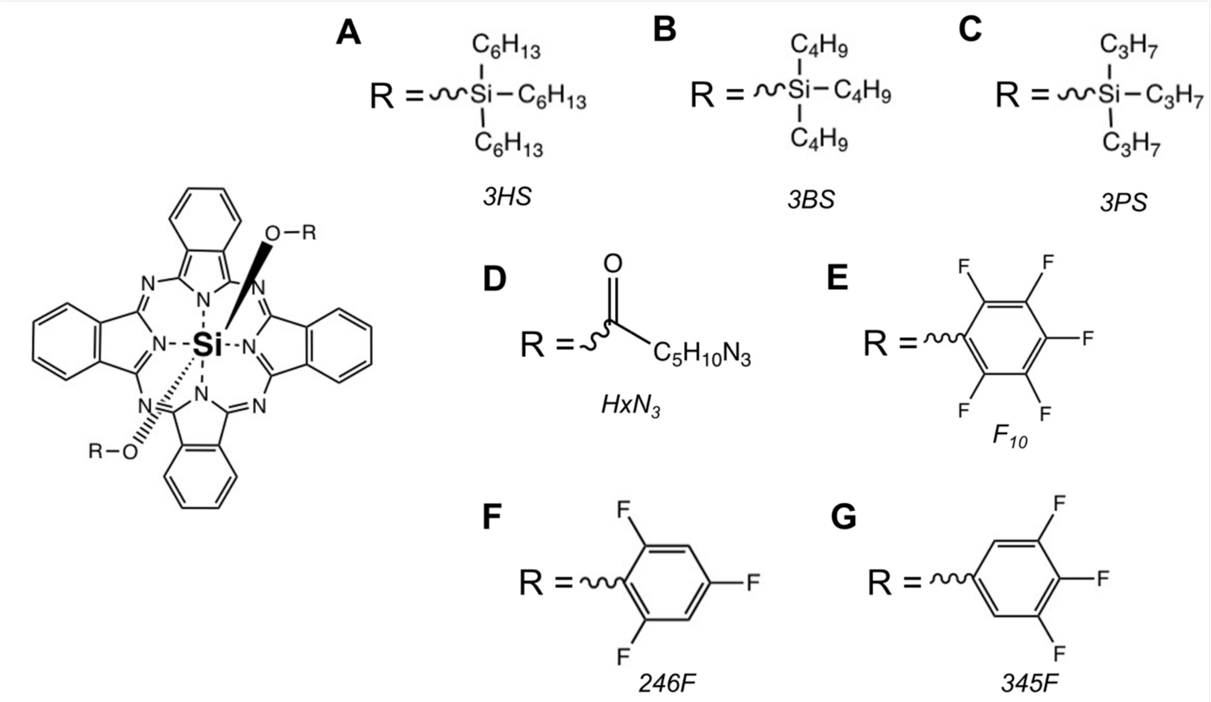

Figure 1.11. Chemical structure of (A) $(3HS)_2$-SiPc, (B) $(3BS)_2$-SiPc, (C) $(3PS)_2$-SiPc, (D) $(HxN3)_2$-SiPc, (E) F_{10}-SiPc, (F) $(246F)_2$-SiPc and (G) $(345F)_2$-SiPc.

As SiPcs have primarily been studied as ternary additives, only a few reports have investigated their potential as donor or acceptor materials. While CuPc and ZnPc were primarily used as electron donors, most SiPcs have demonstrated an n-type behavior and effectively transport electrons motivating their use as NFAs. As regards to BHJ devices, Dang *et. al.* blended $(3TS)_2$-SiPc with P3HT and achieved a modest *PCE* of 1.1%.[109] Other soluble carboxylate-substitued SiPcs synthetized by Zysman-Colman *et. al.* reached 2.7% efficiency when paired with PTB7.[117] Very recently, the Lessard group published two studies where Grant *et. al.* achieved increased performances. In the first study, they blended $(3BS)_2$-SiPc both with P3HT and PBDB-T and obtained a *PCE* of 3.6% and 3.4% respectively, with an impressive *Voc* as high as 1.10 V for the latest thanks to a minimal donor/acceptor energetic offset. [118] Characterization under reduced light showed that SiPc based devices exhibited a higher relative *PCE* compared to the $PC_{61}BM$ reference, suggesting that SiPcs could be more suitable for indoor or diffuse light applications. In the second study, bis(tri-n-propylsilyl oxide) silicon phthalocyanine ($(3PS)_2$-SiPc) (**Figure 1.11C**) was blended with P3HT and a new *PCE* record of 4.3% for SiPc based devices was achieved.[119] A significant phase separation due to strong $(3PS)_2$-SiPc crystallization created a unique P3HT:$(3PS)_2$-SiPc morphology.

As regards to bilayer devices, only sublimable SiPc molecules were used. First, Lessard *et. al.* assessed the potential of Cl_2-SiPc and bis(pentafluoro phenoxy) silicon phthalocyanine

(F_{10}-SiPc) (**Figure 1.11E**) as both donors and acceptors in evaporation processed PHJ devices.[120] While addition of pentafluoro phenoxy substituents had no effects on the optophysical properties, it modified the solid-state arrangement and provided a greater degree of π-π overlap between the neighbouring SiPc molecules. Therefore, F_{10}-SiPc outperformed Cl_2-SiPc both as an electron donor and acceptor when paired with a C_{60} acceptor and a pentacene or an α-sexithiophene (α-6T) donor, with *PCE*s around 0.4%. In a follow-up study, Lessard et. al. investigated the impact of fluoro atoms positions and frequency change on the material properties and arrangement, and therefore on the devices performances.[121] They synthetized bis(2,4,6-trifluorophenoxy) SiPc ($(246F)_2$-SiPc) (**Figure 1.11F**) and (bis(3,4,5-trifluorophenoxy) SiPc ($(345F)_2$-SiPc) (**Figure 1.11G**), but noticed only small changes in UV-Vis absorption, energy levels, and solid state arrangement. When used as NFAs, α-6T/$(246F)_2$-SiPc and α-6T/$(345F)_2$-SiPc systems achieved a *PCE* of 0.87% and 1% respectively for unoptimized devices. However, $(246F)_2$-SiPc emerged as a material with a dual functionality reaching a *PCE* up to 1.8% with a *Voc* as high as 0.9 V for $(246F)_2$-SiPc/C_{60} devices.

1.6.3. A Fabrication Alternative: Layer-by-Layer for Better Scale Up

Commercialization of OPV modules is likely to be achieved through roll-to-roll fabrication processes. However, as pointed out above, current popular lab device fabrication strategies often don't translate to roll-to-roll. Very recently, more attention has been paid to a pseudo-bilayer configuration using a layer-by-bilayer (LbL) fabrication method, where the layers are successively deposited.[62],[122-129] Sequentially processed OPV devices are commonly all-solution processed where both layers are deposited from orthogonal or non-orthogonal solvents. In some cases, the second layer can be thermally evaporated as well.[130],[131] The LbL approach possesses many advantages compared to the BHJ configuration that could help reduce the efficiency-stability gap. The use of the LbL method has shown to promote a more thermodynamically favourable nanoscale morphology where enough donor/acceptor interfacial area is formed, while maintaining neat acceptor and donor layers at the right electrodes to reduce bimolecular recombination.[132] Greater light absorption coefficients, stronger charge transfer driving force, and a more stable morphology have all been observed. This morphology can be controlled and optimized through independent tuning of each layer and processing conditions, and interfacial properties can more easily be characterized helping the design of modules through a better understanding of the link morphology/efficiency.[133] This part has been more deeply reviewed in **Chapter 2**.

1.7. Scope of Thesis

This chapter introduced the OPV technology, including its position in the solar market, its particular aspects and principle of functioning, as well as the commonly used active materials and device architectures. Critical challenges of the OPV technology have been outlined and involve the lack of commercially viable active materials, as well as the poor scalability of lab reported devices. MPcs, and particularly SiPcs, have proved to be promising active compounds that could be obtained through very cheap and straightforward chemistry. Their study remains limited and the few reports existing principally cover their use as ternary additives or as NFAs in BHJ devices. Hence, the aim of this thesis is to suppress the need for the BHJ structure to achieve good performances and assess the role of SiPcs as NFAs into bilayer devices. Focus is set on device engineering in order to assess different ways of fabricating devices and optimizing performances.

1) In **Chapter 2**, a complete review of materials and processing conditions used for the fabrication of all-solution and hybrid solution-evaporation LbL bilayer OPVs along with their performances, have been undertaken. The goal is to reappraise the systematic need for a BHJ structure to achieve top performances, showing that the bilayer architecture is indeed a promising alternative to attain both performing and upscaled devices. Focus has also been set on gathering important processing conditions information for device fabrication, highlighting the lack of crucial experimental details report from researchers in literature.
2) In **Chapter 3**, sublimable SiPc derivatives were further investigated as NFAs in hybrid solution-evaporation bilayer devices with an extended optimization of devices processing conditions, which include spin rate and several thermal treatments. The SiPc derivatives were also paired with several soluble polymer donors.
3) In **Chapter 4**, soluble SiPc derivatives were first introduced into all-solution processed bilayer OPV devices. Extended device engineering was performed with investigation of different solvent systems, spin rates, deposition kinetics, thermal treatments, and variation of the hole transporting layers. Different donor/acceptor systems were also investigated.
4) In **Chapter 5**, the extent of SiPcs application in multiple solar technologies was assessed by using them as electron transporting layers in perovskite solar cells. Different sublimable SiPc derivatives were investigated.

5) Finally, in **Chapter 6** I will identify and highlight the leads that should be pursued in the future.

1.8. References

1. Bastien, D. & Athienitis, A. Le potentiel des énergies solaires au Québec. *Greenpeace* (2011).
2. Kabir, E., Kumar, P., Kumar, S., Adelodun, A. A. & Kim, K. H. Solar energy: Potential and future prospects. *Renew. Sustain. Energy Rev.* **82**, 894–900 (2018).
3. IEA. *World Energy Outlook 2020*. https://www.iea.org/reports/world-energy-outlook-2020 (2020).
4. Chapin, D. M., Fuller, C. S. & Pearson, G. L. A new silicon p-n junction photocell for converting solar radiation into electrical power. *J. Appl. Phys.* **25**, 676–677 (1954).
5. Yoshikawa, K. *et al.* Silicon heterojunction solar cell with interdigitated back contacts for a photoconversion efficiency over 26%. *Nat. Energy* **2**, (2017).
6. Nakamura, M. *et al.* Cd-Free Cu(In, Ga)(Se, S)2 Thin-Film Solar Cell With Record Efficiency of 23. 35 %. *IEEE J. Photovoltaics* **9**, 1863–1867 (2019).
7. Al-Ashouri, A. *et al.* Monolithic perovskite/silicon tandem solar cell with >29% efficiency by enhanced hole extraction. *Science (80-.).* **370**, 1300–1309 (2020).
8. Djurišić, A. B. *et al.* Perovskite solar cells - An overview of critical issues. *Prog. Quantum Electron.* **53**, 1–37 (2017).
9. Coakley, K. M. & Mcgehee, M. D. Conjugated polymer photovoltaic cells. *Chem. Mater.* **16**, 4533–4542 (2004).
10. Lizin, S. *et al.* Life cycle analyses of organic photovoltaics: a review. *Energy Environ. Sci.* **6**, 3136–3149 (2013).
11. Li, N. & Brabec, C. J. Washing away barriers. *Nat. Energy* **2**, 772–773 (2017).
12. Ryu, H. S., Park, S. Y., Lee, T. H., Kim, J. Y. & Woo, H. Y. Recent progress in indoor organic photovoltaics. *Nanoscale* **12**, 5792–5804 (2020).
13. Satharasinghe, A., Hughes-Riley, T. & Dias, T. A review of solar energy harvesting electronic textiles. *Sensors (Switzerland)* **20**, 1–39 (2020).
14. Meitzner, R., Schubert, U. S. & Hoppe, H. Agrivoltaics—The Perfect Fit for the Future of Organic Photovoltaics. *Adv. Energy Mater.* **11**, 2002551 (2021).
15. Knupfer, M. Exciton binding energies in organic semiconductors. *Appl. Phys. A* **626**, 623–626 (2003).
16. Tang, C. W. Two-layer organic photovoltaic cell. *Appl. Phys. Lett.* **48**, 183–185 (1986).
17. Yu, G., Gao, J., C, H. J., Wudl, F. & Heeger, A. J. Polymer Photovoltaic Cells: Enhanced Efficiencies via a Network of Internal Donor-Acceptor Heterojunctions. *Science (80-.).* **270**, 1789–1792 (1995).
18. Moulé, B. A. J. & Meerholz, K. Controlling morphology in polymer – fullerene mixtures **. *Adv. Mater.* **20**, 240–245 (2008).
19. Derby, B., Cui, Y., Baldwin, J. K. & Misra, A. Effects of substrate temperature and deposition rate on the phase separated morphology of co-sputtered, Cu-Mo thin films. *Thin Solid Films* **647**, 50–56 (2018).
20. Verploegen, E. *et al.* Effects of thermal annealing upon the morphology of polymer-fullerene blends. *Adv. Funct. Mater.* **20**, 3519–3529 (2010).
21. Chen, Y., Szuheng, H., Shuyi, L. & Franky, S. Review of recent progress in multilayer solution-processed organic light-emitting diodes. *J. Photonics Energy* **5**, 057611 (2019).
22. Steim, R., Ren, F. & Brabec, C. J. Interface materials for organic solar cells †. *J. Mater. Chem.* **20**, 2499–2512 (2010).
23. Park, Y. S., Kale, T. S., Nam, C. Y., Choi, D. & Grubbs, R. B. Effects of heteroatom substitution in conjugated heterocyclic compounds on photovoltaic performance: From sulfur to tellurium. *Chem. Commun.* **50**, 7964–7967 (2014).
24. Min Nam, Y., Huh, J. & Ho Jo, W. Optimization of thickness and morphology of active layer for high performance of bulk-heterojunction organic solar cells. *Sol. Energy Mater.*

Sol. Cells **94**, 1118–1124 (2010).

25. Wan, X., Long, G., Huang, L. & Chen, Y. Graphene – a promising material for organic photovoltaic cells. *Adv. Mater.* **23**, 5342–5358 (2011).
26. Mikhnenko, O. V, Blom, P. W. M. & Nguyen, T. Exciton diffusion in organic semiconductors. *Energy Environ. Sci.* **8**, 1867–1888 (2015).
27. Lunt, R. R., Benziger, J. B. & Forrest, S. R. Relationship between crystalline order and exciton diffusion length in molecular organic semiconductors. *Adv. Mater.* **22**, 1233–1236 (2010).
28. Scharber, B. M. C. *et al.* Design rules for donors in bulk-heterojunction solar cells — towards 10 % energy-conversion efficiency **. *Adv. Mater.* **18**, 789–794 (2006).
29. Liu, J. *et al.* Fast charge separation in a non-fullerene organic solar cell with a small driving force. *Nat. Energy* **1**, (2016).
30. Tang, A. *et al.* Simultaneously Achieved High Open-Circuit Voltage and Efficient Charge Generation by Fine-Tuning Charge-Transfer Driving Force in Nonfullerene Polymer Solar Cells. *Adv. Funct. Mater.* **28**, 1704507 (2017).
31. Tamura, H. & Burghardt, I. Ultrafast Charge Separation in Organic Photovoltaics Enhanced by Charge Delocalization and Vibronically Hot Exciton Dissociation. *J. Am. Chem. Soc.* **135**, 16364–16367 (2013).
32. Hood, S. N. & Kassal, I. Entropy and Disorder Enable Charge Separation in Organic Solar Cells. *J. Phys. Chem. Lett.* **7**, 4495–4500 (2016).
33. Mihailetchi, V. D., Wildeman, J. & Blom, P. W. M. Space-charge limited photocurrent. *Phys. Rev. Lett.* **94**, 126602 (2005).
34. Kettle, J., Waters, H., Horie, M. & Chang, S. W. Effect of hole transporting layers on the performance of PCPDTBT:PCBM organic solar cells. *J. Phys. D. Appl. Phys.* **45**, 125102 (2012).
35. Riordan, C. & Hulstrom, R. What is an Air Mass 1.5 spectrum? in *Proceedings of the Conference Record 21st IEEE Photovoltaic Specialists Conference 2* 1085–1088 (1990).
36. Kim, D. H., Jeon, Y. P., Lee, S. H., Lee, D. U. & Kim, T. W. Enhancement of the power conversion efficiency for organic photovoltaic devices due to an embedded rugged nanostructural layer. *Org. Electron.* **13**, 1068–1072 (2012).
37. Elumalai, N. K. & Uddin, A. Open circuit voltage of organic solar cells: an in-depth review. *Energy Environ. Sci.* **9**, 391–410 (2016).
38. Bartesaghi, D. *et al.* Competition between recombination and extraction of free charges determines the fill factor of organic solar cells. *Nat. Commun.* **6**, 2–11 (2015).
39. Zhou, N. & Facchetti, A. Naphthalenediimide (NDI) polymers for all-polymer photovoltaics. *Mater. Today* **21**, 377–390 (2018).
40. Collins, S. D., Ran, N. A., Heiber, M. C. & Nguyen, T. Small is Powerful : Recent Progress in Solution-Processed Small Molecule Solar Cells. *Adv. Energy Mater.* **7**, 1602242 (2017).
41. Dang, M. T., Hirsch, L. & Wantz, G. P3HT:PCBM, best seller in polymer photovoltaic research. *Adv. Mater.* **23**, 3597–3602 (2011).
42. Oklobia, O. & Shafai, T. S. A study of donor/acceptor interfaces in a blend of P3HT/PCBM solar cell: Effects of annealing and PCBM loading on optical and electrical properties. *Solid State Electron.* **87**, 64–68 (2013).
43. Gholamkhass, B. & Servati, P. Solvent-vapor induced morphology reconstruction for efficient PCDTBT based polymer solar cells. *Org. Electron. physics, Mater. Appl.* **14**, 2278–2283 (2013).
44. He, Z. *et al.* Single-junction polymer solar cells with high efficiency and photovoltage. *Nat. Photonics* **9**, 174–179 (2015).
45. Kraus, H. *et al.* Analysis of Triplet Exciton Loss Pathways in PTB7:PC71BM Bulk

Heterojunction Solar Cells. *Sci. Rep.* **6**, 29158 (2016).

46. Kooistra, F. B. *et al.* Increasing the open circuit voltage of bulk-heterojunction solar cells by raising the LUMO level of the acceptor. *Org. Lett.* **9**, 551–554 (2007).
47. Lin, Y. *et al.* An Electron Acceptor Challenging Fullerenes for Efficient Polymer Solar Cells. *Adv. Mater.* **27**, 1170–1174 (2015).
48. Xu, Z. *et al.* Understanding the Morphology of High-Performance Solar Cells Based on a Low-Cost Polymer Donor. *Appl. Mater. Interfaces* **12**, 9537–9544 (2020).
49. Sun, C. *et al.* A low cost and high performance polymer donor material for polymer solar cells. *Nat. Commun.* **9**, 1–10 (2018).
50. Yuan, J. *et al.* Single-Junction Organic Solar Cell with over 15 % Efficiency Using Fused-Ring Acceptor with Electron-Deficient Core Single-Junction. *Joule* **3**, 1–12 (2019).
51. Wang, T. *et al.* A 2.16eV bandgap polymer donor gives 16% power conversion efficiency. *Sci. Bull.* **65**, 179–181 (2020).
52. Zheng, Z. *et al.* PBDB-T and its derivatives: A family of polymer donors enables over 17 % efficiency in organic photovoltaics. *Mater. Today* **35**, 115–130 (2020).
53. Liu, Q. *et al.* 18 % Efficiency organic solar cells. *Sci. Bull.* 1–10 (2020) doi:10.1016/j.scib.2020.01.001.
54. Cai, Y. *et al.* A Well-Mixed Phase Formed by Two Compatible Non-Fullerene Acceptors Enables Ternary Organic Solar Cells with Efficiency over 18.6 %. *Adv. Mater.* 2101733 (2021) doi:10.1002/adma.202101733.
55. Machui, F. *et al.* Cost analysis of roll-to-roll fabricated ITO free single and tandem organic solar modules based on data from manufacture. *Energy Environ. Sci.* **7**, 2792–2802 (2014).
56. Osedach, T. P., Andrew, T. L. & Bulovic, V. Effect of synthetic accessibility on the commercial viability of organic photovoltaics †. *Energy Environ. Sci.* **6**, 711–718 (2013).
57. Wadsworth, A. *et al.* Critical review of the molecular design progress in non-fullerene electron acceptors towards commercially viable organic solar cells †. *Chem Soc Rev* **48**, 1596–1625 (2019).
58. Lucera, L. *et al.* Guidelines for Closing the Efficiency Gap between Hero Solar Cells and Roll-To-Roll Printed Modules. *Energy Technol.* **3**, 373–384 (2015).
59. Brabec, C. J., Heeney, M., McCulloch, I. & Nelson, J. Influence of blend microstructure on bulk heterojunction organic photovoltaic performance. *Chem. Soc. Rev.* **40**, 1185–1199 (2011).
60. Schaffer, C. J. *et al.* A direct evidence of morphological degradation on a nanometer scale in polymer solar cells. *Adv. Mater.* **25**, 6760–6764 (2013).
61. Zhang, Y. *et al.* Thermally Stable All-Polymer Solar Cells with High Tolerance on Blend Ratios. *Adv. Energy Mater.* **8**, 1–10 (2018).
62. Sun, R. *et al.* A Layer-by-Layer Architecture for Printable Organic Solar Cells Overcoming the Scaling Lag of Module Efficiency. *Joule* **4**, 1–13 (2020).
63. Fukuhara, T., Tamai, Y. & Ohkita, H. Nongeminate charge recombination in organic photovoltaics. *Sustain. Energy Fuels* **4**, 4321–4351 (2020).
64. Feng, J., Jiang, W. & Wang, Z. Synthesis and Application of Rylene Imide Dyes as Organic Semiconducting Materials. *Chem. an Asian J.* **13**, 20–30 (2018).
65. Chen, G., Sasabe, H., Igarashi, T., Hong, Z. & Kido, J. Squaraine dyes for organic photovoltaic cells. *J. Mater. Chem. A* **3**, 14517–14534 (2015).
66. Zhang, H. *et al.* Semitransparent organic photovoltaics using a near-infrared absorbing cyanine dye. *Sol. Energy Mater. Sol. Cells* **118**, 157–164 (2013).
67. Fallon, K. J. & Bronstein, H. Indolonaphthyridine: A Versatile Chromophore for Organic Electronics Inspired by Natural Indigo Dye. *Acc. Chem. Res.* **54**, 182–193 (2021).

68. Brebels, J. *et al.* Low bandgap polymers based on bay-annulated indigo for organic photovoltaics : Enhanced sustainability in material design and solar cell fabrication. *Org. Electron.* **50**, 264–272 (2017).
69. Rao, R. S., Bagui, A., Rao, G. H., Gupta, V. & Singh, S. P. Achieving the highest efficiency using a BODIPY core decorated with dithiafulvalene wings for small molecule based solution-processed organic. *Chem. Commun.* **53**, 6953–6956 (2017).
70. Aguiar, A. *et al.* Synthesis, characterization and application of meso-substituted fluorinated boron dipyrromethenes (BODIPYs) with different styryl groups in organic photovoltaic cells. *Dye. Pigment.* **168**, 103–110 (2019).
71. Mahmood, A. *et al.* Recent progress in porphyrin-based materials for organic solar cells. *J. Mater. Chem. A* **6**, 16769–16797 (2018).
72. Listigovers, N. A. *et al.* Hydroxygallium phthalocyanine pigments with block copolymer binders. U.S. Patent 5521043. (1996).
73. Giambalvo, V. A. & Lee, W. Non-crystallizing, non-flocculating phthalocyanines. U.S. Patent 3589924. (1971).
74. Gregory, P. Industrial applications of phthalocyanines. *J. Porphyr. Phthalocyanines* **4**, 432–437 (2000).
75. De La Torre, G., Claessens, C. G. & Torres, T. Phthalocyanines: Old dyes, new materials. Putting color in nanotechnology. *Chem. Commun.* 2000–2015 (2007) doi:10.1039/b614234f.
76. Perevalov, V. P., Vinokurov, E. G., Zuev, K. V, Vasilenko, E. A. & Tsivadze, A. Y. Modification and application of metal phthalocyanines in heterogeneous systems. *Prot. Met. Phys. Chem. Surfaces* **53**, 199–214 (2017).
77. Wöhrle, D., Schnurpfeil, G., Makarov, S. G., Kazarin, A. & Suvorova, O. N. Practical Applications of Phthalocyanines – from Dyes and Pigments to Materials for Optical, Electronic and Photo-electronic Devices. *Macroheterocycles* **5**, 191–202 (2012).
78. Li, X. *et al.* Copper phthalocyanine thin film transistors for hydrogen sulfide detection. *Sensors Actuators, B Chem.* **176**, 1191–1196 (2013).
79. Pearson, A. J. *et al.* Silicon phthalocyanines as dopant red emitters for efficient solution processed OLEDs. *J. Mater. Chem. C* **5**, 12688–12698 (2017).
80. Martin-Gomis, L., Fernandez-Lazaro, F. & Sastre-Santos, A. Advances in phthalocyanines-sensitized solar cells (PcSSCs). *J. Mater. Chem. A* **2**, 15672–15682 (2014).
81. Yuen, A. P. *et al.* Photovoltaic properties of M-phthalocyanine/fullerene organic solar cells. *Sol. Energy* **86**, 1683–1688 (2012).
82. Haider, M. *et al.* Nickel phthalocyanine as an excellent hole-transport material in inverted planar perovskite solar cells. *Chem. Commun.* **55**, 5343–5346 (2019).
83. Sorokin, A. B. Phthalocyanine Metal Complexes in Catalysis. *Chem. Rev.* **113**, 8152–8191 (2013).
84. Tewari, U. S. & Sharma, S. K. Physico-chemical studies on potential lubricants: phthalocyanines. *Tribol. Int.* **22**, 253–258 (1989).
85. Zhang, X., Xi, Q. & Zhao, J. Fluorescent and triplet state photoactive J-type phthalocyanine nano assemblies: controlled formation and photosensitizing properties. *J. Mater. Chem.* **20**, 6726–6733 (2010).
86. Williams, G., Sutty, S., Klenkler, R. & Aziz, H. Renewed interest in metal phthalocyanine donors for small molecule organic solar cells. *Sol. Energy Mater. Sol. Cells* **124**, 217–226 (2014).
87. Varotto, A. *et al.* Phthalocyanine Blends Improve Bulk Heterojunction Solar Cells. *J. Am. Chem. Soc.* **132**, 2552–2554 (2010).
88. Yamada, I., Umeda, M., Hayashi, Y., Soga, T. & Shibata, N. Fundamental Study on

Organic Solar Cells Based on Soluble Zinc Phthalocyanine. *Jpn. J. Appl. Phys.* **51**, 04DK09 (2012).

89. Bekalé, L. *et al.* Solution-processed tBu4-ZnPc:C61bulk heterojunction organic photovoltaic cells. *Jpn. J. Appl. Phys.* **55**, 032301 (2016).
90. Kadem, B., Nur Kaya, E., Hassan, A., Durmuş, M. & Basova, T. Composite materials of P3HT:PCBM with pyrene substituted zinc (II) phthalocyanines: Characterisation and application in organic solar cells. *Sol. Energy* **189**, 1–7 (2019).
91. Schumann, S., Hatton, R. A. & Jones, T. S. Organic Photovoltaic Devices Based on Water-Soluble Copper Phthalocyanine. *J. Phys. Chem. C* **115**, 4916–4921 (2011).
92. Chen, W. B. *et al.* Improving efficiency of organic photovoltaic cells with pentacene-doped CuPc layer. *Appl. Phys. Lett.* **91**, (2007).
93. Brumbach, M., Placencia, D. & Armstrong, N. R. Titanyl phthalocyanine/C60 heterojunctions: Band-edge offsets and photovoltaic device performance. *J. Phys. Chem. C* **112**, 3142–3151 (2008).
94. Xue, B. J., Rand, B. P., Uchida, S. & Forrest, S. R. A hybrid planar-mixed molecular heterojunction photovoltaic cell **. *Adv. Mater.* **17**, 66–71 (2005).
95. Song, Q. L. *et al.* Small-molecule organic solar cells with improved stability. *Chem. Phys. Lett.* **416**, 42–46 (2005).
96. Wang, N., Yu, J., Zang, Y., Huang, J. & Jiang, Y. Effect of buffer layers on the performance of organic photovoltaic cells based on copper phthalocyanine and C60. *Sol. Energy Mater. Sol. Cells* **94**, 263–266 (2010).
97. Peumans, P. & Forrest, S. R. Very-high-efficiency double-heterostructure copper phthalocyanine/C60 photovoltaic cells. *Appl. Phys. Lett.* **79**, 126–128 (2001).
98. Zhou, Y. *et al.* Phase separation of co-evaporated ZnPc:C60 blend film for highly efficient organic photovoltaics. *Appl. Phys. Lett.* **100**, 233302 (2012).
99. Zeng, W., Yong, K. S., Kam, Z. M., Zhu, F. & Li, Y. Effect of blend layer morphology on performance of ZnPc/C60 based photovoltaic cells. *Appl. Phys. Lett.* **97**, 133304 (2010).
100. Lowery, M. K., Starshak, A. J., Esposito, J. N., Krueger, P. C. & Kenney, M. E. Dichloro(phthalocyanino)silicon. *Inorg. Chem.* **128**, (1965).
101. Wheeler, B. L. *et al.* A Silicon Phthalocyanine and a Silicon Naphthalocyanine: Synthesis, Electrochemistry, and Electrogenerated Chemiluminescence. *J. Am. Chem. Soc.* **106**, 7404–7410 (1984).
102. Grant, T. M. *et al.* Boron subphthalocyanines and silicon phthalocyanines for use as active materials in organic photovoltaics. *Chem. Rec.* **19**, 1–21 (2019).
103. Lessard, H. The Rise of Silicon Phthalocyanine : From Organic Photovoltaics to Organic Thin Film Transistors. *Appl. Mater. Interfaces* **13**, 31321–31330 (2021).
104. Honda, S., Nogami, T., Ohkita, H., Benten, H. & Ito, S. Improvement of the light-harvesting efficiency in polymer/fullerene bulk heterojunction solar cells by interfacial dye modification. *ACS Appl. Mater. Interfaces* **1**, 804–810 (2009).
105. Honda, S., Ohkita, H., Benten, H. & Ito, S. Multi-colored dye sensitization of polymer/fullerene bulk heterojunction solar cells. *Chem. Commun.* **46**, 6596–6598 (2010).
106. Honda, S., Yokoya, S., Ohkita, H., Benten, H. & Ito, S. Light-harvesting mechanism in polymer/fullerene/dye ternary blends studied by transient absorption spectroscopy. *J. Phys. Chem. C* **115**, 11306–11317 (2011).
107. Honda, S., Ohkita, H., Benten, H. & Ito, S. Selective dye loading at the heterojunction in polymer/fullerene solar cells. *Adv. Energy Mater.* **1**, 588–598 (2011).
108. Lessard, B. H. *et al.* Bis(tri- n -hexylsilyl oxide) silicon phthalocyanine: A unique additive in ternary bulk heterojunction organic photovoltaic devices. *ACS Appl. Mater.*

Interfaces **6**, 15040–15051 (2014).

109. Dang, M. T. *et al.* Bis(tri-n-alkylsilyl oxide) silicon phthalocyanines: A start to establishing a structure property relationship as both ternary additives and non-fullerene electron acceptors in bulk heterojunction organic photovoltaic devices. *J. Mater. Chem. A* **5**, 12168–12182 (2017).
110. Vebber, M. C., Grant, T. M., Brusso, J. L. & Lessard, B. H. Bis(trialkylsilyl oxide) Silicon Phthalocyanines: Understanding the Role of Solubility in Device Performance as Ternary Additives in Organic Photovoltaics. *Langmuir* **36**, 2612–2621 (2020).
111. Grant, T. M., Gorisse, T., Dautel, O., Wantz, G. & Lessard, B. H. Multifunctional ternary additive in bulk heterojunction OPV: Increased device performance and stability. *J. Mater. Chem. A* **5**, 1581–1587 (2017).
112. Ito, S. *et al.* Near-infrared dye sensitization of polymer/polymer thin-film solar cells. *Mol. Cryst. Liq. Cryst.* **578**, 19–25 (2013).
113. Xu, H., Ohkita, H., Hirata, T., Benten, H. & Ito, S. Near-IR dye sensitization of polymer blend solar cells. *Polymer (Guildf).* **55**, 2856–2860 (2014).
114. Lim, B., Bloking, J. T., Ponec, A., Mcgehee, M. D. & Sellinger, A. Ternary Bulk Heterojunction Solar Cells: Addition of Soluble Dyes for Photocurrent Generation beyond 800 nm. *ACS Appl. Mater. Interfaces* **6**, 6905–6913 (2014).
115. Ke, L. *et al.* A Series of Pyrene-Substituted Silicon Phthalocyanines as Near-IR Sensitizers in Organic Ternary Solar Cells. *Adv. Energy Mater.* **6**, 1502355 (2016).
116. Ke, L. *et al.* Panchromatic ternary/quaternary polymer/fullerene BHJ solar cells based on novel silicon naphthalocyanine and silicon phthalocyanine dye sensitizers. *J. Mater. Chem. A* **5**, 2550–2562 (2017).
117. Zysman-Colman, E. *et al.* Solution-processable silicon phthalocyanines in electroluminescent and photovoltaic devices. *ACS Appl. Mater. Interfaces* **8**, 9247–9253 (2016).
118. Grant, T. M. *et al.* High Voc solution-processed organic solar cells containing silicon phthalocyanine as a non-fullerene electron acceptor. *Org. Electron.* **87**, 105976 (2020).
119. Grant, T. M., Dindault, C., Rice, N. A., Swaraj, S. & Lessard, B. H. Synthetically facile organic solar cells with >4% efficiency using P3HT and a silicon phthalocyanine non-fullerene acceptor. *Mater. Adv.* (2021) doi:10.1039/d1ma00165e.
120. Lessard, B. H. *et al.* Assessing the potential roles of silicon and germanium phthalocyanines in planar heterojunction organic photovoltaic devices and how pentafluoro phenoxylation can enhance π-π Interactions and device performance. *ACS Appl. Mater. Interfaces* **7**, 5076–5088 (2015).
121. Lessard, B. H. *et al.* The position and frequency of fluorine atoms changes the electron donor/acceptor properties of fluorophenoxy silicon phthalocyanines within organic photovoltaic devices. *J. Mater. Chem. A* **3**, 24512–24524 (2015).
122. Ayzner, A. L., Tassone, C. J., Tolbert, S. H. & Schwartz, B. J. Reappraising the need for bulk heterojunctions in polymer-fullerene photovoltaics: The role of carrier transport in all-solution-processed P3HT/PCBM bilayer solar cells. *J. Phys. Chem. C* **113**, 20050–20060 (2009).
123. Yang, B., Yuan, Y. & Huang, J. Reduced Bimolecular Charge Recombination Loss in Thermally Annealed Bilayer Heterojunction Photovoltaic Devices with Large External Quantum Efficiency and Fill Factor. *J. Phys. Chem. C* **118**, 5196–5202 (2014).
124. Cheng, P. *et al.* Efficient and stable organic solar cells via sequential process. *J. Mater. Chem. C* **4**, 8086–8093 (2016).
125. Jang, Y. *et al.* Formation of Thermally Stable Bulk Heterojunction by Reducing the Polymer and Fullerene Intermixing. *Sci. Rep.* **7**, 1–9 (2017).
126. Choi, Y., Hoon, B. & Kim, H. Bicontinuous network of electron donor-acceptor

composites achieved by additive-free sequential deposition for efficient polymer solar cells. *Curr. Appl. Phys.* **20**, 760–764 (2020).

127. Sun, R. *et al.* A universal layer-by-layer solution-processing approach for efficient non-fullerene organic solar. *Energy Environ. Sci.* **12**, 384–395 (2019).
128. Arunagiri, L. *et al.* Temperature-Dependent Aggregation Donor Polymers Enable Highly Efficient Sequentially Processed Organic Photovoltaics Without the Need of Orthogonal Solvents. *Adv. Funct. Mater.* **29**, 1–10 (2019).
129. Dong, S. *et al.* High-Performance Large-Area Organic Solar Cells Enabled by Sequential Bilayer Processing via Nonhalogenated Solvents. *Adv. Energy Mater.* **9**, 1–7 (2019).
130. Wei, G. *et al.* Functionalized Squaraine Donors for Nanocrystalline Organic Photovoltaics. *ACS Nano* **6**, 972–978 (2012).
131. Zabihi, F., Chen, Q., Xie, Y. & Eslamian, M. Fabrication of efficient graphene-doped polymer/fullerene bilayer organic solar cells in air using spin coating followed by ultrasonic vibration post treatment. *Superlattices Microstruct.* **100**, 1177–1192 (2016).
132. Sun, R. *et al.* A multi-objective optimization-based layer-by-layer blade-coating approach for organic solar cells: rational control of vertical stratification for high performance. *Energy Environ. Sci.* **12**, 3118–3132 (2019).
133. Nakano, K. & Tajima, K. Organic planar heterojunction : from models for interfaces in bulk heterojunctions to high-performance solar cells. *Adv. Mater.* **29**, 1603269 (2017).

Chapter 2: Material Selection and Processing Conditions of LbL Fabricated OPV Devices

2.1. Context

As outlined in **Chapter 1**, the development of organic photovoltaic devices is mainly limited to the fabrication of BHJ devices where the acceptor and donor are blended. However, I am interested in improving from BHJ devices to a more scalable bilayer device structure where the donor and acceptor materials are deposited sequentially, by layer-by-layer (LbL) in order to increase the control over each layer and facilitate the transition from lab scale to commercial scale. As OPV bilayers are understudied in the field compared to OPV BHJs, I started by compiling an exhaustive survey of LbL based OPVs and highlight their potential as well as point at the research leads. During my own searches, I noticed how it could sometimes be finicky to find the experimental details due to the lack of information communication in scientific papers on fabrication of devices. Thus, I chose to ease researchers search by giving a device orientation to the review and by gathering the devices important fabrication information in tables when reported. I focused the review on all solution-processed bilayers, hybrid solution-vacuum processed, and blade coated processed devices.

2.2. Contribution of Authors

I performed all the literature research and solely wrote the first draft of the manuscript. BHL and I consulted over direction, he provided feedback and edited the manuscript.

This chapter was published in *Journal of Materials Chemistry C*:
M.D.M. Faure, B.H. Lessard., *J. Mater. Chem. C*, **2021**, 9, 14-40.

2.3. Abstract

Layer-by-layer (LbL) processing, otherwise known as sequential deposition, is emerging as the most promising strategy for fabrication of active layers in organic photovoltaic (OPV) devices on both laboratory and industrial scales. In comparison to the bulk heterojunction (BHJ) configuration, LbL facilitates separate and sequential deposition of each layer, enabling greater control and optimization of interfaces and final donor/acceptor morphology. Furthermore, this process encourages formation of an efficient vertical phase separation, where the acceptor and donor aggregations are largest at their respective electrodes, increasing exciton dissociation and transport while reducing unwanted charge recombination. Compared to BHJ OPVs, LbL OPVs are more robust, with less dependence on processing conditions, resulting in increased photo, thermal, and mechanical stability and greater power conversion efficiency retention when applied to large area modules. These advantages have resulted in significant interest in the LbL process and its potential to displace BHJ as the dominant process for large-scale OPV manufacturing. This review summarizes recent developments in OPV fabrication through LbL, with particular emphasis on material selection and thin film processing conditions.

2.4. Introduction

Organic carbon-based photovoltaics (OPVs) are a viable route towards highly flexible, semi-transparent, low manufacturing cost solar cells with an energy payback time on the order of months.[1],[2] While previously disparaged as low performing, over the past 5 years OPV cell efficiencies have increased dramatically, now exceeding 18% and evolving into the realm of commercially viable technology.[3] Development of large-scale manufacturing of OPVs necessitates consideration and optimization of several parameters. A crucial design component is choice of materials, as synthetic complexity will dictate if mass production is feasible, with low yields and significant waste streams being prohibitive. Another key aspect is how the active films are fabricated and processed. Bulk production of devices with consistent thin film morphology and performance is critical, requiring large operating windows and the ability to adjust parameters “on-the-fly” with changing environmental conditions such as humidity or temperature.

High-performing OPVs have an active layer comprised of at least two different materials, referred to as electron donors and electron acceptors. The prerequisite for multiple materials with complimentary energy levels to provide a driving force to facilitate charge separation of photogenerated excitons is the subject of several excellent reviews.[4-6] Tang and coworkers seminal work was realized by sequentially evaporating thin films of donor and acceptor molecules in a planar heterojunction (PHJ) configuration.[7] Photogenerated excitons can only become free carriers when they reach the donor/acceptor interface, with a typical exciton diffusion length of 5 – 15 nm, emphasizing the significance of maximizing the interfacial area.[8] The low interfacial area between the donor and acceptor in PHJ bilayer cells severely curtails performances. PHJ OPVs were quickly surpassed by bulk heterojunction (BHJ) devices, which involve blending the materials in a common solvent before deposition, facilitating the forming of a random interpenetrating network with increased donor/acceptor interfacial area.[9] The BHJ architecture has since become widely implemented in research laboratories, affording a facile processing route for the investigation of large families of donor and acceptor materials.[3],[6],[10-18]

Despite the pervasiveness of the BHJ process, fundamental problems remain in both the fabrication and resulting morphology. The major impediment with BHJ devices is that optimal nanoscale morphology must be spontaneously achieved through a fast deposition and drying. Often the thermodynamically favourable morphology does not yield preeminent device performance, requiring optimization of multiple experimental conditions to promote kinetic film formation. Choice of solvents and additives, processing conditions (such as concentration), shearing speed or drying time, spin speed, ambient conditions such as humidity and temperature, and post annealing steps can all dramatically alter performance.[19] Small changes in processing conditions or operating environment can provoke a transition to another equilibrium state, inducing unfavourable phase separation.[20],[21] The blended nature of BHJ devices makes it challenging to predict and understand how changing one variable will affect the overall nanoscale morphology. The optimal intertwined donor/acceptor morphology, comprised of desirable distribution of components, crystallinity, domain sizes, and molecular order and orientation, is very elaborate. This complexity is amplified when transitioning from lab-scale to commercial-scale, illustrating a significant disadvantage with the BHJ process. The ideal OPV manufacturing process would enable deposition of the donor and acceptor independently as two separate layers, allowing intelligent control over each layer, mimicking conventional printing processes while still maximizing interfacial contact.

A pseudo-bilayer configuration via layer-by-layer (LbL) fabrication facilitates the combination of facile single-layer deposition processes with improved interfacial contact achieved through BHJ architecture. LbL involves the sequential deposition of the OPV active layers by solution processing for the first layer (often the donor in a direct device configuration) followed by either the evaporation or solution deposition of the second layer (the acceptor in direct device configuration, **Scheme 2.1**). Sequential deposition offers a promising route towards commercialization of OPVs through numerous advantages. Each material is deposited independently, allowing control and optimization over discrete layers. Characterization of the interface is facile, which expedites understanding the connection between physical processes and morphology with device performance. The fabrication process results in efficient vertical phase separation, which can be tuned to improve exciton dissociation and reduce charge carrier recombination. Finally, LbL devices have better thermal stability and the technique reduces the dependence on processing conditions, facilitating an easier transition from lab-scale to commercial-scale, with efficiency retention for increased area.

Ayzner et al. explored this strategy to address the inherent problems in BHJ fabrication.[22] They deposited poly(3-hexylthiophene) (P3HT) and [6,6]-phenyl-C_{61}-butyric acid methyl ester ($PC_{61}BM$) separately from orthogonal solvents and achieved OPV devices nearly as efficient as their blended counterparts. Characterization of interfacial morphology exposed the formation of a three-layer structure, with an intermixed donor/acceptor layer sandwiched between two relatively pure donor and acceptor layers.[23] Subsequent studies revealed that sequentially processed devices could be more efficient than BHJ OPVs due to improved vertical phase separation, which enabled stronger photon absorption, higher hole mobility, better charge extraction, and improved thermal stability.[24-26] Optimal vertical grading of the layers can be achieved through controlled swelling of the donor layer, with the magnitude of intermixing with the acceptor modulated by choosing suitable solvents, cosolvents, or solvent additives.[27] The versatility of LbL fabrication was bolstered by the discovery that stringent orthogonal solvents are not required. LbL OPVs have been fabricated using the same solvent for both layers, achieving higher power conversion efficiencies (*PCE*s) and increased area modules through improved control over morphology and reduced dependence on processing conditions.[28-30] Cells produced through LbL outperformed their BHJ equivalents on both small and very large areas up to 11.52 cm^2, resulting in the record efficiency reported for a large-area OPV module of 12%.[31]

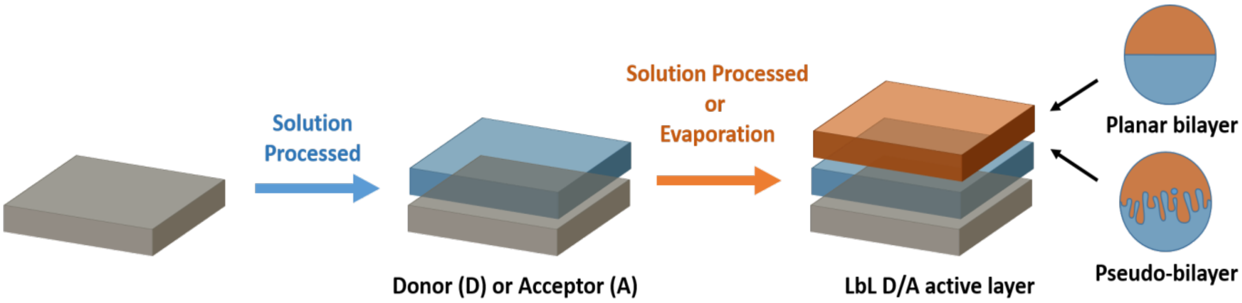

Scheme 2.1. Diagram of pseudo-bilayer or planar bilayer configuration via a layer-by-layer (LbL) sequential deposition of the donor and acceptor materials.

This review highlights the growth and potential of this fabrication process through exploring studies that focus on LbL processing of OPVs. Particular focus is devoted to the choice and combination of donor and acceptor materials in the active layer, processing conditions, and the translation to large-scale production.

2.5. Material Selection for Layer-by-Layer (LbL) Deposition

Since the first report in 2009, a plethora of different donor and acceptor materials have been incorporated into LbL OPVs. While many of these material combinations have also been explored in BHJ OPV configuration, this review will predominantly focus on their performance in LbL OPVs, referencing BHJ performance when used as controls. Candidate donor and acceptor materials for LbL OPVs can be classified as either small molecules or polymers.

2.5.1. Fullerene Small Molecule Acceptors

Since its discovery in 1985, buckminsterfullerene C_{60} (**Figure 2.1 a1**) has prompted significant interest in the OPV community due to its efficiency at accepting and transferring electrons, with charge mobilities on the order of 10^{-4} to 10^{-3} $cm^2V^{-1}s^{-1}$.[32] Haddon et al. determined that this proficiency may be due to the curvature of the fullerene surface, which results in a variable intermediate hybridization between sp^2 and sp^3.[33] Other interesting properties include the functionalization capacity of the surface, along with a photoinduced charge separation acceleration, and a delayed charge recombination in the dark.[34] However, due to its low solubility and high tendency of aggregation, C_{60} incorporation into LbL processed OPV devices is always performed via thermal evaporation.[35] The use of $PC_{61}BM$ (**Figure 2.1 a2**), a soluble C_{60} derivative,[36] enabled a significant increase in the availability of dissociation interfaces with the donor by promoting deeper interdiffusion and better carrier collection efficiency. Interdiffusion is also encouraged by π-π interactions between the phenyl groups of $PC_{61}BM$ with both itself and with aromatic groups of donor polymers.[37] C_{60} and $PC_{61}BM$ have wide bang gaps of around 2 eV (HOMO = -5.9 eV, LUMO = -3.9 eV) that cover the UV-region, with a weak absorption in the visible region of the solar spectrum. Increasing the fullerene molecular weight from C_{60} to C_{70} (**Figure 2.1 a4**), or from $PC_{61}BM$ to $PC_{71}BM$ (**Figure 2.1 a5**), results in a slight red-shift of the absorption into the 400 – 600 nm range, and a corresponding increase in the short circuit current (*Jsc*).[38]

Other families of soluble fullerene compounds have also been investigated in LbL based OPVs. Up-shifting the LUMO level of the fullerene results in a larger difference between the HOMO level of the donor and the LUMO level of the acceptor, which induces a greater open circuit voltage (*Voc)*.[15],[39] Indene fullerenes such as IC60BA (**Figure 2.1 a8**) and IC70BA (**Figure 2.1 a9**) possess LUMO levels 0.17 eV and 0.19 eV greater than their fullerene counterparts, yielding an increase in *Voc* of +0.3 V when incorporated into LbL OPVs.[40] Troshin et al. developed fullerenes bearing chelating pyridyl moieties, such as pyrrolidinofullerene (PyF) (**Figure 2.1 a3**), which can form complexes to increase miscibility with metalloporphyrins and metallophthalocyanines donors, leading to enhanced *Jsc* compared to $PC_{61}BM$.[41-43] Cross-linked fullerene derivatives bearing two styryl groups for each unit like [6,6]-phenyl-C_{61}-butyric acid styryl dendron ester (PCBSD) (**Figure 2.1 a6**) and p-PCBVB (**Figure 2.1 a7**) have also been studied, and were shown to produce very robust films through LbL.[44],[45]

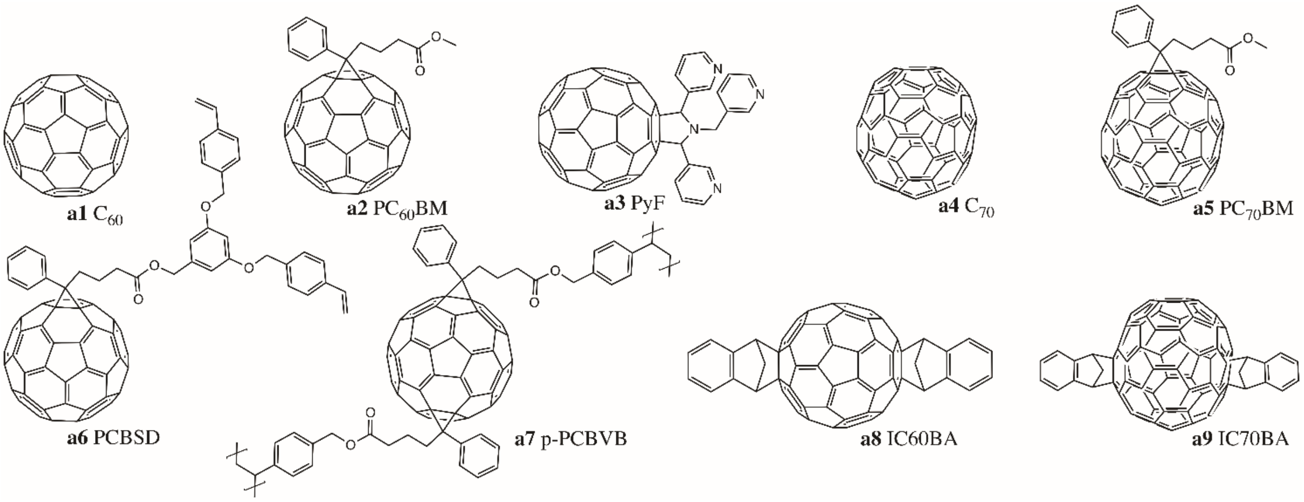

Figure 2.1. Chemical structures of select fullerene-based acceptors incorporated into LbL devices.

Table 2.1. Energy levels of select fullerene-based acceptors incorporated into LbL devices.

Material	HOMO (eV)	LUMO (eV)	Ref
C_{60} (**a1**)	-6.2	-4.5	[46]
$PC_{61}BM$ (**a2**)	-5.93	-3.91	[47]
$PC_{71}BM$ (**a5**)	-5.87	-3.91	[47]
IC60BA (**a8**)	/	-3.74	[47]
IC70BA (**a9**)	-5.61	-3.72	[47]

2.5.2. Non-fullerene Small Molecule Acceptors

Fullerene derivatives have weak absorption in the visible and near-infrared region of the solar spectrum; the fullerene structure also curtails tuning of the band gap, limiting *Voc* values. Additionally, they have a strong tendency to crystallise and form aggregates which reduces device stability.[39],[47],[48] Non-fullerene acceptors (NFAs) were developed to overcome the impediments of fullerene acceptors. Zhan and coworkers synthesized a novel acceptor, (3,9-bis(2-methylene-(3-(1,1-dicyanomethylene)-indanone))-5,5,11,11-tetrakis(4-hexylphenyl)dithieno[2,3-*d*:2′,3′-*d*′]-s-indaceno[1,2-*b*:5,6-*b*′]dithiophene) (ITIC, **Figure 2.2 a10**), based on an acceptor-donor-acceptor (A-D-A) push-pull architecture.[49] The donor core consists of an indacenodithiophene (IDT) unit with four 4-hexylphenyl substituents, while 2-(3-oxo-2,3-dihydroinden-1-ylidene)malononitrile (INCN) was incorporated as the acceptor end groups. Substituents were included to inhibit planarity in the molecule, which would result in excessive π-π aggregation and phase separation with donor materials. The A-D-A structure can promote intramolecular charge transfer and strong absorption in the visible spectrum from 500 – 780 nm. The optical band gap, HOMO and LUMO energy levels were estimated to be 1.59 eV, -5.48 eV and -3.83 eV, respectively. In LbL devices, this novel low band gap NFA achieved a power conversion efficiency (*PCE*) of 7% when combined with a wide band gap polymer PBDB-T (**Figure 2.6 b41**), whose HOMO and LUMO energy levels are -5.33 eV and -3.53 eV, respectively.[50]

In subsequent iterations of the ITIC structure, Zhan and coworkers substituted the phenyl rings of the out-of-plane side-chains on the IDT core with thiophene rings (ITIC-Th, **Figure 2.2 a11**) to lower the HOMO level to -5.66 eV to improve compatibility with wider band gap high-performing donor polymers.[51] Small and weakly electron-donating methyl substituents on the phenyl end groups (ITIC-M, **Figure 2.2 a12**) were also investigated and found to increase the LUMO level (+0.04 eV) and improve the *Voc*.[52] Other strategies focused on replacing the phenyl ring end groups by more electron-donating thiophene rings (ITCC/MeIC, **Figure 2.2 a13-14**) or introducing hexyl alkyl chains onto the central fused ring (ITC6-IC, **Figure 2.2 a15**), both of which increased the LUMO by +0.11 eV and +0.09 eV, respectively.[53],[54] Incorporation of highly electronegative fluorine atoms on the INCN unit ends (ITIC-4F/NCBDT, **Figure 2.2 a16-17**) reduced both the HOMO and LUMO levels and narrowed the band gap, particularly for NCBDT (E_g = 1.47 eV).[55-57] Reducing the number of fused ring in the core from seven to five (IDIC, **Figure 2.2 a18**) decreased crystallinity and improved phase separation.[58],[59] Incorporation of these ITIC based NFAs enabled *PCE*s greater than 10% when fabricated into LbL OPV devices, with a maximum *PCE* of 13% obtained for PBDB-TFS1/ITIC-4F devices.[28],[60]

Recently, Yuan et al. adapted the A-D-A system by replacing the donor core with a new dithienothiophen[3.2-*b*]-pyrrolobenzothiadiazole (TPBT) fused-unit and substituting the INCN acceptor units with fluorine atoms to synthesize (2,2'-((2Z,2'Z)-((12,13-bis(2-ethylhexyl)-3,9-diundecyl-12,13-dihydro-[1,2,5]thiadiazolo[3,4-e]thieno[2,"3'':4',5']thieno[2',3':4,5]pyrrolo[3,2-g]thieno[2',3':4,5]thieno[3,2-b]indole-2,10-diyl)bis(methanylylidene))bis(5,6-difluoro-3-oxo-2,3-dihydro-1H-indene-2,1-diylidene))dimalononitrile) (Y6, **Figure 2.2 a19**).[17] The TPBT core is conjugated, with solubility preserved by incorporation of alkyl chains that can also facilitate tuning of the electron affinity, while end groups promote both photon absorption and intermolecular interactions via non-covalent F-S and F-H bond formation. HOMO and LUMO levels were estimated to be -5.65 eV and -4.02 eV, respectively, and replacement of fluorine atoms with chlorine atoms (Y6-2Cl, **Figure 2.2 a20**) further reduced both energy levels and the band gap

(-70 meV).[61] Increasing the alkyl chain length on the donor unit (Y6-C2, **Figure 2.2 a21**) did not alter optical properties but did improve the molecular packing and enhance crystallinity.[62] LbL processed devices based on these small molecules achieved record efficiencies greater than 16%.[31]

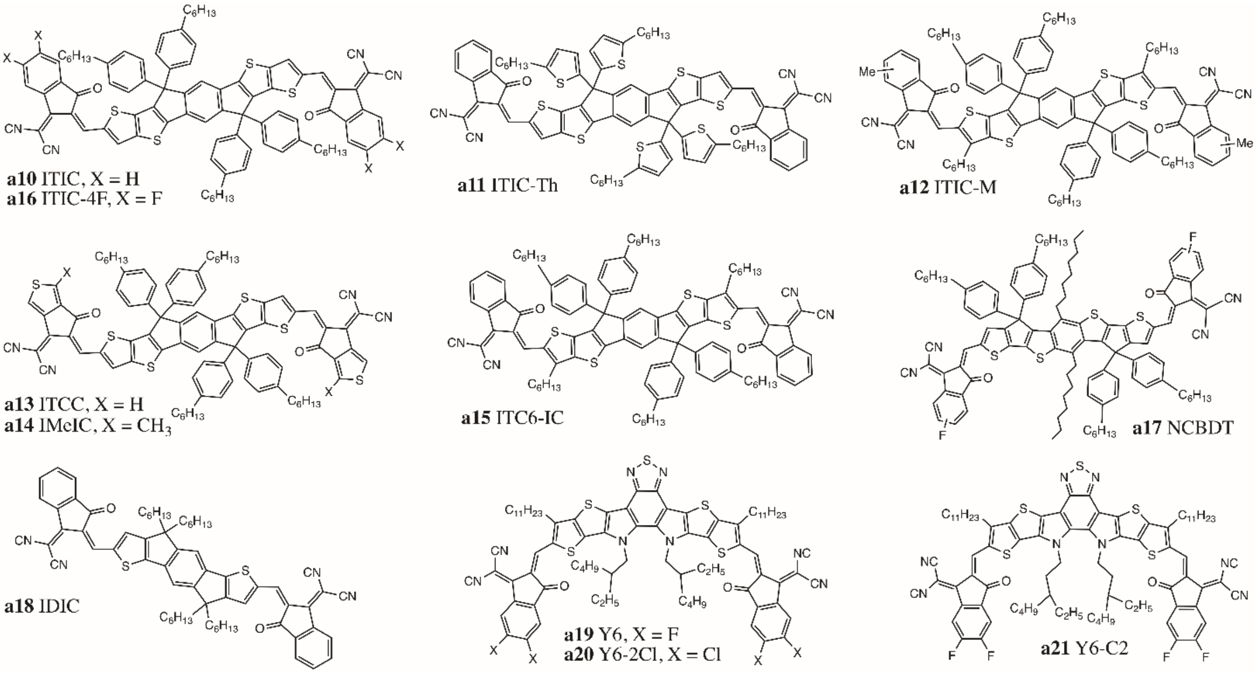

Figure 2.2. Chemical structures of select non-fullerene acceptors (NFAs) incorporated into LbL devices.

Table 2.2. Energy levels of select non-fullerene acceptors (NFAs) incorporated into LbL devices.

Material	HOMO (eV)	LUMO (eV)	Ref
ITIC (**a10**)	-5.48	-3.83	[49]
ITIC-Th (**a11**)	-5.66	-3.93	[51]
ITIC-M (**a12**)	-5.58	-3.98	[52]
ITCC (**a13**)	-5.47	-3.76	[53]
ITC6-IC (**a15**)	-5.73	-3.92	[54]
ITIC-4F (**a16**)	-5.73	-4.02	[55]
NCBDT (**a17**)	-5.36	-3.89	[57]
Y6 (**a19**)	-5.65	-4.02	[61]
Y6-2Cl (**a20**)	-5.68	-4.12	[61]

2.5.3. Small Molecule Donors

One of the earliest classes of donor molecules to be utilized in LbL fabrication of OPVs was pentacene, due to the ease with which it can be functionalized to modify hole mobility, solubility, and optical properties.[63],[46] Pentacene molecules were first integrated into LbL devices through sublimation, with subsequent reports investigating the use of soluble derivatives such as 6,13-di(2-thienyl)pentacene (BTP, **Figure 2.3 b1**), containing two thiophene rings pendent to the central phenyl unit, and bis(triisopropylsilylethynyl)pentacene (TIPS-pentacene, **Figure 2.3 b2**) which possesses two alkyl substituted silyl groups. For BTP, a HOMO level of -5.1 eV and a LUMO level of -3.0 eV were reported, with a *PCE* of 1.4% when paired with C_{60}.

Squaraine dyes have attracted significant attention as donor molecules due to their high absorption coefficient (10^5 cm^{-1}) in the visible region and tunable band gaps.[64],[65] Contrary to NFAs described above, squaraine dyes are based on a donor-acceptor-donor (D-A-D) push-pull structure, with a central four-membered acceptor ring linked to electron-rich moieties such as phenols, N,N-dialkylanilines, or arylamines. The isobutylamine end groups of the initial squaraine derivative 2,4-bis[4-(N,N-diisobutylamino)-2,6-dihydroxy-phenyl]squaraine (SQ, **Figure 2.3 b3**) were substituted with arylamines (1-NPSQ, DPSQ, DPASQ, ASSQ, **Figure 2.3 b4-7**) or N-propyl groups (PSQ, **Figure 2.3 b8**) to suppress steric hindrance and increase π-stacking between donor molecules; this allows for better hole collection efficiency and stronger electron-withdrawing behavior to improve *Voc*.[66] Champion LbL OPV *PCE* of 5.7% was obtained for the 1-NPSQ paired with a C_{60} acceptor.

Diketopyrrolopyrrole (DPP) dyes are another common class of small molecule donors which possess strong intermolecular interactions and high charge carrier mobilities; their electron-deficient nature also affords them outstanding light harvesting properties.[67] However, the poor solubility of DPP necessitates the incorporation of branched ethyl hexyl alkyl substituents on the nitrogen atoms (EH-DPP-TFP, EH-DPP-TFPV, **Figure 2.3 b9-10**) before utilization as donors in LbL devices with *PCE*s of up to 3.3%.[68]

Chen and coworkers investigated a donor small molecule with an A-D-A structure comprised of an electron-rich benzodithiophene (BDT) core linked to alkyl cyanoacetate (BDT-3T-CA, **Figure 2.3 b11**) or to ethylrhodanine (DR3TBDTT, **Figure 2.3 b12**) through terthiothiophene spacers.[69],[70] When paired with $PC_{61}BM$, BDT-3T-CA achieved a *PCE* of 4.16% with a fill factor (*FF*) as high as 0.75.[71]

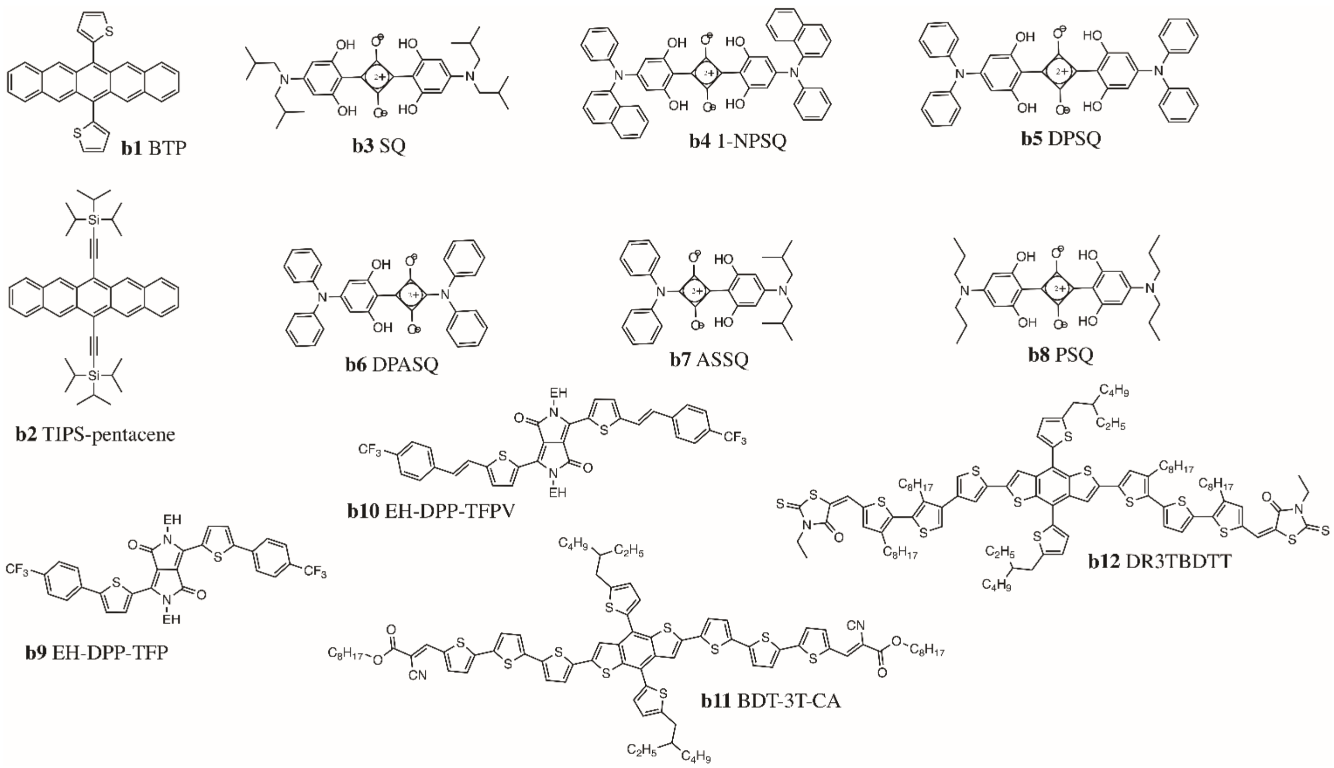

Figure 2.3. Chemical structures of select donor small molecules incorporated into LbL devices.

Table 2.3. Energy levels of select donor small molecules incorporated into LbL devices.

Material	**HOMO (eV)**	**LUMO (eV)**	**Ref**
BTP (**b1**)	-5.1	-3.0	46
SQ (**b3**)	-5.1	-3.5	66
1-NPSQ (**b4**)	-5.3	-3.7	66
ASSQ (**b7**)	-5.3	3.2	66
EH-DPP-TFP (**b9**)	5.24	-3.50	68
BDT-3T-CA (**b11**)	-5.20	-2.90	71

2.5.4. Ambipolar Small Molecules

There are several classes of molecules that can be integrated into LbL OPVs as either acceptors or donors, depending on how the molecules are functionalized and the resultant HOMO and LUMO energy levels. Cyanine (Cy) dyes were among the first small molecules investigated as donors with fullerenes in LbL OPV devices, particularly with C_{60}. These dyes possess high extinction coefficients, tunable absorption spectra, excellent solubility, and suitable HOMO and LUMO energy levels, which motivated their incorporation into OPV cells. Cy dyes also form H and J aggregates with highly delocalized excitons that account both for broaden spectral absorption and larger *Voc*. In 2003, Nüesh and coworkers fabricated devices through spin casting a perchlorate counterion, 1,1-diethyl-3,3,3',3'-tetramethylcarbocyanine perchlorate (Cy3-ClO_4^-, **Figure 2.4 c1**).[72] Subsequent investigations compared this compound to a cyanine derivative with a linked counterion (Cy10, **Figure 2.4 c2**), and determined that mobile ions were responsible for an important C_{60} contribution at the donor/acceptor heterojunction.[73] They also demonstrated that both doping of Cy3-ClO_4^- in the presence of ambient air increased hole mobility and switching to a hexafluorophosphate counterion (Cy3-PF_6^-, **Figure 2.4 c3**) yielded devices with *PCE* greater than 3%.[74],[75] Application of Cy as both a donor and an acceptor was achieved through substitution of the phenyl groups for naphthalene rings (CyA, CyBs, CyBl, **Figure 2.4 c4-6**), resulting in modified redox levels, with superior performance achieved when used as donors with an hexafluorophosphate counterion (Cy7-P, **Figure 2.4 c7**).[76],[77] Bolink and coworkers further investigated Cys as donors with different alkyl chains (CyA, Cy0363, Cy2046, Cy0619, **Figure 2.4 c4/c8-10**) and attained *PCE*s of 3%.[78] A Cy derivative (Cy5-Cl, **Figure 2.4 c11**) was also incorporated as a counterion in a polyelectrolyte polymer in an attempt to fabricate an all-solution processed bilayer device with $PC_{61}BM$.[79]

Porphyrins (Por) are conjugated macrocyclic dyes that have high molar absorptivity (in both the blue and red regions of the visible solar spectrum), excellent air and thermal stability, and efficient photon absorption and electron transfer.[80],[81] Por are often integrated as complexes with C_{60}, but have also been investigated as donors or acceptors in BHJ cells with soluble fullerene derivatives or low band gap polymers. In LbL devices both benzene-functionalized Por and more complex liquid crystalline Por molecules were introduced as donors (BP, PtTPBP, C12/C14Por, **Figure 2.4 c12-15**),[82-84] while a Por with quaternized pyridyl side groups (**Figure 2.4 c16**) was studied as an acceptor.[85]

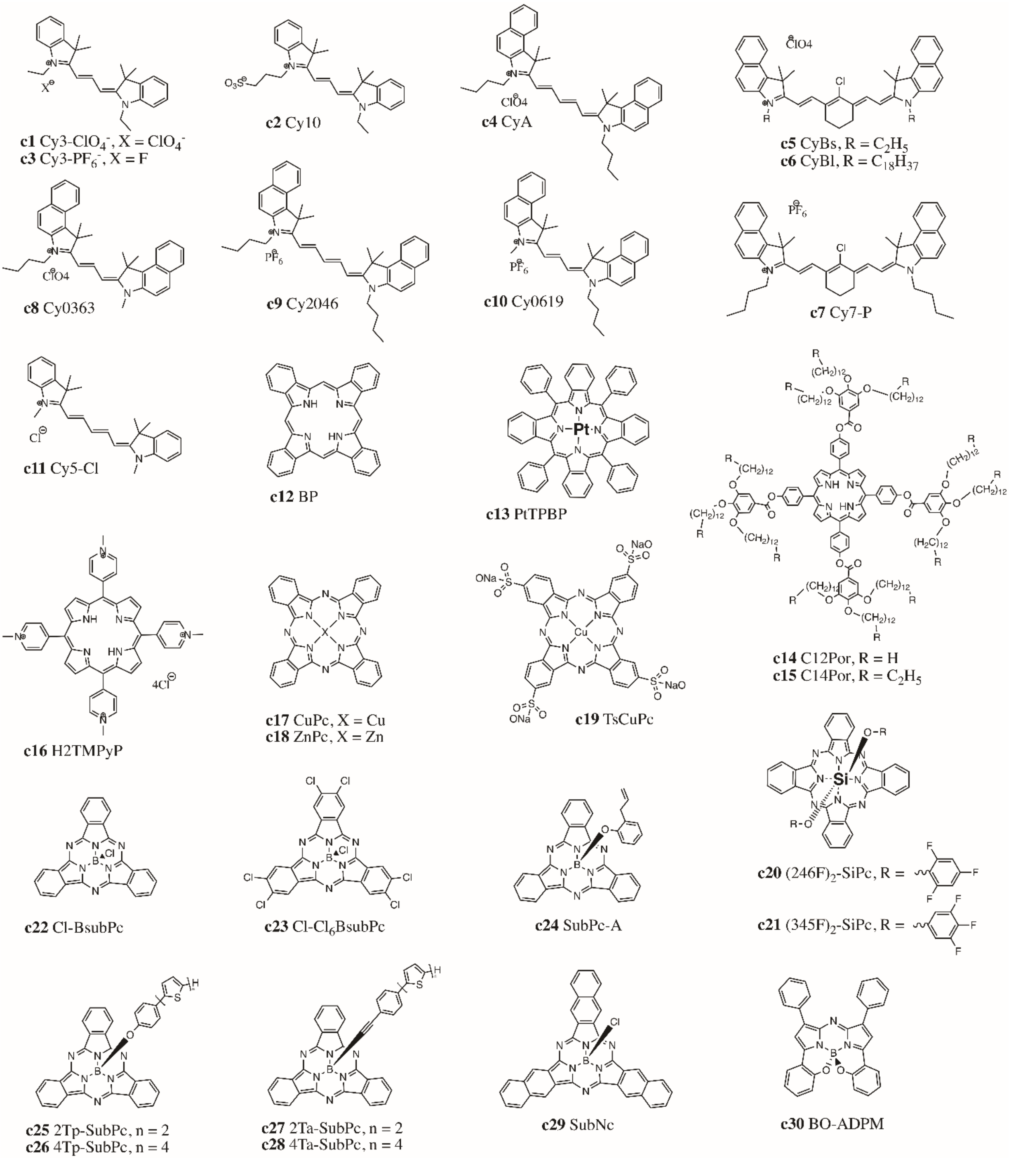

Figure 2.4. Chemical structures of select ambipolar small molecules incorporated into LbL devices.

Table 2.4. Energy levels of select ambipolar small molecules incorporated into LbL devices.

Material	**HOMO (eV)**	**LUMO (eV)**	**Ref**
Cy3-ClO_4^- (**c1**)	-5.8	-3.7	72
Cy3-PF_6^- (**c3**)	-5.7	-3.9	86
CyA (**c4**)	-5.4	-3.9	76

CyBl/CyBs (**c5/c6**)	-5.2	-4.2	76
Cy7-P (**c7**)	-5.28	-3.79	77
C12-Por/C14-Por (**c14/c15**)	-5.4	-3.3	83
CuPc (**c17**)	-5.06	-3.35	82
(246F)$_2$-SiPc (**c20**)	-5.4	-3.5	87
(345F)$_2$-SiPc (**c21**)	-5.9	-4.0	87
Cl-BSubPc (**c22**)	-5.6	-3.6	88
SubNc (**c29**)	-5.4	-3.6	89
BO-ADPM (**c30**)	-5.48	-4.02	90

Metal phthalocyanines (MPcs), a type of Por, are conjugated macrocycles comprised of four isoindoline groups which chelate a central metal atom. MPcs encompass a wide family of molecules, with a variety of core metals reported; they can also be functionalized both in peripheral and axial positions to tune both electronics and solubility. The most common divalent MPcs, zinc phthalocyanines (ZnPc) and copper phthalocyanines (CuPc) (**Figure 2.4 c17-18**), were introduced into LbL devices as donors but efficiencies were low.[43],[91] Jones and coworkers synthetized a water-soluble CuPc derivative through the addition of a tetrasulfonic acid tetrasodium salt substituent on the periphery (TsCuPc, **Figure 2.4 c19**), which resulted in a *Voc* of 0.6 V.[92] A tetravalent silicon phthalocyanine (SiPc) functionalized in the axial position with fluorophenoxy groups ((246F)$_2$/(345F)$_2$-SiPc, **Figure 2.4 c20-21**) was reported in bilayer cells as an acceptor by Faure et al.[87] Bender and coworkers investigated boron subphthalocyanine (SubPc),[88] which consist of a bowl shaped macrocycle chelating a central boron atom, resulting in increased solubility and reduced propensity to aggregate.[93] Josey et al. investigated axially-substituted chloro SubPc without and with peripheral chlorination (Cl-BSubPc, Cl-Cl$_6$BSubPc, **Figure 2.4 c22-23**) as evaporated acceptors with a standard donor polymer.[88] Soluble SubPc donor derivates have been synthesized by Fréchet and coworkers, incorporating phenoxy or alkynyl bonded thiophene axial substituents (SubPc-A, 2/4Ta/Tp-SubPc, **Figure 2.4 c24-28**) to tune flexibility and molecular packing in the solid state.[94],[95] This group also reported a SubPc analogue with similar properties, subnaphthalocyanine (SubNc), obtained by replacing isoindoline by benzoisoindole units (**Figure 2.4 c29**).[89] Overall the use of SubPcs and MPcs led to modest *PCE*s between 1 – 2% through LbL. Similar boron-based dyes like azadipyrromethene (BO-ADPM, **Figure 2.4 c30**) with downshifted HOMO and LUMO levels were reported to give slightly improved *PCE*s through LbL processing.[90]

2.5.5. Donor Conjugated Polymers

In the first iterations of LbL OPV devices, donor polymers were selected to compliment C_{60} acceptors. In 1993, Heeger and coworkers prepared LbL devices by spin coating the conjugated polymer poly(2-methoxy,5-(2'-ethyl-hexyloxy)-*p*-phenylenevinylene) (MEH-PPV, **Figure 2.5 b13**)[96-98] followed by evaporation of the C_{60} acceptor layer. MEH-PPV is a soluble derivative of poly(*p*-phenylenevinylene) (PPV),[99],[100] with a much lower glass transition temperature than PPV; however, it proved to be a weak donor with a relatively wide band gap of 2.2 eV. Drees et al. explored the film properties of MEH-PPV films and reported using LbL as a first approach towards fabricating BHJ devices, using a concentration gradient of MEH-PPV and C_{60} to increase the donor/acceptor interface via thermally controlled interdiffusion.[101],[102] Another PPV derivative (MDMO-PPV, **Figure 2.5 b14**) was also investigated using the same interdiffusion of layers with $PC_{61}BM$ as an acceptor and thermal annealing.[103],[104] However, overall performances again remained limited.

A first approach to increase performances of donor polymers was to replace the phenyl rings with thiophene rings. Schlebusch et al. paired C_{60} with poly(3-octylthiophene) (P3OT, **Figure 2.5 b15**), a soluble thiophene-based polymer with a long alkyl side chain, and discovered that interdiffusion between P3OT and C_{60} was occurring even at room temperature.[105] Heflin and coworkers utilized the improved solubility of C_{60} in P3OT to pursue the formation of a thermally-induced concentration gradient, and achieved improved active layer morphology with a monochromatic *PCE* = 1.5%.[106],[107] However, the breakthrough in LbL OPV performance occurred with P3HT (**Figure 2.5 b16**), which has since become the most researched donor polymer for fullerene acceptors in LbL OPVs. P3HT has a shorter alkyl chain and a lower band gap of 2 eV (HOMO = -5 eV, LUMO = -3 eV) compared to P3OT.[22],[108] P3HT also has strong self-organisation capacity, high hole mobility, and strong absorption in the visible region. Moreover, thermal annealing of P3HT near its melting point improves the crystallization of the active layer, resulting in significantly enhanced *PCE* of 3.5%. A plethora of P3HT derivatives have since been synthesized and integrated into LbL OPVs, including: P3HT-grafted graphene (G-P3HT),[109] poly(3-butylthiophene-2,5-diyl) (P3BT, **Figure 2.5 b17**),[110] poly(3-hexyl-2,5-thienylene vinylene) (P3HTV, **Figure 2.5 b18**),[111] poly(3-butylthiophene-*co*-3-octylthiophene)s (RBOs, **Figure 2.5 b19**),[112] poly(3-butylthiophene-*co*-(3-(2-ferrocen-1-yl-vinyl)thiophene)) (P1, **Figure 2.5 b20**) and poly(3-butylthiophene-*co*-(3-(1-cyano-2-ferrocen-1-yl-vinyl)thiophene)) (P2, **Figure 2.5 b21**).[110] These modifications in the P3HT donor polymer structure resulted in OPVs with *PCE*s < 5%. An alternating fluorene and bithiophene copolymer poly(9,9'-dioctyl-fluorene-*co*-bithiophene) (F8T2, **Figure 2.5 b22**) with a band gap of 2.4 eV was studied as well due to its excellent hole transport properties and inherent molecular stacking, resulting in a *PCE* of 3.4% with C_{70}.[113]

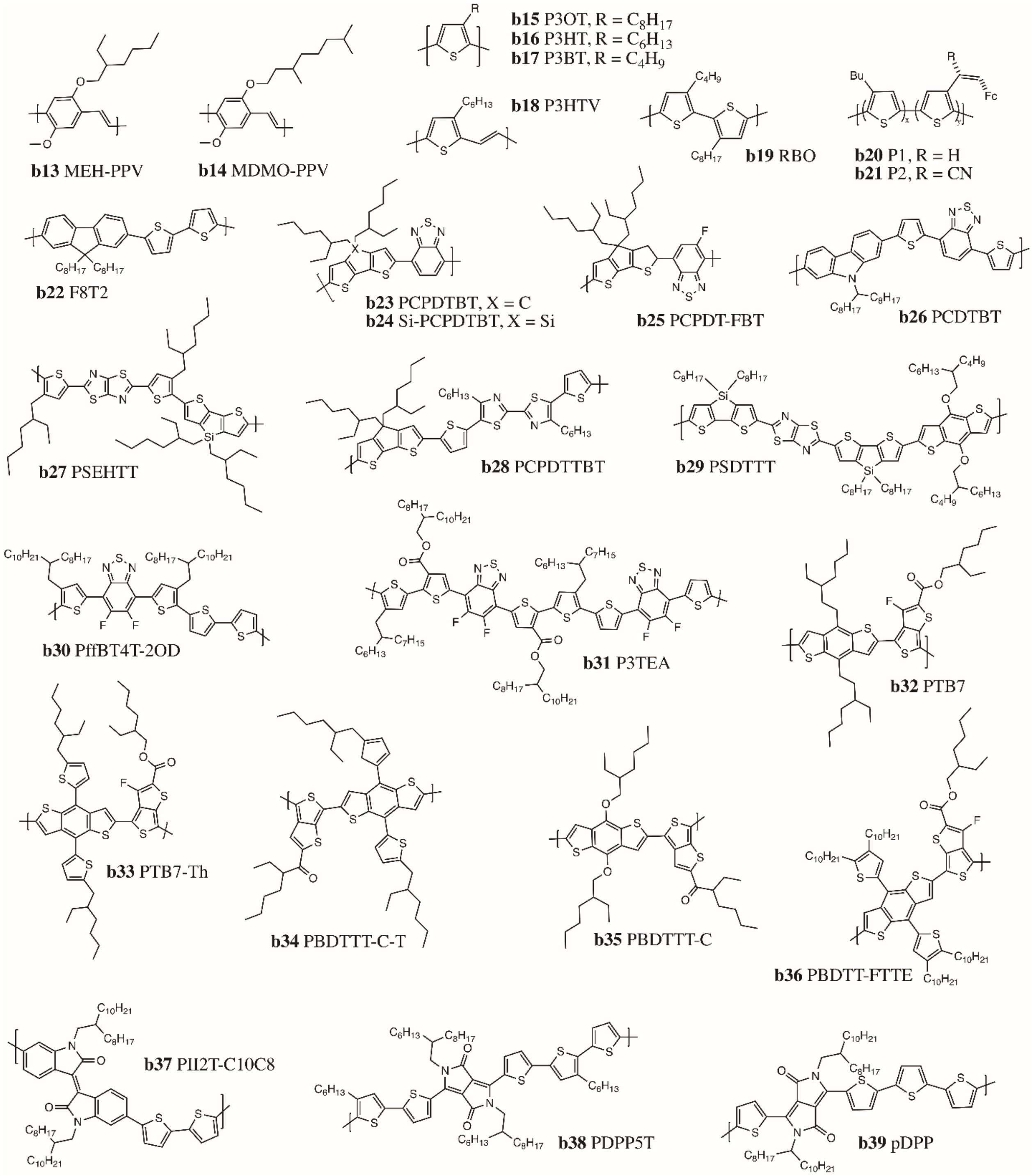

Figure 2.5. Chemical structures of common polymer donors (**b13-b22**) and low band gap polymer donors (**b23-b39**) incorporated into LbL devices.

Table 2.5. Energy levels of select common polymer donors and low band gap polymers incorporated into LbL devices.

Material	HOMO (eV)	LUMO (eV)	Ref
MEH-PPV (**b13**)	-5.1	-2.9	[76]
P3HT (**b16**)	-5.0	-3.0	[87]
Si-PCPDTBT (**b24**)	-4.8	-3.31	[114]
PCDTBT (**b26**)	-5.5	-3.6	[87]
PTB7-Th (**b33**)	-5.20	-3.59	[115]

Analogous to the BHJ OPV field, significant *PCE* improvements were achieved in LbL OPVs with the incorporation of low band gap donor polymers, resulting in increased coverage of the solar spectrum compared to P3HT. The so-called "push-pull" polymers consist of an electron rich unit and an electron deficient unit within the polymer backbone.[5] Monomers are typically fused heterocycles with extended π-conjugation and good planarity to enable tuning of both the band gap and charge carrier mobilities. Some of the most thoroughly investigated electron-rich units include BDT, carbazole (CZ) and cyclopentadithiophene (CPDT), usually coupled with DPP, thienothiophene (TT), benzothiadiazole (BTH) or thiazolo(5,4-d)thiazole (TzTz) electron-poor units. Representative copolymers based on these structures and employed in LbL OPV devices are depicted in **Figure 2.5 b23-39**.

Efficiencies of fullerene-based diffused bilayers increased significantly with these push-pull polymers. For example, copolymers based on BDT and TT units (**Figure 2.5 b32-36**) including poly[4,8-bis(5-(2-ethylhexyl)thiophen-2-yl)benzo[1,2-*b*;4,5-*b*']dithiophene-2,6-diyl-*alt*-(4-(2-ethylhexyl)-3-fluorothieno[3,4-*b*]thiophene-)-2-carboxylate-2-6-diyl)] (PTB7-Th, **Figure 2.5 b33**) have reported *PCE*s of up to 9% in LbL OPVs.[25] The HOMO and LUMO levels of PTB7-Th are -5.20 eV and -3.59 eV, respectively, with a band gap of 1.61 eV. Another common polymer incorporating CZ and BTH, poly[*N*-9'-heptadecanyl-2,7-carbazole-*alt*-5,5-(4',7'-di-2-thienyl-2',1',3'-benzothiadiazole)] (PCDTBT, **Figure 2.5 b26**), as well as copolymers of CPDT with BTH (**Figure 2.5 b23-25**), have resulted in *PCE*s > 7%.[116]

Moving away from fullerene acceptors, these push-pull polymers do not perform well when paired with NFAs due to energy level mismatch. Therefore, to increase the *Jsc* and *Voc* of LbL OPV devices wider band gap (WBG) polymers (> 2 eV) with deeper HOMO levels were designed to be paired with higher-performing emerging NFAs.[115] Representative WBG copolymers employed in LbL OPVs are illustrated in **Figure 2.6 b40-51**, and can be divided into two families of copolymers. The first type are donor-donor WBG copolymers, comprised only of alternating electron-rich units in the backbone, such as poly[5,5′-bis(2-butyloctyl)-(2,2′-

bithiophene)-4,4′-dicarboxylate-*alt*-5,5′-2,2′-bithiophene] (PDCBT, **Figure 2.6 b40**).[117] The second class are donor-acceptor copolymers synthesized with alternating electron-rich and electron-poor units in their backbones, including polymers based on a bithienyl-BDT (BBDT) electron-rich unit coupled with a benzodithiophene-4,8-dione (BDD) electron-poor unit (**Figure 2.6 b41-43**).[118] Sun et al. reported poly[(2,6-(4,8-bis(5-(2-ethylhexyl-3-fluoro)thiophen-2-yl)-benzo[1,2-*b*:4,5-*b*']dithiophene))-*alt*-(5,5-(1',3'-di-2-thienyl-5',7'-bis(2-ethylhexyl)benzo[1',2'-*c*:4',5'-*c*']dithiophene-4,8-dione)] (PM6, **Figure 2.6 b42**) which achieved a *PCE* above 16% when paired with Y6 in a LbL OPV device.[31] Other high performing D-A copolymers include poly[(thiophene)-*alt*-(6,7-difluoro-2-(2-hexyldecyloxy)quinoxaline)] (PTQ10, **Figure 2.6 b44**), comprised of a simple thiophene ring donor unit and a difluorine-substitued quinoxaline acceptor unit; fluoro and alkoxy substituents are incorporated to lower the HOMO level and ensure sufficient solubility, respectively.[119] J61/J71(**Figure 2.6 b45-46**) are both based on a BBDT electron-rich unit paired with fluorobenzotriazole (FTAZ) as the electron-deficient unit, with alkylthio or Si-C side chains that further downshift the HOMO level.[120],[121] The FTAZ units promote co-planarity in the backbone, resulting in improved π-π stacking and overall charge transport properties compared to previously synthetized copolymers (**Figure 2.6 b47/b49/b51**).[122],[123] LbL OPV devices based on these copolymers reached *PCE*s > 12%.[28]

Table 2.6. Energy levels of representative wider band gap (WBG) polymer donors incorporated into LbL devices.

Material	HOMO (eV)	LUMO (eV)	Ref
PDCBT (**b140**)	-5.26	-3.36	[117]
PBDB-T (**b41**)	-5.33	-3.53	[52]
PM6 (**b42**)	-5.56	-3.50	[17]
PTQ10 (**b44**)	-5.54	-2.98	[119]
J61 (**b45**)	-5.32	-3.08	[120]

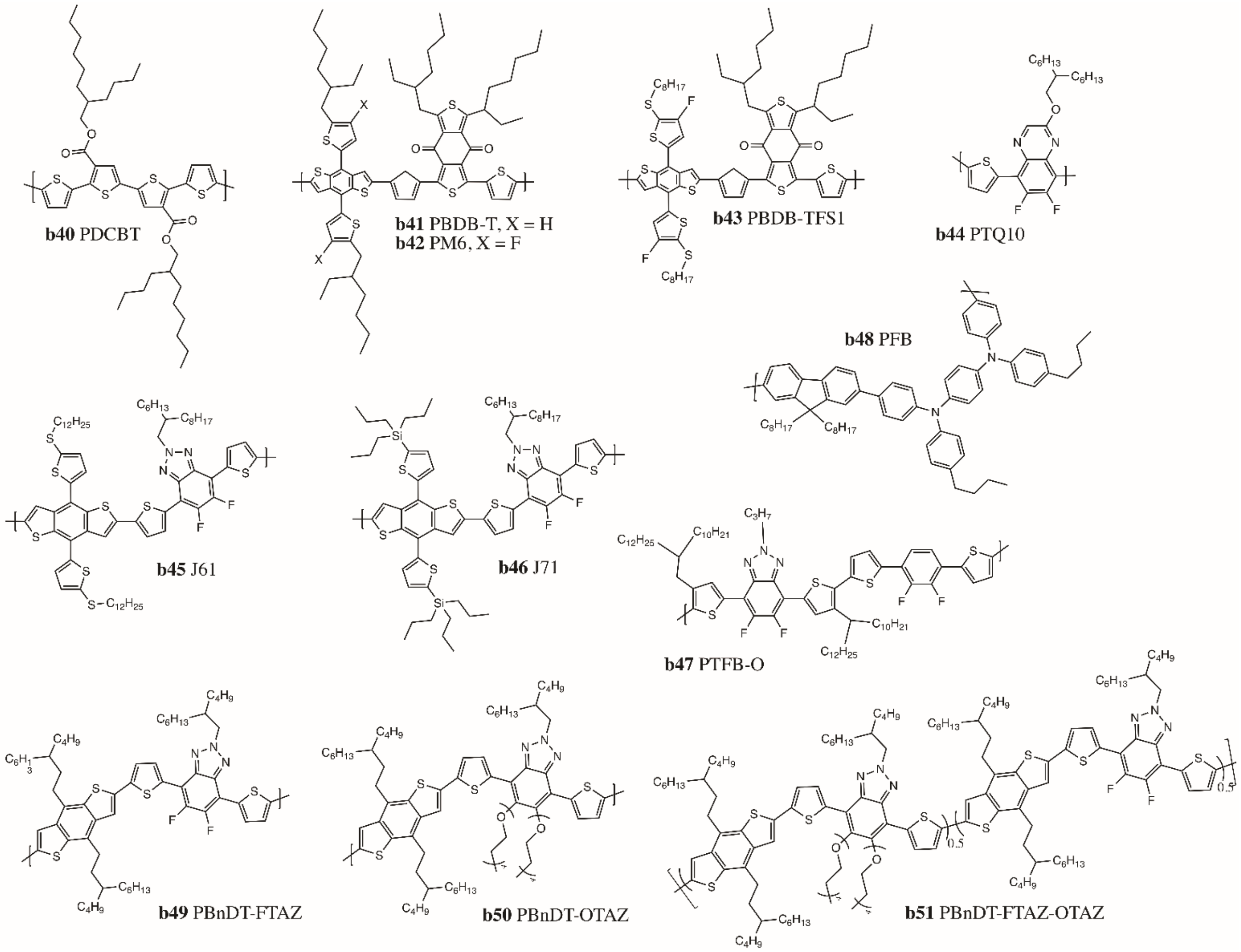

Figure 2.6. Chemical structures of representative wider band gap (WBG) polymer donors incorporated into LbL devices.

2.5.6. Acceptor Conjugated Polymers

Naphthalenediimide (NDI) based conjugated polymers were among the first acceptor conjugated polymers to be investigated, due to a low lying LUMO analogous to fullerenes.[124] They have high thermal and oxidative stability, good solubility, favourable electron mobility, and a morphology that can be easily manipulated through side chain engineering with substituents on the bay region or on the nitrogen atom. Jenekhe et al. reported the use of poly(benzimidazobenzophenanthroline ladder) (BBL, **Figure 2.7 a22**) paired with PPV as the first LbL dual polymer system.[125] Poly[N,N9-bis(2-octyldodecyl)-naphthalene-1,4,5,8-bis(dicarboximide)-2,6-diyl]-*alt*-5,59-(2,29-bithiophene) (P(NDI2OD-T2) or N2200, **Figure 2.7 a23**), is a well established planar push-pull copolymer acceptor containing NDI acceptor and thiophene donor units that is an air-stable n-type semiconductor utilized in organic field-effect transistors (OTFTs), with electron mobility of 0.45 – 0.85 $cm^2V^{-1}s^{-1}$.[126] Strong interactions between polymer chain backbones, combined with relatively high molecular weights, drastically reduced the solubility of N2200, which facilitated integration into all-polymer LbL OPVs to yield *PCE* of almost 10% with PBDB-T (**Figure 2.6 b41**).[127]

Burn and coworkers recently developed a polymeric acceptor with an acceptor-acceptor'-acceptor (A-A'-A) structure (PNNT, **Figure 2.7 a24**), where NDI was used as the A' unit and thiazole groups as the A units, linked together in an alternating polymer with thiophene units, resulting in decreased LUMO level to -4.3 eV.[128]

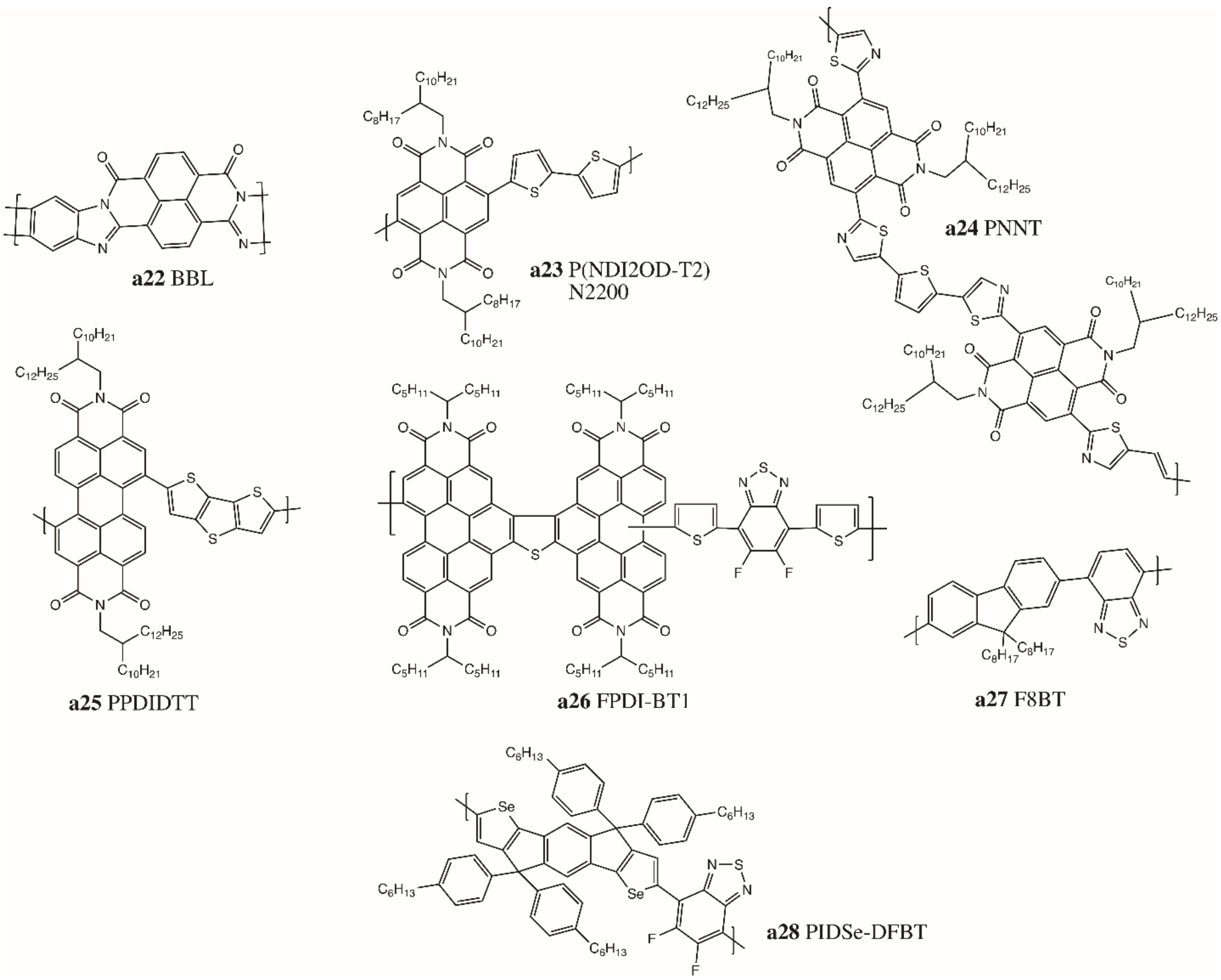

Figure 2.7. Chemical structures of representative polymer acceptors incorporated into LbL devices.

Table 2.7. Energy levels of representative polymer acceptors incorporated into LbL devices.

Material	HOMO (eV)	LUMO (eV)	Ref
BBL (**a22**)	-5.9	-4.0	125
N2200 (**a23**)	-5.4	-3.9	126
PNNT (**a24**)	/	-4.3	128

PPDIDTT (**a25**)	-5.9	-3.9	[129]
PIDSe-DFBT (**a28**)	-5.3	-3.5	[130]

Another monomeric building block that has been explored for use in polymeric acceptors is perylene diimide (PDI). While PDI is structurally similar to NDI, it has a tendency to form large aggregate domains, promoting separation with the polymer donor and reduced exciton dissociation.[131] PDIs have been evaporated as small molecules, as well as integrated into soluble copolymers for solution processing.[110] Marder and coworkers synthetized a polymer with electron-rich dithienothiophene (DTT) and electron-poor PDI (PPDIDTT, **Figure 2.7 a25**) that exhibited good thermal stability, a LUMO level of -3.9 eV, and a high electron mobility of $1.3\text{x}10^{-2}$ $cm^2V^{-1}s^{-1}$.[129] However, when introduced into LbL OPV devices it only resulted in a *PCE* of 1%.[132] Ade and coworkers developed a rigid, planar copolymer containing two PDI units fused with thiophene moieties to a fluorinated BTH unit (FPDI-BT1, **Figure 2.7 a26**).[133] The rigid nature of the backbone, combined with the specific twist angle of the fused PDI dimer, reduced both the formation of large aggregates and the reorganization energy during film formation, producing devices with *PCE* of > 7%.[134] Fluorene and IDT building blocks have also been coupled with BTH units (F8BT, PIDSe-DFBT, **Figure 2.7 a27-28**) leading to favourable electron affinity and good electron mobility but poor performance when integrated into LbL OPV devices.[130],[135]

2.6. LbL OPV Device Fabrication by Sequential Spin Coating Processes

The properties of the LbL active layer can be decoupled through separate optimization of the first and the second layers. The first layer is solution processed, and can be annealed prior to deposition of the second layer to yield the desired morphology, crystallinity, and roughness. Deposition of the second layer can be achieved by one of three route: use of an orthogonal solvent to the first layer (resulting in a bilayer interface), utilizing a compatible solvent (to create a pseudo-bilayer, **Scheme 2.1**), or evaporation (**Scheme 2.2 c, d**). Additional processing and annealing steps can be exploited to enhance interdiffusion of the bilayer or expansion of the pseudo-bilayer.[82],[136] **Table 2.8** is a summary of the performance (*PCE*) and processing conditions for solution-processed LbL OPV devices prepared via spin coating, with emphasis on material composition, solution concentration, spin rate, and annealing conditions. High-performing devices can only be achieved with optimal intermixing to yield favorable vertical phase separation. Compared to BHJ devices, which produce a random blend of the acceptor and donor materials, the LbL method facilitates superior separation over the entire length of the active layer, promoting improved charge transportation and collection.[23-25],[30],[71],[127],[137],[138] This vertical active layer separation is often described as a three phase morphology, where a substantial concentration of the donor can be found at the anode, acceptor at the cathode and a blend in the center, enabling LbL solution-processed devices to outperform BHJ devices.

Table 2.8. Photovoltaic device properties and processing conditions of LbL OPV devices prepared via spin-coated processes.

Donor/ concentration (mg/ml)	Acceptor/ concentration (mg/ml)	Structure Direct (Di) or Indirect (In)	Solvent (D)[a)]/spin rate (rpm)	Solvent (A)/spin rate (rpm)	Thermal treatment[b)] (°C/min)	PCE (%)	Ref
BP (**c12**)/10	$PC_{61}BM$ (**a2**)/6	Di	CF:CB/ -	Tol/3000	D: 160/20 A : 65/10	2.25	82
P3OT (**b15**)/8	$PC_{61}BM$ (**a2**)/20	Di	CF/2750	Pyridine/2450	D: 120/10 A: 150/20	1	136
P3HT (**b16**)/20	$PC_{61}BM$ (**a2**)/10	Di	DCB/1000	DCM/4000	150/20	3.5	22
P3HT (**b16**)/40 (*4 wt%*)	$PC_{61}BM$ (**a2**)/50 (*5 wt%*)	Di	CB/ -	DCM/ -	150/30	2.6	139
P3HT (**b16**)/15	$PC_{61}BM$ (**a2**)/5	Di	DCB/1000	DCM/2000	100/10	3.6	140
P3HT (**b16**)/40 (*4 wt%*)	$PC_{61}BM$ (**a2**)/50 (*5 wt%*)	Di	CB/ -	DCM/ -	150/30	2.18	141
P3HT (**b16**)/20	$PC_{61}BM$ (**a2**)/5	In	CB/2500	DCM/4500	D: 150/10 A: 150/5	2.6	142
P3HT (**b16**)/15	$PC_{61}BM$ (**a2**)/5	Di	DCB/1000	DCM/4000	D: 60/20 A: 150/20	3.8	143
P3HT (**b16**)/15	$PC_{61}BM$ (**a2**)/5	Di	DCB/1000	DCM/4000	150/5	4	144
P3HT (**b16**)/20	$PC_{61}BM$ (**a2**)/5	Di	CB/1500	DCM/4000	150/10	3.45	145
P3HT:F_4-TCNQ /20 (0.5 wt%)	$PC_{61}BM$ (**a2**)/5	Di	CB/1500	DCM/4000	150/10	4.02	145
P3HT (**b16**)/30	$PC_{61}BM$ (**a2**)/10	Di	CB/2000	DCM/2000	140/10	3.25	146
P3HT (**b16**)/30	$PC_{61}BM$ (**a2**)/10	Di	CB/2500	DCM/4000	-	3.09	147
P3HT:RRa-P3HT/30 (15 wt%)	$PC_{61}BM$ (**a2**)/10	Di	CB/2500	DCM/4000	-	3.83	147
P3HT (**b16**)/ -	$PC_{61}BM$ (**a2**)/ -	Di	DCB/ -	DCM/ -	140-180/30	3.93	148
P3HT (**b16**)/ -	$PC_{61}BM$ (**a2**)/ -	Di	CB/ -	DCM/ -	150/10	3.45	149

P3HT (**b16**)/15 (*1.5 wt%*)	PC$_{61}$BM (**a2**)/15 (*1.5 wt%*)	Di	p-XY/1000	p-XY/1000	150/3	2.70	150
P3HT (**b16**)/22	PC$_{61}$BM (**a2**)/ -	Di	DCB/900	DCM/3000	150/20	4.12	40
P3HT (**b16**)/30	PC$_{61}$BM (**a2**)/10	Di	CB/2500	DCM/4000	140/10	3.81	151
P3HT (**b16**)/ -	PC$_{61}$BM (**a2**)/5 (*0.5 wt%)*	Di	CB/2000	DCM/ -	180/20	2.8	152
P3HT:PEG/ - (6 wt%)	PC$_{61}$BM (**a2**)/5 (*0.5 wt%*)	Di	CB/2000	DCM/ -	180/20	3.71	152
P3HT (**b16**)/ -	PC$_{61}$BM (**a2**)/ -	Di	CB/ -	DCM/ -	-	1.80	153
P3HT (**b16**)/20	PC$_{61}$BM (**a2**)/5	Di	DCB/700	DCM/3000	D: 140/ - A: 120/10	3.39	154
P3HT (**b16**)/10	PC$_{61}$BM (**a2**)/5	Di	DCB/1000	DCM/4000	140/30	1.8	155
P3HT (**b16**)/ -	PC$_{61}$BM:PEG/ - (5wt%)	Di	DCB/ -	DCM/3000	150/20	4.40	156
P3HT (**b16**)/15	PC$_{61}$BM (**a2**)/5	Di	DCB/1000	DCM/4000	D: 90/5 A: 150/20	3.25	157
P3HT (**b16**)/15	PC$_{61}$BM (**a2**)/5	Di	DCB/1000	DCM/4000	D: 60/20 A: 150/20	3.24	158
PCDTBT (**b26**)/7	PC$_{61}$BM (**a2**)/10	Di	DCB/700	DCM/4000	-	4.27	23
PBDTTT-C-T (**b34**)/15	PC$_{61}$BM (**a2**)/8	Di	DCB/ -	DCM/ -	110/30	6.86	137
P3HT (**b16**)/20	PC$_{61}$BM (**a2**)/ -	Di	DCB/1000	DCM/4000	150/20	3.4	159
P3HT (**b16**)/5	PC$_{61}$BM (**a2**)/10	Di	CF/ -	DCM/ -	-	2.16	160
P3HT (**b16**)/30	PC$_{61}$BM (**a2**)/10	Di	CB/2500	- /4000	140/10	3.09	161
P3HT:PS/30	PC$_{61}$BM (**a2**)/10	Di	CB/2500	- /2000	140/10	3.25	161
P3HT:RRa-P3HT/30(15 wt%)	PC$_{61}$BM (**a2**)/10	Di	CB/2500	- /4000	140/10	3.83	161
BDT-3T-CA (**b11**)/7.5	PC$_{61}$BM (**a2**)/ -	Di	CF/-	DCM/3500	-	4.16	71
P3HT (**b16**)/20	PC$_{61}$BM (**a2**)/10	Di	DCB/1000	DCM/4000	150/20	2.97	162
P3HT (**b16**)/15	PC$_{61}$BM (**a2**)/4	Di	CB/1000	DCM/4000	150/20	3.54	163
Cy5-Cl (**c11**)/2	PC$_{61}$BM (**a2**)/ -	Di	TFP/ -	CB/ -	-	0.93	79
P3HT:TES-ADT/ 20 (5 wt%)	PC$_{61}$BM (**a2**)/10	Di	CB/ -	DCM/4000	150/1	2.70	164

P3HT (**b16**)/ -	PC$_{61}$BM (**a2**)/5	Di	DCB/1000	DCM/350+4000	D: 50/5 A: 150/20	5.1	24
P3HT (**b16**)/15	PC$_{61}$BM (**a2**)/4	Di	CB/1000	DCM/4000	150/20	3.71	165
P3HT (**b16**)/20	PC$_{61}$BM (**a2**)/10	Di	DCB/ -	DCM/ -	150/30	2.79	166
P3HT (**b16**)/ -	PC$_{61}$BM (**a2**)/ -	Di	DCB/ -	DCM/4000	-	3.11	167
P3HT (**b16**)/12	PC$_{61}$BM (**a2**)/8	Di	DCB/1000	DCM/800	D: 70/10	1.96	168
P3HT (**b16**)/14	PC$_{61}$BM (**a2**)/3.5	Di	CB:1-CN/1000	DCM/2000	D: 110/60	3.25	169
P3HT (**b16**)/10	PC$_{61}$BM (**a2**)/10	Di	CB/1000	Tol:2-CP/ -	150/10	3.1	170
PTB7 (**b32**)/10	PC$_{61}$BM (**a2**)/10	Di	CB/1000	1-Butanol:2-CP/ -	-	6.0	170
PSDTTT (**b29**)/ 10	PC$_{61}$BM (**a2**)/10	Di	CB/1000	Tol:2-CP/ -	-	3.8	170
P3HT (**b16**)/30	PC$_{61}$BM (**a2**)/ -	Di	CB:s-TCB/ 2500	DCM/4000	140/10	3.30	171
P3HT (**b16**)/10	PC$_{61}$BM (**a2**)/6.4	Di	DCB/ -	DCM/ -	150/10	2.0	172
P3HT (**b16**)/ -	PC$_{61}$BM (**a2**)/5	Di	Tol/ -	DCM/4000	150/1	3.25	173
P3HT (**b16**)/20	PC$_{61}$BM (**a2**)/10	Di	DCB:DIO/1000	DCM/4000	150/15	1.84	174
PSEHTT (**b27**)/10	PC$_{61}$BM (**a2**)/10	Di	DCB:DIO/2200	DCM/4000	150/15	4.13	174
PBDTTT-C (**b16**)/10	PC$_{61}$BM (**a2**)/10	Di	DCB:DIO/2000	DCM/4000	150/15	5.33	174
P3HT (**b16**)/5	PC$_{61}$BM (**a2**)/5	Di	CF/5000	DCM/2500	-	0.3	175
PCDTBT (**b26**)/7	PC$_{71}$BM (**a5**)/28	Di	DCB:CB/5000	DCM:DCB:CB/ 2000	80/10	6.34	176
PCDTBT (**b26**)/7	PC$_{71}$BM (**a5**)/28	Di	DCB/700	DCM:DCB:CB/ 4000	-	5.29	23
P3HT (**b16**)/22	PC$_{71}$BM (**a5**)/ -	Di	DCB/900	DCM/3000	150/20	4.38	40
PCDTBT (**b26**)/4	PC$_{71}$BM (**a5**)/16	Di	CB/ -	DCM/5000	-	2.11	177
PII2T-C10C8 (**b37**)/7	PC$_{71}$BM (**a5**)/ -	Di	CF/ -	DCB/ -	D: 150/30 A: 110/10	5.02	178
PCDTBT (**b26**)/8	PC$_{71}$BM (**a5**)/6	Di	CB:DIO/2500	DCM:DIM/4000	100/15	7.12	179
Si-PCPDTBT (**b24**)/10	PC$_{71}$BM (**a5**)/20	Di	DCB/2000	DCM:DCB/2000	120/10	4.6	114
pDPP (**b39**)/5	PC$_{71}$BM (**a5**)/30	Di	CF:DCB/1000	DCB/ -	-	7.59	138

PDPP5T (**b38**)/6	PC$_{71}$BM (**a5**)/24	Di	CF/ -	DCB/ -	-	5.0	[180]
PTB7-Th (**b33**)/ 10	PC$_{71}$BM (**a5**)/ -	Di	DCB/ -	DCM/ -	-	8.5	[25]
PCDTBT (**b26**)/ 10	PC$_{71}$BM (**a5**)/6	Di	CB:DIO/2500	DCM:DIO/4000	D: 110/15, 150 A: 110/15	5.03	[181]
PCPDT-FBT (**b25**)/6	PC$_{71}$BM (**a5**)/16	In	o-XY/ -	o-XY:DCB/ -	110/30	5.84	[182]
PCPDTBT (**b23**)/ 8	PC$_{71}$BM (**a5**)/5	Di	CB:DIO/2200	DCM:DPE/1500	D: 110/15 A: 110/15	3.36	[183]
PTB7 (**b32**)/14	PC$_{71}$BM (**a5**)/ 3.25	Di	CB:DIO:1-CN/ 1000	DCM/4000	-	7.43	[26]
PffBT4T-2OD (**b30**)/ -	PC$_{71}$BM (**a5**)/ -	Di	XY/ -	XY/ -	100/ -	8.9	[30]
PffBT4T-2OD (**b30**)/10	PC$_{71}$BM (**a5**)/10	Di	CB/ -	CB/ -	D: 80/10 A: 150/1.5	7.64	[184]
P3HT (**b16**)/22	IC60BA (**a8**)/7.5	Di	DCB/900	DCM/3000	150/20	6.22	[40]
P3HT (**b16**)/22	IC70BA (**a9**)/7.5	Di	DCB/900	DCM/3000	150/20	6.48	[40]
P3HT (**b16**)/15	IC60BA (**a8**)/5	Di	DCB/1000	DCM/3000	150/20	5.12	[185]
P3HT (**b16**)/22.5	IC60BA (**a8**)/7.4	Di	DCB/2200	DCM/3000	140/50	5.6	[186]
P3HT-NW/24	IC60BA (**a8**)/10	Di	DCB/800	DCM/3000	D: 140/10 A: 150/30	3.64	[187]
DR3TBDTT (**b12**)/ -	PCBSD (**a6**)/ -	In	CF/ -	DCB/ -	A: 170/40	1.1	[44]
PPV/ -	BBL(**a22**)/ -	Di	MeOH/ -	GaCl$_3$:nitromethane/ -	D: 250/60 A: 40/600	0.7	[125]
P3HT (**b16**)/4	PIDSe-DFBT (**a28**)/7.5	In	DCM:CB/1500	DCB/1000	140/10	2.34	[130]
SQ (**b3**)/7	PPDIDTT (**a25**)/8	In	DCM/ -	DCB/800	100/1	1.08	[132]
PBDB-TFS1 (**b43**)/10	ITIC-4F (**a16**)/ -	Di	CB/ -	DCB:THF/ -	100/10	13	[60]
PTB7 (**b32**)/10.5	N2200 (**a23**)/12	In	DCM:CB/2600	DCB:CB/1200	-	2.94	[188]
PBDTT-FTTE (**b36**)/6	PNNT(**a24**)/6	In	DCB/1000	DCB/1000	-	4.1	[128]
PBDB-T (**b41**)/6	NCBDT (**a17**)/6	Di	CF/1900	DCM/2500	-	10.04	[189]
PBDB-T (**b41**)/6	ITIC (**a10**)/6	Di	CF/1900	DCM/2500	-	5.86	[189]

PTB7-Th (**b33**)/6	NCBDT (**a17**)/6	Di	CF/1900	DCM/2500	-	8.27	[189]
PTB7-Th (**b33**)/6	ITIC (**a10**)/6	Di	CF/1900	DCM/2500	-	7.13	[189]
PDCBT (**b40**)/6	NCBDT (**a17**)/6	Di	CF/1900	DCM/2500	-	3.28	[189]
PDCBT (**b40**)/6	ITIC (**a10**)/6	Di	CF/1900	DCM/2500	-	2.38	[189]
PM6 (**b42**)/ -	ITIC-4F (**a16**)/ -	Di	XY/ -	XY/ -	100/ -	12.5	[30]
FTAZ (**b49**)/5	ITIC-M (**a12**)/10	Di	LM/1000	2-MeTHF/2000	150/10	12.2	[190]
OTAZ (**b50**)/5	ITIC-M (**a12**)/10	Di	LM/1000	2-MeTHF/2000	150/10	4.7	[190]
FTAZ-OTAZ (**b51**)/5	ITIC-M (**a12**)/10	Di	LM/1000	2-MeTHF/2000	150/10	5.8	[190]
PTFB-O (**b44**)/10	ITIC-Th (**a11**)/ -	Di	CB/2000	THF/ -	100/10	11.8	[29]
P3TEA (**b31**)/12	ITIC-4F (**a16**)/ -	Di	1,2,4-trimethylbenzene/2000	THF/ -	100/10	9.80	[29]
PBDB-T (**b41**)/8	ITIC (**a10**)/10	In	CB/1500	o-XY/2000	-	6.7	[50]
PBDB-T (**b41**)/7	FPDI-BT1 (**a26**)/ -	Di	DCB/1000	CB:DCB/3500	-	6.93	[133]
J71 (**b46**)/12	ITC6-IC (**a15**)/12	Di	CF/2000	CF/2000	150/5	12.08	[28]
PTQ10 (**b44**)/12	IDIC (**a18**)/12	Di	CF/4000	CF/4000	140/5	12.32	[28]
J71 (**b46**)/12	MeIC (**a14**)/12	Di	CF/2000	CF/2000	150/2	11.43	[28]
J71 (**b46**)/12	ITCC (**a13**)/12	Di	CF/2000	CF/2000	150/2	10.44	[28]
J71 (**b46**)/12	ITIC (**a10**)/12	Di	CF/3500	CF/3500	150/10	10.94	[28]
PBDB-T (**b41**)/6	NCBDT (**a17**)/6	In	CF/1900	DCM/2500	-	10.62	[191]
PBDB-T (**b41**)/4	N2200(**a23**)/4	In	CF/2000	CB/2000	- /10	9.52	[127]

a) Solvent acronyms: chlorobenzene (CB), 1,2-dichlorobenzene (DCB), chloroform (CF), *p*-xylene (p-XY), toluene (Tol), 1,2,4-trichlorobenzene (TCB), (R)-(+)-limonene (LM), 2-methyltetrahydrofuran (2-MeTHF), diodooctane (DIO), 1,8-octanedithiol (ODT).

b) Non-existent step or value not reported designated with "-".

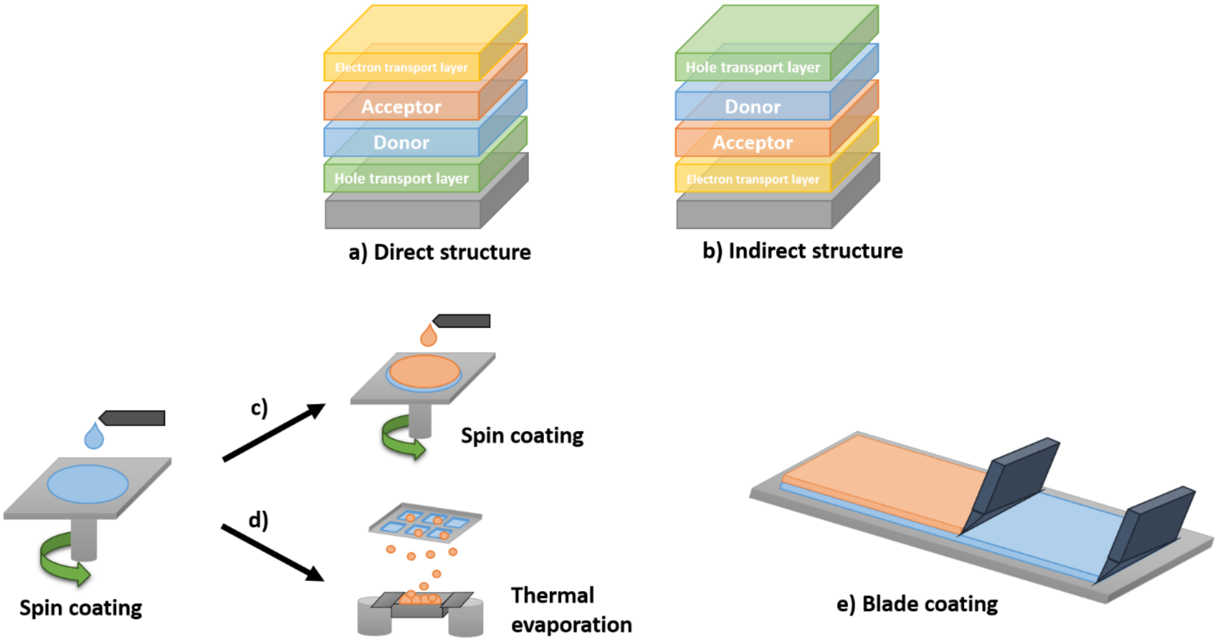

Scheme 2.2. Diagram of (a) a direct structure configuration and (b) an indirect structure configuration of OPV devices, and fabrication process via (c) sequential spin coating, (d) hybrid spin coating/thermal evaporation route, (e) blade coating.

Ayzner et al. initially reported the spin casting of P3HT (**Figure 2.5 b16**)/$PC_{61}BM$ (**Figure 2.1 a2**) LbL OPV devices by depositing the donor (P3HT) from o-dichlorobenzene (DCB), followed by the acceptor ($PC_{61}BM$) in dichloromethane (DCM), a solvent which does not dissolve the P3HT layer. The authors reported a well-defined planar interface resulting in a *PCE* of 3.5%, which is comparable to performances obtained with BHJ devices.[22] The P3HT/$PC_{61}BM$ system has since been investigated by numerous groups, using a similar methodology to achieve efficiencies comparable or greater than their BHJ counterparts.[24,40,139-175] The best reported efficiency of this donor/acceptor system in LbL devices is 5.1%, realized by formation of a bicontinuous donor/acceptor network which resulted in significantly reduced bimolecular recombination.[24] However, these literature reports consistently determined that even without optimization of these processing conditions, interdiffusion between P3HT and $PC_{61}BM$ was occurring. Despite the use of orthogonal solvents, intermixing between the two materials is transpiring due to swelling of the P3HT layer from the solvent used for the fullerene deposition.[139,143,144,149,192]

Thermal annealing of the bilayer increases the degree of intermixing by inducing miscibility and penetration of $PC_{61}BM$ molecules into the amorphous region of P3HT, without disruption of the ordered polymeric domains.[193] By annealing devices at 150 °C for 20 min, Lee et al. increased the *PCE* from 1.31 to 3.8%.[143]

Cheng et al. demonstrated efficient vertical phase separation of PBDTTT-C-T (**Figure 2.5 b34**)/$PC_{61}BM$ (**Figure 2.1 a2**) devices that exhibited an average *PCE* of 6.86%, exceeding performances measured from analogous BHJ blends (4.31%).[137] Further iterations consisted of substituting $PC_{61}BM$ with $PC_{71}BM$ (**Figure 2.1 a5**) or ICBA (**Figure 2.1 a8-9**) fullerene small molecules, paired with lower band gap conjugated polymers, permitting increased efficiencies up to almost 9%.[23,25,26,30,114,137,138,176-187]

Recently, NFAs have been integrated into spin casted bilayer devices, enabling *PCE*s in excess of 10%.[28,29,44,50,60,125,127,128,130,132,133,188-191] One example of a NFA system is PBTB-TFS1 (**Figure 2.6 b43**)/ITIC-4F (**Figure 2.2 a16**), which was reported to produce a *PCE* of 13%, surpassing blend-based devices (11.8%).[60] Cui et al. demonstrated that solubility and solvent choice are key for high performing LbL OPV devices.[60] Numerous studies have since shown the pseudo-bilayer morphology is susceptible to variations in the solvent or cosolvent,[114,133,148-150,160,170,171,173,176,178,188,190] but is also influenced by other parameters such as thermal annealing,[24,135-137,141,156,157,159,163,164,182,185,192,194,195] use of additives,[26,169,171,174,179,181,183] or addition of binary components to the donor polymer.[145,147,152,161,164]

Cho et al. explored how solvent choice influenced morphology and phase separation in P3HT layers. Chlorobenzene (CB), DCB, chloroform (CF) and p-xylene (p-XY) were all investigated for processing the P3HT layer, with p-XY also utilized for the $PC_{61}BM$ acceptor layer.[150] A *PCE* around 3% was obtained for p-XY, while devices prepared from CB had a *PCE* of only 0.5%, indicating that the formation and extent of the phase separation is highly influenced by solvents. Similarly, Yi et al. investigated CF, toluene (Tol), CB, DCB and 1,2,4-trichlorobenzene (TCB) as solvents for P3HT, while using DCM to process $PC_{61}BM$.[173] P3HT solutions prepared from low boiling point solvents formed films with reduced crystallinity and numerous amorphous regions, promoting better fullerene diffusion and faster interdiffusion. Kim et al. also reported that modification of the processing solvent for $PC_{61}BM$ induces a change in the molecular orientation of polymer crystallite from edge-on to more isotropic in PII2T-C10C8 (**Figure 2.5 b37**) films, improving vertical charge transportation.[178]

Non-halogenated solvents have also been investigated. Ye et al. used (R)-(+)-limonene (LM) for FTAZ-based donors (**Figure 2.6 b49-51**), and 2-methyltetrahydrofuran (2-MeTHF) for the ITIC-M (**Figure 2.2 a12**) acceptor.[190] LM promoted molecular order in amorphous FTAZ polymer films, facilitating the formation of larger domain spacing and enabling an efficiency of 12.2%, again outperforming BHJ control blends (11.7%). To reach 13% *PCE*, Cui et al. controlled both the bulk interface and nanoscale phase separation by employing specific ratios of cosolvents (DCB:tetrahydrofuran (THF)) for the ITIC-4F film deposition.[60] Comparable improved nanoscale phase separation was also demonstrated by Ahn et al., with controlled penetration of the acceptor through adjustment of the DCM:DCB cosolvent ratio for $PC_{61}BM$.[114] Cosolvents also facilitate interdiffusion by optimizing the degree of polymer swelling (without dissolving the layer), as reported by Aguirre et al. who used a blend of Tol and 2-chlorophenol (2-CP).[170]

Solvent additives can also be exploited to tune the vertical phase separation. Vohra et al used a high-boiling point solvent (o-TCB) as an additive for CB solutions of P3HT, which resulted in increased P3HT crystallinity leading to reduced PCBM interdiffusion and thinner intermixed region.[171] On the contrary, low vapor pressure solvents such as diodooctane (DIO) or 1,8-octanedithiol (ODT) act as polymer swelling agents when incorporated as additives, enabling improved mixing between fullerenes and the polymer, enhancing performances.[174] However, the need for orthogonal solvent, cosolvents or solvent additives in LbL devices is not critical for all combinations of donors and acceptors. For example, Sun et al explored five different donor/acceptor pairs, J71 (**Figure 2.6 b46**)/ITC6-IC (**Figure 2.2 a15**), PTQ10 (**Figure 2.6 b44**)/IDIC (**Figure 2.2 a18**), J71/MeIC (**Figure 2.2 a14**), J71/ITCC (**Figure 2.2 b13**) and J71/ITIC (**Figure 2.2 a10**), using only CF as a solvent for the sequential spin casting.[28] Fabricated LbL devices systematically exhibited similar or greater efficiencies (10.44 – 12.32%) than their BHJ blend counterparts (10.46 – 11.75%), with improved vertical phase separation, stronger absorption spectra, increased charge transport and collection, and reduced energy loss. Dong et al. investigated the use of halogen-free xylene (XY) as a solvent for the deposition of PM6 (**Figure 2.6 b42**)/ITIC-4F bilayers.[30] The graded separation of layers was preserved, while simultaneously reducing dependence on processing conditions and improving performances compared to BHJ control devices.

Another strategy to tune film morphology is the addition of a binary component to the donor layer. Doping of P3HT with p-type solution-processable small molecules such as tetrafluoro-tetracyanoquinodimethane (F_4-TCNQ) and 5,11-bis(triethylsilylethynyl) anthradithiophene (TES-ADT) impacts aggregate formation, crystallinity and mobility.[145],[164] Film nanostructures can also be controlled through the addition of polyethylene glycol (PEG) or polysterene (PS) in P3HT solutions.[152],[161] After extraction of the PS or PEG, the resulting P3HT films contain porous circular depressions whose diameter and depth can be controlled by modification of the polymer ratios during film deposition. Optimization of the PEG content up to 6 wt% increased the *PCE* from 2.80 to 3.71% for P3HT/$PC_{61}BM$ devices. Regioregular P3HT blended with less crystalline regiorandom P3HT (RRa-P3HT) promotes intermixing and control of the vertical concentration gradient with PC$_{61}$BM.[161] An optimal content of 15 wt% RRa-P3HT improved the *PCE* from 3.09 to 3.83%.

2.7. Other Processing Methods

2.7.1. Hybrid Spin Casting/Evaporation Process

The use of all-solution processing for LbL devices necessitates that both donor and acceptor materials are sufficiently soluble to be processed. However, many small molecule acceptors, such as C$_{60}$ and C$_{70}$ (**Figure 2.1 a1/a4**), are highly insoluble. In such cases a combination of solution processing and thermal evaporation is employed. The insoluble acceptor is deposited via thermal evaporation, with the donor polymer or small molecule layer formed through spin casting to facilitate formation of the bilayer (**Scheme 2.2 d**). This hybrid route of LbL OPV fabrication enabled the incorporation of C$_{60}$ and C$_{70}$ acceptors with donor polymers or soluble small molecule such as ADPM, cyanines, squaraines and porphyrins.[46,63,66,68,72,73,75,77,78,83,84,86,89-92,94-102,105-109,111,113,169,195-207] Some examples of evaporated phthalocyanine-based NFAs have also been reported.[87,110,208] A summary of device performances and processing conditions from hybrid LbL OPVs prepared from thermally evaporated acceptors can be found in **Table 2.9.**

Thermal annealing of hybrid LbL films can induce interpenetration of the donor and the acceptor by promoting diffusion of fullerenes, improving the degree of crystallization and creating a controlled gradient concentration within the active layer.[68,101,102,107,108,111,113,197,206] Early studies involving P3HT (**Figure 2.5 b16**)/C$_{60}$ (**Figure 2.1 a1)** devices demonstrated that annealing the bilayer near the melting point of P3HT (220 °C) produced an intercalated BHJ-like morphology along the interface and enhanced P3HT crystallinity, resulting in *PCE* values that were an order of magnitude larger compared to the untreated bilayer.[108] However, Stevens et al. demonstrated that reducing this annealing temperature results in higher *PCE*. Heating P3HT/C$_{60}$ devices above 190 °C could induce P3HT to migrate to the top surface, while C$_{60}$ penetrated into the P3HT amorphous regions, reducing the concentration gradient and negatively impacting *PCE* values.[111] Annealing at a lower temperature of 170 °C resulted in devices with a *PCE* of 1.19%.

Huang et al. investigated the impact of both pre-annealing and post-annealing on PCPDTTBT (**Figure 2.5 b28**)/C$_{70}$ (**Figure 2.1 a4)** devices.[206] Pre-annealing the bottom PCPDTTBT layer at 200 °C resulted in a fibrillar morphology with increased donor/acceptor interfacial area and an improved *PCE* of 1.65%. Further post-annealing of the entire bilayer at

200 °C induced nanostructural transformations that reorganized the PCPDTTBT and C_{70} interface, expanding the contact area and improving the *PCE* to 2.85%. Kekuda et al. demonstrated that post-annealing of F8T2 (**Figure 2.5 b22**)/C_{70} hybrid devices at 200 °C increased the *PCE* from 0.40 to 3.40% due to the creation of an interdigitated structure with well-aligned polymer crystal nanodomain features.[113] The extent of nanocrystalline morphology in 1-NPSQ (**Figure 2.3 b4**)/C_{60} hybrid devices was also improved through annealing, resulting in an enhanced *PCE* of 5.7%.[66]

Solvent choice for processing the first layer can also drastically influence interface morphology and significantly improve *PCE*. Kekuda et al. used CF, XY, DCB and 1,2,4-trichlorobenzene (TCB) for P3HT deposition, producing donor films with surface roughness values of 1.14, 4.83, 8.62 and 9.2 nm, respectively.[207] Solvent-induced crystallinity of the polymer, along with increased surface roughness, improved the *PCE* of P3HT/C_{70} hybrid devices from 1.04% (for CB) to 3.56% (for TCB), without a thermal treatment step.

Finally, improved active layer morphology can also be achieved with dopants in the solution-processed layer. The nanostructure of P3HT was modified through blending with graphene (G-P3HT, **Table 2.9**) followed by ultrasonic vibration post-treatment of the G-P3HT film, leading to a *PCE* of 5.17% when paired with C_{60}.[205] Doping is also utilized to increase the donor layer conductivity, such as $NOBF_4$ doped Cy3-ClO_4^- (**Figure 2.4 c1**).[75],[200]

Table 2.9. Photovoltaic properties and processing conditions of selected hybrid processed LbL OPV devices.

Donor/concentration (mg/ml)	Donor solvent/spin rate (rpm)	Acceptor evaporated/thickness (nm)	Thermal treatment[a)] (°C/min)	PCE (%)	Ref
MEH-PPV (**b13**)/2	XY/ -	C_{60} (**a1**)/40	170/-	0.92	197
P3HTV (**b18**)/15	DCB/ -	C_{60} (**a1**)/40	170/20	1.19	111
P3HT (**b16**)/5	CB/2000	C_{60} (**a1**)/40	150/30	2.6	198
G-P3HT/ -	DMF:CB/ -	C_{60} (**a1**)/6	140/15	5.17	205
SubNc (**c29**)/ -	CB/2000	C_{60} (**a1**)/35.5	120/40	1.47	89
SubPc-A (**c24**)/6	CB/2000	C_{60} (**a1**)/32	-	1.71	94
2Tp-SubPc (**c25**)/3	CB/2000	C_{60} (**a1**)/32	-	1.39	95
Cy3-ClO_4^-:$NOBF_4$ (**c1**)/10	CB/ -	C_{60} (**a1**)/40	-	2.0	200
Cy0619 (**c10**)/7	CB/1000	C_{60} (**a1**)/30	-	2.5	78

Cy3-PF$_6^-$ b) (**c3**)/ -	TFP/ -	C$_{60}$ (**a1**)/ -	-	3.7	204
BO-ADPM (**c30**)/2	THF/2000	C$_{60}$ (**a1**)/45	-	2.53	90
SQ (**b3**)/1	CF/3000	C$_{60}$ (**a1**)/40	90/ -	4.6	66
DPSQ (**b5**)/1	CF/3000	C$_{60}$ (**a1**)/40	80/ -	5.2	66
1-NPSQ (**b4**)/1	CF/3000	C$_{60}$ (**a1**)/40	70/ -	5.7	66
PCDTBT (**b26**)/8	DCB/2000	C$_{60}$ (**a1**)/	-	1.48	87
F8T2 (**b22**)/20	TCB/2000	C$_{70}$ (**a4**)/40	200/60	3.40	113
P3HT (**b16**)/ -	TCB/2000	C$_{70}$ (**a4**)/40	D: 100/60 A:150/30	3.56	207
PCPDTTBT (**b28**)/10	TCB/2500	C$_{70}$ (**a4**)/40	D: 200/60 A: 200/60	2.85	206
P3HT (**b16**)/15	DCB/1000	Cl-Cl$_6$BsubPc (**c23**)/20	-	0.52	208
P3HT (**b16**)/15	DCB/1000	Cl-BsubPc (**c22**)/20	-	0.98	208
PCDTBT (**b26**)/8	DCB/2000	(345F)$_2$-SiPc (**c21**)/93	150/30	1.52	87

a) Non-existent step or value not reported designated with "-".
b) Indirect structure.

2.7.2. Blade Coating

One of the core objectives of OPV research is to develop large-scale, roll-to-roll manufacturing of devices. It is therefore essential to transition away from lab-scale spin coating and focus on scalable solution-processing techniques. The majority of high-performing OPV devices have been fabricated from spin coating methods, with the adaptation to industrial printing techniques non-trivial, as minimization of the geometric fill factor (GFF) losses inherent to any type of PV technology is complex.[209] Compared to BHJ OPVs, performances of LbL-processed OPVs have proven to be less dependent on processing conditions, which is often the first barrier encountered.[30]

Some preliminary examples of BHJ OPV devices fabricated using roll-to-roll compatible deposition techniques have been reported, such as slot coating[210-214] or blade coating.[215-220] However, analogous investigations employing LbL processes using similar scalable techniques remain limited. Initial reports focused on hybrid processing, where the first layer was deposited through blade coating.[221],[180] Investigations involving deposition of both layers via blade coating (**Scheme 2.2 e**) were only reported in 2019.[28],[30],[31],[222] A summary of device performance and processing conditions for LbL OPVs fabricated from blade coating can be found in **Table 2.10**.

Impressive *PCE*s of > 16% have been achieved through blade coating using a combination of NFAs and a single solvent system.[31] Additionally, authors have consistently reported improved performances for LbL-based devices compared to analogous BHJ-based devices. Sun et al. attained a *PCE* of 11.47% for 0.04 cm^2 J71 (**Figure 2.6 b46**)/ITC6-IC (**Figure 2.2 a15**) LbL OPV blade coated cells using CF as a solvent for both layers, which was superior to BHJ OPVs prepared from blade coating (10.41%).[222] Detailed characterization of film morphology revealed that LbL blade coating achieved a more thermodynamically favourable nanomorphology, with suitable donor/acceptor interfaces and larger separation between donor/acceptor domains, which was facilitated through independent optimization of each layer. Furthermore, the 3D geometry of the bilayer enabled higher charge generation, increasing the light absorption coefficient. Creation of a well-defined bicontinuous network with a p-i-n like structure also facilitated highways for charge transport and collection at the appropriate electrodes, reducing the rate of charge recombination. Improved photo, thermal, and bending stability compared to the BHJ OPVs was also observed due to the vertical phase separation achieved in LbL devices.

Dong et al. fabricated larger area (1 cm^2) LbL OPVs based on PM6 (**Figure 2.6 b42**)/ITIC-4F (**Figure 2.2 a16**) using xylene as a non-halogenated processing solvent, and observed similar device performance improvements compared to the BHJ OPV analogues. Advantages with the LbL system included better graded separation of donor and acceptor materials, resulting in an improved *PCE* of 11% and enhanced photo-stability.[30]

The ubiquity of blade coating processing for LbL OPVs was demonstrated by Sun et al., who performed a comprehensive investigation involving multiple bilayer donor/acceptor systems and compared them to their BHJ OPV equivalents.[28],[31] LbL OPVs were prepared from J71 (**Figure 2.6 b46**)/ITC6-IC (**Figure 2.2 a15**), PTQ10 (**Figure 2.6 b44**)/IDIC (**Figure 2.2 a18**), PTQ10/Y6 (**Figure 2.2 a19**), PM6/Y6, PM6/Y6-2Cl (**Figure 2.5 a20**) and PM6/Y6-C2 (**Figure 2.5 a21**), with areas ranging from 0.04 to 11.86 cm^2. For 0.04 cm^2 cells with Y6 derivatives, *PCE* values above 15% were systematically achieved, with a maximum *PCE* of 16.4% for PM6/Y6 LbL OPVs, which exceeded the BHJ OPV module (15.4%). When the active area was increased to 11.52 cm^2, the GFF for the same LbL system was over 90% and delivered a *PCE* of 11.86% compared to 10.15% for BHJ; this represents the superlative reported *PCE* so far for large-area OPV devices. These promising results demonstrate that LbL blade-coating is an easy and efficient strategy for the up-scaling of OPVs towards future industrial applications.

Table 2.10. Photovoltaic properties and processing conditions of blade coated LbL OPV devices.

Donor/ concentration (mg/ml)	**Solvent (D)/blade spin (mm.s^{-1})/blade height (μm)**	**Acceptor/ concentration (mg/ml)**	**Solvent (A)/blade spin (mm.s^{-1})/blade height (μm)**	**Thermal annealing[a] (°C/min)**	**Cell area (cm^2)**	**PCE (%)**	**Ref**
PBDTTT-C-T[b] (**b34**)/9	Tol:o-XY/200/ -	C$_{70}$ (**a4**)/ N/A (Evap)	N/A	-	0.05	6.23	221
PTB7[b] (**b32**)/9	Tol:o-XY/ -	C$_{70}$ (**a4**)/ N/A (Evap)	N/A	-	0.05	7.15	221
PDPP5T (**b38**)/6	CF/ N/A (spin coating)	PC$_{71}$BM (**a5**)/20	TMB/20/254	-	0.09	5.3	180
J71 (**b46**)/12	CF/18/-	ITC6-IC (**a15**)/12	CF/18/-	150/5	0.04	11.47	222
PffBT4T-2OD (**b30**)/ -	XY/6/400	PC$_{71}$BM (**a5**)/ -	XY/6/400	-	0.04	8.2	30
PffBT4T-2OD (**b30**)/ -	XY/6/400	PC$_{71}$BM (**a5**)/ -	XY/6/400	-	1	7.8	30
PM6 (**b42**)/ -	XY/6/400	ITIC-4F (**a16**)/ -	XY/6/400	-	0.04	11.9	30
PM6 (**b42**)/ -	XY/6/400	ITIC-4F (**a16**)/ -	XY/6/400	-	1	11.0	30
J71 (**b46**)/12	CF/ - /400	ITC6-IC (**a15**)/12	CF/ - /400	-	0.04	11.42	28
J71 (**b46**)/12	CF/ - /400	ITC6-IC (**a15**)/12	CF/ - /400	-	1	10.35	28
PTQ10 (**b44**)/12	CF/ - /400	IDIC (**a18**)/12	CF/ - /400	-	0.04	11.28	28
PTQ10 (**b44**)/12	CF/ - /400	IDIC (**a18**)/12	CF/ - /400	-	1	10.42	28
PTQ10 (**b44**)/8	CF/12/ -	Y6 (**a19**)/8	CF/12/ -	-	0.04	15.10	31
PM6 (**b42**)/8	CF/12/ -	Y6-2Cl (**a20**)/8	CF/12/ -	-	0.04	15.89	31
PM6 (**b42**)/8	CF/12/ -	Y6-C2 (**a21**)/8	CF/12/ -	-	0.04	15.93	31
PM6 (**b42**)/8	CF/12/ -	Y6 (**a19**)/8	CF/12/ -	-	0.04	16.35	31
PM6 (**b42**)/8	CF/12/ -	Y6 (**a19**)/8	CF/12/ -	-	3.3	13.88	31
PM6 (**b42**)/8	CF/12/ -	Y6 (**a19**)/8	CF/12/ -	-	11.52	11.86	31

a) Non-existent step or value not reported designated with “-“.
b) Indirect structure.

2.8. Conclusion

Layer-by-layer (LbL) processing has become increasingly popular as a promising alternative to the widely adopted blended bulk heterojunction (BHJ) process for fabricating the donor/acceptor active layer in high-performing OPVs. In this review, we systematically explored the current literature associated with LbL OPVs, with particular focus on the various donor and acceptor materials utilized and processing conditions. We highlight advances in materials structure and thin film morphology which have resulted in significant improvements in *PCE*, and how state-of-the-art LbL OPVs consistently outperform their BHJ counterparts.

LbL processing is superior to BHJ blending in numerous ways. Firstly, each layer can be deposited separately and sequentially, enabling independent control and optimization of parameters, such as viscosity, temperature and deposition speed. Each layer can be characterized in-situ prior to the disposition of the subsequent layer, facilitating optimization and device fabrication troubleshooting, both of which are significant challenges in BHJ blends. Secondly, LbL enables the formation of a graded vertical phase separation between the donor and the acceptor, which is believed to be the preeminent morphology for OPV devices. This vertical separation results in improved OPV performance through an interpenetrated bicontinuous network, where accumulation of each component is greatest at its respective desired electrode, providing sufficient interfacial area for charge separation, optimal percolation pathways for charge transport, and reduced charge recombination. Compared to the BHJ blend process, LbL processing is easier to optimize through modification of processing conditions such as choice of solvents, incorporation of additives and dopants, deposition rate, and annealing steps, resulting in significantly improved fabrication reproducibility. Finally, the LbL approach produces cells with better thermal, mechanical and optical stability over cells fabricated from the BHJ blend technique, which makes LbL more attractive for scaling of modules and eventual industrial fabrication of OPVs. To date, LbL processing has produced the most significant power conversion efficiency retention when transitioning from lab-scale to large-scale devices. Despite these significant advantages, application of LbL remains limited compared to blended BHJ processing. Many researchers gravitate towards the BHJ approach, resulting in the majority of record efficiencies obtained from this technique, perpetuating its dominance in the literature.

As new higher-performing OPV materials and systems are developed, the popularity of the LbL approach is expected to grow. Recent reports of significant improvements in *PCE* (currently > 16%) and the advancement of LbL OPV fabrication with scalable techniques such as blade coating further underscore the importance of this technology. Larger systematic studies that compare various processing conditions and incorporate different materials using LbL blade coating are still necessary. Furthermore, implementation into roll-to-roll compatible techniques such as gravure and flexography need to be explored to fully assess this technology and facilitate a truly comparison to the standard BHJ blended processing. Overall, LbL is emerging as a promising alternative to BHJ blending for OPV fabrication, but more work is required to establish if it is truly the favoured approach.

2.9. References

1. Hengevoss, D., Baumgartner, C., Nisato, G. & Hugi, C. Life Cycle Assessment and eco-efficiency of prospective, flexible tandem organic photovoltaic module. *Sol. Energy* **137**, 317–327 (2016).
2. Lizin, S. *et al.* Life cycle analyses of organic photovoltaics: a review. *Energy Environ. Sci.* **6**, 3136–3149 (2013).
3. Liu, Q. *et al.* 18 % Efficiency organic solar cells. *Sci. Bull.* 1–10 (2020) doi:10.1016/j.scib.2020.01.001.
4. Chamberlain, G. A. Organic solar cells: a review. *Sol. Cells* **8**, 47–83 (1983).
5. Jemison, R. C. & Mccullough, R. D. Techniques for the Molecular Design of Push-Pull Polymers towards Enhanced Organic Photovoltaic Performance. *ACS Symp. Ser.* **1161**, 71–109 (2014).
6. Yan, C. *et al.* Non-fullerene acceptors for organic solar cells. *Nat. Rev. Mater.* **3**, 1–19 (2018).
7. Tang, C. W. Two-layer organic photovoltaic cell. *Appl. Phys. Lett.* **48**, 183–185 (1986).
8. Mikhnenko, O. V, Blom, P. W. M. & Nguyen, T. Exciton diffusion in organic semiconductors. *Energy Environ. Sci.* **8**, 1867–1888 (2015).
9. Brabec, B. C. J., Sariciftci, N. S. & Hummelen, J. C. Plastic Solar Cells **. *Adv. Funct. Mater.* **11**, 15–26 (2001).
10. Dang, M. T., Hirsch, L. & Wantz, G. P3HT:PCBM, best seller in polymer photovoltaic research. *Adv. Mater.* **23**, 3597–3602 (2011).
11. Oklobia, O. & Shafai, T. S. A study of donor/acceptor interfaces in a blend of P3HT/PCBM solar cell: Effects of annealing and PCBM loading on optical and electrical properties. *Solid State Electron.* **87**, 64–68 (2013).
12. Gholamkhass, B. & Servati, P. Solvent-vapor induced morphology reconstruction for efficient PCDTBT based polymer solar cells. *Org. Electron. physics, Mater. Appl.* **14**, 2278–2283 (2013).
13. He, Z. *et al.* Single-junction polymer solar cells with high efficiency and photovoltage. *Nat. Photonics* **9**, 174–179 (2015).
14. Zhao, J. *et al.* Efficient organic solar cells processed from hydrocarbon solvents. *Nat. Energy* **1**, 1–7 (2016).
15. Kooistra, F. B. *et al.* Increasing the open circuit voltage of bulk-heterojunction solar cells by raising the LUMO level of the acceptor. *Org. Lett.* **9**, 551–554 (2007).
16. Xu, Z. *et al.* Understanding the Morphology of High-Performance Solar Cells Based on a Low-Cost Polymer Donor. *Appl. Mater. Interfaces* **12**, 9537–9544 (2020).
17. Yuan, J. *et al.* Single-Junction Organic Solar Cell with over 15 % Efficiency Using Fused-Ring Acceptor with Electron-Deficient Core Single-Junction. *Joule* **3**, 1–12 (2019).
18. Wang, T. *et al.* A 2.16eV bandgap polymer donor gives 16% power conversion efficiency. *Sci. Bull.* **65**, 179–181 (2020).
19. Brabec, C. J., Heeney, M., McCulloch, I. & Nelson, J. Influence of blend microstructure on bulk heterojunction organic photovoltaic performance. *Chem. Soc. Rev.* **40**, 1185–1199 (2011).
20. Schaffer, C. J. *et al.* A direct evidence of morphological degradation on a nanometer scale in polymer solar cells. *Adv. Mater.* **25**, 6760–6764 (2013).
21. Zhang, Y. *et al.* Thermally Stable All-Polymer Solar Cells with High Tolerance on Blend Ratios. *Adv. Energy Mater.* **8**, 1–10 (2018).
22. Ayzner, A. L., Tassone, C. J., Tolbert, S. H. & Schwartz, B. J. Reappraising the Need for Bulk Heterojunctions in Polymer - Fullerene Photovoltaics : The Role of Carrier Transport in All-Solution-Processed P3HT / PCBM Bilayer Solar Cells. *J. Phys. Chem.*

C **113**, 20050–20060 (2009).

23. Clulow, A. J. *et al.* Time-Resolved Neutron Reflectometry and Photovoltaic Device Studies on Sequentially Deposited PCDTBT-Fullerene Layers. *Langmuir* **30**, 11474–11484 (2014).
24. Yang, B., Yuan, Y. & Huang, J. Reduced Bimolecular Charge Recombination Loss in Thermally Annealed Bilayer Heterojunction Photovoltaic Devices with Large External Quantum Efficiency and Fill Factor. *J. Phys. Chem. C* **118**, 5196–5202 (2014).
25. Cheng, P. *et al.* Efficient and stable organic solar cells via sequential process. *J. Mater. Chem. C* **4**, 8086–8093 (2016).
26. Jang, Y. *et al.* Formation of Thermally Stable Bulk Heterojunction by Reducing the Polymer and Fullerene Intermixing. *Sci. Rep.* **7**, 1–9 (2017).
27. Fontana, M. T., Aubry, T. J., Scholes, D. T., Hawks, S. A. & Schwartz, B. J. Sequential Processing : A Rational Route for Bulk Heterojunction Formation via Polymer Swelling. in *Handbook of Organic* vol. 4 1–40 (2018).
28. Sun, R. *et al.* A universal layer-by-layer solution-processing approach for efficient non-fullerene organic solar. *Energy Environ. Sci.* **12**, 384–395 (2019).
29. Arunagiri, L. *et al.* Temperature-Dependent Aggregation Donor Polymers Enable Highly Efficient Sequentially Processed Organic Photovoltaics Without the Need of Orthogonal Solvents. *Adv. Funct. Mater.* **29**, 1–10 (2019).
30. Dong, S. *et al.* High-Performance Large-Area Organic Solar Cells Enabled by Sequential Bilayer Processing via Nonhalogenated Solvents. *Adv. Energy Mater.* **9**, 1–7 (2019).
31. Sun, R. *et al.* A Layer-by-Layer Architecture for Printable Organic Solar Cells Overcoming the Scaling Lag of Module Efficiency. *Joule* **4**, 1–13 (2020).
32. Collavini, S. & Delgado, J. L. Fullerenes : the stars of photovoltaics. *Sustain. Energy Fuels* **2**, 2480–2493 (2018).
33. Haddon, R. C., Palmer, R. E., Kroto, H. W. & Sermon, P. A. The fullerenes : powerful carbon-based electron acceptors. *Philos. Trans. R. Soc. London A* **343**, 53–62 (1993).
34. Imahori, B. H. & Sakata, Y. Donor-Linked Fullerenes : Photoinduced Electron Transfer and Its Potential Application **. *Adv. Mater.* **9**, 537–546 (1997).
35. Sivaraman, N. *et al.* Solubility of C60 in Organic Solvents. *J. Org. Chem.* **57**, 6077–6079 (1992).
36. Yu, G., Gao, J., C, H. J., Wudl, F. & Heeger, A. J. Polymer Photovoltaic Cells: Enhanced Efficiencies via a Network of Internal Donor-Acceptor Heterojunctions. *Science (80-.).* **270**, 1789–1792 (1995).
37. Mortuza, S. M., Cisneros, C., Bartolo, M. & Banerjee, S. Molecular Modeling of Nanoparticles and Conjugated Polymers During Synthesis of Photoactive Layers of Organic Photovoltaic Solar Cells. in *2013 AlChE Annual Meeting* (2013).
38. Potscavage, W. J., Yoo, S., Domercq, B., Kim, J. & Kippelen, B. Integrated organic photovoltaic modules. *Proc. Spie* **6656**, 1–10 (2007).
39. Hoke, E. T. *et al.* Recombination in Polymer:Fullerene Solar Cells with Open-Circuit Voltages Approaching and Exceeding 1.0 V. *Adv. Energy Mater.* **3**, 220–230 (2013).
40. Li, H. & Wang, J. Layer-by-layer processed high-performance polymer solar cells. *Appl. Phys. Lett.* **101**, 1–5 (2012).
41. Troshin, P. A. *et al.* Efficient 2 + 3 Cycloaddition Approach to Synthesis of Pyridinyl Based [60] Fullerene Ligands Synthesis of Pyridinyl Based. *Fullerenes, Nanotub. Carbon Nanostructures* **12**, 413–419 (2004).
42. Egginger, M. *et al.* Comparative studies on solar cell structures using zinc phthalocyanine. *Proc. Spie* **6192**, 1–8 (2006).
43. Koeppe, R., Sariciftci, N. S., Troshin, P. A. & Lyubovskaya, R. N. Complexation of pyrrolidinofullerenes and zinc-phthalocyanine in a bilayer organic solar cell structure.

Appl. Phys. Lett. **87**, 1–3 (2007).

44. Zhang, Y. *et al.* Enhanced exciton harvesting in a planar heterojunction organic photovoltaic device by solvent vapor annealing. *Org. Electron.* **70**, 162–166 (2019).
45. Wang, Y. *et al.* Measurement of Exciton Diffusion in a Well-Defined Donor/Acceptor Heterojunction based on a Conjugated Polymer and Cross-Linked Fullerene Derivative. *Appl. Mater. Interfaces* **6**, 14108–14115 (2014).
46. Gorodetsky, A. A., Cox, M., Tremblay, N. J., Kymissis, I. & Nuckolls, C. Solar Cells from a Solution Processable Pentacene with Improved Air Stability. *Chem. Mater.* **21**, 4090–4092 (2009).
47. Li, C. Z., Yip, H. L. & Jen, A. K. Y. Functional fullerenes for organic photovoltaics. *J. Mater. Chem.* **22**, 4161–4177 (2012).
48. Polman, A., Knight, M., Garnett, E. C., Ehrler, B. & Sinke, W. C. Photovoltaic materials: Present efficiencies and future challenges. *Science (80-.).* **352**, 1–10 (2016).
49. Lin, Y. *et al.* An Electron Acceptor Challenging Fullerenes for Efficient Polymer Solar Cells. *Adv. Mater.* **27**, 1170–1174 (2015).
50. Huang, L. *et al.* Unraveling the Morphology in Solution-Processed Pseudo-Bilayer Planar Heterojunction Organic Solar Cells. *Appl. Mater. Interfaces* **11**, 26213–26221 (2019).
51. Lin, Y. *et al.* High-Performance Electron Acceptor with Thienyl Side Chains for Organic Photovoltaics. *J. Am. Chem. Soc.* **138**, 4955–4961 (2016).
52. Li, S. *et al.* Energy-Level Modulation of Small-Molecule Electron Acceptors to Achieve over 12 % Efficiency in Polymer Solar Cells. *Adv. Mater.* **28**, 9423–9429 (2016).
53. Yao, H. *et al.* Achieving Highly Efficient Nonfullerene Organic Solar Cells with Improved Intermolecular Interaction and Open-Circuit Voltage. *Adv. Mater.* **29**, 1–8 (2017).
54. Zhang, Z. *et al.* Conformation Locking on Fused-Ring Electron Acceptor for High-Performance Nonfullerene Organic Solar Cells. *Adv. Funct. Mater.* **28**, 1–8 (2018).
55. Li, X. *et al.* Improvement of Photovoltaic Performance of Polymer Solar Cells by Rational Molecular Optimization of Organic Molecule Acceptors. *Adv. Energy Mater.* **8**, 1–7 (2018).
56. Zhang, Y. *et al.* Fluorination vs. chlorination: a case study on high performance organic photovoltaic materials. *Sci. China Chem.* **61**, 1328–1337 (2018).
57. Kan, B. *et al.* Fine-Tuning the Energy Levels of a Nonfullerene Small-Molecule Acceptor to Achieve a High Short-Circuit Current and a Power Conversion Efficiency over 12 % in Organic Solar Cells. *Adv. Energy Mater.* **30**, 1–8 (2018).
58. Lin, Y. *et al.* A Facile Planar Fused-Ring Electron Acceptor for As-Cast Polymer Solar Cells with 8.71% Efficiency. *J. Am. Chem. Soc.* **138**, 2973–2976 (2016).
59. Li, H. *et al.* Improve the Performance of the All-Small-Molecule Nonfullerene Organic Solar Cells through Enhancing the Crystallinity of Acceptors. *Adv. Energy Mater.* **8**, 1–8 (2018).
60. Cui, Y. *et al.* Toward Efficient Polymer Solar Cells Processed by a Solution-Processed Layer-By-Layer Approach. *Adv. Mater.* **30**, 1–7 (2018).
61. Cui, Y. *et al.* Over 16% efficiency organic photovoltaic cells enabled by a chlorinated acceptor with increased open-circuit voltages. *Nat. Commun.* **10**, 1–8 (2019).
62. Luo, Z., Jiao, X., Min, J. & Yang, C. Altering alkyl-chains branching positions for boosting the performance of small-molecule acceptors for highly efficient nonfullerene organic solar cells. *Sci. China Chem.* **63**, 361–369 (2020).
63. Lloyd, M. T. *et al.* Photovoltaic cells from a soluble pentacene derivative. *Org. Electron.* **7**, 243–248 (2006).
64. Sreejith, S., Carol, P., Chithra, P. & Ajayaghosh, A. Squaraine dyes : a mine of molecular

materials. *J. Mater. Chem.* **18**, 264–274 (2008).

65. Chen, G., Sasabe, H., Igarashi, T., Hong, Z. & Kido, J. Squaraine dyes for organic photovoltaic cells. *J. Mater. Chem. A* **3**, 14517–14534 (2015).
66. Wei, G. *et al.* Functionalized Squaraine Donors for Nanocrystalline Organic Photovoltaics. *ACS Nano* **6**, 972–978 (2012).
67. Liu, Q., Bottle, S. E. & Sonar, P. Developments of Diketopyrrolopyrrole-Dye-Based Organic Semiconductors for a Wide Range of Applications in Electronics. *Adv. Mater.* **32**, 1–46 (2020).
68. Kylberg, W. *et al.* Synthesis, thin-film morphology, and comparative study of bulk and bilayer heterojunction organic photovoltaic devices using soluble diketopyrrolopyrrole molecules. *Energy Environ. Sci.* **4**, 3617–3624 (2011).
69. Liu, Y. *et al.* High-Performance Solar Cells using a Solution-Processed Small Molecule Containing Benzodithiophene Unit. *Adv. Mater.* **23**, 5387–5391 (2011).
70. Zhou, J. *et al.* Solution-Processed and High-Performance Organic Solar Cells Using Small Molecules with a Benzodithiophene Unit. *J. Am. Chem. Soc.* **135**, 8484–8487 (2013).
71. Lin, Y. *et al.* Small-Molecule Solar Cells with Fill Factors up to 0.75 via a Layer-by-Layer Solution Process. *Adv. Energy Mater.* **4**, 1–6 (2014).
72. Meng, F., Chen, K., Tian, H., Zuppiroli, L. & Nüesch, F. Cyanine dye acting both as donor and acceptor in heterojunction photovoltaic devices. *Appl. Phys. Lett.* **82**, 3788–3790 (2003).
73. Nüesch, F. *et al.* Counterion effects in cyanine heterojunction photovoltaic devices. *J. Mater. Sci.* **40**, 1353–1357 (2005).
74. Fan, B., Hany, R., Moser, J.-E. & Nüesch, F. Enhanced cyanine solar cell performance upon oxygen doping. *Org. Electron.* **9**, 85–94 (2008).
75. Hany, R. *et al.* Strategies to improve cyanine dye multi layer organic solar cells. *Prog. Photovoltaics Res. Appl.* **19**, 851–857 (2011).
76. Castro, F. A. *et al.* On the use of cyanine dyes as low-bandgap materials in bulk heterojunction photovoltaic devices. *Synth. Met.* **156**, 973–978 (2006).
77. Zhang, H. *et al.* Semitransparent organic photovoltaics using a near-infrared absorbing cyanine dye. *Sol. Energy Mater. Sol. Cells* **118**, 157–164 (2013).
78. Malinkiewicz, O. *et al.* Efficient, Cyanine Dye Based Bilayer Solar Cells. *Adv. Energy Mater.* **3**, 472–477 (2013).
79. Wang, L. *et al.* Cyanine dye polyelectrolytes for organic bilayer solar cells. *Polymer (Guildf).* **55**, 3195–3201 (2014).
80. Mahmood, A. *et al.* Recent progress in porphyrin-based materials for organic solar cells. *J. Mater. Chem. A* **6**, 16769–16797 (2018).
81. Zope, R. R., Olguin, M. & Baruah, T. Charge transfer excitations in cofacial fullerene-porphyrin complexes. *J. Chem. Phys.* **137**, 1–8 (2012).
82. Sato, Y., Niinomi, T., Hashiguchi, M., Matsuo, Y. & Nakamura, E. Organic photovoltaic based on solution-processed benzoporphyrin. *Proc. Spie* **6656**, 1–9 (2007).
83. Sun, Q., Dai, L., Zhou, X., Li, L. & Li, Q. Bilayer- and bulk-heterojunction solar cells using liquid crystalline porphyrins as donors by solution processing. *Appl. Phys. Lett.* **91**, 1–3 (2007).
84. Perez, B. M. D. *et al.* Organic Photovoltaics Using Tetraphenylbenzoporphyrin Complexes as Donor Layers. *Adv. Mater.* **21**, 1517–1520 (2009).
85. Huijser, A., Savenije, T. J., Shalav, A. & Siebbeles, L. D. A. An experimental study on the molecular organization and exciton diffusion in a bilayer of a porphyrin and poly(3-hexylthiophene). *J. Appl. Phys.* **104**, 1–10 (2008).
86. Jenatsch, S. *et al.* Influence of Molybdenum Oxide Interface Solvent Sensitivity on

Charge Trapping in Bilayer Cyanine Solar Cells. *J. Phys. Chem. C* **118**, 17036–17045 (2014).

87. Faure, M. D. M., Grant, T. M. & Lessard, B. H. Silicon Phthalocyanines as Acceptor Candidates in Mixed Solution/Evaporation Processed Planar Heterojunction Organic Photovoltaic Devices. *Coatings* **9**, 1–13 (2019).
88. Josey, D. S., Castrucci, J. S., Dang, J. D., Lessard, B. H. & Bender, T. P. Evaluating thiophene electron-donor layers for the rapid assessment of boron subphthalocyanines as electron acceptors in organic photovoltaics: Solution or vacuum deposition? *ChemPhysChem* **16**, 1245–1250 (2015).
89. Ma, B., Woo, C. H., Miyamoto, Y. & Fréchet, J. M. J. Solution Processing of a Small Molecule, Subnaphthalocyanine, for Efficient Organic Photovoltaic Cells. *Chem. Mater.* **21**, 1413–1417 (2009).
90. Leblebici, S. Y. *et al.* Near-Infrared Azadipyrromethenes as Electron Donor for Efficient Planar Heterojunction Organic Solar Cells. *Appl. Mater. Interfaces* **3**, 4469–4474 (2011).
91. Ghani, F., Bochukov, I., Fostiropoulos, K. & Riegler, H. Hybrid solution/vacuum-processed bilayer heterojunction organic solar cells: Structural characterization and performance. *Thin Solid Films* **525**, 177–181 (2012).
92. Schumann, S., Hatton, R. A. & Jones, T. S. Organic Photovoltaic Devices Based on Water-Soluble Copper Phthalocyanine. *J. Phys. Chem. C* **115**, 4916–4921 (2011).
93. Claessens, C. G., Gonzalez-Rodriguez, D. & Torres, T. Subphthalocyanines: Singular Nonplanar Aromatic Compounds-Synthesis, Reactivity, and Physical Properties. *Chem. Rev.* **102**, 835–853 (2002).
94. Jean, M., Ma, B., Miyamoto, Y., Woo, C. H. & Fréchet, J. M. J. Solution processable boron subphthalocyanine derivatives as active materials for organic photovoltaics. *Proc. Spie* **7416**, 1–6 (2009).
95. Mauldin, C. E. *et al.* Axial Thiophene-Boron(subphthalocyanine) Dyads and Their Application in Organic Photovoltaics. *Appl. Mater. Interfaces* **2**, 2833–2838 (2010).
96. Sariciftci, N. S., Smilowitz, L., Heeger, A. J. & Wudl, F. Semiconducting polymers (as donors) and buckminsterfullerene (as acceptor): photoinduced electron transfer and heterojunction devices. *Synth. Met.* **59**, 333–352 (1993).
97. Sariciftci, N. S. *et al.* Semiconducting polymer- buckminsterfullerene heterojunctions: Diodes, photodiodes, and photovoltaic cells. *Appl. Phys. Lett.* **62**, 585–587 (1993).
98. Vacar, D., Maniloff, E. S., Mcbranch, D. W. & Heeger, A. J. Charge-transfer range for photoexcitation in conjugated polymer/fullerene bilayers and blends. *Phys. Rev. B* **56**, 4573–4577 (1997).
99. Halls, J. J. M., Pichler, K., Friend, R. H., Moratti, S. C. & Holmes, A. B. Exciton diffusion and dissociation in a poly(p-phenylenevinylene)/C60 heterojunction photovoltaic cell. *Appl. Phys. Lett.* **68**, 3120–3122 (1996).
100. Stübinger, T. & Brütting, W. Exciton diffusion and optical interference in organic donor – acceptor photovoltaic cells. *J. Appl. Phys.* **90**, 3632–3641 (2001).
101. Drees, M. *et al.* Creation of a gradient polymer-fullerene interface in photovoltaic devices by thermally controlled interdiffusion. *Appl. Phys. Lett.* **81**, 4607–4609 (2002).
102. Drees, M., Davis, R. M. & Heflin, J. R. Thickness dependence, in situ measurements, and morphology of thermally controlled interdiffusion in polymer-C60 photovoltaic devices. *Phys. Rev. B* **69**, 1–6 (2004).
103. Chen, L. *et al.* Polymer Photovoltaic Devices from Stratified Multilayers of Donor-Acceptor Blends. *Adv. Mater.* **12**, 1367–1370 (2000).
104. Collins, B. A. *et al.* Molecular Miscibility of Polymer - Fullerene Blends. *J. Phys. Chem. Lett.* **1**, 3160–3166 (2010).
105. Schlebusch, C., Kessler, B., Cramm, S. & Eberhardt, W. Organic photoconductors and

C60. *Synth. Met.* **77**, 151–154 (1996).
106. Gopal, A., Drees, M., Davis, R. M. & Heflin, J. R. Modelling of external quantum efficiency spectra as a function of varying P3OT thickness in P3OT-C60 polymer photovoltaic devices. *Proc. Spie* **5938**, 1–10 (2005).
107. Drees, M., Davis, R. M. & Heflin, J. R. Improved morphology of polymer-fullerene photovoltaic devices with thermally induced concentration gradients. *J. Appl. Phys.* **97**, 1–3 (2005).
108. Kim, K., Liu, J. & Carroll, D. L. Thermal diffusion processes in bulk heterojunction formation for poly-3- hexylthiophene/single heterojunction photovoltaics. *Appl. Phys. Lett.* **88**, 1–3 (2006).
109. Yu, D., Yang, Y., Durstock, M., Baek, J. & Dai, L. Soluble P3HT-Grafted Graphene for Efficient Bilayer-Heterojunction Photovoltaic Devices. *ACS Nano* **4**, 5633–5640 (2010).
110. Tan, L., Curtis, M. D. & Francis, A. H. Charge Transfer in Ferrocene-Bearing Poly(thiophene)s and Application in Organic Bilayer Photocells. *Macromolecules* **35**, 4628–4635 (2002).
111. Stevens, D. M., Qin, Y., Hillmyer, M. A. & Frisbie, C. D. Enhancement of the Morphology and Open Circuit Voltage in Bilayer Polymer/Fullerene Solar Cells. *J. Phys. Chem. C* **113**, 11408–11415 (2009).
112. Ferreira, A. S. *et al.* Understanding How Polymer Properties Control OPV Device Performance: Regioregularity, Swelling, and Morphology Optimization Using Random Poly(3-butylthiophene-co-3-octylthiophene) Polymers. *J. Phys. Chem. C* **120**, 22115–22125 (2016).
113. Kekuda, D., Huang, J., Ho, K. & Chu, C. Modulation of Donor - Acceptor Interface through Thermal Treatment for Efficient Bilayer Organic Solar Cells. *J. Phys. Chem. C* **114**, 2764–2768 (2010).
114. Ahn, S., Jang, W., Hyeok, J. & Hwan, D. Enhanced performance of layer-evolved bulk-heterojunction solar cells with Ag nanoparticles by sequential deposition. *Org. Electron.* **24**, 325–329 (2015).
115. Tang, Y. *et al.* A New Wide Bandgap Donor Polymer for Efficient Nonfullerene Organic Solar Cells with a Large Open-Circuit Voltage. *Adv. Sci.* **6**, 1–10 (2019).
116. Seok, J. *et al.* Efficient Organic Photovoltaics Utilizing Nanoscale Heterojunctions in Sequentially Deposited Polymer/fullerene Bilayer. *Sci. Rep.* **5**, 1–9 (2015).
117. Zhang, M., Guo, X., Ma, W., Ade, H. & Hou, J. A Polythiophene Derivative with Superior Properties for Practical Application in Polymer Solar Cells. *Adv. Mater.* **26**, 5880–5885 (2014).
118. Zheng, B., Huo, L. & Li, Y. Benzodithiophenedione-based polymers : recent advances in organic photovoltaics. *NPG Asia Mater.* **12**, 1–22 (2020).
119. Sun, C. *et al.* A low cost and high performance polymer donor material for polymer solar cells. *Nat. Commun.* **9**, 1–10 (2018).
120. Bin, H. *et al.* Non-Fullerene Polymer Solar Cells Based on Alkylthio and Fluorine Substituted 2D-Conjugated Polymers Reach 9.5% Efficiency. *J. Am. Chem. Soc.* **138**, 4657–4664 (2016).
121. Bin, H. *et al.* 11.4% Efficiency non-fullerene polymer solar cells with trialkylsilyl substitued 2D-conjugated polymer as donor. *Nat. Commun.* **7**, 1–11 (2016).
122. Li, Z. *et al.* Donor polymer design enables efficient non-fullerene organic solar cells. *Nat. Commun.* **7**, 1–9 (2016).
123. Smith, B. H. *et al.* Fluorination of Donor−Acceptor Copolymer Active Layers Enhances Charge Mobilities in Thin-Film Transistors. *ACS Macro Lett.* **6**, 1162–1167 (2017).
124. Zhou, N. & Facchetti, A. Naphthalenediimide (NDI) polymers for all-polymer photovoltaics. *Mater. Today* **21**, 377–390 (2018).

125. Jenekhe, S. A. & Yi, S. Efficient photovoltaic cells from semiconducting polymer heterojunctions. *Appl. Phys. Lett.* **77**, 2635–2637 (2000).
126. Brixi, S. *et al.* Air and temperature sensitivity of n-type polymer materials to meet and exceed the standard of N2200. *Sci. Rep.* **10**, 1–10 (2020).
127. Xu, Y. *et al.* Simultaneously Improved Efficiency and Stability in All-Polymer Solar Cells by a P-i-N Architecture. *ACS Energy Lett.* **4**, 2277–2286 (2019).
128. Fang, Y. *et al.* Application of an A−A′−A-Containing Acceptor Polymer in Sequentially Deposited All-Polymer Solar Cells. *Appl. Mater. Interfaces* **10**, 24046–24054 (2018).
129. Zhan, X. *et al.* A High-Mobility Electron-Transport Polymer with Broad Absorption and Its Use in Field-Effect Transistors and All-Polymer Solar Cells. *J. Am. Chem. Soc.* **129**, 7246–7247 (2007).
130. Yao, K., Intemann, J. J., Yip, H., Liang, P. & Chang, C. Efficient all polymer solar cells from layer-evolved processing of a bilayer inverted structure. *J. Phys. Chem. C* **2**, 416–420 (2014).
131. Zhang, Z. *et al.* A Self-Assembly Phase Diagram from Amphiphilic Perylene Diimides. *Chem. a Eur. J.* **18**, 12305–12313 (2012).
132. Wang, Y., Zhao, X. & Zhan, X. Layer by layer solution processed organic solar cells based on a small molecule donor and acceptor. *J. Mater. Chem. C* **3**, 447–452 (2015).
133. Shan, T. *et al.* Achieving Optimal Bulk Heterojunction in All-Polymer Solar Cells by Sequential Processing with Nonorthogonal Solvents. *Appl. Mater. Interfaces* **11**, 42438–42446 (2019).
134. Zhong, H. *et al.* Rigidifying Nonplanar Perylene Diimides by Ring Fusion Toward Geometry-Tunable Acceptors for High-Performance Fullerene-Free Solar Cells. *Adv. Mater.* **28**, 951–958 (2016).
135. Yan, B. H. *et al.* Influence of Annealing and Interfacial Roughness on the Performance of Bilayer Donor / Acceptor Polymer Photovoltaic Devices. *Adv. Funct. Mater.* **20**, 4329–4337 (2010).
136. Kaur, M., Gopal, A., Davis, R. M. & Heflin, J. R. Concentration gradient P3OT/PCBM photovoltaic devices fabricated by thermal interdiffusion of separately spin-cast organic layers. *Sol. Energy Mater. Sol. Cells* **93**, 1779–1784 (2009).
137. Cheng, P., Hou, J., Li, Y. & Zhan, X. Layer-by-Layer Solution-Processed Low-Bandgap Polymer-PC61BM Solar Cells with High Efficiency. *Adv. Energy Mater.* **4**, 1–7 (2014).
138. Liu, Y. *et al.* Sequential Deposition: Optimization of Solvent Swelling for High-Performance Polymer Solar Cells. *ACS Appl. Mater. Interfaces* **7**, 653–661 (2015).
139. Wang, D. H., Lee, H. K., Choi, D.-G., Park, J. H. & Park, O. O. Solution-processable polymer solar cells from a poly(3-hexylthiophene)/[6,6]-phenylC61-butyric acidmethyl ester concentration graded bilayers. *Appl. Phys. Lett.* **95**, 1–3 (2009).
140. Moon, J. S., Takacs, C. J., Sun, Y. & Heeger, A. J. Spontaneous Formation of Bulk Heterojunction Nanostructures: Multiple Routes to Equivalent Morphologies. *Nano Lett.* **11**, 1036–1039 (2011).
141. Wang, D. H., Kim, J. K., Park, O. O. & Park, J. H. Analysis of surface morphological changes in organic photovoltaic devices: bilayer versus bulk-heterojunction. *Energy Environ. Sci.* **4**, 1434–1439 (2011).
142. Zhu, R., Kumar, A. & Yang, Y. Polarizing Organic Photovoltaics. *Adv. Mater.* **23**, 4193–4198 (2011).
143. Lee, K. H. *et al.* Morphology of All-Solution-Processed “ Bilayer ” Organic Solar Cells. *Adv. Mater.* **23**, 766–770 (2011).
144. Rochester, C. W., Mauger, S. A. & Moule, A. J. Investigating the Morphology of Polymer/Fullerene Layers Coated Using Orthogonal Solvents. *J. Phys. Chem. C* **116**, 7287–7292 (2012).

145. Loiudice, A., Rizzo, A., Biasiucci, M. & Gigli, G. Bulk Heterojunction versus Diffused Bilayer: The Role of Device Geometry in Solution p-Doped Polymer-Based Solar Cells. *J. Phys. Chem. Lett.* **3**, 1908–1915 (2012).
146. Vohra, V., Campoy-Quiles, M., Garriga, M. & Murata, H. Organic solar cells based on nanoporous P3HT obtained from self-assembled P3HT:PS templates. *J. Mater. Chem.* **22**, 20017–20025 (2012).
147. Vohra, V., Higashimine, K., Murakami, T. & Murata, H. Addition of regiorandom poly(3-hexylthiophene) to solution processed poly(3-hexylthiophene):[6,6]-phenyl-C61-butyric acid methyl ester graded bilayers to tune the vertical concentration gradient. *Appl. Phys. Lett.* **101**, 1–4 (2012).
148. Gadisa, A. *et al.* The role of solvent and morphology on miscibility of methanofullerene and poly(3-hexylthiophene). *Thin Solid Films* **520**, 5466–5471 (2012).
149. Loiudice, A. *et al.* Graded vertical phase separation of donor / acceptor species for polymer solar cells. *Sol. Energy Mater. Sol. Cells* **100**, 147–152 (2012).
150. Cho, S.-M. *et al.* Solvent effect of the fibrillar morphology on the power conversion efficiency of a polymer photovoltaic cell in a diffusive heterojunction. *Semicond. Sci. Technol.* **27**, 1–7 (2012).
151. Vohra, V. *et al.* Enhanced Vertical Concentration Gradient in Rubbed P3HT:PCBM Graded Bilayer Solar Cells. *J. Phys. Chem. Lett.* **3**, 1820–1823 (2012).
152. Yeon, H., Su, N., Hong, J., Song, Y. & Whan, T. Efficient bilayer heterojunction polymer solar cells with bumpy donor – acceptor interface formed by facile polymer blend. *Org. Electron.* **13**, 2688–2695 (2012).
153. Park, H. J., Lee, J. Y., Lee, T. & Guo, L. J. Advanced Heterojunction Structure of Polymer Photovoltaic Cell Generating High Photocurrent with Internal Quantum Efficiency Approaching 100 %. *Adv. Energy Mater.* **3**, 1135–1142 (2013).
154. Wong, M. K. & Wong, K. Y. Investigation of the factors affecting the power conversion efficiency of all-solution-processed 'bilayer' P3HT:PCBM solar cells. *Synth. Met.* **170**, 1–6 (2013).
155. Chen, H., Hu, S., Zang, H., Hu, B. & Dadmun, M. Precise Structural Development and its Correlation to Function in Conjugated Polymer: Fullerene Thin Films by Controlled Solvent Annealing. *Adv. Funct. Mater.* **23**, 1701–1710 (2013).
156. Li, H., Qi, Z. & Wang, J. Layer-by-layer processed polymer solar cells with self-assembled electron buffer layer. *Appl. Phys. Lett.* **102**, 1–5 (2013).
157. Tao, C. *et al.* Controlling Hierarchy in Solution-processed Polymer Solar Cells Based on Crosslinked P3HT. *Adv. Energy Mater.* **3**, 105–112 (2013).
158. Lee, K. H. *et al.* Correlation of diffusion and performance in sequentially processed P3HT/PCBM heterojunction films by time-resolved neutron reflectometry. *J. Phys. Chem. C* **1**, 2593–2598 (2013).
159. Hawks, S. A. *et al.* Comparing Matched Polymer : Fullerene Solar Cells Made by Solution- Sequential Processing and Traditional Blend Casting : Nanoscale Structure and Device Performance. *J. Phys. Chem. C* **118**, 17413–17425 (2014).
160. Kim, K. D., Park, S., Nho, S., Baek, G. & Cho, S. The effects of P3HT crystallinity in bilayer structure organic solar cells. *Curr. Appl. Phys.* **14**, 1369–1373 (2014).
161. Vohra, V., Higashimine, K., Tsuzaki, S., Ohdaira, K. & Murata, H. Formation of vertical concentration gradients in poly(3hexylthiophene-2,5diyl): Phenyl-C61-butyric acid methyl ester-graded bilayer solar cells. *Thin Solid Films* **554**, 41–45 (2014).
162. Zhang, G. *et al.* Crystallinity Effects in Sequentially Processed and Blend-Cast Bulk-Heterojunction Polymer / Fullerene Photovoltaics. *J. Phys. Chem. C* **118**, 18424–18435 (2014).
163. Lin, X. *et al.* Morphological investigation of P3HT / PCBM heterojunction and its effects

on the performance of bilayer organic solar cells. *Synth. Met.* **196**, 145–150 (2014).

164. Syu, Y. *et al.* Enhanced Performance of Pseudo-Bilayer Organic Photovoltaic Devices via Small Molecule Doping. *J. Phys. Chem. C* **118**, 9958–9965 (2014).
165. Xie, L., Yoon, S., Cho, Y. J. & Kim, K. Effective protection of sequential solution-processed polymer / fullerene bilayer solar cell against charge recombination and degradation. *Org. Electron.* **25**, 212–218 (2015).
166. Casalegno, M. *et al.* The effect of donor content on the efficiency of P3HT:PCBM bilayers: optical and photocurrent spectral data analyses. *Phys. Chem. Chem. Phys.* **17**, 2447–2456 (2015).
167. Lee, J. *et al.* Enhanced efficiency of bilayer polymer solar cells by the solvent treatment method. *Synth. Met.* **199**, 408–412 (2015).
168. Zhang, C., Hu, Y., Tang, A., Deng, Z. & Teng, F. Investigating the reduction in the absorption intensity of P3HT in polymer/fullerene “bilayers” coated using orthogonal solvents. *J. Appl. Polym. Sci.* **41757**, 1–5 (2015).
169. Jang, Y., Seo, J., Seok, J., Lee, J. & Kim, K. Roughening Conjugated Polymer Surface for Enhancing the Charge Collection Efficiency of Sequentially Deposited Polymer/Fullerene Photovoltaics. *Polym. Eng. Sci.* **7**, 1497–1509 (2015).
170. Aguirre, J. C. *et al.* Sequential Processing for Organic Photovoltaics : Design Rules for Morphology Control by Tailored Semi-Orthogonal Solvent Blends. *Adv. Drug Deliv. Rev.* **5**, 1–11 (2015).
171. Vohra, V., Dörling, B., Higashimine, K. & Murata, H. Investigating the effect of solvent boiling temperature on the morphology of P3HT:PCBM diffusive bilayer solar cells. *Appl. Phys. Express* **9**, 1–4 (2016).
172. Huh, Y. H., Bae, I.-G., Jeon, H. G. & Park, B. Homogeneous PCBM layers fabricated by horizontal-dip coating for efficient bilayer heterojunction organic photovoltaic cells. *Opt. Express* **24**, 732–742 (2016).
173. Yi, A., Chae, S., Hong, S., Lee, H. H. & Kim, H. J. Manipulating the crystal structure of a conjugated polymer for efficient sequentially processed organic solar cells. *Nanoscale* **10**, 21052–21061 (2018).
174. Fontana, M. T. *et al.* Low-Vapor-Pressure Solvent Additives Function as Polymer Swelling Agents in Bulk Heterojunction Organic Photovoltaics. *J. Phys. Chem. C* **122**, 16574–16588 (2018).
175. Thakur, S. *et al.* Self-Organized Large-Scale Integration of Mesoscale-Ordered Heterojunctions for Process-Intensified Photovoltaics. *Phys. Rev. Appl.* **10**, 1–15 (2018).
176. Wang, D. H. *et al.* Sequential Processing: Control of Nanomorphology in Bulk Heterojunction Solar Cells. *Nano Lett.* **11**, 3163–3168 (2011).
177. Kim, T., Yang, S. J., Kim, S. K., Choi, H. S. & Park, C. R. Preparation of PCDTBT nanofibers with a diameter of 20mm and their application to air-processed organic solar cells †. *Nanoscale* **6**, 2847–2854 (2014).
178. Kim, D. H. *et al.* Sequentially solution-processsed, nanostructured polymer photovoltaics using selective solvents †. *Energy Environ. Sci.* **7**, 1103–1109 (2014).
179. Seok, J. *et al.* Efficient organic photovoltaics utilizing nanoscale heterojunctions in sequentially deposited polymer/fullerene bilayer. *Sci. Rep.* **5**, 1–9 (2015).
180. Franeker, J. J. Van *et al.* Depositing Fullerenes in Swollen Polymer Layers via Sequential Processing of Organic Solar Cells. *Adv. Energy Mater.* **5**, 1–10 (2015).
181. Kim, M., Park, S., Yeol, D. & Kim, K. Improving thermal stability of organic photovoltaics via constructing interdiffused bilayer of polymer/fullerene. *Polymer (Guildf).* **103**, 132–139 (2016).
182. Lang, C., Fan, J., Zhang, Y., Guo, F. & Zhao, L. Utilizing intermixing of conjugated polymer and fullerene from sequential solution processing for efficient polymer solar

cells. *Org. Electron.* **36**, 82–88 (2016).
183. Hwang, H. *et al.* Thermally Stable Bulk Heterojunction Prepared by Sequential Deposition of Nanostructured Polymer and Fullerene. *Polymers (Basel).* **9**, 1–13 (2017).
184. Choi, Y., Hoon, B. & Kim, H. Bicontinuous network of electron donor-acceptor composites achieved by additive-free sequential deposition for efficient polymer solar cells. *Curr. Appl. Phys.* **20**, 760–764 (2020).
185. Li, H., Li, Y.-F. & Wang, J. Optimizing performance of layer-by-layer processed polymer solar cells. *Appl. Phys. Lett.* **101**, 1–4 (2012).
186. Thummalakunta, L. N. S. A., Yong, C. H., Ananthanarayanan, K. & Luther, J. P3HT based solution-processed pseudo bi-layer organic solar cell with enhanced performance. *Org. Electron.* **13**, 2008–2016 (2016).
187. Yim, J. H. *et al.* True nature of active layers in organic solar cells fabricated by sequential casting of donor and acceptor layers. *Phys. Status Solididi RRL* **11**, 1–4 (2017).
188. Kim, Y. J. & Park, C. E. Well defined double layers via binary solvent mixtures for highly efficient inverted all-polymer solar cells. *Org. Electron.* **52**, 301–308 (2018).
189. Zhang, J. *et al.* Efficient non-fullerene organic solar cells employing sequentially deposited donor–acceptor layers†. *J. Mater. Chem. A* **6**, 18225–18233 (2018).
190. Ye, L. *et al.* Sequential Deposition of Organic Films with Eco-Compatible Solvents Improves Performance and Enables Over 12 %-Efficiency Nonfullerene Solar Cells. *Adv. Mater.* **31**, 1–9 (2019).
191. Zhang, J. *et al.* Sequentially Deposited versus Conventional Nonfullerene Organic Solar Cells: Interfacial Trap States, Vertical Stratification, and Exciton Dissociation. *Adv. Energy Mater.* **9**, 1–9 (2019).
192. Gevaerts, V. S., Koster, L. J. A., Wienk, M. M. & Janssen, A. J. Discriminating between Bilayer and Bulk Heterojunction Polymer : Fullerene Solar Cells Using the External Quantum Efficiency. *ACS Appl. Mater. Interfaces* **3**, 3252–3255 (2011).
193. Treat, N. D. *et al.* Interdiffusion of PCBM and P3HT Reveals Miscibility in a Photovoltaically Active Blend. *Adv. Energy Mater.* **1**, 82–89 (2011).
194. Môn, D., Higgins, A. M. & James, D. Mixing in PCBM/P3HT bilayers, using in situ and ex situ neutron reflectivity. *J. Mater. Res.* **32**, 1946–1956 (2017).
195. Nardes, A. M. *et al.* Photoinduced Charge Carrier Generation and Decay in Sequentially Deposited Polymer / Fullerene Layers : Bulk Heterojunction vs Planar Interface. *J. Phys. Chem. C* **116**, 7293–7305 (2012).
196. Nüesch, F. *et al.* Interface modification to optimize charge separation in cyanine heterojunction photovoltaic devices. *Sol. Energy Mater. Sol. Cells* **87**, 817–824 (2005).
197. Jiang, X., Dai, J., Wang, H. & Yan, D. The effect of annealing treatment on performance of interdiffused organic photovoltaic devices. *Thin Solid Films* **516**, 6487–6491 (2008).
198. Geiser, A. *et al.* Poly(3-hexylthiophene)/C60 heterojunction solar cells: Implication of morphology on performance and ambipolar charge collection. *Sol. Energy Mater. Sol. Cells* **92**, 464–473 (2008).
199. Fan, B. *et al.* Improved performance of cyanine solar cells with polyaniline anodes. *J. Mater. Chem.* **20**, 2952–2955 (2010).
200. Fan, B., Castro, F. A. De, Heier, J., Hany, R. & Nüesch, F. High performing doped cyanine bilayer solar cell. *Org. Electron.* **11**, 583–588 (2010).
201. Wei, G. *et al.* Arylamine-Based Squaraine Donors for Use in Organic Solar Cells. *Nano Lett.* **11**, 4261–4264 (2011).
202. Lenes, M. & Bolink, H. J. Ionic Space-Charge Effects in Solid State Organic Photovoltaics. *Appl. Mater. Interfaces* **2**, 3664–3668 (2010).
203. Wicht, G. *et al.* Stability of bilayer trimethine cyanine dye/fullerene organic solar cells. *Sol. Energy Mater. Sol. Cells* **117**, 585–591 (2013).

204. Berner, E. *et al.* Influence of crystalline titanium oxide layer smoothness on the performance of inverted organic bilayer solar cells. *Appl. Phys. Lett.* **183903**, 98–102 (2013).
205. Zabihi, F., Chen, Q., Xie, Y. & Eslamian, M. Fabrication of efficient graphene-doped polymer/fullerene bilayer organic solar cells in air using spin coating followed by ultrasonic vibration post treatment. *Superlattices Microstruct.* **100**, 1177–1192 (2016).
206. Huang, J. *et al.* Efficient bilayer polymer solar cells possessing planar mixed-heterojunction structures †. *J. Mater. Chem.* **20**, 3295–3300 (2010).
207. Kekuda, D. *et al.* The effect of solvent induced crystallinity of polymer layer on poly(3-hexylthiophene)/C70 bilayer solar cells. *Sol. Energy Mater. Sol. Cells* **95**, 419–422 (2011).
208. Josey, D. S., Castrucci, J. S., Dang, J. D. & Lessard, B. H. Evaluating Thiophene Electron-Donor Layers for the Rapid Assessment of Boron Subphthalocyanines as Electron Acceptors in Organic Photovoltaics: Solution or Vacuum Deposition? *ChemPhysChem* **16**, 1245–1250 (2015).
209. Lucera, L. *et al.* Guidelines for Closing the Efficiency Gap between Hero Solar Cells and Roll-To-Roll Printed Modules. *Energy Technol.* **3**, 373–384 (2015).
210. Hong, S., Lee, J., Kang, H. & Lee, K. Slot-die coating parameters of the low-viscosity bulk-heterojunction materials used for polymer solar cells. *Sol. Energy Mater. Sol. Cells* **112**, 27–35 (2013).
211. Vak, D. *et al.* 3D Printer Based Slot-Die Coater as a Lab-to-Fab Translation Tool for Solution-Processed Solar Cells. *Adv. Energy Mater.* **5**, 1–8 (2015).
212. Hong, S. *et al.* A series connection architecture for large-area organic photovoltaic modules with 7.5% module efficiency. *Nat. Commun.* **7**, 1–6 (2016).
213. Song, S. *et al.* Hot slot die coating for additive-free fabrication of high performance roll-to-roll processed polymer solar cells. *Energy Environ. Sci.* **11**, 3248–3255 (2018).
214. Wu, Q. *et al.* Slot-die printed non-fullerene organic solar cells with the highest efficiency of 12.9% for low-cost PV-driven water splitting. *Nano Energy* **61**, 559–566 (2019).
215. Ji, G. *et al.* 12.88% efficiency in doctor-blade coated organic solar cells through optimizing the surface morphology of a ZnO cathode buffer layer†. *J. Mater. Chem. A* **7**, 212–220 (2019).
216. Kang, Q. *et al.* A Printable Organic Cathode Interlayer Enables over 13% Efficiency for 1-cm2 Organic Solar Cells. *Joule* **3**, 227–239 (2019).
217. Ye, L. *et al.* Surpassing 10% Efficiency Benchmark for Nonfullerene Organic Solar Cells by Scalable Coating in Air from Single Nonhalogenated Solvent. *Adv. Mater.* **30**, 1–9 (2018).
218. Zhao, W. *et al.* Environmentally Friendly Solvent-Processed Organic Solar Cells that are Highly Efficient and Adaptable for the Blade-Coating Method. *Adv. Mater.* **30**, 1–7 (2018).
219. Kang, Q. *et al.* p-Doped Conducting Polyelectrolyte as an Anode Interlayer Enables High Efficiency for 1 cm2 Printed Organic Solar Cells. *Appl. Mater. Interfaces* **11**, 20205–20213 (2019).
220. Kang, Q., Yang, B., Xu, Y., Xu, B. & Hou, J. Printable MoOx Anode Interlayers for Organic Solar Cells. *Adv. Mater.* **30**, 1–7 (2018).
221. Chang, J. *et al.* Efficient inverted quasi-bilayer organic solar cells fabricated by using non-halogenated solvent. *J. Mater. Chem. A* **2**, 13398–13406 (2014).
222. Sun, R. *et al.* A multi-objective optimization-based layer-by-layer blade-coating approach for organic solar cells: rational control of vertical stratification for high performance. *Energy Environ. Sci.* **12**, 3118–3132 (2019).

Chapter 3: SiPc Integration into LbL Hybrid Solution-Vacuum Processed OPV Devices

3.1. Context

As outlined in **Chapter 1**, when I started my thesis the use of SiPcs as NFAs in bilayer devices was limited to a very few studies that involved all-evaporation fabrication processes, and with only moderate but promising results. Therefore, I focused my preliminary work trying to further investigate and improve performances of bilayer devices based on some thermally evaporated SiPcs NFAs, bis(3,4,5-trifluorophenoxy) silicon phthalocyanine ($(345F)_2$-SiPc)) and bis(2,4,6-trifluorophenoxy) silicon phthalocyanine ($(246F)_2$-SiPc)). I switched from an all-evaporation fabrication process to a hybrid fabrication solution-evaporation process, where the donor was spin coated followed by evaporation of acceptor layer. This hybrid approach facilitated the pairing of these SiPcs NFAs with common high performing conjugated polymers such as P3HT or PCDTBT. I investigated the effect of frontier orbital energy levels of the materials, and the effect of fabrication parameters variation such as film thickness and thermal treatments at different stages. PCDTBT/$(345F)_2$-SiPc devices outperformed their fullerene-based counterparts and the previously reported all-evaporated devices.

3.2. Contribution of Authors

I performed the fabrication, optimization, and characterization of all OPV devices. I solely wrote the first draft of the manuscript and received editing contribution from all other authors. TMG performed the chemical synthesis and purification of the phthalocyanine compounds, which were previously reported.

This chapter was published in *Coatings*:
M.D.M. Faure, T.M. Grant, B.H. Lessard., *Coatings*, **2019**, 9, 203.

3.3. Abstract

Silicon phthalocyanines (SiPc) are showing promise as both ternary additives and non-fullerene acceptors in organic photovoltaics (OPVs) as a result of their ease of synthesis, chemical stability and strong absorption. In this study, bis(3,4,5-trifluorophenoxy) silicon phthalocyanine ($(345F)_2$-SiPc)) and bis(2,4,6-trifluorophenoxy) silicon phthalocyanine ($(246F)_2$-SiPc)) are employed as acceptors in mixed solution/evaporation planar heterojunction (PHJ) devices. The donor layer, either poly(3-hexylthiophene) (P3HT) or poly[N-9'-heptadecanyl-2,7-carbazole-alt-5,5-(4',7'-di-2-thienyl-2',1',3'-benzothiadiazole)] (PCDTBT), was spin coated followed by the evaporation of the SiPc acceptor thin film. Several different donor/acceptor combinations were investigated in addition to investigations to determine the effect of film thickness on device performance. Finally, the effects of annealing, prior to SiPc deposition, after SiPc deposition, and during SiPc deposition were also investigated. The devices which performed the best were obtained using PCDTBT as the donor, with a 90 nm film of $(345F)_2$-SiPc as the acceptor, followed by thermal annealing at 150 °C for 30 min of the entire mixed solution/evaporation device. An open-circuit voltage (Voc) of 0.88 V and a fill factor (FF) of 0.52 were achieved leading to devices that outperformed corresponding fullerene-based PHJ devices.

3.4. Introduction

Organic photovoltaics (OPVs) have been of major interest over the past years as a potentially lightweight, flexible, and semi-transparent renewable energy source. Indeed, solar energy holds great potential[1],[2], and inexpensive processing of OPVs can lead to a shorter energy payback compared to inorganic silicon cells.[3-5] The most common OPV device configuration is a bulk heterojunction (BHJ), which is based on a random network of electron donating semiconductive polymers and electron accepting small molecules.[3] The most studied donor/acceptor pair is P3HT (poly[3-hexylthiophene]) and $PC_{61}BM$ (phenyl-C61-butyric acid methyl ester) resulting in baseline power conversion efficiencies (*PCE*s) ranging from 2% to 5%.[6] Recently, BHJ OPV devices have reached high *PCE*s (sometimes above 15%) when employing small band gap polymers and non-fullerene acceptors (NFAs).[7-10] In a BHJ, the active layer is a kinetically trapped blend of acceptor and donor materials that, with time and heat, will undergo a detrimental phase separation.[11],[12] Secondly, the active layer blend morphology is a function of the processing conditions and will therefore depend on factors such as shearing speed and drying time, thus presenting significant challenges in transitioning from lab-scale device fabrication to scale-up and commercialization. The use of a planar heterojunction (PHJ), where the donor/acceptor bilayer is formed through successive physical vapor depositions, can lead to more interesting morphologies by engineering greater charge percolation to the respective electrodes followed by a simpler development through independent thickness optimization (as compared to blend engineering for BHJ). PHJ devices can also be fabricated through sequential depositions of solutions, in a structure known as a diffuse planar heterojunction (DPHJ) OPV, as a result of the second solution swelling or diffusing into the first layer, producing a mixed or blended interface.[13],[14] In the literature, DPHJ devices have achieved similar *PCE*s compared to BHJ devices, with values exceeding 3.5% using fullerene derivatives.[12],[15] Poly[N-9'-heptadecanyl-2,7-carbazole-alt-5,5-(4',7'-di-2-thienyl-2',1',3'-benzothiadiazole)] (PCDTBT), is a well-studied donor polymer which outperforms P3HT-based BHJ when paired with $PC_{61}BM$ and $PC_{71}BM$ resulting in *PCE*s of >7%,[16-18], with long-term stability.[19] However, to the best of our knowledge, only one application of DPHJ devices with $PC_{71}BM$ has been reported using PCDTBT.[20] Only a few studies have explored the combination of a solution processed layer followed by the evaporation of C_{60} resulting in a hybrid processed bilayer device.[21],[22] Despite their good accepting abilities and their high electron mobility, fullerene derivatives only have a small absorption overlap with the solar spectrum, and their relatively small band gap limits the resulting device open-circuit voltage (*Voc*), which is directly related to the energy difference between the donor highest occupied molecular orbital (HOMO) and the acceptor lowest unoccupied molecular orbital (LUMO).[23-25] Secondly, the synthesis of fullerene derivatives is very energy demanding because of the numerous low yielding steps and non-effective purification procedures.[26],[27]

Metal containing phthalocyanines (MPcs) are planar aromatic macrocycles consisting of four linked isoindoline units bound to a central metal atom. They have been used widely as dyes and pigments in industry due to their general chemical stability and low production cost. [28-30] MPcs are also employed in organic electronic applications as the semiconductor. Their high molar extinction coefficient (in the order of 10^5 $M^{-1}.cm^{-1}$)[31],[32] and their relatively high charge transport properties (mobilities in the order of 10^{-5} up to 2.5 $cm^2.V^{-1}.s^{-1}$), due to favorable molecular stacking, have facilitated their application in organic thin film transistors (OTFTs)[33-37], organic light emitting diode (OLEDs)[38-41], and OPVs[42-46]. Even if divalent MPcs such as zinc MPc (ZnPc) or copper MPc (CuPc) are well studied, the use of tetravalent MPcs such as tin MPcs (SnPc) or silicon MPcs (SiPc) remain limited.[35],[47]

Recently, SiPcs have attracted significant interest from our group and others for their integration into OPVs, both as an additive in BHJ devices[48-51] or as an acceptor or donor in either BHJ or PHJ devices.[52-54] We reported the use of bis(6-azidohexanoate) silicon phthalocyanine ($(HxN3)_2$-SiPc) as the first dual function ternary additive for OPV, which improved the device stability through cross linking while simultaneously increasing the *PCE* by absorbing in the near IR region.[49] Through axial substitution such as phenoxylation, it is also possible to engineer the solid state stacking of the resulting SiPc derivatives in the thin films. Lessard et al. fabricated a series of thermally evaporated PHJ OPV devices using SiPc as both the donor materials when paired with fullerene (C_{60}), and as acceptor materials when paired with pentacene or α-sexithiophene (α-6T). In all device configurations, as a result of favorable solid state arrangement, bis(pentafluorophenoxy) SiPc (F_{10}-SiPc) resulted in devices with a 3-fold increase of both *Voc* and short circuit current (*Jsc*) compared to dichloro SiPc (Cl_2-SiPc)-based devices.[52] Following this study, the researchers explored synthetizing different SiPcs with distinct frequencies and positions of the fluoro atoms, as this would change the material properties and arrangement and the resulting device performance. Bis(3,4,5-trifluorophenoxy) SiPc ($(345F)_2$-SiPc) and bis(2,4,6-trifluorophenoxy) SiPc ($(246F)_2$-SiPc) were determined to further outperform F_{10}-SiPc, with a *Voc* as high as 0.87 V and a *PCE* as much as 1.8%.[53] These performances are quite promising for unoptimized devices that are already outperforming other PHJ devices based on well-studied phthalocyanines such as chloro aluminum MPc (Cl-AlPc) [43],[46],[55-57] or CuPc[43],[58-60], further justifying the exploration of SiPcs as thermally evaporated NFAs.

In this study, we aim to combine the benefits of using conjugated polymers as the donor layer while incorporating SiPcs as the acceptor layer through thermal evaporation in a mixed solution/evaporation PHJ device structure. Both P3HT and PCDTBT were used as the polymer donor layer, while $(246F)_2$-SiPc and $(345F)_2$-SiPc were used as the evaporated acceptor layer. We also report the effect of the frontier orbital energy levels of the materials, the film thickness, and the results of the thermal treatment.

3.5. Results and Discussion

3.5.1. Determination of the Acceptor/Donor Couple

Mixed solution/evaporation planar heterojunction (PHJ) OPV devices were fabricated by spin coating either P3HT or PCDTBT onto a PEDOT:PSS layer followed by the thermal evaporation of $(345F)_2$-SiPc or $(246F)_2$-SiPc with the structure glass/ITO/PEDOT:PSS/P3HT or PCDTBT/$(246F)_2$-SiPc or $(345F)_2$-SiPc/BCP/Ag represented in **Figure 3.1**. More than 80 P3HT:$PC_{61}BM$ bulk heterojunction (BHJ) OPV baseline devices were also fabricated in parallel to exclude sporadic fabrication errors. All devices were characterized and the corresponding short circuit current (*Jsc*), open circuit voltage (*Voc*), and fill factor (*FF*) are presented in **Table 3.1**. P3HT:$PC_{61}BM$ BHJ OPV baseline devices performed according to literature[6] with a *Jsc* = 8.19 ± 0.43 mA.cm^{-2}, *Voc* = 0.56 ± 0.02 V and *FF* = 0.61 ± 0.04 resulting in an average power conversion efficiency (*PCE*) of 2.87% ± 0.21%. Our P3HT/C_{60} PHJ OPV baseline devices also performed according to literature [21] with a *Jsc* = 2.58 ± 0.05 mA.cm^{-2}, *Voc* = 0.22 ± 0.01 V, *FF* = 0.48 ± 0.02, and *PCE* = 0.28 ± 0.02%. It should be noted that our devices have an area of 0.325 cm^2, which is larger than other commonly reported devices in literature.

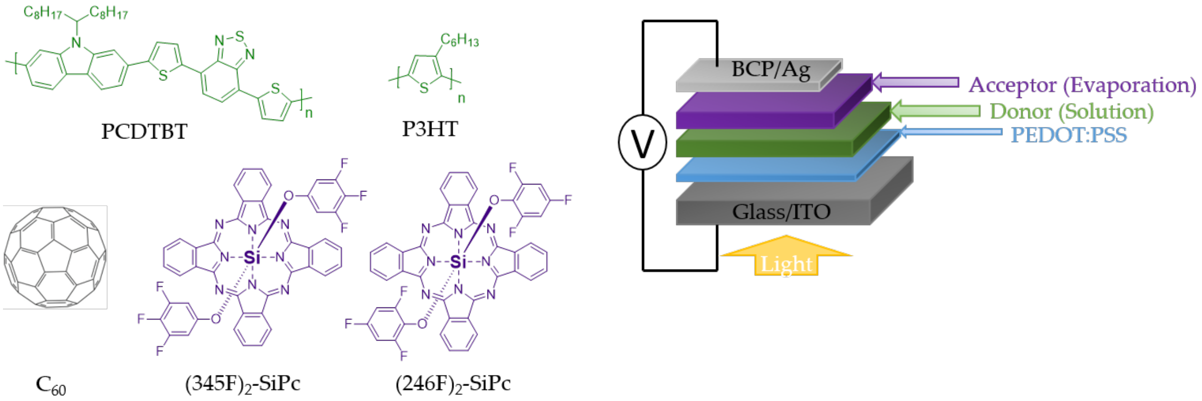

Figure 3.1. Chemical structure of poly[N-9'-heptadecanyl-2,7-carbazole-alt-5,5-(4',7'-di-2-thienyl-2',1',3'-benzothiadiazole)] (PCDTBT), poly(3-hexylthiophene) (P3HT), fullerene (C_{60}), bis(3,4,5-trifluorophenoxy) silicon phthalocyanine ($(345F)_2$-SiPc) and bis(2,4,6-trifluorophenoxy) silicon phthalocyanine ($(246F)_2$-SiPc), and the mixed solution/evaporation planar heterojunction (PHJ) organic photovoltaic (OPV) device structure.

Table 3.1. Characterization of fullerene-based devices, both the bulk (BHJ) and planar heterojunction(PHJ), and the silicon phthalocyanine-based mixed solution/evaporation PHJ OPV device.

Sample [a]	# of devices	***Jsc*** **($mA.cm^{-2}$)**	***Voc*** **(V)**	***FF***	***PCE*** **(%)**
P3HT/$PC_{61}BM$ [a]	84	8.2 ± 0.4	0.56 ± 0.02	0.61±0.036	2.87 ± 0.21
P3HT / C_{60} (40nm)	8	2.58 ± 0.05	0.22 ± 0.01	0.48±0.019	0.28 ± 0.02
PCDTBT / C_{60} (40nm)	9	4.7 ± 0.1	0.56 ± 0.01	0.57±0.019	1.48 ± 0.06
P3HT / $(345F)_2$-SiPc (60nm)	9	1.09 ± 0.06	0.34± 0.03	0.48±0.07	0.19 ± 0.04
P3HT / $(246F)_2$-SiPc (40nm)	6	0.62 ± 0.06	0.49 ± 0.02	0.47±0.04	0.14 ± 0.09
PCDTBT / $(246F)_2$-SiPc (20nm)	5	0.47 ± 0.03	0.07 ± 0.02	0.25±0.01	0.01 ± 0.004
PCDTBT / $(345F)_2$-SiPc (93nm)	9	3.3 ± 0.1	0.87 ± 0.03	0.33±0.008	0.97 ± 0.06
PCDTBT / $(345F)_2$-SiPc (93nm) [b]	7	3.4 ± 0.2	0.87 ± 0.02	0.51±0.019	1.52 ± 0.06

[a] P3HT/$PC_{61}BM$ (1.0:0.8) were bulk heterojunction baseline devices fabricated at the same time as the others to confirm the deposition of electrodes and other layers was performed properly. [b] This sample was annealed at 150 °C for 30 min after deposition of $(345F)_2$-SiPc but before deposition of BCP/Ag. No treatments were applied to all other sets of bilayer devices.

Initially we paired $(345F)_2$-SiPc with P3HT in our PHJ OPV devices. The P3HT thickness was kept constant while the $(345F)_2$-SiPc thickness was varied between 10 and 60 nm. **Figure 3.2 a** demonstrates the J-V curves for the resulting bilayer devices while **Figure 3.2 b** plots the average *Jsc* and *Voc* evolution as a function of $(345F)_2$-SiPc thickness. As the thickness increases from 10 to 60 nm, both the *Jsc* and *Voc* values increase, reaching a maximum value of 1.09 ± 0.06 $mA.cm^{-2}$ and 0.34 ± 0.03 V, respectively **(Table 3.1**). The increase in *Jsc* with increasing thickness of SiPc is likely caused by the increase in light absorption and exciton generation. The increase in *Voc* with the increase in SiPc thickness might be due to the enhancement of polaron-pair bounding energy (EB), which indicates that a higher polaron-pair dissociation energy barrier has to be overcome, and that a higher applied voltage is required to fully dissociate the accumulated excitons near the polymer/SiPc interface.[61-63] As a result, higher *Voc* is essential. Compared to the P3HT/C_{60} baseline devices, when using $(345F)_2$-SiPc, a greater *Voc* was obtained, however the *Jsc* appears to be substantially reduced which led to the limited performances of the devices. These results illustrate that tuning the thickness of $(345F)_2$-SiPc is a straight-forward way to optimize the PHJ OPV device performance.

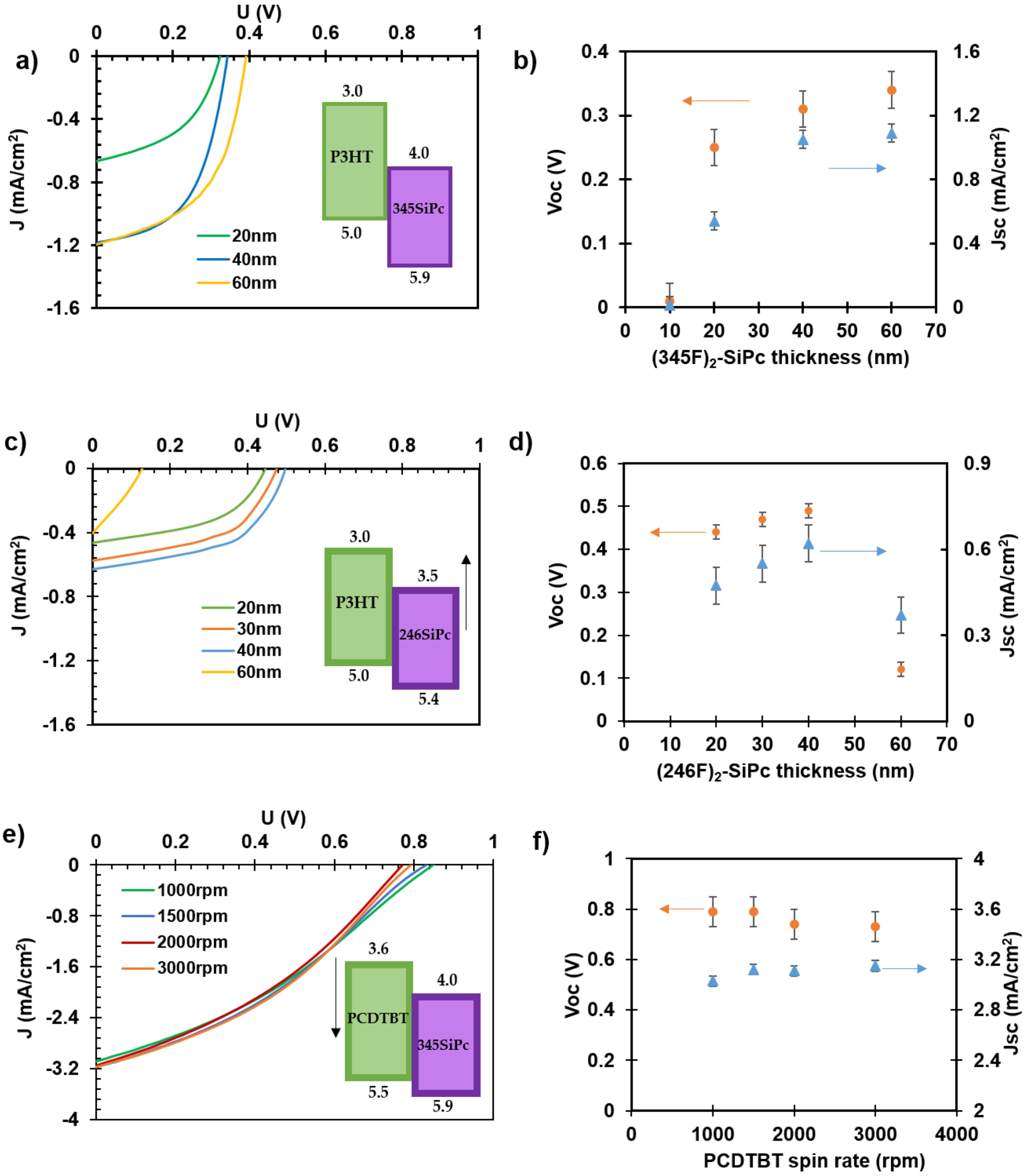

Figure 3.2. (a, c, e) Characteristic current vs. voltage (J-V) and (b, d, f) averaged open-circuit voltage (*Voc*), and short circuit current (*Jsc*) as a function of (b, d) acceptor thickness or (f) spin speed of PCDTBT layer. (a, b) (345F)$_2$-SiPc on P3HT; (c, d) (246F)$_2$-SiPc on P3HT; (e, f) 60 nm (345F)$_2$-SiPc on different films of PCDTBT. Values for the figure inset band diagrams were taken from literature.[18],[48],[53]

In attempts to increase the *Voc*, (345F)$_2$-SiPc was substituted with (246F)$_2$-SiPc which has been characterized to have a shallower (~0.5 eV) LUMO energy level.[53] This increase in LUMO level will lead to a bigger energy difference with the P3HT HOMO, which is known to raise the resulting *Voc*.[25] **Figure 3.2 c** demonstrates the performance for P3HT/(246F)$_2$-SiPc in terms of averaged *Jsc* and *Voc* evolution according to the SiPc thickness. An improvement of 0.2 V for *Voc* is observed for 40 nm (246F)$_2$-SiPc compared to devices with the same (345F)$_2$-SiPc thickness with a maximum *Voc* of 0.49 ± 0.02 V (**Table 3.1**, **Figure 3.2 a**). When comparing the corresponding bilayer devices, P3HT/(246F)$_2$-SiPc has a greater *Voc* than P3HT/C$_{60}$ baseline devices. In addition, when comparing the BHJ equivalent, P3HT:bis(tri-n-butylsilyl oxide) silicon phthalocyanine ((3BS)$_2$-SiPc) has a greater *Voc* than P3HT:PC$_{61}$BM.[45] Therefore, the fact that the baseline P3HT:PC$_{61}$BM BHJ OPV has a greater *Voc* than bilayer P3HT/(246F)$_2$-SiPc shows that it must be a function of device structure and not a function of the HOMO/LUMO levels of the SiPc materials. However, it is clear that the use of (246F)$_2$-SiPc also results in a significant drop in *Jsc* compared to the use of (345)$_2$-SiPc, which was 0.6 ± 0.06 mA.cm^{-2}, as shown in **Figure 3.2 c,d**. As the thickness of (246F)$_2$-SiPc is increased to 60 nm we observe a drop in *Jsc* which is likely due to the greater series resistance related to the relatively low electron mobility of SiPcs.[37]

In an attempt to increase the energy difference between the donor HOMO and the SiPc acceptor LUMO, P3HT was replaced with PCDTBT, leading to a decrease in the donor HOMO from -5.0 eV for P3HT to -5.5 eV for PCDTBT.[18] For this first set of experiments, the (345F)$_2$-SiPc thickness was kept constant at 60 nm, while the PCDTBT thickness was varied by changing the spin coating rate. **Figure 3.2 e,f** demonstrates the performance for PCDTBT/(345F)$_2$-SiPc PHJ OPV devices in terms of averaged *Jsc* and *Voc* as a function of the PCDTBT spin coating rate, and their corresponding J-V curves. These experiments show very little variations in results between 1000 and 3000 rpm. However, compared to P3HT/(345F)$_2$-SiPc, these devices demonstrated an improvement of 132% and 186% in both the *Voc* and *Jsc*, respectively. The optimum devices were characterized by a *Jsc* = 3.15 ± 0.04 mA.cm^{-2} and a *Voc* of 0.79 ± 0.06 V, outperforming the PCDTBT/C$_{60}$ baseline in **Table 3.1**. PHJ OPV devices were fabricated using (246F)$_2$-SiPc on the PCDTBT and as expected a very poor device performance was obtained (**Table 3.1**). This drop in performance is a result of the mismatch of HOMO/LUMO levels of PCDTBT and (246F)$_2$-SiPc.

3.5.2. (345F)$_2$-SiPc Thickness Improvement

The effect of the (345F)$_2$-SiPc thickness on the PCDTBT-based PHJ OPV device performances was assessed. The (345F)$_2$-SiPc thickness was varied between 20 and 120 nm and its effect on the corresponding device performance was plotted for the *Voc* (**Figure 3.3 a**), *Jsc* (**Figure 3.3 b**), *FF* (**Figure 3.3 c**), and *PCE* (**Figure 3.3 d**). We found that consistent and optimal PHJ OPV device performances were obtained with (345F)$_2$-SiPc films of thickness 60-105 nm. For thicknesses <60 nm and >105 nm, performances dropped significantly (**Figure 3.3**). The best results were obtained for a (345F)$_2$-SiPc thickness of roughly 90 nm characterized by a *Voc* of 0.87 ± 0.03 V, a *Jsc* of 3.32 ± 0.04 mA.cm^{-2}, a *FF* of 0.37 ± 0.01, and a *PCE* of 1.05% ± 0.04%. Compared to PCDTBT/C$_{60}$ baselines, the use of SiPc resulted in superior *Voc* but lower *Jsc* and *FF* values, which led to a reduced *PCE*. Therefore, a series of thermal treatments were explored to attempt to enhance the device performance.

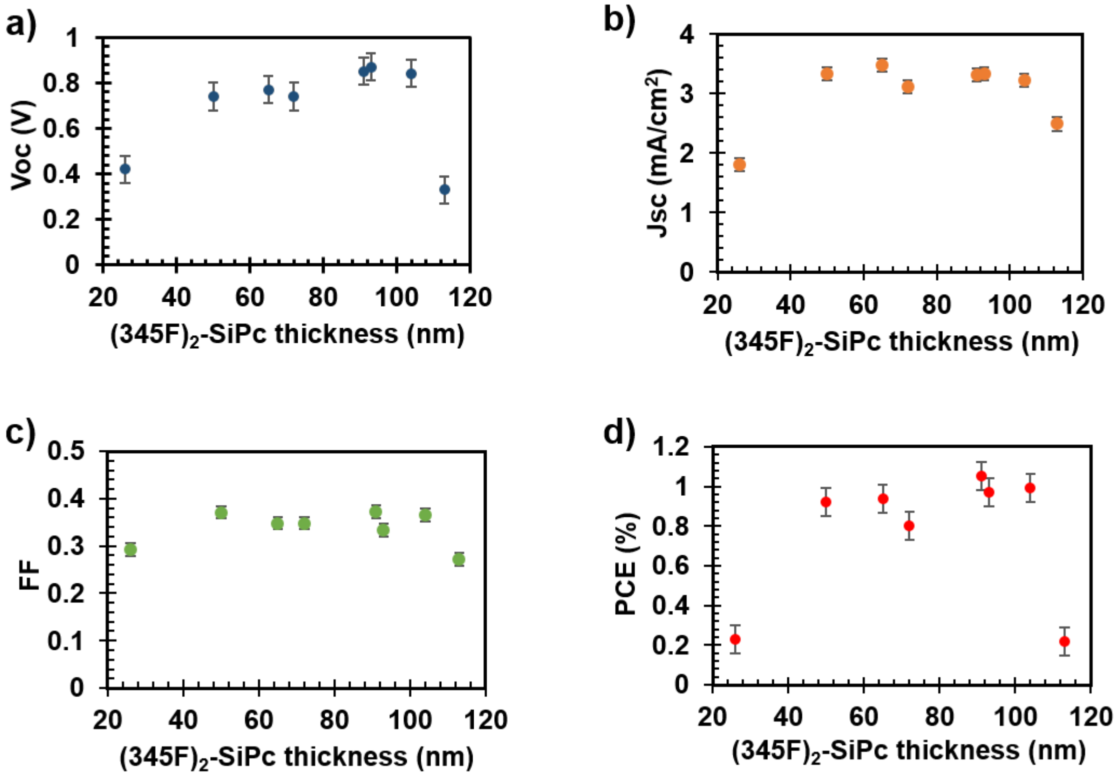

Figure 3.3. Averaged (a) open-circuit voltage (*Voc*), (b) short circuit current (*Jsc*), (c) fill factor (*FF*), (d) power conversion efficiency (*PCE*) as a function of (345F)$_2$-SiPc thickness on a film of PCDTBT.

3.5.3. Thermal Treatment

Annealing before the evaporation of of (345F)$_2$-SiPc

Reports have shown that the ordering of the PCDTBT layer by thermal annealing or through the addition of an ordering agent can help prevent degradation during the deposition of the subsequent layer.[20] Therefore, after PCDTBT was spin coated, it was placed in an oven at 150 °C for 10, 30, and 60 min. The polymer film was removed from the oven and the (345F)$_2$-SiPc layer was evaporated on all the films. **Figure S3.1** shows the evolution of the device J-V curves with increasing anneal time. The greatest *Voc* = 0.74 ± 0.08 V and *Jsc* = 3.34 ± 0.08 mA.cm^{-2} were obtained for devices that underwent no annealing. The longer the annealing, the worse the devices became. Secondly, we explored the use of an ordering agent, such as 1,8-diiodooctane (DIO) as reported in Reference[20], in the PCDTBT layer. **Figure S3.2 a** shows the impact on the J-V curves with the addition of different DIO concentrations in the PCDTBT layer followed by the subsequent evaporation of a 113 nm thick $(345F)_2$-SiPc. The baseline containing no DIO displays a poor J-V curve with a low *FF*, *Voc*, and *Jsc* equal to 0.29, 0.43 V, and 2.6 mA.cm^{-2}, respectively. The addition of 1 vol % of DIO in the o-DCB led to a great improvement in the *Voc* to around 0.7 V while the *Jsc* remained similar, and the addition of 3 vol % DIO helped increase the *Voc* a bit more to above 0.8 V whilst also improving the *FF* to 0.37. **Figure S3.2 b** shows the impact on the J-V curves of an addition of 3 vol % DIO in the PCDTBT layer, also followed by a thermal annealing at 100 °C for 15 min, followed by the deposition of 104 nm of $(345F)_2$-SiPc. The addition of DIO alone led to a drastic decrease in both *Voc* and *Jsc* of roughly 0.2 V and 0.5 mA.cm^{-2}, respectively. The annealing step after the PCDTBT spin coating appeared to counteract the DIO effect, but the values still show an underperformance as compared to the baseline devices. **Figure S3.2 c** shows the previous result for a $(345F)_2$-SiPc thickness of 65 nm. Again, the addition of DIO still has a negative impact, decreasing the resulting *Voc*. Performing the annealing step again raises the *Voc* value and improves the *FF*, but by no more than would be the case after omitting the DIO altogether. Overall, these results indicate that thermal treatment and the use of DIO did not offer any advantage.

Annealing after the $(345F)_2$-SiPc Evaporation

We explored the annealing of the PCDTBT/$(345F)_2$-SiPc bilayer (in a vacuum oven at 150 °C for 30 min) prior to the deposition of the BCP/Ag layers. Results for these devices are shown in **Table 3.1** and **Figure 3.4**. The application of the annealing step (post $(345F)_2$-SiPc deposition) led to a significant gain in performances for PCDTBT/$(345F)_2$-SiPc (93nm) devices due to the improvement in *Jsc* to 3.44 ± 0.18 mA.cm^{-2} and the significant increase of the *FF* to 0.51 ± 0.02. The final *PCE* of the PCDTBT/$(345F)_2$-SiPc resulted in a superior *PCE* increase from 0.97% ± 0.06% to 1.52% ± 0.06%, slightly surpassing the PCDTBT/C_{60} PHJ OPV devices that showed a *PCE* of 1.48% ± 0.06%. These results suggest that straightforward annealing can improve SiPc-based PHJ OPV devices.

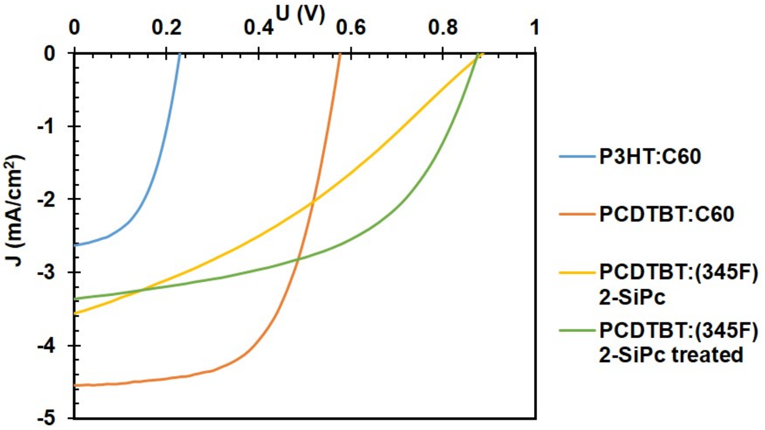

Figure 3.4. Characteristic current vs. voltage (J-V) for PHJ OPV devices where the active layer is P3HT/C_{60}, PCDTBT/C_{60}, PCDTBT/$(345F)_2$-SiPc (93nm), and PCDTBT/$(345F)_2$-SiPc (93nm) annealed at 150 °C for 30min devices.

Annealing during the $(345F)_2$-SiPc Evaporation

It is well known that an increased surface area between the acceptor and the donor will result in improved exciton dissociation which can lead to a raised *PCE*.[64] Therefore, a fuzzy or blended interface could result in better device performance. For this set of devices during the fabrication of the PCDTBT/$(345F)_2$-SiPc interface, we heated the substrates to 150 °C under vacuum during the SiPc evaporation. The hypothesis was that a higher surface energy (or softening of the PCDTBT) during the deposition would facilitate the penetration of the SiPc molecule deeper into the PCDTBT layer resulting in a fuzzy interface. As the PHJ annealing after the SiPc deposition seemed beneficial, it was also performed on devices before the deposition of the last BCP/Ag layers in a vacuum oven at 150 °C for 0, 5, 15, and 30 min.

Figure 3.5 shows the evolution of the average *Voc* (**Figure 3.5 a**), *Jsc* (**Figure 3.5 b**), *FF* (**Figure 3.5 c**), and *PCE* (**Figure 3.5 d**) as a function of the variation of post annealing time after the heated SiPc deposition. For devices that were only heated during the evaporation (time = 0 min), the performances were well below what was achieved previously with *Voc* < 0.1 V, the *Jsc* ~1.5 mA.cm^{-2}, the *FF* ~0.26, and the *PCE* ~0.03%. The addition of the PHJ annealing step after the evaporation helped increase these parameters, the best device being achieved after 15 min annealing with a *Voc*, *Jsc*, *FF*, and *PCE* of 0.47 ± 0.09 V, 2.6 ± 0.23 mA.cm^{-2}, 0.34% ± 0.02%, and 0.43% ± 0.12%, respectively. These results suggest that heating during the deposition of the $(345F)_2$-SiPc is not an effective route towards improved device performance.

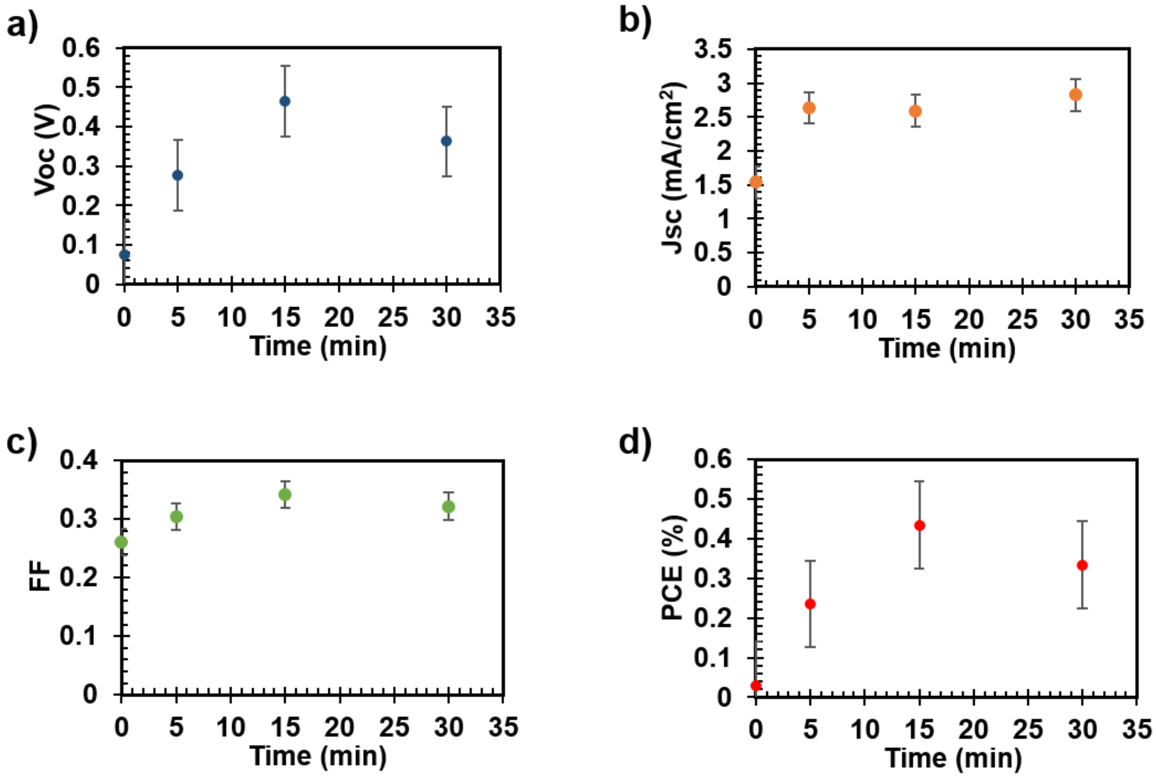

Figure 3.5. (a) Open-circuit voltage (*Voc*), (b) short circuit current (*Jsc*), (c) fill factor (*FF*), (d) power conversion efficiency (*PCE*) vs. annealing time at 150 °C. All devices underwent substrate heating at 150 °C during the evaporation of $(345F)_2$-SiPc on PCDTBT/$(345F)_2$-SiPc (85 nm).

3.6. Experimental

Materials

o-Dichlorobenzene (o-DCB, >99%) was purchased from Sigma-Aldrich (St. Louis, MO, USA). Poly(3,4-ethylenedioxythiophene) poly(styrene sulfonate) (PEDOT:PSS, CleviosTM HTL Solar) was purchased from Heraeus (Hanau, Germany). PCDTBT (Lot#SX7283CH, Mw 40k) was acquired from 1-Material (Dorval, QC, Canada) and P3HT (Lot# PTL24-94, RR 93%, Mw 83K) was purchased from Rieke Metals (Lincoln, Nebraska). The fullerene $PC_{61}BM$ was purchased from Nano-C (Westwood, MA, USA). Bathocuprione (BCP, >99%) and silver (Ag) were purchased from Lumtec (New Taipei City, Taiwan) and Angstrom Engineering (Kitchener, ON, Canada), respectively. All materials were used as received unless otherwise specified. Bis(3,4,5-trifluorophenoxy) silicon phthalocyanine ($(345F)_2$-SiPc) and bis(2,4,6-trifluorophenoxy) silicon phthalocyanine ($(246F)_2$-SiPc) were synthetized and purified according to the literature.[53]

Device Fabrication

Bilayer devices were made by first dissolving P3HT (15 mg/mL) or PCDTBT (8 mg/mL) in o-DCB and were stirred overnight at 50 °C. Substrates of glass coated with indium tin oxide (ITO) were cleaned by subsequent sonication of 5 min in detergent, deionized water, acetone, and methanol, followed by an air-plasma treatment for 10 min. PEDOT:PSS was spin-coated onto the ITO at 3000 rpm for 30 s, and dried in a vacuum oven for 15 min at 140 °C. The donor polymer layer was then spin-coated on top of the PEDOT:PSS layer at 2000 rpm for 60 s under a nitrogen atmosphere and allowed to dry for at least 2 h at room temperature. The silicon phthalocyanine (SiPc) acceptor layer, BCP (9 nm) and Ag (70 nm) were thermally evaporated onto the polymer layer in a custom Angstrom Engineering vacuum chamber system built into a glove box (base pressure = 1×10^{-7} Torr). A shadow mask was used for the evaporation of BCP/Ag for defining the device electrodes, providing five 0.325 cm^2 devices per glass substrate. The resulting devices had the following structure: glass/ITO/PEDOT:PSS/donor layer/acceptor layer/BCP/Ag. For some sets of devices, annealing was performed in a vacuum oven. The PCDTBT layer was annealed before the evaporation of the SiPc layer at 150 °C for 10, 30, and 60 min. Other devices were also annealed during the evaporation of the SiPc layer at 150 °C using an in situ substrate heater, and after the SiPc evaporation but before the deposition of the BCP and Ag at 150 °C for 30 min.

Device Characterization

Current density vs. voltage curves were measured under nitrogen atmosphere using simulated solar light supplied by a Xenon arc lamp (Abet Technologies, Milford, CT, USA) with an Air Mass 1.5 Global filter, with a Keithley 2401 Low Voltage source meter. The solar simulator was calibrated with a silicon reference cell (Abet 15150) to 1000 W/m^2. Devices were mounted on an opaque holder, which eliminated diffuse light. Thicknesses were assessed using a Brucker Dektak XT Profilometer (Billerica, MA, USA). Small samples areas were scratched using a tweezer tip and then wiped with acetone to fully remove the layers. An average of 20 measurements were taken for each sample at different locations on the substrate.

3.7. Conclusion

A series of PHJ OPV mixed solution/evaporation devices were fabricated using $(246F)_2$-SiPc or $(345F)_2$-SiPc as the acceptor material, which were evaporated on either P3HT or PCDTBT as the solution processed donor layer. The devices were optimized through the substitution of materials and through controlling the acceptor thickness. We found that the spin rate of the PCDTBT had little effect on the device performance while the thickness of SiPc played a critical role. The optimal SiPc thickness was found to be roughly 90 nm. In attempts to improve these devices, a series of thermal treatments were applied to the most promising PCDTBT/$(345F)_2$-SiPc devices. Annealing of the PCDTBT layer alone, prior to $(345F)_2$-SiPc deposition with and without the addition of a small volume percentage of DIO, resulted in no significant improvement. However, annealing of the PHJ after $(345F)_2$-SiPc deposition, but before the BCP and Ag evaporation, led to increased *FF* = 0.51 ± 0.02 outperforming the PCDTBT/C_{60} baseline PHJ devices with a *PCE* of 1.52 ± 0.06%. These devices also surpassed previously reported all-evaporated PHJ devices based on $(246F)_2$-SiPc and $(345F)_2$-SiPc as NFAs when using α-sexithiophene as the donor layer.[53] Therefore, this study further justifies the continued investigation into using SiPcs as acceptor candidates in fullerene free devices.

3.8. References

1. Battaglia, C., Cuevas, A. & Wolf, S. De. High-efficiency crystalline silicon solar status: status and perspectives. *Energy Environ. Sci.* **9**, 1552–1576 (2016).
2. Lee, Michael M; Teuscher, Joel; Miyasaka, Tsutomu; Murakami, Takurou N.; Snaith, H. J. Efficient Hybrid Solar Cells Based on Meso-Superstructured Organometal Halide Perovskites. *Science (80-.).* **338**, 643–648 (2012).
3. Hoppe, H. & Sariciftci, N. S. Organic solar cells: An overview. *J. Mater. Res.* **19**, 1924–1945 (2004).
4. Forrest, S. R. The path to ubiquitous and low-cost organic electronic appliances on plastic. *Nature* **428**, 911–918 (2004).
5. Nørgaard, L. H. *et al.* Declarative process models in government centric case and document management. *CEUR Workshop Proc.* **1985**, 38–51 (2017).
6. Dang, M. T., Hirsch, L. & Wantz, G. P3HT:PCBM, best seller in polymer photovoltaic research. *Adv. Mater.* **23**, 3597–3602 (2011).
7. Yuan, J. *et al.* Single-Junction Organic Solar Cell with over 15 % Efficiency Using Fused-Ring Acceptor with Electron-Deficient Core Single-Junction. *Joule* **3**, 1–12 (2019).
8. Yan, C. *et al.* Non-fullerene acceptors for organic solar cells. *Nat. Rev. Mater.* **3**, 1–19 (2018).
9. Wang, C. *et al.* Si-Bridged Ladder-Type Small-Molecule Acceptors for High-Performance Organic Photovoltaics. *ACS Appl. Mater. Interfaces* **11**, 1125–1134 (2018).
10. Yu, Y., Tsai, T. & Chen, C. Efficient Ternary Organic Photovoltaics Using Two Conjugated Polymers and a Nonfullerene Acceptor with Complementary Absorption and Cascade Energy-Level Alignment. *J. Phys. Chem. C* **122**, 24585–24591 (2018).
11. Schaffer, C. J. *et al.* A direct evidence of morphological degradation on a nanometer scale in polymer solar cells. *Adv. Mater.* **25**, 6760–6764 (2013).
12. Ayzner, A. L., Tassone, C. J., Tolbert, S. H. & Schwartz, B. J. Reappraising the need for bulk heterojunctions in polymer-fullerene photovoltaics: The role of carrier transport in all-solution-processed P3HT/PCBM bilayer solar cells. *J. Phys. Chem. C* **113**, 20050–20060 (2009).
13. Lee, K. H. *et al.* Morphology of All-Solution-Processed “ Bilayer ” Organic Solar Cells. *Adv. Mater.* **23**, 766–770 (2011).
14. Vohra, V. *et al.* Enhanced Vertical Concentration Gradient in Rubbed P3HT:PCBM Graded Bilayer Solar Cells. *J. Phys. Chem. Lett.* **3**, 1820–1823 (2012).
15. Moon, J. S., Takacs, C. J., Sun, Y. & Heeger, A. J. Spontaneous formation of bulk heterojunction nanostructures: Multiple routes to equivalent morphologies. *Nano Lett.* **11**, 1036–1039 (2011).
16. Gholamkhass, B. & Servati, P. Solvent-vapor induced morphology reconstruction for efficient PCDTBT based polymer solar cells. *Org. Electron. physics, Mater. Appl.* **14**, 2278–2283 (2013).
17. Wakim, S. *et al.* Highly efficient organic solar cells based on a poly(2,7-carbazole) derivative. *J. Mater. Chem.* **19**, 5351–5358 (2009).
18. Park, S. H. *et al.* Bulk heterojunction solar cells with internal quantum efficiency approaching 100%. *Nat. Photonics* **3**, 297–303 (2009).
19. Wang, D. H., Kim, J. K., Seo, J. H., Park, O. O. & Park, J. H. Stability comparison: A PCDTBT/PC 71BM bulk-heterojunction versus a P3HT/PC 71BM bulk-heterojunction. *Sol. Energy Mater. Sol. Cells* **101**, 249–255 (2012).
20. Seok, J. *et al.* Efficient Organic Photovoltaics Utilizing Nanoscale Heterojunctions in Sequentially Deposited Polymer/fullerene Bilayer. *Sci. Rep.* **5**, 1–9 (2015).
21. Josey, D. S., Castrucci, J. S., Dang, J. D. & Lessard, B. H. Evaluating Thiophene

Electron-Donor Layers for the Rapid Assessment of Boron Subphthalocyanines as Electron Acceptors in Organic Photovoltaics: Solution or Vacuum Deposition? *ChemPhysChem* **16**, 1245–1250 (2015).

22. Yang, Y., Aryal, M., Mielczarek, K., Hu, W. & Zakhidov, A. Nanoimprinted P3HT/C60 solar cells optimized by oblique deposition of C60. *J. Vac. Sci. Technol. B* **28**, (2010).
23. Li, C. Z., Yip, H. L. & Jen, A. K. Y. Functional fullerenes for organic photovoltaics. *J. Mater. Chem.* **22**, 4161–4177 (2012).
24. Hoke, E. T. *et al.* Recombination in Polymer:Fullerene Solar Cells with Open-Circuit Voltages Approaching and Exceeding 1.0 V. *Adv. Energy Mater.* **3**, 220–230 (2013).
25. Kooistra, F. B. *et al.* Increasing the open circuit voltage of bulk-heterojunction solar cells by raising the LUMO level of the acceptor. *Org. Lett.* **9**, 551–554 (2007).
26. Anctil, A., Babbitt, C. W., Raffaelle, R. P. & Landi, B. J. Material and energy intensity of fullerene production. *Environ. Sci. Technol.* **45**, 2353–2359 (2011).
27. Anctil, A., Babbitt, C. W., Raffaelle, R. P. & Landi, B. J. Cumulative energy demand for small molecule and polymer photovoltaics. *Progress in Photovoltaics: Research and Applications* (2013) doi:10.1002/pip.2226.
28. Listigovers, N. A. *et al.* Hydroxygallium phthalocyanine pigments with block copolymer binders. U.S. Patent 5521043. (1996).
29. Giambalvo, V. A. & Lee, W. Non-crystallizing, non-flocculating phthalocyanines. U.S. Patent 3589924. (1971).
30. De La Torre, G., Claessens, C. G. & Torres, T. Phthalocyanines: Old dyes, new materials. Putting color in nanotechnology. *Chem. Commun.* 2000–2015 (2007) doi:10.1039/b614234f.
31. Lim, B. *et al.* Silicon-Naphthalo / Phthalocyanine-Hybrid Sensitizer for Efficient Red Response in Dye-Sensitized Solar Cells. 2011–2014 (2013) doi:10.1021/ol303436q.
32. El-nahass, M. M., El-gohary, Z. & Soliman, H. S. Structural and optical studies of thermally evaporated CoPc thin films. **35**, 523–531 (2003).
33. Roberts, M. E., Sokolov, A. N. & Bao, Z. Material and device considerations for organic thin-film transistor sensors. *J. Mater. Chem.* **19**, 3351–3363 (2009).
34. Li, X. *et al.* Copper phthalocyanine thin film transistors for hydrogen sulfide detection. *Sensors Actuators, B Chem.* **176**, 1191–1196 (2013).
35. Melville, O. A., Lessard, B. H. & Bender, T. P. Phthalocyanine-Based Organic Thin-Film Transistors: A Review of Recent Advances. *ACS Appl. Mater. Interfaces* **7**, 13105–13118 (2015).
36. Boileau, N. T., Melville, O. A., Mirka, B., Cranston, R. & Lessard, B. H. P and N type copper phthalocyanines as effective semiconductors in organic thin-film transistor based DNA biosensors at elevated temperatures. *RSC Adv.* **9**, 2133–2142 (2019).
37. Melville, O. A., Grant, T. M. & Lessard, B. H. Silicon phthalocyanines as N-type semiconductors in organic thin film transistors. *J. Mater. Chem. C* **6**, 5482–5488 (2018).
38. Deng, Z. *et al.* Aluminum phthalocyanine chloride as a hole injection enhancer in organic light-emitting diodes. *Solid. State. Electron.* **89**, 22–25 (2013).
39. Lessard, B. H., Sampson, K. L., Plint, T. & Bender, T. P. Boron subphthalocyanine polymers: Avoiding the small molecule side product and exploring their use in organic light-emitting diodes. *J. Polym. Sci. Part A Polym. Chem.* **53**, 1996–2006 (2015).
40. Pearson, A. J. *et al.* Silicon phthalocyanines as dopant red emitters for efficient solution processed OLEDs. *J. Mater. Chem. C* **5**, 12688–12698 (2017).
41. Plint, T., Lessard, B. H. & Bender, T. P. Assessing the potential of group 13 and 14 metal/metalloid phthalocyanines as hole transport layers in organic light emitting diodes. *J. Appl. Phys.* **119**, (2016).
42. Xue, J., Uchida, S., Rand, B. P. & Forrest, S. R. Asymmetric tandem organic

photovoltaic cells with hybrid planar-mixed molecular heterojunctions. *Appl. Phys. Lett.* **85**, 5757–5759 (2004).

43. Kim, D. Y., So, F. & Gao, Y. Aluminum phthalocyanine chloride/C60 organic photovoltaic cells with high open-circuit voltages. *Sol. Energy Mater. Sol. Cells* **93**, 1688–1691 (2009).
44. Cnops, K. *et al.* 8.4% efficient fullerene-free organic solar cells exploiting long-range exciton energy transfer. *Nat. Commun.* **5**, 1–6 (2014).
45. Dang, M. T. *et al.* Bis(tri-n-alkylsilyl oxide) silicon phthalocyanines: A start to establishing a structure property relationship as both ternary additives and non-fullerene electron acceptors in bulk heterojunction organic photovoltaic devices. *J. Mater. Chem. A* **5**, 12168–12182 (2017).
46. Yuen, A. P. *et al.* Photovoltaic properties of M-phthalocyanine/fullerene organic solar cells. *Sol. Energy* **86**, 1683–1688 (2012).
47. Williams, G., Sutty, S., Klenkler, R. & Aziz, H. Renewed interest in metal phthalocyanine donors for small molecule organic solar cells. *Sol. Energy Mater. Sol. Cells* **124**, 217–226 (2014).
48. Lessard, B. H. *et al.* Bis(tri- n -hexylsilyl oxide) silicon phthalocyanine: A unique additive in ternary bulk heterojunction organic photovoltaic devices. *ACS Appl. Mater. Interfaces* **6**, 15040–15051 (2014).
49. Grant, T. M., Gorisse, T., Dautel, O., Wantz, G. & Lessard, B. H. Multifunctional ternary additive in bulk heterojunction OPV: Increased device performance and stability. *J. Mater. Chem. A* **5**, 1581–1587 (2017).
50. Honda, S., Ohkita, H., Benten, H. & Ito, S. Multi-colored dye sensitization of polymer/fullerene bulk heterojunction solar cells. *Chem. Commun.* **46**, 6596–6598 (2010).
51. Honda, S., Ohkita, H., Benten, H. & Ito, S. Selective dye loading at the heterojunction in polymer/fullerene solar cells. *Adv. Energy Mater.* **1**, 588–598 (2011).
52. Lessard, B. H. *et al.* Assessing the potential roles of silicon and germanium phthalocyanines in planar heterojunction organic photovoltaic devices and how pentafluoro phenoxylation can enhance π-π Interactions and device performance. *ACS Appl. Mater. Interfaces* **7**, 5076–5088 (2015).
53. Lessard, B. H. *et al.* The position and frequency of fluorine atoms changes the electron donor/acceptor properties of fluorophenoxy silicon phthalocyanines within organic photovoltaic devices. *J. Mater. Chem. A* **3**, 24512–24524 (2015).
54. Zysman-Colman, E. *et al.* Solution-processable silicon phthalocyanines in electroluminescent and photovoltaic devices. *ACS Appl. Mater. Interfaces* **8**, 9247–9253 (2016).
55. Chauhan, K. V., Sullivan, P., Yang, J. L. & Jones, T. S. Efficient organic photovoltaic cells through structural modification of chloroaluminum phthalocyanine/fullerene heterojunctions. *J. Phys. Chem. C* **114**, 3304–3308 (2010).
56. Lessard, B. H. *et al.* From chloro to fluoro, expanding the role of aluminum phthalocyanine in organic photovoltaic devices. *J. Mater. Chem. A* **3**, 5047–5053 (2015).
57. Bailey-Salzman, R. F., Rand, B. P. & Forrest, S. R. Near-infrared sensitive small molecule organic photovoltaic cells based on chloroaluminum phthalocyanine. *Appl. Phys. Lett.* **91**, 1–4 (2007).
58. Chen, W. B. *et al.* Improving efficiency of organic photovoltaic cells with pentacene-doped CuPc layer. *Appl. Phys. Lett.* **91**, (2007).
59. Kumar, H. *et al.* Broad spectral sensitivity and improved efficiency in CuPc/Sub-Pc organic photovoltaic devices. *J. Phys. D. Appl. Phys.* **42**, 0–6 (2009).
60. Brumbach, M., Placencia, D. & Armstrong, N. R. Titanyl phthalocyanine/C60

heterojunctions: Band-edge offsets and photovoltaic device performance. *J. Phys. Chem. C* **112**, 3142–3151 (2008).

61. Yu, Jungsheng; Huang, Jiang; Zhang, Lei; Jiang, Y. Energy losing rate and open-circuit voltage analysis of organic solar cells based on detailed photocurrent simulation. **063103**, (2009).
62. Li, N., Lassiter, B. E., Lunt, R. R., Wei, G. & Forrest, S. R. Open circuit voltage enhancement due to reduced dark current in small molecule photovoltaic cells Open circuit voltage enhancement due to reduced dark current in small molecule photovoltaic cells. **023307**, 1–4 (2011).
63. Du, C., Yu, J., Huang, J. & Jiang, Y. Organic Solar Cells Using Tin (II) Phthalocyanine as Donor Material. *Energy Procedia* **12**, 519–524 (2011).
64. Nguyen, L. H. *et al.* Effects of annealing on the nanomorphology and performance of poly(alkylthiophene):Fullerene bulk-heterojunction solar cells. *Adv. Funct. Mater.* **17**, 1071–1078 (2007).

Chapter 4: Layer-By-Layer Organic Photovoltaic Solar Cells using a Solution-Processed Silicon Phthalocyanine Non-Fullerene Acceptor

4.1. Context

In **Chapter 3**, a hybrid solution-vacuum fabrication route was employed for the deposition of the active layer. Promising but limited performances were obtained, potentially due to limited interfacial area between the donor polymers and the SiPc acceptors. Therefore, I switched to a layer-by-layer all-solution process where both layers are sequentially solution deposited, as in **Chapter 2** it showed to improve the swelling between the active materials and to produce enough interfaces for charges dissociation. The evolution to an all-solution process also improves the transition potential to roll-to-roll more affordable large-scale deposition techniques. As previously used SiPc derivatives ($(246F)_2$-SiPc) and $(345F)_2$-SiPc)) were not soluble, I had to select another soluble SiPc derivative as the NFA, $(3BS)_2$-SiPc. It was paired with two commonly used donor polymers, P3HT and PBDB-T. I investigated different solvent systems, spin rates, deposition kinetics and thermal treatments for the deposition of the active bilayer. I also investigated a replacement for the PEDOT:PSS HTL that could provide inconsistent results and involve storage issues. The SiPc-based LbL all-solution processed OPV devices showed to perform similarly to BHJ devices, proving that the BHJ configuration is not essential to reach good *PCE*s.

4.2. Contribution of Authors

I performed most of the fabrication, optimization, and characterization of OPV devices. I received help from CD for the fabrication of LbL VOx/P3HT/$(3BS)_2$-SiPc devices and UV-Vis characterization. I received help from NAR for the AFM characterization. I solely wrote the first draft of the manuscript and received editing contribution from all other authors.

This chapter is currently in press:
M.D.M. Faure, C. Dindault, N.A. Rice, B.H. Lessard, ACS Applied Energy Materials, *Under Review*, **2021**.

4.3. Abstract

Silicon phthalocyanines (SiPcs) are promising inexpensive and easy to synthesize non-fullerene acceptor (NFA) candidates for all-solution sequentially processed layer-by-layer (LbL) organic photovoltaic (OPV) devices. Here, we report the use of bis(tri-*n*-butylsilyl oxide) SiPc ($(3BS)_2$-SiPc) paired with poly(3-hexylthiophene) (P3HT) and poly[(2,6-(4,8-bis(5-(2-ethylhexyl)thiophen-2-yl)-benzo[1,2-b:4,5-b’]dithiophene))-*alt*-(5,5-(1′,3′-di-2-thienyl-5′,7′-bis(2-ethylhexyl)benzo[1′,2′-c:4′,5′-c’]dithiophene-4,8-dione)] (PBDB-T) donors in a LbL OPV structure. Using a direct architecture, P3HT/$(3BS)_2$-SiPc LbL devices show power conversion efficiencies (*PCE*s) up to 3.0%, which is comparable or better than the corresponding BHJ devices with either $(3BS)_2$-SiPc or $PC_{61}BM$. PBDB-T/$(3BS)_2$-SiPc LbL devices resulted in *PCE*s up to 3.3%, with an impressive open circuit voltage (*Voc*) as high as 1.06 V, which is among the highest *Voc* obtained employing the LbL approach. We also compared devices incorporating vanadium oxide (VOx) or poly(3,4-ethylenedioxythiophene) polystyrene sulfonate (PEDOT:PSS) as a hole transporting layer, and found that VOx modified the donor layer morphology and led to improved *Voc*. Probing the composition as a function of the film layer depths revealed a similar distribution of active material for both BHJ and LbL structure when using $(3BS)_2$-SiPc as an NFA. These findings suggest $(3BS)_2$-SiPc is a promising NFA that can be processed using the LbL technique, an inherently easier fabrication methodology for large area production of OPVs.

4.4. Introduction

Organic photovoltaics (OPVs) are capable of rivaling the performance of other solar technologies, with state of the art OPV devices exhibiting power conversion efficiencies (*PCE*s) as high as 18%.[1-3] This improved efficiency, combined with the potential of semi-transparency, flexibility, and low-cost mass production through techniques such as roll-to-roll printing, has been the main reason for continuing research interest.[4],[5] However, for OPVs to become competitive the selection of active materials, their synthetic complexity, as well as the processes to fabricate and assemble the different layers is critical. Bulk heterojunction (BHJ) morphology has often been preferred over planar heterojunction (PHJ) morphology, due to significant improvements in device performance.[6-9] Compared to the PHJ, which has a defined interface between the independently deposited donor and acceptor materials and therefore limited active area available for charge dissociation, the bulk blend of the acceptor and donor materials in BHJ results in increased interfacial area.[10],[11] However, the random mixing of materials in BHJs makes it challenging to consistently reproduce device performances, particularly high performance with larger area devices, and complicates isolation of the photocharge behavior as a result of morphology changes, all of which significantly hinder a straightforward transition from lab-scale fabrication to mass-production.[12],[13]

A pseudo-bilayer configuration provides a convenient alternative, where the sequential layer-by-layer (LbL) deposition does not hinder favourable intermixing of the active layers while simultaneously providing a fabrication technique that is easier to optimize and translate to commercial printing processes.[14] In LbL, the first active layer is often deposited via solution deposition, followed by either thermal evaporation[15],[16] or, more commonly, solution deposition of the second layer.[17-23] All solution LbL deposition can promote a more efficient morphology, with a vertical phase separation resulting in increased donor and acceptor concentrations at the respective electrodes and an intermixed region between the electrodes (fuzzy interface).[24],[25] This composition provides enough interfacial contact for excitons to be dissociated, with the free charges readily extracted into neat layers to reduce unwanted charge recombination. Additionally, donor swelling and regional depth can be easily tuned and controlled through parameters such as solvents,[26-28] additives,[29],[30] or thermal treatments.[25],[31],[32] Compared to BHJ devices, LbL devices have demonstrated better mechanical and thermal stability, and are more robust to variances in experimental parameters including increased surface area,[22],[23],[33] while achieving equivalent or superior performances for many donor/acceptor systems. Efficiencies as high as 13% have been reported for spin coated devices,[34] over 16% for small-area blade coated devices, and an OPV record of 12% for a large-area blade coated LbL devices of 11.82 cm^2.[23]

Preeminent BHJ and LbL devices are normally achieved with novel small molecule non-fullerene acceptors (NFAs) based on acceptor-donor-acceptor push-pull architectures, [20-34],[35],[36] such as (3,9-bis(2-methylene-(3-(1,1-dicyanomethylene)-indanone))-5,5,11,11-tetrakis-(4-hexylphenyl)dithieno[2,3-d:20,30-d0]-s-indaceno[1,2-b:5,6-b0]dithiophene) (ITIC).[22],[34] While these elaborate architectures enable favorable molecule properties in OPVs, they require multiple complex synthetic steps with very low (<1%) overall synthetic yields, prohibiting commercialization of this technology[37] and emphasizing the need for simple, inexpensive, and high-performing OPV materials that can be synthetized and purified through scalable processes.

Silicon phthalocyanines ($(R)_2$-SiPc) are established molecules in the dye and pigment industries due to their chemical stability and low production costs.[38] $(R)_2$-SiPcs are tetravalent molecules that can undergo simple axial functionalization through straightforward and scalable chemistry,[39],[40] providing a synthetic handle for improving solubility and tuning aggregation in the solid state,[41] while modification of the $(R)_2$-SiPc macrocycle can be used to adjust the frontier energy levels.[42] $(R)_2$-SiPc derivatives have been investigated in BHJ devices, as either ternary additives or NFAs. An addition of 3 wt% $(R)_2$-SiPc derivative as a ternary additive in a poly(3-hexylthiophene):phenyl-C_{61}-butyric acid methyl ester (P3HT:PC_{61}BM) blend improved photocurrent generation and increased the *PCE* by 25% through enhanced light absorption around 700 nm.[43] When bis(tri-*n*-butylsilyl oxide) SiPc ($(3BS)_2$-SiPc, **Figure 1**) was used as an NFA with P3HT or poly[(2,6-(4,8-bis(5-(2-ethylhexyl)thiophen-2-yl)-benzo[1,2-b:4,5-b']dithiophene))-*alt*-(5,5-(1′,3′-di-2-thienyl-5′,7′-bis(2-ethylhexyl)benzo[1′,2′-c:4′,5′-c']dithiophene-4,8-dione)] (PBDB-T), BHJ OPVs with an averaged *PCE* of 3.6% and 3.4% were obtained, respectively, with *Voc* surpassing 1 V for the devices with PBDB-T.[44] Moreover, under reduced illumination, $(3BS)_2$-SiPc devices retained higher *PCE* compared to fullerene-based devices, affording exciting opportunities for indoor applications.[44] Insoluble phenoxylated SiPcs derivatives have been incorporated into bilayer devices through evaporation,[40],[45],[46] and Bender and coworkers recently reported the use of a boron subphthalocyanine as an NFA in all solution-processed LbL OPV devices with *PCE* up to 3.6%.[47] To the best of our knowledge, all solution-processed LbL OPV devices using soluble $(R)_2$-SiPc derivatives have never been reported.

The majority of reported LbL fabricated OPV devices utilize a direct structure incorporating poly(3,4-ethylenedioxythiophene) polystyrene sulfonate (PEDOT:PSS) as the hole transporting layer (HTL).[14] PEDOT:PSS is a highly conductive (between 2×10^{-3} and $1\ S.cm^{-1}$) transparent (> 75% in the visible range) polymer, normally processed in aqueous solvents to facilitate orthogonal processing.[48],[49] However, PEDOT:PSS is acidic (pH ≈1- 4),[48] degrading both its interface to the ITO electrode and the organic active material, causing indium diffusion into the PEDOT:PSS layer and shortening device lifetime, respectively.[50],[51] Since the early 2000s, transition metal oxides (TMO) with high work functions, such as MoO_3, WO_3, NiO, ZnO, and V_2O_5, have attracted interest as charge transporting layers in organic electronic devices.[52] TMOs in OPVs can avoid several of the aforementioned pitfalls with PEDOT:PSS, increasing both efficiency and stability of the devices.[53],[54] While most TMOs are thermally evaporated, vanadium oxide (VOx) can be easily obtained from a soluble vanadium precursor (like vanadyl acetylacetonate or vanadium oxytriisopropoxide) dissolved in isopropanol, and deposited in ambient conditions without any post-treatment to yield amorphous, smooth layers with electrical properties comparable to those of evaporated V_2O_5,[54],[55] making it a promising candidate for the replacement of PEDOT:PSS in fully solution-processed OPVs.

In this study, we employed $(3BS)_2$-SiPc as an NFA in all solution-processed LbL devices, and compared device performance to both analogous and P3HT:$PC_{61}BM$ BHJ devices. We paired it with P3HT, which remains one of the most commercially viable polymers for OPVs despite declining interest from academia,[56],[57] and with PBDB-T, a high performing p-type conjugated polymer. We also explored the use of VOx as an alternative to PEDOT:PSS as the HTL. We demonstrate that devices fabricated by the LbL approach perform as well as, and sometimes outperform, analogous BHJ devices, with $(R)_2$-SiPc based LbL devices characterized to have *PCE*s of ≈3% and *Voc* > 1 V, which are among the highest *Voc* reported for OPVs fabricated through the LbL approach.

4.5. Results and Discussion

$(3BS)_2$-SiPc (**Figure 4.1 a**) is a promising candidate as an acceptor molecule for OPVs due to its high solubility, proven performance as an acceptor in BHJ OPVs,[41],[44],[58] and its elevated n-type mobility as reported in organic thin film transistors.[59],[60] However, it's performance as a NFA in LbL OPV devices has yet to be evaluated. In the previous study, BHJ cells were fabricated with an inverted structure (glass/ITO/ZnO/active layer/MoOx/Ag).[44] Inverted LbL structures are rare in the literature compared to direct LbL devices, due to the convenience of first depositing the donor polymer followed by deposition of a small molecule acceptor.[14] For a more accurate comparison between our BHJ and LbL devices, both were fabricated with a direct (glass/ITO/HTL/active layer/BCP/Ag, **Figure 4.1 b**) architecture, using either PEDOT:PSS or VOx as the hole transporting layer. Additionally, baseline P3HT:PC$_{61}$BM devices were also prepared.[7]

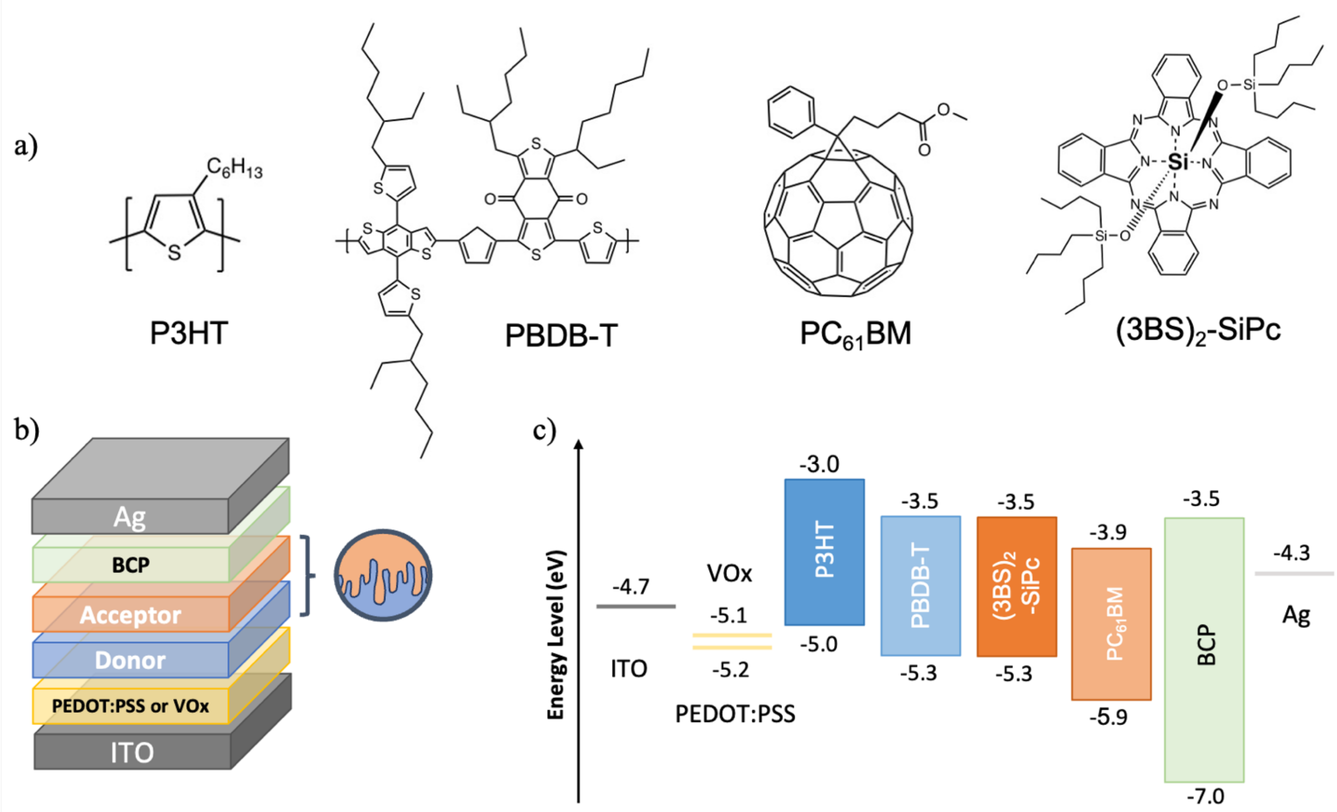

Figure 4.1. (a) Molecular structures of materials used in the active layer, (b) layer-by-layer direct device structure, and (c) electronic energy levels for all materials incorporated into OPVs.

While LbL device structures offer many advantageous over BHJ, significant initial optimization of processing conditions is required for new systems. For example: solvent combinations (orthogonal or non-orthogonal), dispensing volumes, dispensing kinetics, spin rates, and thermal treatments can all play significant roles in the resulting film morphology and device performance. Details of the full optimization of the LbL devices prepared in this study can be found in the Supporting Information (**Tables S4.1** and **S4.2**). We found the solvent combination which yielded optimal device performance was chloroform (CF) for the donor polymer (P3HT) and chlorobenzene (CB) for the acceptor molecule ((3BS)$_2$-SiPc). The low boiling point of CF facilitates rapid formation of a homogeneous and relatively thick P3HT film, while CB enabled the (3BS)$_2$-SiPc to swell into the P3HT layer. It was essential to deposit both layers dynamically to prevent the complete dissolution of the P3HT layer during deposition of the (3BS)$_2$-SiPc.

Current density-voltage (J-V) curves under 1 sun illumination for all devices using P3HT as the donor polymer and either PEDOT:PSS or VOx as the HTL are shown in **Figures 4.2 a-c**, with corresponding electrical parameters summarized in **Table 4.1**. P3HT:$PC_{61}BM$ BHJ devices displayed very similar *Voc*, short-circuit current density (*Jsc*), fill factor (*FF*) and *PCE* regardless of choice of HTL, which is consistent with previous reports comparing VOx to different HTLs, including PEDOT:PSS.[54],[61-64] For devices based on PEDOTS:PSS and VOx an average *PCE* of 2.7 ± 0.3% and 2.6 ± 0.1%, with an averaged *Voc* of 0.58 ± 0.01 V and 0.56 ± 0.01 V , an averaged *Jsc* of 7.7 ± 0.8 mA/cm^2 and 7.6 ± 0.3 mA/cm^2, and an averaged *FF* of 0.62 ± 0.02 and 0.63 ± 0.01 were obtained, respectively (for n=14 devices). It is worth noting that the use of VOx seems to improve reproducibility in the baseline devices as demonstrated by a drop in standard deviation (**Table 4.1**) and tightening in the spread of J-V curves (**Figure 4.2 a**).

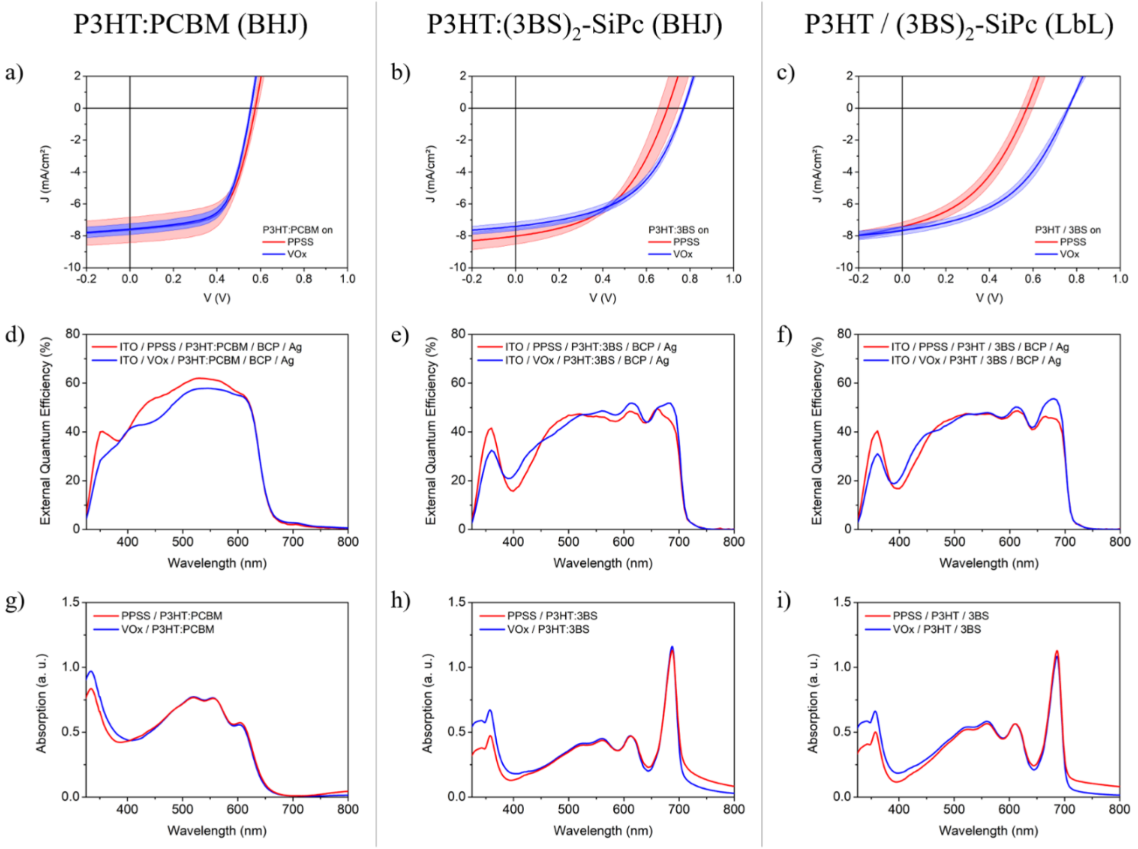

Figure 4.2. (a, b, c) Current vs. voltage (J-V) curves, (d, e, f) external quantum efficiency (EQE) spectra, and (g, h, i) UV-Vis absorption spectra for P3HT:PCBM BHJ, P3HT:$(3BS)_2$-SiPc BHJ, and P3HT/$(3BS)_2$-SiPc LbL on PEDOT:PSS (red) or VOx (blue) HTL. For convenience, $(3BS)_2$-SiPc is referred to as 3BS and PEDOT:PSS as PPSS.

Incorporation of $(3BS)_2$-SiPc as the acceptor in BHJ devices with either HTL led to similar *PCE* performances compared to the baseline devices with $PC_{61}BM$ acceptor, which represents a significant improvement over initial reports using $(3BS)_2$-SiPc as an NFA in direct BHJ device configurations.[41] While our $PC_{61}BM$-based devices consistently achieved more favorable *FF*, the use of $(3BS)_2$-SiPc resulted in higher *Voc* (**Table 4.1**). Unlike $PC_{61}BM$-based BHJ devices, the choice of HTL did impact *Voc* in $(3BS)_2$-SiPc-based devices, with an additional improvement from 0.70 V for PEDOT:PSS-based devices to 0.77 V for VOx-based devices, along with a slight improvement of the *FF* from 0.48 to 0.50, and improved consistency in performance. The increased *Voc,* 0.58 V to 0.70 V going from one acceptor to the other, is due to the increased energy gap between the $(3BS)_2$-SiPc LUMO and the P3HT HOMO (**Figure 4.1**), while the drop in *FF*, 0.62 to 0.48, is likely attributed to the reduced electron mobility of $(3BS)_2$-SiPc compared to $PC_{61}BM$ and unfavorable morphology.

Table 4.1. J-V characteristics for P3HT and $(3BS)_2$-SiPc integrated into bulk and bilayer heterojunction organic photovoltaic devices (0.325 cm^2) with PEDOT:PSS (abbreviated as PPSS) or VOx HTL.

HTL	**Active layer**	**I-V parameters**		average ± SD [max]	
		V_{oc} (V)	J_{sc} (mA/cm²)	FF	PCE (%)
PPSS	P3HT:PCBM *BHJ*	0.58 ± 0.01 [0.60]	7.7 ± 0.8 [8.8]	0.62 ± 0.02 [0.64]	2.7 ± 0.3 [3.1]
VOx		0.56 ± 0.01 [0.56]	7.6 ± 0.3 [8.1]	0.63 ± 0.01 [0.65]	2.6 ± 0.1 [2.8]
PPSS	P3HT:3BS *BHJ*	0.70 ± 0.05 [0.77]	8.0 ± 0.5 [8.6]	0.48 ± 0.02 [0.52]	2.7 ± 0.2 [3.0]
VOx		0.77 ± 0.01 [0.78]	7.4 ± 0.3 [7.9]	0.50 ± 0.02 [0.52]	2.8 ± 0.1 [3.0]
PPSS	P3HT / 3BS *LbL*	0.57 ± 0.03 [0.61]	7.4 ± 0.3 [7.9]	0.41 ± 0.02 [0.45]	1.8 ± 0.2 [2.1]
VOx		0.76 ± 0.01 [0.77]	7.7 ± 0.3 [7.4]	0.46 ± 0.02 [0.49]	2.7 ± 0.2 [3.0]

**At least 14 devices were taken into consideration for the averages' calculation.*

Similar trends in improved *Voc* and HTL dependency were also observed in P3HT/(3BS)$_2$-SiPc LbL devices (**Figure 4.2 c**). In general, (3BS)$_2$-SiPc LbL devices performed on par to their BHJ counterparts. When deposited on VOx, P3HT/(3BS)$_2$-SiPc LbL devices had an enhanced *PCE* of 2.7 ± 0.2%, compared to 1.8 ± 0.2% for PEDOT:PSS, due to an increase in *Voc* from 0.57 V to 0.76 and *FF* from 0.41 to 0.46 (**Table 4.1**). The increase in *Voc* when using VOx instead of PEDOT:PSS could arise from a reduction of the injection barrier between the P3HT donor and the HTL. In literature, the work function of VOx is reported between -5.1 eV to -5.6 eV,[55],[62] compared to that of PEDOT:PSS with a work function of -5.2 eV.[54] Moreover, PEDOT:PSS being a polymer, it provides a softer and smoother surface compared to a metal oxide such as VOx that is more rough. This difference in interface could impact how P3HT forms and crystallizes, and how charges are collected and recombine. Analogous to BHJ results, the use of VOx resulted in more consistent (3BS)$_2$-SiPc-based LbL devices (**Figure 4.2 c** and **Table 4.1**), suggesting that for P3HT devices a VOx HTL layer can result in superior OPV performances compared to PEDOT:PSS-based devices. Furthermore, our optimized results demonstrate that (3BS)$_2$-SiPc is a viable alternative to PC$_{61}$BM in P3HT-based OPVs, capable of producing devices with comparable performances in either BHJ or LbL architectures.

To gain further insight on the relative contributions of the materials to photocurrent generation, external quantum efficiency (EQE) and UV-Vis absorption measurements were conducted. UV-Vis absorption measurements of individual materials are available in the Supporting Information (**Figure S4.1**). **Figure 4.2 d** shows the EQE spectra of P3HT:PC$_{61}$BM BHJ devices deposited on either PEDOT:PSS (red curve) or VOx (blue curve), which appear to be relatively similar in accordance with the J-V results. The EQE maximums around 525 nm for samples made on PEDOT:PSS or VOx are slightly above or below 60%, respectively, with a more prominent absorption peak for PEDOT:PSS around 340 nm and a dramatic decrease in absorption above 650 nm for both HTLs. The corresponding UV-Vis absorption spectra (**Figure 4.2 g**) are almost indistinguishable for the two HTLs, in accordance with the EQE trends.

Figure 4.2 e shows the EQE spectra of P3HT:(3BS)$_2$-SiPc BHJ devices deposited on either PEDOT:PSS or VOx. A more intense absorption peak is observed around 365 nm for samples made using PEDOT:PSS, while for films deposited on VOx there is a more intense absorption peak around 680 nm and an absorption shoulder between 400 and 450 nm. In comparison to P3HT:PC$_{61}$BM EQEs, the spectra have lower maxima around 50% but the global absorptions are extended to after 700 nm thanks to the $(3BS)_2$-SiPc contribution between 600 and 700 nm. This is confirmed with the corresponding UV-Vis absorption spectra (**Figure 4.2 h**), where the global absorption intensity before 650 nm dropped in comparison to P3HT:$PC_{61}BM$, but a new highly intense absorption peak around 680 nm is observed for $(3BS)_2$-SiPc.

EQE spectra for LbL devices of P3HT/$(3BS)_2$-SiPc deposited on either PEDOT:PSS or VOx (**Figure 4.2 f**) exhibit very similar trends compared to the BHJ devices. The same extension of the absorption range by approximately 70 nm compared to $PC_{61}BM$-based devices is observed. The EQE maxima are still around 50%, with only a slight increase for devices made on VOx around 680 nm. Corresponding UV-Vis spectra shown in **Figure 4.2 i** for both HTLs are very similar to the blended active layers. These results further confirm that LbL fabrication imparts equivalent active layer optical properties compared to the BHJ approach, and that $(3BS)_2$-SiPc can enable an extension of the absorption range. Moreover, choice of the HTL seems to only have little impacts on the active layer absorption.

We surmised that the nature of the HTL layer provides different templating effects on the formation of P3HT layer during deposition, which could influence the P3HT and $(3BS)_2$-SiPc interface, ultimately leading to changes in device performances. Contact angle measurements did not reveal wettability differences between the two HTLs, with similar hydrophilic behaviors and angle values around 10° to water, and angle values around 4° to chloroform (solvent used for the P3HT layer) (**Table S4.3**). Atomic force microscopy (AFM) was used to characterize P3HT films (no acceptor molecules) deposited under identical conditions, either on PEDOT:PSS or VOx, with representative images shown in **Figure 4.3**. The P3HT film deposited on PEDOT:PSS (**Figure 4.3 a**) was relatively smooth, with fairly consistent morphology and features, resulting in a low root-mean-square (RMS) roughness of 0.85 nm. In contrast, P3HT deposited on VOx (**Figure 4.3 b**) is characterized by more pronounced peak-to-valley height differences in the line height section, with a dramatically larger RMS roughness of 1.40 nm, confirming that the choice of HTL does influence the morphology of the donor layer. From these findings we assume that the VOx layer facilitates a more favorable templating surface for $(3BS)_2$-SiPc onto P3HT, encouraging deeper interpenetration of the donor and acceptor at the interface, and potentially leading to increased donor/acceptor interfacial area and reduced charge recombination. This is consistent with the increased *FF* and *Voc* of LbL VOx/P3HT/$(3BS)_2$-SiPc devices discussed previously.

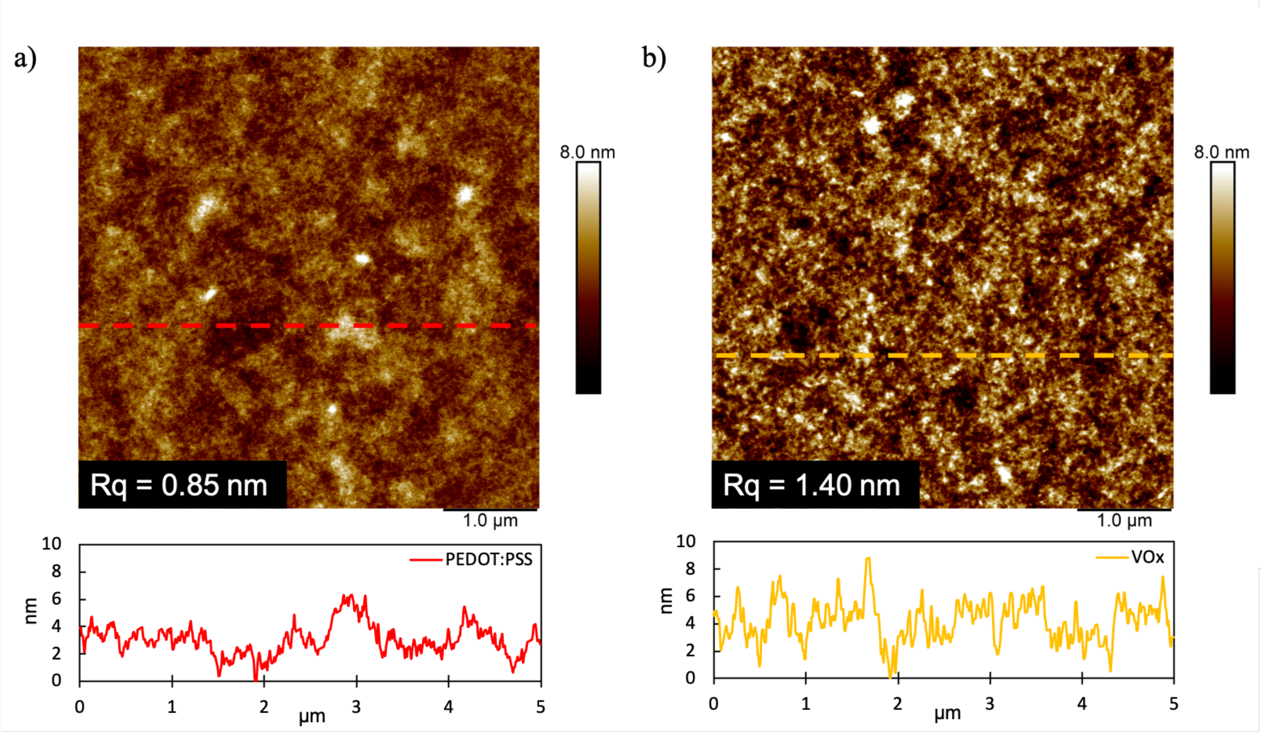

Figure 4.3. AFM height images of P3HT layers deposited onto (a) PEDOT:PSS and (b) VOx. The dashed lines indicate the location of the line segment height analysis, shown below the two images.

We conducted time-of-flight secondary ion mass spectroscopy (TOF-SIMS) measurements to elucidate the vertical concentration gradient profiles of P3HT and $(3BS)_2$-SiPc through the entire thickness of both a BHJ (**Figure 4.4 a**) and LbL (**Figure 4.4 b**) active layer deposited on a VOx HTL. Sulfur ion (S^-) was used to track P3HT, silicon ion (Si^-) used for the $(3BS)_2$-SiPc acceptor, vanadium oxide ion (VO_2^-) for the VOx HTL layer, and indium oxide ion (InO_2^-) was used to track the ITO electrode. No significant differences were noticed between the two architectures; the intensity profile of S^- and Si^- signals are similar and homogeneous throughout the whole layer, suggesting that P3HT and $(3BS)_2$-SiPc are evenly distributed throughout the films. For the BHJ structure the sputter time is longer, indicating it takes more time to go through the active layer compared to the LbL structure, which is consistent with the relative active layer thickness of the BHJ versus LbL devices obtained by profilometry. TOF-SIMS results for the LbL devices suggest a complete dissolution and intermixing of the $(3BS)_2$-SiPc layer into the P3HT layer despite their sequential processing. The hypothesis is that the deposition of $(3BS)_2$-SiPc induces a resolubilization of the P3HT layer despite the solvents' immiscibility. Indeed, when looking at thicknesses values, a decrease from roughly 160 nm for the P3HT neat layer to 110 nm for the P3HT/$(3BS)_2$-SiPc bilayer can be noted. Moreover, during the dynamic spin coating of $(3BS)_2$-SiPc, discolouration of the P3HT layer was noticed.

These observations imply that swelling of $(3BS)_2$-SiPc causes the partial washing of P3HT, helping $(3BS)_2$-SiPc to reach the bottom. Similar absence of a vertical separation for LbL devices has been reported for other systems, even when using orthogonal solvents.[26],[65],[66] The equivalent vertical phase separation obtained by BHJ and LbL processing of the active layer confirms that LbL processing results in analogous film morphologies and ultimately similar device performances compared to the conventional BHJ processing while requiring less active materials and being more suitable for eventual module commercialization.

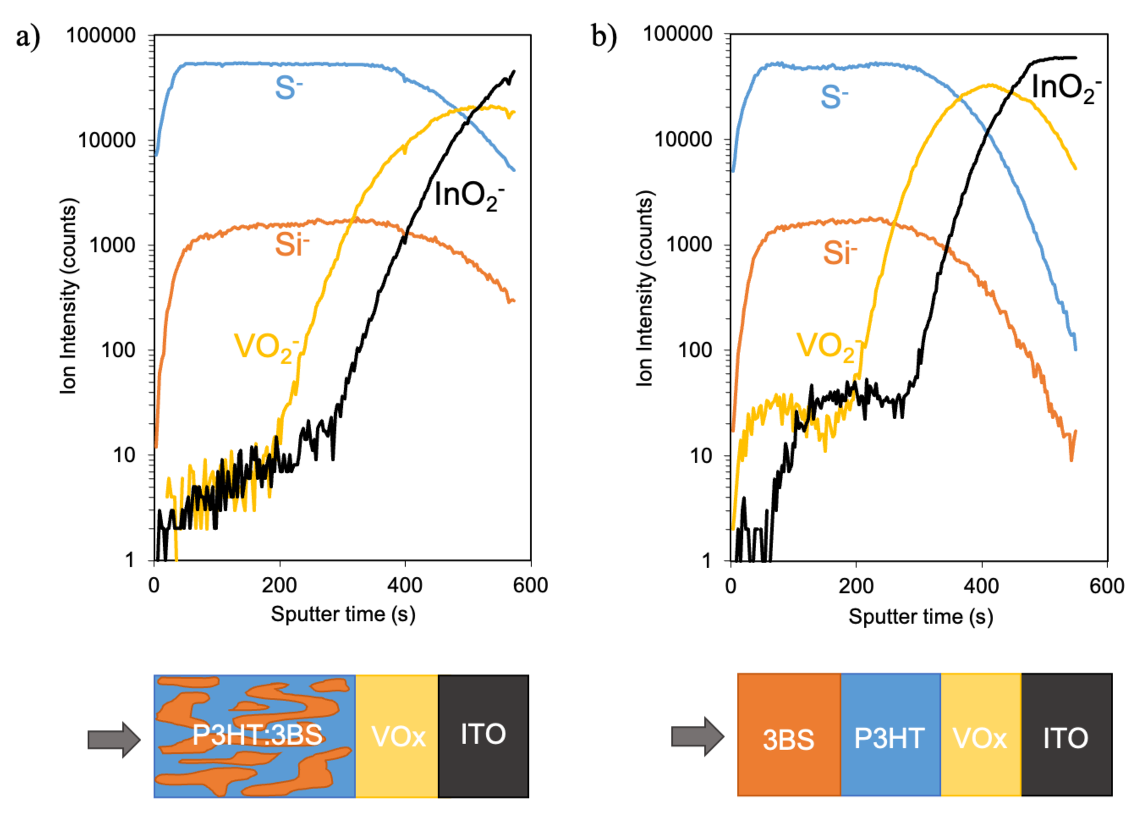

Figure 4.4. TOF-SIMS depth profiles of (a) blend VOx/P3HT:$(3BS)_2$-SiPc and (b) LbL VOx/P3HT/$(3BS)_2$-SiPc photoactive layers.

To assess the universality of our findings incorporating $(3BS)_2$-SiPc into OPVs through the LbL approach, we combined our acceptor with another donor polymer. PBDB-T was chosen as PBDB-T/$(3BS)_2$-SiPc has been demonstrated in an indirect BHJ device configuration to provide OPVs with *PCE* > 3.0% with *Voc* > 1.0 V.[44] PBDB-T:$(3BS)_2$-Si BHJ devices and PBDB-T/$(3BS)_2$-Si LbL devices were prepared using VOx as the HTL layer. The LbL process necessitated re-optimization of experimental conditions, resulting in slight changes in device fabrication conditions from P3HT to PBDB-T (described in detail in Experimental Section and Supporting Information, **Table S4.4**). J-V curves, EQE spectra and UV-Vis absorption spectra for both LbL and BHJ device architectures are shown in **Figure 4.5 a, 4.5 b** and **4.5 c,** respectively, with electrical parameters summarized in **Table 4.2**. As with our P3HT system, the BHJ devices and LbL devices using PBDB-T as the donor polymer had very similar devices performances. PBDB-T:$(3BS)_2$-SiPc BHJ devices achieved a *PCE* of 3.19 ± 0.13%, with a *Voc* of 1.07 V, while the LbL devices had an average *PCE* of 3.02 ± 0.02%, with a *Voc* of 1.06 V. These results are comparable to the performances obtained in the literature with a similar system using an indirect architecture.[44] Even though BHJ devices attained a slightly improved average *PCE* compared to LbL devices, both devices displayed an impressive *Voc* above 1 V due to the favorable frontier orbital offsets. These values are amongst the highest *Voc* obtained for all-solution-processed LbL devices.[14] As expected, the EQE spectra for both films (**Figure 4.5 b**) are comparable, with a maximum slightly above 40%, and an extended spectra up to 700 nm from the $(3BS)_2$-SiPc contribution. Compared to the P3HT/$(3BS)_2$-SiPc LbL system, the $(3BS)_2$-SiPc contribution is decreased due to the similarities in band gaps between the two materials (**Figure 4.1 c**). UV-Vis absorption spectra for the two donor-acceptor films (**Figure 4.5 c**) have matching trends, with an intense absorption peak just before 700 nm. These results demonstrate that $(3BS)_2$-SiPc is an extremely versatile NFA for LbL processing, capable of replicating BHJ performances in different polymer systems.

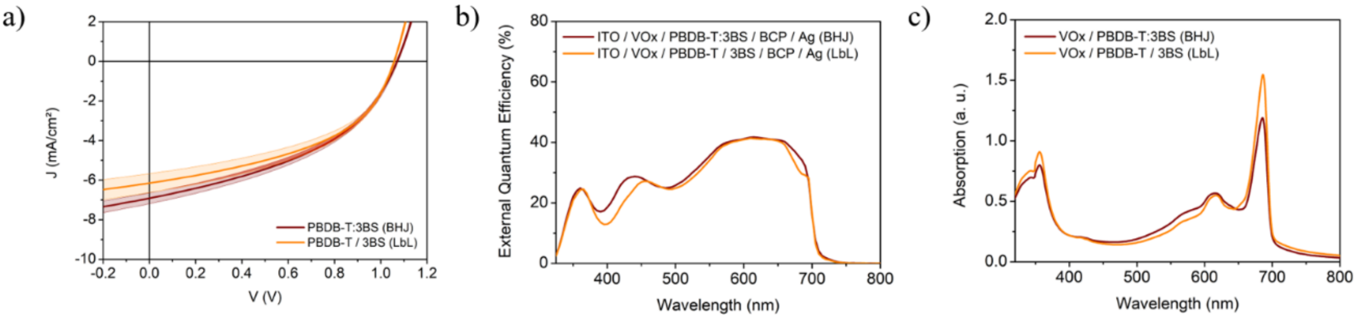

Figure 4.5. (a) Current vs voltage (J-V) curves with lines indicating the averaged curve and shades indicating the standard deviations, (b) external quantum efficiency (EQE) spectra and (c) UV-Vis absorption spectra for PBDB-T:$(3BS)_2$-SiPc BHJ (dark red) and PBDB-T/$(3BS)_2$-SiPc LbL (orange) on VOx HTL. Both active layers were annealed at 100 °C for 10 min. For convenience $(3BS)_2$-SiPc is referred to as 3BS.

Table 4.2. J-V characteristics for PBDB-T and $(3BS)_2$-SiPc integrated into bulk and bilayer heterojunction organic photovoltaic devices (0.325 cm^2) with VOx HTL.

Active layer Annealed at 100°C for 10 min	**I-V parameters**	average ± SD [max]		
	V_{oc} (V)	J_{sc} (mA/cm²)	FF	PCE (%)
PBDB-T:3BS *BHJ*	1.1 ± 0.01 [1.1]	6.9 ± 0.3 [7.4]	0.43 ± 0.01 [0.44]	3.2 ± 0.1 [3.4]
PBDB-T / 3BS *LbL*	1.1 ± 0.0 [1.1]	6.2 ± 0.5 [6.8]	0.46 ± 0.01 [0.47]	3.0 ± 0.2 [3.3]

**At least 10 devices were taken into consideration for the averages' calculation.*

4.6. Experimental

Materials

PEDOT:PSS (Clevios^{TM} HTL Solar, Batch#SCA388-47) was purchased from Heraeus, and vanadium(V) oxytriisopropoxide (VOx precursor, Lot#MKBK2918V) and 2-propanol (IPA, 99.9%) were purchased from Sigma Aldrich. P3HT (Lot#BLS26-24, RR ≥95%, M_w = 45 kDa) was purchased from Rieke Metals and PBDB-T (Batch#BM8-071, M_w = 107 kDa, M_n = 53 kDa) was acquired from Brilliant Matters. $PC_{61}BM$ (99.5%) was acquired from Nano-C and $(3BS)_2$-SiPc was synthetized in house according to literature[44] and purified using train sublimation. Bathocuproine (BCP, sublimed >99.5%) powder was purchased from Lumtec and Ag (99.99%) pellets from Angstrom Engineering. All compounds were used as received unless otherwise specified.

Devices were prepared on 25 mm x 25 mm (± 0.2 mm) 0.7 mm thick glass substrates coated (via sputtering) with 1450 ± 100 Å of ITO (15 ± 3 ohms/sq, transmission: 89% Avg. @ 550nm) that were purchased from Thin Film Devices Inc.

General Device Fabrication

Direct structure, bilayer devices with an active area of 0.325 cm^2 were fabricated with the following structure: glass/ITO/HTL/donor layer/acceptor layer/BCP/Ag. ITO-coated glass substrates were cleaned by successive 5-min sonication baths of soapy water (water + detergent), water, acetone, and finally methanol prior to an air plasma treatment for 15 min. The vanadium-based HTL solution was prepared under N_2 atmosphere by dissolution of VOx precursor in IPA with a volume ratio of 1:70 in the absence of heat or agitation. The solution was then spin coated at 10,000 rpm for 30 s in air (Spincoat G3P from Specialy Coating Systems) before letting the samples rest in air for at least 1 h, to yield an approximately 10 nm thick layer. The PEDOT:PSS solution was spin coated at 3000 rpm for 30 s on substrates before being annealed under air at 140 °C for 15 min, resulting in a layer that was approximately 30 nm thick. Substrates were then transferred to a nitrogen glovebox.

After deposition of the active layers (see below), BCP (9 nm) and Ag (70 nm) were thermally evaporated in a vacuum chamber (base pressure < 2 x 10^{-6} Torr) using an Angstrom EvoVac through a custom shadow mask to yield 5 devices per substrate, with an active area of 0.325 cm^2 per device.

LbL Active Layer

The following formulations are for optimal conditions; however, all parameters were optimized for each device structure and can be found in the Supporting Information. P3HT (15 mg/mL) or PBDB-T (12 mg/mL) were dissolved in chloroform (≥99%) and stirred for 4 h. P3HT (150 µL) was deposited by dynamic spin-coating at 1000 rpm for 80 s (Spincoat G3P from Specialty Coating Systems), while PBDB-T (300 µL) was deposited via static spin-coating using the same speed and time. $(3BS)_2$-SiPc was dissolved in chlorobenzene (99.8%) at a concentration of either 15 mg/mL (for P3HT devices) or 12 mg/mL (for PBDB-T devices) and stirred overnight at 50 °C. $(3BS)_2$-SiPc was deposited by dynamic spin-coating (40 µL) at 3500 rpm for 60 s onto P3HT or by static spin-coating (300 µL) onto PBDB-T; PBDB-T/$(3BS)_2$-SiPc layers were then annealed in a nitrogen atmosphere at 100 °C for 10 min. The combined LbL active layer thicknesses were approximately 110 and 90 nm for P3HT/$(3BS)_2$-SiPc and PBDB-T/$(3BS)_2$-SiPc layers, respectively.

BHJ Active Layer

P3HT (20 mg/mL) and $PC_{61}BM$ were dissolved in 1,2-dichlorobenzene (99%) with a 1:1 mass ratio and stirred overnight at 50 °C before deposition by static spin-coating at 800 rpm for 90 s. P3HT (15 mg/mL) and $(3BS)_2$-SiPc were dissolved in 1,2-dichlorobenzene (99%) with a 1:1 mass ratio, stirred overnight at 50 °C, and deposited by static spin-coating at 2000 rpm for 80 s. PBDB-T (10 mg/mL) and $(3BS)_2$-SiPc were dissolved in 1,2-dichlorobenzene (99%) with a 1:1 mass ratio, stirred at 35°C overnight, and deposited by static spin-coating at 1000 rpm for 120 s before annealing at 100 °C for 10 min under a nitrogen atmosphere. Thicknesses of approximately 150 and 120 nm were obtained for P3HT:$(3BS)_2$-SiPc and PBDB-T:$(3BS)_2$-SiPc BHJ layers, respectively.

Device Characterization

Current density vs. voltage (J-V) characteristics were measured using an Abet Technologies Sunlite 11,002 solar simulator under a nitrogen atmosphere (Xenon arc lamp) with an Air Mass 1.5 Global filter calibrated to 1 sun (1000 W/m^2) using a silicon reference cell (Abet 15150). External quantum efficiency (EQE) was measured over a 325 – 900 nm wavelength range using a Newport Oriel CS130-QUANTX. Layer thickness was assessed using a Brucker Dektak XT Profilometer, and AFM height images were obtained with a Bruker Dimension Icon in ScanAsyst mode, using ScanAsyst-Air probes and a scan rate of 0.8 Hz. Calculation of root-mean-square (RMS) roughness and image processing were performed using NanoScope Analysis v1.8. Depth profiles were obtained by time-of-flight secondary ion mass spectrometry (TOF-SIMS) using an ION-TOF (GmbH) TOF-SIMS IV equipped with a Bi cluster liquid metal ion source (25 keV Bi_3^+, pulsed at 10 kHz). A depth profile was obtained by repeating the cycle of alternatively sputtering the surface in an area of 250 μm × 250 μm with a 3 keV Cs^+ beam for 3 s, waiting 1 s, and collecting an ion mass spectrum using the Bi_3^+ primary ion beam at 128 × 128 pixels over an area of 128 μm × 128 μm within the sputtered area (1 shot per pixel). Contact angle measurements were performed from three-point curve fitting using a VCA Optima goniometer (AST Products Inc) where droplets of DI water or chloroform were deposited by syringe onto glass/ITO/HTL substrates. UV-visible spectra of thin films were measured using an Agilent Cary 5000 UV-vis-NIR spectrophotometer in the 300 – 900 nm range.

4.7. Conclusion

In this study we investigated the use of the synthetically facile phthalocyanine derivative $(3BS)_2$-SiPc as a NFA in sequentially all solution-processed LbL OPV devices. Two HTLs, PEDOT:PSS and VOx, were investigated as HTLs with VOx found to facilitate favorable changes in the P3HT film morphology, which resulted in improved *FF* and *Voc* for $(3BS)_2$-SiPc-based devices processed by LbL. After optimization, direct LbL devices fabricated with VOx achieved *PCE*s up to 3.0% when integrating P3HT as the donor polymer, and *PCE*s up to 3.3% for devices with PBDB-T as the donor polymer, with an impressive *Voc* up to 1.06 V. These represent the greatest reported *PCE* for SiPc-based LbL OPV devices, with the *Voc* value above 1 V amongst the highest achieved for both LbL and PBDB-T-based devices. When compared to their BHJ counterparts, LbL devices demonstrated equivalent efficiencies, with analogous EQE responses and absorption spectra, and commensurate vertical film composition. These results substantiate the promise of inexpensive and synthetical-facile SiPc-based derivatives as NFAs that can be incorporated into LbL devices fabricated through a more scalable and roll-to-roll transferable method, demonstrating significant potential for commercially viable OPV modules.

4.8. References

1. Liu, Q. *et al.* 18 % Efficiency organic solar cells. *Sci. Bull.* 1–10 (2020) doi:10.1016/j.scib.2020.01.001.
2. Cui, Y. *et al.* Over 16% efficiency organic photovoltaic cells enabled by a chlorinated acceptor with increased open-circuit voltages. *Nat. Commun.* **10**, 1–8 (2019).
3. Lin, Y. *et al.* 17% Efficient organic solar cells based on liquid exfoliated WS2 as a replacement for PEDOT:PSS. *Adv. Mater.* **31**, 1902965 (2019).
4. Lizin, S. *et al.* Life cycle analyses of organic photovoltaics: a review. *Energy Environ. Sci.* **6**, 3136–3149 (2013).
5. Hengevoss, D., Baumgartner, C., Nisato, G. & Hugi, C. Life Cycle Assessment and eco-efficiency of prospective, flexible tandem organic photovoltaic module. *Sol. Energy* **137**, 317–327 (2016).
6. Tang, C. W. Two-layer organic photovoltaic cell. *Appl. Phys. Lett.* **48**, 183–185 (1986).
7. Dang, M. T., Hirsch, L. & Wantz, G. P3HT:PCBM, best seller in polymer photovoltaic research. *Adv. Mater.* **23**, 3597–3602 (2011).
8. Yuan, J. *et al.* Single-Junction Organic Solar Cell with over 15 % Efficiency Using Fused-Ring Acceptor with Electron-Deficient Core Single-Junction. *Joule* **3**, 1–12 (2019).
9. Wang, T. *et al.* A 2.16eV bandgap polymer donor gives 16% power conversion efficiency. *Sci. Bull.* **65**, 179–181 (2020).
10. Xu, Z. *et al.* Understanding the Morphology of High-Performance Solar Cells Based on a Low-Cost Polymer Donor. *Appl. Mater. Interfaces* **12**, 9537–9544 (2020).
11. Gholamkhass, B. & Servati, P. Solvent-vapor induced morphology reconstruction for efficient PCDTBT based polymer solar cells. *Org. Electron. physics, Mater. Appl.* **14**, 2278–2283 (2013).
12. Brabec, C. J., Heeney, M., McCulloch, I. & Nelson, J. Influence of blend microstructure on bulk heterojunction organic photovoltaic performance. *Chem. Soc. Rev.* **40**, 1185–1199 (2011).
13. Schaffer, C. J. *et al.* A direct evidence of morphological degradation on a nanometer scale in polymer solar cells. *Adv. Mater.* **25**, 6760–6764 (2013).
14. Faure, M. D. M. & Lessard, B. H. Layer-by-layer fabrication of organic photovoltaic devices: material selection and processing conditions. *J. Mater. Chem. C* **9**, 14–40 (2021).
15. Wei, G. *et al.* Functionalized Squaraine Donors for Nanocrystalline Organic Photovoltaics. *ACS Nano* **6**, 972–978 (2012).
16. Zabihi, F., Chen, Q., Xie, Y. & Eslamian, M. Fabrication of efficient graphene-doped polymer/fullerene bilayer organic solar cells in air using spin coating followed by ultrasonic vibration post treatment. *Superlattices Microstruct.* **100**, 1177–1192 (2016).
17. Jang, Y. *et al.* Formation of Thermally Stable Bulk Heterojunction by Reducing the Polymer and Fullerene Intermixing. *Sci. Rep.* **7**, 1–9 (2017).
18. Aguirre, J. C. *et al.* Sequential Processing for Organic Photovoltaics : Design Rules for Morphology Control by Tailored Semi-Orthogonal Solvent Blends. *Adv. Drug Deliv. Rev.* **5**, 1–11 (2015).
19. Cheng, P. *et al.* Efficient and stable organic solar cells via sequential process. *J. Mater. Chem. C* **4**, 8086–8093 (2016).
20. Sun, R. *et al.* A universal layer-by-layer solution-processing approach for efficient non-fullerene organic solar. *Energy Environ. Sci.* **12**, 384–395 (2019).
21. Arunagiri, L. *et al.* Temperature-Dependent Aggregation Donor Polymers Enable Highly Efficient Sequentially Processed Organic Photovoltaics Without the Need of Orthogonal Solvents. *Adv. Funct. Mater.* **29**, 1–10 (2019).

22. Dong, S. *et al.* High-Performance Large-Area Organic Solar Cells Enabled by Sequential Bilayer Processing via Nonhalogenated Solvents. *Adv. Energy Mater.* **9**, 1–7 (2019).
23. Sun, R. *et al.* A Layer-by-Layer Architecture for Printable Organic Solar Cells Overcoming the Scaling Lag of Module Efficiency. *Joule* **4**, 1–13 (2020).
24. Clulow, A. J. *et al.* Time-Resolved Neutron Reflectometry and Photovoltaic Device Studies on Sequentially Deposited PCDTBT-Fullerene Layers. *Langmuir* **30**, 11474–11484 (2014).
25. Yang, B., Yuan, Y. & Huang, J. Reduced Bimolecular Charge Recombination Loss in Thermally Annealed Bilayer Heterojunction Photovoltaic Devices with Large External Quantum Efficiency and Fill Factor. *J. Phys. Chem. C* **118**, 5196–5202 (2014).
26. Shan, T. *et al.* Achieving Optimal Bulk Heterojunction in All-Polymer Solar Cells by Sequential Processing with Nonorthogonal Solvents. *Appl. Mater. Interfaces* **11**, 42438–42446 (2019).
27. Kim, K. D., Park, S., Nho, S., Baek, G. & Cho, S. The effects of P3HT crystallinity in bilayer structure organic solar cells. *Curr. Appl. Phys.* **14**, 1369–1373 (2014).
28. Ahn, S., Jang, W., Hyeok, J. & Hwan, D. Enhanced performance of layer-evolved bulk-heterojunction solar cells with Ag nanoparticles by sequential deposition. *Org. Electron.* **24**, 325–329 (2015).
29. Jang, Y., Seo, J., Seok, J., Lee, J. & Kim, K. Roughening Conjugated Polymer Surface for Enhancing the Charge Collection Efficiency of Sequentially Deposited Polymer/Fullerene Photovoltaics. *Polym. Eng. Sci.* **7**, 1497–1509 (2015).
30. Fontana, M. T. *et al.* Low-Vapor-Pressure Solvent Additives Function as Polymer Swelling Agents in Bulk Heterojunction Organic Photovoltaics. *J. Phys. Chem. C* **122**, 16574–16588 (2018).
31. Lang, C., Fan, J., Zhang, Y., Guo, F. & Zhao, L. Utilizing intermixing of conjugated polymer and fullerene from sequential solution processing for efficient polymer solar cells. *Org. Electron.* **36**, 82–88 (2016).
32. Yan, B. H. *et al.* Influence of Annealing and Interfacial Roughness on the Performance of Bilayer Donor / Acceptor Polymer Photovoltaic Devices. *Adv. Funct. Mater.* **20**, 4329–4337 (2010).
33. Sun, R. *et al.* A multi-objective optimization-based layer-by-layer blade-coating approach for organic solar cells: rational control of vertical stratification for high performance. *Energy Environ. Sci.* **12**, 3118–3132 (2019).
34. Cui, Y. *et al.* Toward Efficient Polymer Solar Cells Processed by a Solution-Processed Layer-By-Layer Approach. *Adv. Mater.* **30**, 1–7 (2018).
35. Zhang, J. *et al.* Efficient non-fullerene organic solar cells employing sequentially deposited donor–acceptor layers†. *J. Mater. Chem. A* **6**, 18225–18233 (2018).
36. Ye, L. *et al.* Sequential Deposition of Organic Films with Eco-Compatible Solvents Improves Performance and Enables Over 12 %-Efficiency Nonfullerene Solar Cells. *Adv. Mater.* **31**, 1–9 (2019).
37. Wadsworth, A. *et al.* Critical review of the molecular design progress in non-fullerene electron acceptors towards commercially viable organic solar cells †. *Chem Soc Rev* **48**, 1596–1625 (2019).
38. De La Torre, G., Claessens, C. G. & Torres, T. Phthalocyanines: Old dyes, new materials. Putting color in nanotechnology. *Chem. Commun.* 2000–2015 (2007) doi:10.1039/b614234f.
39. Sasa, N., Okada, K., Nakamura, K. & Okada, S. Synthesis, structural, and conformational analysis and chemical properties of phthalocyaninatometal complexes. *J. Mol. Struct.* **446**, 163–178 (1998).
40. Lessard, B. H. *et al.* Assessing the potential roles of silicon and germanium

phthalocyanines in planar heterojunction organic photovoltaic devices and how pentafluoro phenoxylation can enhance π-π Interactions and device performance. *ACS Appl. Mater. Interfaces* **7**, 5076–5088 (2015).
41. Dang, M. T. *et al.* Bis(tri-n-alkylsilyl oxide) silicon phthalocyanines: A start to establishing a structure property relationship as both ternary additives and non-fullerene electron acceptors in bulk heterojunction organic photovoltaic devices. *J. Mater. Chem. A* **5**, 12168–12182 (2017).
42. Honda, S., Ohkita, H., Benten, H. & Ito, S. Multi-colored dye sensitization of polymer/fullerene bulk heterojunction solar cells. *Chem. Commun.* **46**, 6596–6598 (2010).
43. Vebber, M. C., Grant, T. M., Brusso, J. L. & Lessard, B. H. Bis(trialkylsilyl oxide) Silicon Phthalocyanines: Understanding the Role of Solubility in Device Performance as Ternary Additives in Organic Photovoltaics. *Langmuir* **36**, 2612–2621 (2020).
44. Grant, T. M. *et al.* High Voc solution-processed organic solar cells containing silicon phthalocyanine as a non-fullerene electron acceptor. *Org. Electron.* **87**, 105976 (2020).
45. Lessard, B. H. *et al.* The position and frequency of fluorine atoms changes the electron donor/acceptor properties of fluorophenoxy silicon phthalocyanines within organic photovoltaic devices. *J. Mater. Chem. A* **3**, 24512–24524 (2015).
46. Faure, M. D. M., Grant, T. M. & Lessard, B. H. Silicon Phthalocyanines as Acceptor Candidates in Mixed Solution/Evaporation Processed Planar Heterojunction Organic Photovoltaic Devices. *Coatings* **9**, 1–13 (2019).
47. Sampson, K. L., Nyikos, S. R., Morse, G. E. & Bender, T. P. Sequentially Solution-Deposited Active Layer: Ideal Organic Photovoltaic Device Architecture for Boron Subphthalocyanine as a Nonfullerene Acceptor. *ACS Appl. Energy Mater.* 1237–1249 (2021) doi:10.1021/acsaem.0c02528.
48. Cameron, J. & Skabara, P. J. The damaging effects of the acidity in PEDOT:PSS on semiconductor device performance and solutions based on non-acidic alternatives. *Mater. Horizons* **7**, 1759–1772 (2020).
49. Singh, A., Katiyar, M. & Garg, A. Understanding the formation of PEDOT:PSS films by ink-jet printing for organic solar cell applications. *RSC Adv.* **5**, 78677–78685 (2015).
50. de Jong, M. P., van IJzendoorn, L. J. & de Voigt, M. J. A. Stability of the interface between indium-tin-oxide and poly(3,4-ethylenedioxythiophene)/poly(styrenesulfonate) in polymer light-emitting diodes. *Appl. Phys. Lett.* **77**, 2255–2257 (2000).
51. Garcia, A. *et al.* Improvement of Interfacial Contacts for New Small-Molecule Bulk-Heterojunction Organic Photovoltaics. *Adv. Mater.* **24**, 5368–5373 (2012).
52. Meyer, J. *et al.* Transition Metal Oxides for Organic Electronics: Energetics, Device Physics and Applications. *Adv. Mater.* **24**, 5408–5427 (2012).
53. Schumann, S. *et al.* Inverted organic photovoltaic devices with high efficiency and stability based on metal oxide charge extraction layers. *J. Mater. Chem.* **21**, 2381–2386 (2011).
54. Zilberberg, K., Trost, S., Schmidt, H. & Riedl, T. Solution Processed Vanadium Pentoxide as Charge Extraction Layer for Organic Solar Cells. *Adv. Energy Mater.* **1**, 377–381 (2011).
55. Tan, Z. *et al.* Solution-processed vanadium oxide as a hole collection layer on an ITO electrode for high-performance polymer solar cells. *Phys. Chem. Chem. Phys.* **14**, 14589 (2012).
56. Po, R. *et al.* From lab to fab: How must the polymer solar cell materials design change?- an industrial perspective. *Energy Environ. Sci.* **7**, 925–943 (2014).
57. Chatterjee, S., Jinnai, S. & Ie, Y. Nonfullerene acceptors for P3HT-based organic solar cells. *J. Mater. Chem. A* (2021) doi:10.1039/d1ta03219d.

58. Vebber, M., Rice, N. A., Brusso, J. L. & Lessard, B. H. High Voc Fullerene-Free Organic Photovoltaics Composed of PTB7 and Axially-Substituted Silicon Phthalocyanines. *RSC Adv.* (2021).
59. Cranston, R. R. *et al.* Thin-Film Engineering of Solution-Processable n-Type Silicon Phthalocyanines for Organic Thin-Film Transistors. *ACS Appl. Mater. Interfaces* **13**, 1008–1020 (2021).
60. Cranston, R. R. *et al.* N-Type Solution-Processed Tin versus Silicon Phthalocyanines: A Comparison of Performance in Organic Thin-Film Transistors and in Organic Photovoltaics. *ACS Appl. Electron. Mater.* **3**, 1873–1885 (2021).
61. Shrotriya, V., Li, G., Yao, Y., Chu, C. W. & Yang, Y. Transition metal oxides as the buffer layer for polymer photovoltaic cells. *Appl. Phys. Lett.* **88**, 073508 (2006).
62. Hancox, I. *et al.* Optimization of a high work function solution processed vanadium oxide hole-extracting layer for small molecule and polymer organic photovoltaic cells. *J. Phys. Chem. C* **117**, 49–57 (2013).
63. Xie, F. *et al.* Low-temperature solution-processed hydrogen molybdenum and vanadium bronzes for an efficient hole-transport layer in organic electronics. *Adv. Mater.* **25**, 2051–2055 (2013).
64. Alsulami, A. *et al.* Thermally stable solution processed vanadium oxide as a hole extraction layer in organic solar cells. *Materials (Basel).* **9**, (2016).
65. Moon, J. S., Takacs, C. J., Sun, Y. & Heeger, A. J. Spontaneous formation of bulk heterojunction nanostructures: Multiple routes to equivalent morphologies. *Nano Lett.* **11**, 1036–1039 (2011).
66. Chen, D., Liu, F., Wang, C., Nakahara, A. & Russell, T. P. Bulk Heterojunction Photovoltaic Active Layers via Bilayer Interdiffusion. *Nano Lett.* **11**, 2071–2078 (2011).

Chapter 5: SiPcs as ETL in Perovskite Solar Cells

5.1. Context

In addition to demonstrating great potential as NFAs for OPV devices, SiPc's have found application in organic thin film transistors (OTFT) devices as the semiconductor while displaying very good electron mobilities. This promising electron mobility should be favourable for use in electron transport layer or hole blocking layer in perovskite-based solar cells. A collaboration between the Lessard Research Group and the Laboratoire de Physique des Interfaces et des Couches Minces (LPICM) in France was started in 2019. The LPICM has a research program that fabricates and studies perovskite-based solar cells. The goal of the collaboration was to explore the use of SiPc derivatives as electron transport layers as replacements for conventional fullerenes. The LPICM hosted me for a duration of 2 months to perform the experimental work in their laboratories. The following chapter provides our initial results and showcases the potential for SiPcs in a broader context.

5.2. Introduction to Perovskite Solar Cells

Perovskite solar cells (PSCs) have attracted a huge interest among photovoltaic (PV) researchers due to incredible performances evolution since the emergence of the technology (**Figure 5.1**).[1] In a single decade, the PCE increased from 3% to over 25%, while in comparison, other PV technologies required nearly 30 years to reach similar results. Perovskites were first introduced into PV in 2009 through their use as liquid sensitizer in dye-sensitized solar cells by Kojima and coworkers with 3.8% efficiency.[2] In 2012, Kim et al. evolved perovskites into solid-state PSC with PCEs approaching 10%.[3] In 2015 devices with 20% PCE were already reported.[4] Today the PCE record for a single-junction cell is now held by Jeong et al. and is reaching 25.6%.[5]

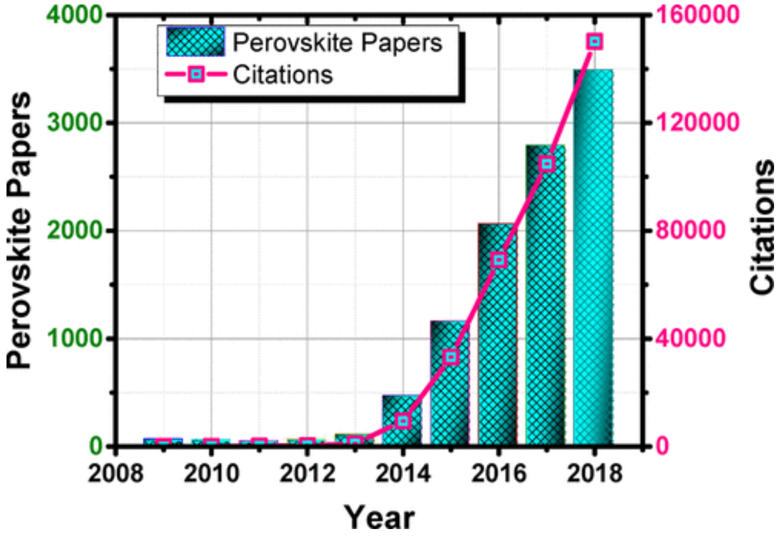

Figure 5.1. Rise of perovskite research as viewed through the published papers and their citation impact over the 2009−2018 period (Source: Web of Science, Clarivate Analytics March 3, 2019).[1]

The 3D crystal structure of perovskite materials follows the same arrangement as the calcium titanate ($CaTiO_3$) mineral consisting of TiO_6 octahedron inside a Ca_8 cube. It can be reduced to a general formula ABX_3 for a unit cell, where A represents the corner atoms in the cubic lattice, B the center atom, and X the face centered atoms. Ideally, the perovskite structure is as symmetrical as possible, with B-cations that coordinate with 6 X-anions creating octahedral geometries (**Figure 5.2 a**) and A-cations that coordinate with 12 X-anions creating cuboctahedral geometries (**Figure 5.2 b**). The corners of the structure are occupied by the BX_6 octahedral geometries, while interstices are filled by A-cations (**Figure 5.2 c**). Perovskite subfamilies exist depending on the nature of the X atoms, such as oxide perovskites (X = O)[6-8] and halide perovskite (X = Cl^-, Br^-, I^-, F^-). Halide perovskites comprise of divalent B-cation such as Pb^{2+},[4] Sn^{2+},[9] Bi^{2+},[10] or Ge^{2+} [11] that can be pure or mixed[12],[13]. Depending on the A-cation, the halide family can be divided in two types. The first type is alkali halide perovskite and involves a monovalent alkali A-cation such as Cs+, Rb^+, Na^+ or Li^+.[10],[14], The second type is hybrid organic-inorganic perovskite that comprises of an organic A-cation such as $CH_3NH_3^+$, $CH_3CH_2NH_3^+$ or $NH_2CHNH_2^+$.[4],[5],[9],[11-13] The two types of A-cation can be mixed as well.[15] The most common used perovskite materials is methylammonium lead trihalide ($CH_3NH_3PbX_3$ or $MAPbX_3$, where X = Cl, Br, I or mix) with a bandgap ranging from around 1.5 eV for $MAPbI_3$ to 2.3 eV for $MAPbBr_3$.[16] In particular, $MAPbI_3$ (MAPI) has been extensively studied with great PCEs reaching above 20%,[3],[17-20] and the current PCE record was achieved using formamidinium lead triiodide ($CH(NH_2)_2PbI_3$ or $FAPbI_3$ or FAPI).[5]

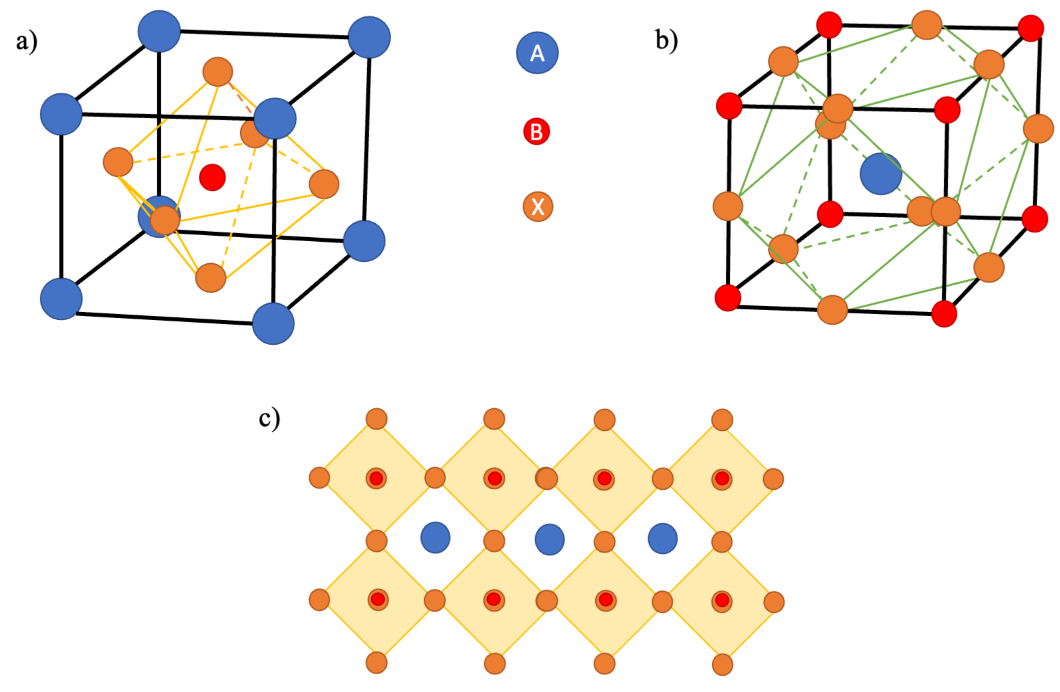

Figure 5.2. Unit cell of ABX_3 perovskite 3D structure showing (a) BX_6 octahedral geometries and (b) AX_{12} cuboctahedral geometries. (c) 2D representation of the perovskite structure.

Perovskites are characterized by a bandgap that can range from 1.5 to 2.5 eV, and have a high absorption coefficient exceeding 10^5 cm^{-1}.[21] They also have a high electron mobility up to 800 $cm^2.V^{-1}.s^{-1}$,[22] high carrier lifetime and diffusion length that can exceed 300 ns and 1 µm respectively,[23],[24] a less than 10 meV exciton binding energy,[25] and a great tolerance to structural defect. Perovskites also enable thin films application and deposition on flexible substrates. However, PSC devices suffer from poor stability, reproducibility and short lifetime.[26],[27] Moreover, best perovskite materials incorporate a lead core, a toxic element which poses an environmental hazard.[28] Therefore, commercialization of PSC modules is lagging.

5.3. PSCs Architectures, Fabrication, and Transport Materials

5.3.1. Devices Structures and Fabrication Methods

PSCs working principle is very similar to OPV, with only minor differences. In contrast to its organic counterpart, the source of free carriers generation in perovskite-based PV devices is still discussed. It was first believed that dissociation of the photogenerated excitons within the perovskite layer was driven by the built-in electrical field induced by the energy level offset of the adjacent charge transporting layers; however, more recent studies have showed that due to very low exciton-binding energy most of incident photons resulted in almost instantaneous generation of free charges.[29] Many device architectures exist for perovskites, however, there are four primary types of structures.[30] The first type is the "regular" direct structure and is based on a meso-porous scaffold of TiO_2 ETL completely infiltrated with the perovskite films, sandwiched between a thin compact layer of TiO_2 to avoid shunting losses, and a HTL (**Figure 5.3 a**). The PSC efficiency record was obtained using this architecture. The second type is a direct planar heterojunction structure where the perovskite layer (i) is sandwiched with non-porous n-type ETL and p-type HTL, forming a similar structure as n-i-p inorganic cells (**Figure 5.3 b**). The third type, known as mesoporous superstructured solar cells (MSSC), involves an insulating mesoporous scaffold layer of inert Al_2O_3 helping the suppression of pinholes and the pace of charge collection (**Figure 5.3 c**). The fourth structure is the inverted planar heterojunction forming a p-i-n configuration (**Figure 5.3 d**), equivalent to an OPV direct structure such as ITO/PEDOT:PSS/active layer/BCP/Ag.

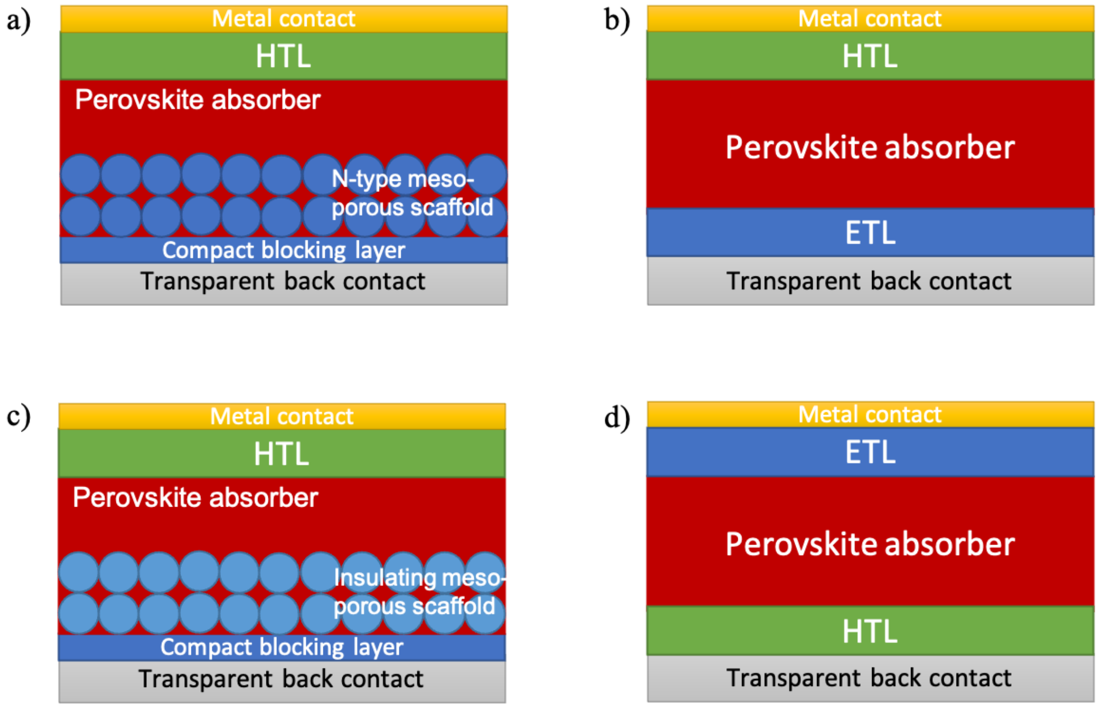

Figure 5.3. The primary structural configuration of PSCs: (a) regular direct structure, (b) direct planar heterojunction structure, (c) direct meso-porous superstructured structure, and (d) inverted planar heterojunction structure.

Various methods have been developed for the deposition of the perovskite film. The first PSC devices consisted of an absorber formed by a one-step spin coating.[2] A mixture of CH_3NH_3X and PbX_2 (X= Cl, I, Br) precursors is dissolved in a polar aprotic solvent like N,N-dimethylformamide (DMF), dimethyl sulfoxide (DMSO) or γ-butyrolactone (GBL) and spin coated onto a substrate to form a precursor film.The film is then converted into a perovskite film by a thermal annealing step removing residual solvent. However, perovskite films formed are not uniform and very sensitive to experimental conditions making it difficult to achieve highly efficient cells.[31-33] Improvement of the technique was achieved by solvent engineering.[34] Precursors are dissolved in a mixed GBL/DMSO solvent system, and spin coating of the solution onto the substrate is rapidly followed by a toluene drop while spinning (**Figure 5.4 a**).[35] The toluene anti-solvent treatment helps the rapid and homogeneous formation of an intermediate perovskite film by removal of DMSO solvent excess. The final perovskite film is then produced via thermal annealing. Due to rapid, ease of processing and low cost, this one-step spin coating method is a widely used technique to fabricate devices on a lab-scale. Nonetheless, the anti-solvent treatment remains a very finicky step and requirement for a thermal annealing increases the cost of production, impeding commercialization of PSCs.

Therefore, many other deposition techniques have been developed including two-step sequential spin coating/dipping (**Figure 5.4 b**)[36], vapor-assisted solution process (**Figure 5.4 c**)[37], sequential evaporation[38], coevaporation (**Figure 5.4 d**)[39], hybrid chemical vapor deposition (**Figure 5.4 e**)[40], or vacuum flash evaporation[41]. Perovskite modules were also fabricated using scalable techniques such as doctor blading[42], inkjet printing[43], or slot die coating[44].

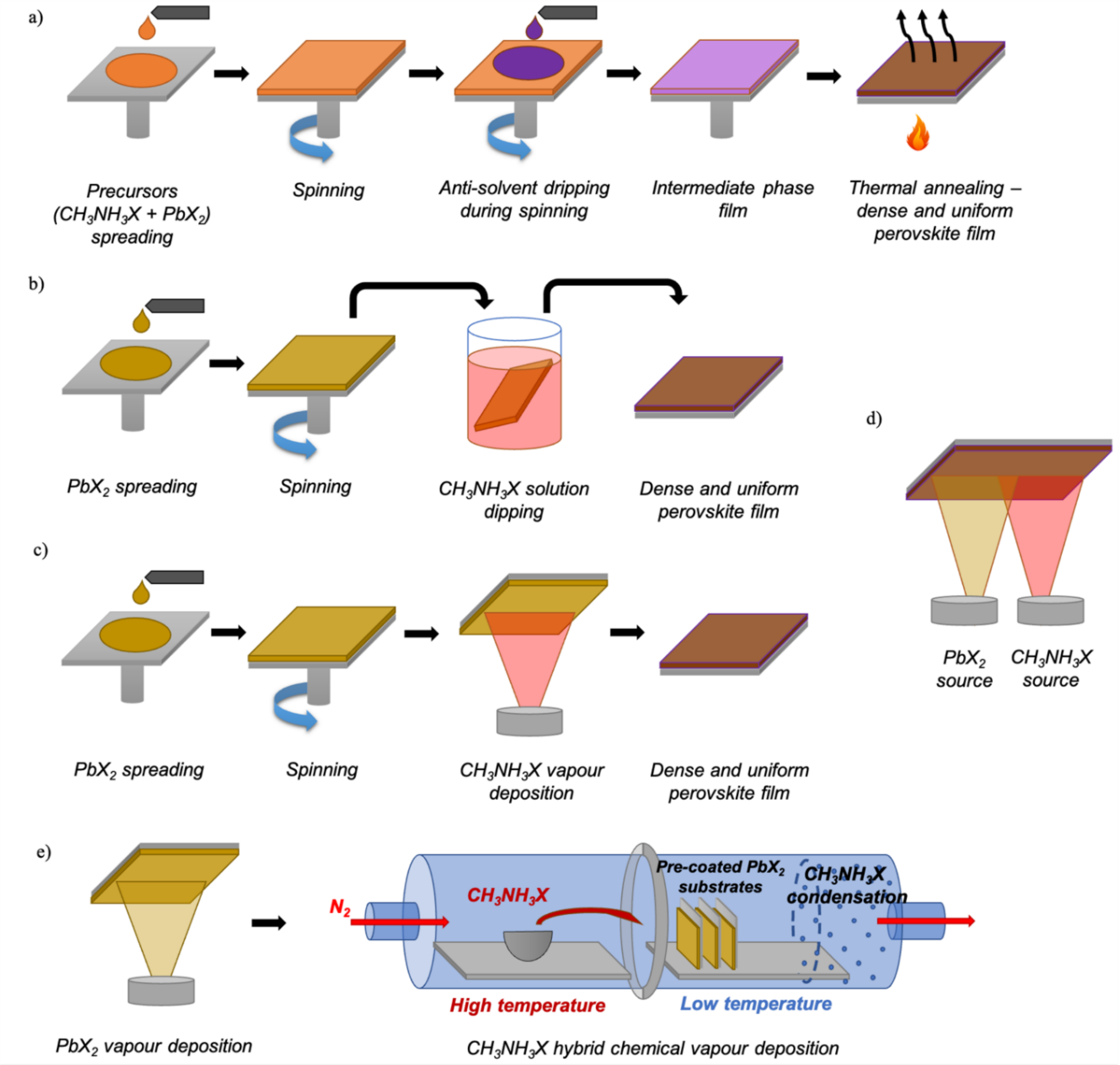

Figure 5.4. Schematic illustration of fabrication method of perovskite layer via (a) one-step spin coating/anti-solvent, (b) two-step sequential spin coating/dipping, (c) vapor-assisted solution process, (d) coevaporation, (e) hybrid chemical vapor deposition.

5.3.2. Hole Transport Layers (HTLs) and Electron Transport Layers (ETLs) Materials

The most common HTL used with oxide ETLs in direct structures is 2,2’,7,7’-tetrakis[N,N-di(4-methoxyphenyl) amino]-9,9’-spirobifluorene (spiro-OMeTAD)[5,45-49] while the most common HTL used with organic ETLs in inverted structures is PEDOT:PSS[50-55] (**Figure 5.5**). However, the acidic and hygroscopic nature of PEDOT:PSS and the low intrinsic conductivity, low hole mobility, along with energy levels mismatching and lengthy low-yielding synthetic steps of spiro-OMeTAD have led researchers to look for alternatives to these HTLs.[49],[56] Other organic, but also inorganic, materials have been investigated as alternatives and examples include PTAA[57], P3HT[58], PFDT-2F-COOH[59], CuPc[60], Co(II)/Co(III) porphyrin[61], CuSCN[62], Cu_2O[63], NiO_x[64], with efficiencies ranging from around 15% to above 20%.

ETLs for PSCs can be organic or inorganic and in a direct architecture, the most popular choice is TiO_2 due to its favorable energy levels, long electron lifetimes and being able to provide devices with high PCEs.[5],[48],[58],[60],[61],[63],[65-67] However, deposition usually through spin coating or spray pyrolysis is followed by a high sintering temperature step around 500 °C, which increases the production cost of modules and limits the applications. Moreover it has a relatively low thin film electron mobility ($\approx 2.10^{-5}$ $cm^2.V^{-1}.s^{-1}$), and inefficient extraction of the electrons could led to significant hysteresis behaviors in devices.[56],[67] Therefore, the development of low temperature deposition methods, dopants and surface treatments were employed to improve transport properties and reduce the hysteresis effects.[68] However, other materials are being explored such as ZnO due to its similar band gap, greater electron mobility of up to 6.10^{-2} $cm^2.V^{-1}.s^{-1}$, and low temperature deposition methods such as sol-gel or atomic layer deposition.[69-71] Unfortunately, performances and thermal/chemical stability of ZnO-based devices are inferiors to their TiO_2-based counterparts.[70],[72],[73] SnO_2 has emerged as another promising candidate with greater energy levels alignment, thin films electron mobility around 2.10^{-3} $cm^2.V^{-1}.s^{-1}$, better overall device stability compared to TiO_2 and ZnO, and high efficiencies above 23% obtained with low temperature processing methods (sol-gel, colloidal dispersion, atomic layer deposition).[45],[74-76] Nevertheless, some of SnO_2 drawbacks involve low wettability, increased surface defects, and poor long-term stability.[76],[77] Other investigated oxides include CdS[78], Zn_2SnO_4[79], In_2O_3[80] or WO_3[81].

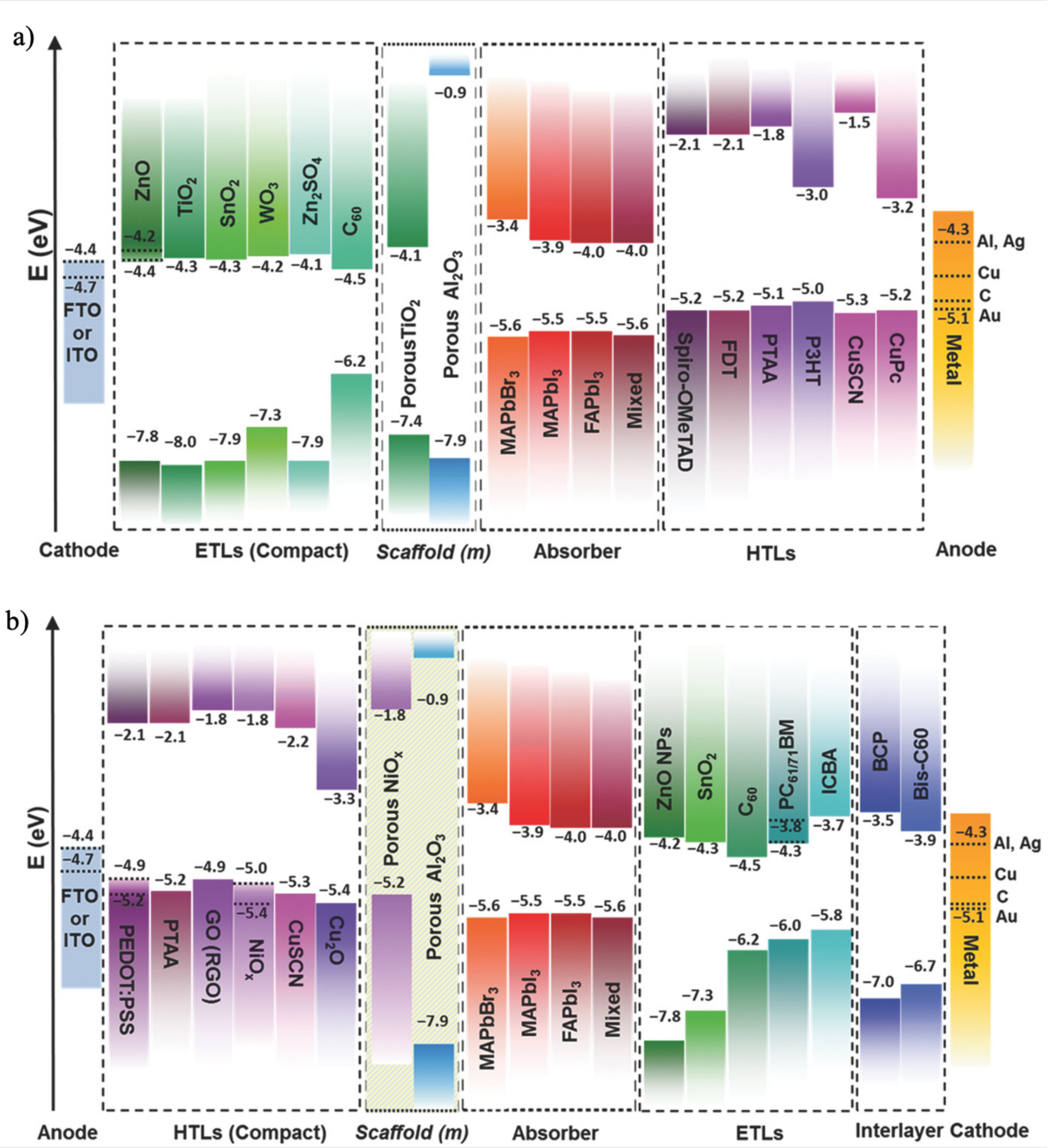

Figure 5.5. Energy level diagrams of several hole and electron transport layers for (a) direct n-i-p structure and (b) inverted p-i-n structure.[82]

Another possibility is the use of organic ETLs, as inverted planar heterojunction PSCs. Ideal candidates revealed to be fullerene derivatives such as C_{60} and $PC_{61}BM$ due to their suitable energy levels, decent electron mobility (1.6 $cm^2.V^{-1}.s^{-1}$ and 6.10^{-2} $cm^2.V^{-1}.s^{-1}$ respectively), and easy deposition through thermal evaporation or low-temperature solution processing.[59],[83] Devices based on fullerene ETLs exhibited efficiencies up to 22%.[57],[84-88] Nonetheless, restricted tuning of energy levels limiting materials combinations, relatively poor morphological stability and high synthesis and purification costs of fullerene derivatives has stimulated the search for non-fullerene organic ETLs.[88],[89] Rylene diimide small molecules, in particular perylene diimide (PDI) and naphthalene diimide (NDI) soluble derivatives, have been considered due to good chemical/thermal stability, inexpensive starting materials and facile high molecular engineering potential.[90],[91] However, PDIs have a strong π-π stacking tendency leading to poor solubility and film morphology, requiring introduction of functional groups or novel molecular designs. Compared to PDIs, NDIs are very similar but have a larger optical band gap and a more easily adjustable π-π packing. Devices integrating imide-based ETLs displayed promising but still lower performances compared to fullerene-based devices, with PCEs usually bellow 20%.[92-98] Other materials investigated include azaacene-based[99],[100] and indacenodithiophene-based[101],[102] small molecules, and have also shown promise. While porphyrin and phthalocyanines analogues were mainly incorporated into devices as HTLs,[103] only one example of their use as thermally evaporated ETLs existed before the collaboration between our group and the host laboratory LPICM. Air stability of devices was improved upon use of hexadecafluorophthalocyaninatocopper (F_{16}-CuPc) with a PCE of 12.6%.[104] In the meantime, Xie et al. published a study where they used a pyrene-substitued SiPc (SiPc-Py-2) derivative as an interfacial layer between the perylenetetracarboxylic dianhydride (PTCDA) ETL and the perovskite absorber.[105] The SiPc layer has shown to passivate the trap states on the perovskite's surface, and devices based on PTCDA/SiPc-Py-2 ETL achieved 19.2% efficiency, further justifying the investigation of SiPc derivatives as ETL materials for PSCs.

The following section is a report on our primary study of using a SiPc derivative as an ETL layers in perovskite based PVs.

5.4. Experimental

ITO coated glass substrates (Xin Yan Tech.) were etched using hydrochloric acid (HCl) and zinc powder to remove the ITO over one third of the sample surface and pattern the two poles of the device. Substrates were then cleaned by subsequent ultrasonic baths of 15 min in detergent, deionized water (three times), acetone, and 2-isopropanol. Samples were then transferred into a custom Riber vacuum chamber (base pressure = 5.10^{-6} mbar) where Cr (8 nm) and Au (80 nm) contacts were deposited by physical vapor deposition (PVD). The patterned and contacted ITO samples were cleaned once more in ultrasonic baths of acetone and isopropanol followed by a UV-ozone treatment for 15 minutes. A PEDOT:PSS (AI 4083, Ossila) hole transport layer (approximately 50 nm thick) was then spin-coated at 4500 rpm for 40 s and annealed at 120 °C for 20 min. Before annealing of PEDOT:PSS, Cr/Au contacts were cleaned using a cotton tip dipped in deionized water. PbI_2 (>99.99%, Alfa Aesar) and CH_3NH_3I (Solaronix) were dissolved with a 1:1 molar ratio and a concentration of 1.23 mol/L in a cosolvent system 8:2 v/v of GBL (< 99%, Sigma Aldrich) and DMSO (99.9%, Sigma Aldrich). The solution was stirred for 1 h at 70 °C under nitrogen atmosphere before deposition. The perovskite solution was filtered using a 0.45 µm PVDF filter and spincoated on PEDOT:PSS at 2500 rpm for 30 s. An anti-solvent treatment was performed by dropping 0.5 mL of toluene (99.8%, Sigma Aldrich) 5 seconds before the end of the spinning. Samples were then annealed for 1 min at 70 °C and 5 min at 100 °C in N_2 conditions. Cr/Au contacts were cleaned again using a cotton tip dipped in DMF (99.8%, Sigma Aldrich) right after annealing while the substrate was still hot to prevent any DMF diffusion and film destruction. Different electron transport layers were used. For device baselines, $PC_{61}BM$ (99%, Ossila) was dissolved in CB (99.8%, Sigma Aldrich) with a concentration of 40 mg/mL and stirred under nitrogen atmosphere for 1 h. $PC_{61}BM$ was filtered using a 0.45 µm PVDF filter and spincoated on top of the perovskite layer at 2000 rpm for 30 s. The samples were annealed 3 min at 90 °C. Cr/Au contacts were cleaned using a cotton tip dipped in CB. F_{10}-SiPc was previously synthetized in our lab according to literature.[106] It was thermally evaporated (40 nm) in a custom 8-sources Meca2000 (Vinci Technologies) vacuum chamber (base pressure = 5.10^{-7} mbar). The solar stack was completed by the deposition via PVD of a silver top electrode through a shadow mask defining a 0.28 cm² cell. Each sample was comprising of one cell only. **Figure 5.6** illustrates the structure of a cell along with a picture of an actual final cell fabricated in the LPICM lab.

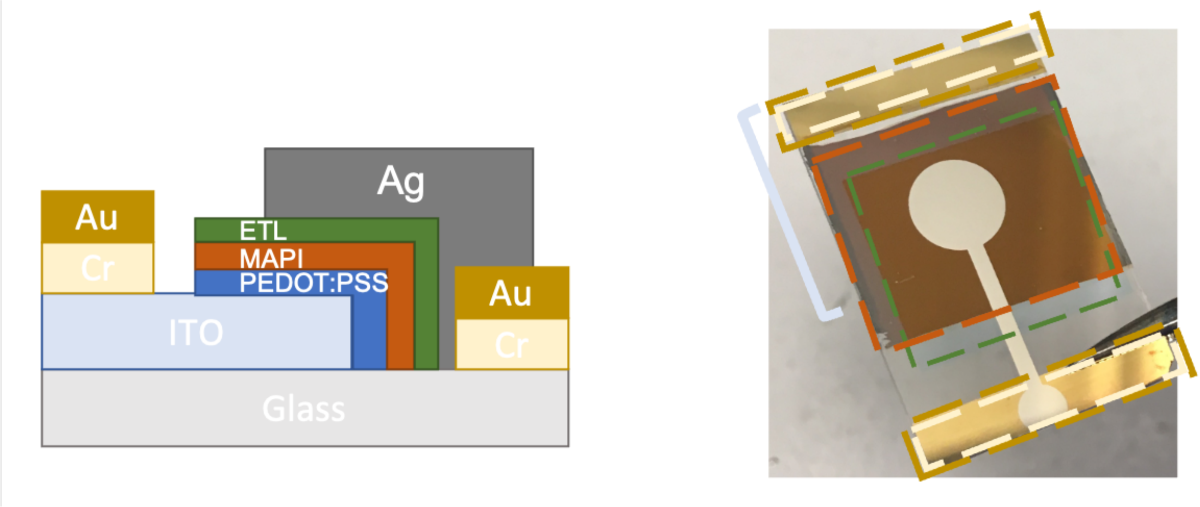

Figure 5.6. Schematic structure of the inverted planar configuration PSC device fabricated at the host laboratory (side view) and picture of a real cell.

The J-V characteristics of perovskite-based devices were measured under nitrogen atmosphere using a source meter Keithley 2635 under illumination conditions. An AM1.5 Solar Constant 575 PV simulator (Steuernagel Lichttecknik, equipped with a metal halogen lamp) with 1000 W/cm^2 was used as the light source. External quantum efficiency (EQE) was measured using a QUESA-1200 (TFSC Instrument). Thicknesses were assessed using a Brucker Dektak XT Profilometer (Billerica, MA, USA).

5.5. Results and Discussion

F_{10}-SiPc has been characterized to have very good electron transport properties with electron field-effect mobilities up to 0.54 cm^2.V^{-1}.s^{-1}, which was the motivation for its use as an ETL.[107] A $PC_{61}BM$ ETL was used as a reference as it has been widely studied in literature, and was the reference ETL used by LPICM researchers. Preliminary devices were fabricated using F_{10}-SiPc as an ETL compared to the references using $PC_{61}BM$ as an ETL. Current density-voltage (J-V) curves for these devices under 1 sun illumination are shown in **Figure 5.7** and corresponding parameters are summarized in **Table 5.1** with a corresponding color system. Measurements were carried both in the forward (from negative to positive voltage bias [-0.2; +1.2 V]) and the reverse (from positive to negative voltage bias [+1.2; -0.2 V]) direction to assess the hysteresis behavior of the devices.

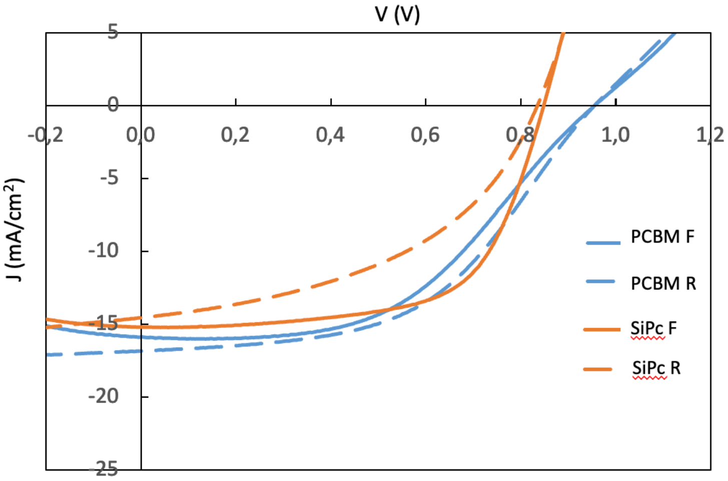

Figure 5.7. Current vs. voltage (J-V) curves of $PC_{61}BM$ ETL-based devices and F_{10}-SiPc ETL-based devices. Full lines represent measurements in the forward scan direction (F) while doted lines represent measurements in the reverse scan direction (R).

Table 5.1. J-V characteristics for PSC integrating either $PC_{61}BM$ or F_{10}-SiPc as the ETL.

ETL	Run number	Number of cells working	Scan direction	*Jsc* (mA/cm^2)	*Voc* (V)	*FF*	*PCE* (%)	Max *PCE* (%)
$PC_{61}BM$	1	2	Forward	15.9 ± 3.7	0.95 ± 0.02	0.50 ± 0.03	7.5 ± 1.4	8.5
			Reverse	16.9 ± 1.6	0.95 ± 0.02	0.51 ± 0.06	8.1 ± 0.01	8.1
F_{10}-SiPc	1	4	Forward	15.2 ± 1.3	0.85 ± 0.03	0.65 ± 0.06	8.4 ± 1.3	9.9
			Reverse	14.5 ± 2.2	0.83 ± 0.04	0.46 ± 0.06	5.7 ± 1.7	7.3

When examining the device performances it is obvious there is significant performance variation between forward and backwards as well as from device to device. Standard deviations for PCE values are above 1% for both ETLs. This lack of device consistency is likely a result of the toluene anti-solvent dropping step during the fabrication process of cells. This antistep step is crucial and highly user-dependent: the height and speed at which the user dispenses the toluene will largely impact the perovskite crystallization and morphology. This challenge is well known among researchers developing perovskite based solar technologies.

For both $PC_{61}BM$ and F_{10}-SiPc ETL, performances obtained with forward scans differ from the performances obtained with reverse scans. For $PC_{61}BM$-based devices, the *PCE*s in the forward and reverse direction are 7.5% and 8.1% respectively, with a *Jsc* of 15.9 mA.cm^{-2} and 16.9 mA.cm^{-2}, a *Voc* of 0.95 V and 0.95 V, and a *FF* of 0.50 and 0.51. For F_{10}-SiPc-based devices, the *PCE*s in the forward and reverse direction are 8.4% and 5.7% respectively, with a *Jsc* of 15.2 mA.cm^{-2} and 14.5 mA.cm^{-2}, a *Voc* of 0.85 V and 0.83 V, and a *FF* of 0.65 and 0.46. Interestingly, best performances for $PC_{61}BM$-based devices are achieved in the reverse direction, while inversely for F_{10}-SiPc-based devices best performances are systematically achieved in the forward direction. Hysteresis behavior in PSCs is widely known to be a recuring issue, and several hypotheses on its source have been reported.[108] Different studies reveal that it can arises from ion migration phenomenon, trapping/detrapping of charge carriers, unbalanced charge carrier transportation, or a ferroelectric effect.

$PC_{61}BM$-based devices have curves exhibiting a so-called "S-shape" both in forward and reverse directions (**Figure 5.7**). S-shaped J-V curves have been frequently reported for PSCs, and again, several reasons for its origins have been proposed depending on the system studied.[109] For inverted MAPI/$PC_{61}BM$ systems, S-shapes have sometime been observed due to the offset in energy between the $PC_{61}BM$ ETL and the Ag electrode causing non-favorable electron transport and was solved by insertion of an interlayer or doping of the $PC_{61}BM$

layer.[110],[111],[112] The observation of S-shapes has also been linked to the morphology and surface of the MAPI film itself in some cases. It was shown that non-favorable MAPI crystallinity induced poor surface properties and could lead to a poor coverage of the $PC_{61}BM$ film forming electrical barriers at the MAPI/$PC_{61}BM$ interface.[113] More importantly, a report highlighted the drastic dependance of the MAPI film surface morphology, wettability and crystallinity on the dropping time of the antisolvent.[114] Thus, a 2-second delay in toluene dropping during spin coating resulted in a significant impact on devices performances. For example, for dropping times of 9, 7, or 5 s before the end of the spin coating, very poor *PCE*s of 1.3%, 5.5% and 6.6% respectively with S-shaped J-V curves were observed. For a dropping time of 3 s, the *PCE* impressively increased to 12.3%, before decreasing back to 6.8% for a dropping time of 1 s before the end of the spin. Therefore we assume the resulting S-shapes obtained here are most likely due to poor MAPI morphology and poor interfaces due to the poor control over the antisolvent deposition time. In comparison, when looking at the F_{10}-SiPc related J-V curves shown in **Figure 5.7**, even though *Jsc* and *Voc* values are lower, no S-shapes are observed independently of the scan direction. The J-V curve in the forward direction (full lines) exhibit a good square shape in coherence with the great *FF* value and, thus, the comparable or better performances up to 9.9% obtained for F_{10}-SiPc devices compared to $PC_{61}BM$ devices. The hypothesis for the absence of S-shapes in this case is that the deposition through thermal evaporation of the SiPc ETL enables a better coverage of the MAPI film, improving the MAPI/ETL interface and therefore the *FF*.

Finally, according to these initial results, it appears that F_{10}-SiPc could be a promising alternative to fullerenes as an ETL in PSCs devices. Comparing results from our study to others in the literature is challenging due to missing information and inconsistencies in reporting. Furthermore, knowing how finicky and time sensitive the process can be, it is hard to replicate other researchers work, making the process operator dependent.

5.6. Conclusion

We performed a primary study looking at a SiPc derivative, F_{10}-SiPc, as a thermally evaporated ETL for PSCs devices. A fullerene derivative, $PC_{61}BM$, was used as the reference ETL as comparison. We found that the fabrication of perovskite devices was a highly finicky process that was highly user-dependent, which needed an extended user experience in order to get good performing and reproducible devices. Compared to $PC_{61}BM$, SiPc derivatives seem to perform similarly but to promote better interfaces with the MAPI film and therefore to provide J-V curves without S-shapes. These preliminary results suggest that F_{10}-SiPc and likely other SiPcs are promising candidates for low cost ETL in perovskite based solar cells.

5.7. References

1. De Angelis, F. Celebrating 10 years of perovskite photovoltaics. *ACS Energy Lett.* **4**, 853–854 (2019).
2. Kojima, A., Teshima, K., Shirai, Y. & Miyasaka, T. Organometal halide perovskites as visible-light sensitizers for photovoltaic cells. *J. Am. Chem. Soc.* **131**, 6050–6051 (2009).
3. Kim, H. S. *et al.* Lead iodide perovskite sensitized all-solid-state submicron thin film mesoscopic solar cell with efficiency exceeding 9%. *Sci. Rep.* **2**, (2012).
4. Yang, W. S. *et al.* High-performance photovoltaic perovskite layers fabricated through intramolecular exchange. *Science (80-.).* **348**, 1234–1237 (2015).
5. Jeong, J. *et al.* Pseudo-halide anion engineering for α-FAPbI3 perovskite solar cells. *Nature* **592**, 381–385 (2021).
6. Nestola, F. *et al.* CaSiO3 perovskite in diamond indicates the recycling of oceanic crust into the lower mantle. *Nature* **555**, 237–241 (2018).
7. Huang, H., Liu, Q., Lu, B., Wang, X. & Hu, J. LaMnO3-diamond composites as efficient oxygen reduction reaction catalyst for Zn-air battery. *Diam. Relat. Mater.* **91**, 199–206 (2019).
8. Wang, Q. & Ma, L. NO oxidative activity of mesoporous LaMnO3 and LaCoO3 perovskite nanoparticles by facile molten-salt synthesis. *New J. Chem.* **43**, 2974–2980 (2019).
9. Hao, F., Stoumpos, C. C., Cao, D. H., Chang, R. P. H. & Kanatzidis, M. G. Lead-free solid-state organic-inorganic halide perovskite solar cells. *Nat. Photonics* **8**, 489–494 (2014).
10. Park, B. W. *et al.* Bismuth Based Hybrid Perovskites A3Bi2I9 (A: Methylammonium or Cesium) for Solar Cell Application. *Adv. Mater.* **27**, 6806–6813 (2015).
11. Stoumpos, C. C. *et al.* Hybrid germanium iodide perovskite semiconductors: Active lone pairs, structural distortions, direct and indirect energy gaps, and strong nonlinear optical properties. *J. Am. Chem. Soc.* **137**, 6804–6819 (2015).
12. Lee, S., Ha, T. J. & Kang, D. W. Mixed-halide Pb-Sn binary perovskite films with various Sn-content for Pb-reduced solar cells. *Mater. Lett.* **227**, 311–314 (2018).
13. Ito, N. *et al.* Mixed Sn-Ge Perovskite for Enhanced Perovskite Solar Cell Performance in Air. *J. Phys. Chem. Lett.* **9**, 1682–1688 (2018).
14. Nyayban, A., Panda, S., Chowdhury, A. & Sharma, B. I. First principle studies of rubidium lead halides towards photovoltaic application. *Mater. Today Commun.* **24**, 101190 (2020).
15. Li, C. *et al.* Emerging alkali metal ion (Li+, Na+, K+ and Rb+) doped perovskite films for efficient solar cells: Recent advances and prospects. *J. Mater. Chem. A* **7**, 24150–24163 (2019).
16. Noh, J. H., Im, S. H., Heo, J. H., Mandal, T. N. & Seok, S. Il. Chemical management for colorful, efficient, and stable inorganic-organic hybrid nanostructured solar cells. *Nano Lett.* **13**, 1764–1769 (2013).
17. Yin, W. J., Yang, J.-H., Kang, J., Yan, Y. & Wei, S.-H. Halide perovskite materials for solar cells: A theoretical review. *J. Mater. Chem. A* **3**, 8926–8942 (2015).
18. Dong, H. *et al.* Pseudohalide-Induced Recrystallization Engineering for CH3NH3PbI3 Film and Its Application in Highly Efficient Inverted Planar Heterojunction Perovskite Solar Cells. *Adv. Funct. Mater.* **28**, 1704836 (2018).
19. Zhou, Z. *et al.* Methylamine-Gas-Induced Defect-Healing Behavior of CH3NH3PbI3 Thin Films for Perovskite Solar Cells. *Angew. Chemie* **127**, 9841–9845 (2015).
20. Najafi, L. *et al.* MoS2 Quantum Dot/Graphene Hybrids for Advanced Interface Engineering of a CH3NH3PbI3 Perovskite Solar Cell with an Efficiency of over 20%. *ACS Nano* **12**, 10736–10754 (2018).

21. Qaid, S. M. H. *et al.* Band-gap tuning of lead halide perovskite using a single step spin-coating deposition process. *Mater. Lett.* **164**, 498–501 (2016).
22. Valverde-Chávez, D. A. *et al.* Intrinsic femtosecond charge generation dynamics in single crystal CH3NH3PbI3. *Energy Environ. Sci.* **8**, 3700–3707 (2015).
23. Chen, T. *et al.* Origin of long lifetime of band-edge charge carriers in organic–inorganic lead iodide perovskites. *Proc. Natl. Acad. Sci. U. S. A.* **114**, 7519–7524 (2017).
24. Stranks, S. D. *et al.* Electron-Hole Diffusion Lengths Exceeding 1 Micrometer in an Organometal Trihalide Perovskite Absorber. *Science (80-.).* **342**, 341–344 (2013).
25. Miyata, A. *et al.* Direct measurement of the exciton binding energy and effective masses for charge carriers in organic-inorganic tri-halide perovskites. *Nat. Phys.* **11**, 582–587 (2015).
26. Meng, L., You, J. & Yang, Y. Addressing the stability issue of perovskite solar cells for commercial applications. *Nat. Commun.* **9**, (2018).
27. Asghar, M. I., Zhang, J., Wang, H. & Lund, P. D. Device stability of perovskite solar cells – A review. *Renew. Sustain. Energy Rev.* **77**, 131–146 (2017).
28. Babayigit, A., Ethirajan, A., Muller, M. & Conings, B. Toxicity of organometal halide perovskite solar cells. *Nat. Mater.* **15**, 247–251 (2016).
29. Collavini, S., Völker, S. F. & Delgado, J. L. Understanding the outstanding power conversion efficiency of perovskite-based solar cells. *Ange* **54**, 9757–9759 (2015).
30. Roy, P., Kumar Sinha, N., Tiwari, S. & Khare, A. A review on perovskite solar cells: Evolution of architecture, fabrication techniques, commercialization issues and status. *Sol. Energy* **198**, 665–688 (2020).
31. Eperon, G. E., Burlakov, V. M., Docampo, P., Goriely, A. & Snaith, H. J. Morphological control for high performance, solution-processed planar heterojunction perovskite solar cells. *Adv. Funct. Mater.* **24**, 151–157 (2014).
32. Wang, Q. *et al.* Large fill-factor bilayer iodine perovskite solar cells fabricated by a low-temperature solution-process. *Energy Environ. Sci.* **7**, 2359–2365 (2014).
33. McLeod, J. A., Wu, Z., Sun, B. & Liu, L. The influence of the I/Cl ratio on the performance of CH3NH3PbI3-xClx-based solar cells: Why is CH3NH3I : PbCl2 = 3:1 the 'magic' ratio? *Nanoscale* **8**, 6361–6368 (2016).
34. Cao, X. *et al.* A Review of the Role of Solvents in Formation of High-Quality Solution-Processed Perovskite Films. *ACS Appl. Mater. Interfaces* **11**, 7639–7654 (2019).
35. Jeon, N. J. *et al.* Solvent engineering for high-performance inorganic-organic hybrid perovskite solar cells. *Nat. Mater.* **13**, 897–903 (2014).
36. Burschka, J. *et al.* Sequential deposition as a route to high-performance perovskite-sensitized solar cells. *Nature* **499**, 316–319 (2013).
37. Chen, Q. *et al.* Planar heterojunction perovskite solar cells via vapor-assisted solution process. *J. Am. Chem. Soc.* **136**, 622–625 (2014).
38. Chen, C.-W. *et al.* Efficient and Uniform Planar-Type Perovskite Solar Cells by Simple Sequential Vacuum Deposition. *Adv. Mater.* **26**, 6647–6652 (2014).
39. Liu, M., Johnston, M. B. & Snaith, H. J. Efficient planar heterojunction perovskite solar cells by vapour deposition. *Nature* **501**, 395–398 (2013).
40. Leyden, M. R. *et al.* High performance perovskite solar cells by hybrid chemical vapor deposition. *J. Mater. Chem. A* **2**, 18742–18745 (2014).
41. Longo, G., Gil-Escrig, L., Degen, M. J., Sessolo, M. & Bolink, H. J. Perovskite solar cells prepared by flash evaporation. *Chem. Commun.* **51**, 7376–7378 (2015).
42. Mallajosyula, A. T. *et al.* Large-area hysteresis-free perovskite solar cells via temperature controlled doctor blading under ambient environment. *Appl. Mater. Today* **3**, 96–102 (2016).
43. Mathies, F. *et al.* Multipass inkjet printed planar methylammonium lead iodide

perovskite solar cells. *J. Mater. Chem. A* **4**, 19207–19213 (2016).
44. Whitaker, J. B. *et al.* Scalable slot-die coating of high performance perovskite solar cells. *Sustain. Energy Fuels* **2**, 2442–2449 (2018).
45. Jiang, Q. *et al.* Surface passivation of perovskite film for efficient solar cells. *Nat. Photonics* **13**, 460–466 (2019).
46. Wu, Z. *et al.* Highly Efficient Perovskite Solar Cells Enabled by Multiple Ligand Passivation. *Adv. Energy Mater.* **10**, 1903696 (2020).
47. Liu, Y. *et al.* Inhibited aggregation of lithium salt in spiro-OMeTAD toward highly efficient perovskite solar cells. *Nano Energy* **70**, 104483 (2020).
48. Kim, G. *et al.* Impact of strain relaxation on performance of α-formamidinium lead iodide perovskite solar cells. *Science (80-.).* **370**, 108–112 (2020).
49. Ren, G. *et al.* Strategies of modifying spiro-OMeTAD materials for perovskite solar cells: a review. *J. Mater. Chem. A* **9**, 4589–4625 (2021).
50. Jiang, K. *et al.* Inverted planar perovskite solar cells based on CsI-doped PEDOT:PSS with efficiency beyond 20% and small energy loss. *J. Mater. Chem. A* **7**, 21662–21667 (2019).
51. Wang, Q., Chueh, C. C., Eslamian, M. & Jen, A. K. Y. Modulation of PEDOT:PSS pH for efficient inverted perovskite solar cells with reduced potential loss and enhanced stability. *ACS Appl. Mater. Interfaces* **8**, 32068–32076 (2016).
52. Liu, D. *et al.* Improved performance of inverted planar perovskite solar cells with F4-TCNQ doped PEDOT:PSS hole transport layers. *J. Mater. Chem. A* **5**, 5701–5708 (2017).
53. Zhang, X. F., Zhou, X., Zhang, L. & Xu, B. Facile phthalocyanine doping into PEDOT leads to highly efficient and stable inverted metal halide perovskite solar cells. *J. Mater. Chem. A* **6**, 12515–12522 (2018).
54. Xue, Q. *et al.* Efficient and Stable Perovskite Solar Cells via Dual Functionalization of Dopamine Semiquinone Radical with Improved Trap Passivation Capabilities. *Adv. Funct. Mater.* **28**, 1707444 (2018).
55. Han, W. *et al.* Recent Progress of Inverted Perovskite Solar Cells with a Modified PEDOT:PSS Hole Transport Layer. *ACS Appl. Mater. Interfaces* **12**, 49297–49322 (2020).
56. Djurišić, A. B. *et al.* Perovskite solar cells - An overview of critical issues. *Prog. Quantum Electron.* **53**, 1–37 (2017).
57. Zheng, X. *et al.* Managing grains and interfaces via ligand anchoring enables 22.3%-efficiency inverted perovskite solar cells. *Nat. Energy* **5**, 131–140 (2020).
58. Jung, E. H. *et al.* Efficient, stable and scalable perovskite solar cells using poly(3-hexylthiophene). *Nature* **567**, 511–515 (2019).
59. Wan, L. *et al.* Achieving over 21% efficiency in inverted perovskite solar cells by fluorinating a dopant-free hole transporting material. *J. Mater. Chem. A* **8**, 6517–6523 (2020).
60. Kim, Y. C. *et al.* Engineering interface structures between lead halide perovskite and copper phthalocyanine for efficient and stable perovskite solar cells. *Energy Environ. Sci.* **10**, 2109–2116 (2017).
61. Cao, J. *et al.* Plant Sunscreen and Co(II)/(III) Porphyrins for UV-Resistant and Thermally Stable Perovskite Solar Cells: From Natural to Artificial. *Adv. Mater.* **30**, 1800568 (2018).
62. Liu, C. *et al.* Highly Stable and Efficient Perovskite Solar Cells with 22.0% Efficiency Based on Inorganic–Organic Dopant-Free Double Hole Transporting Layers. *Adv. Funct. Mater.* **30**, 1908462 (2020).
63. Liu, C. *et al.* Hydrophobic Cu2O Quantum Dots Enabled by Surfactant Modification as

Top Hole-Transport Materials for Efficient Perovskite Solar Cells. *Adv. Sci.* **6**, 1801169 (2019).

64. Wang, K. *et al.* Isothermally crystallized perovskites at room-temperature. *Energy Environ. Sci.* **13**, 3412–3422 (2020).
65. Min, H. *et al.* Efficient, stable solar cells by using inherent bandgap of α-phase formamidinium lead iodide. *Science (80-.).* **366**, 749–753 (2019).
66. Kim, M. *et al.* Methylammonium Chloride Induces Intermediate Phase Stabilization for Efficient Perovskite Solar Cells. *Joule* **3**, 2179–2192 (2019).
67. Lin, L. *et al.* Inorganic Electron Transport Materials in Perovskite Solar Cells. *Adv. Funct. Mater.* **31**, 2008300 (2021).
68. Valadi, K. *et al.* Metal oxide electron transport materials for perovskite solar cells: a review. *Environ. Chem. Lett.* **19**, 2185–2207 (2021).
69. Zhang, J., Juárez-Pérez, E. J., Mora-Seró, I., Viana, B. & Pauporté, T. Fast and low temperature growth of electron transport layers for efficient perovskite solar cells. *J. Mater. Chem. A* **3**, 4909–4915 (2015).
70. Zheng, D. *et al.* Combustion Synthesized Zinc Oxide Electron-Transport Layers for Efficient and Stable Perovskite Solar Cells. *Adv. Funct. Mater.* **29**, 1900265 (2019).
71. Liu, D. & Kelly, T. L. Perovskite solar cells with a planar heterojunction structure prepared using room-temperature solution processing techniques. *Nat. Photonics* **8**, 133–138 (2014).
72. Yang, J., Siempelkamp, B. D., Mosconi, E., De Angelis, F. & Kelly, T. L. Origin of the Thermal Instability in CH3NH3PbI3 Thin Films Deposited on ZnO. *Chem. Mater.* **27**, 4229–4236 (2015).
73. Schutt, K. *et al.* Overcoming Zinc Oxide Interface Instability with a Methylammonium-Free Perovskite for High-Performance Solar Cells. *Adv. Funct. Mater.* **29**, 1900466 (2019).
74. Jiang, Q. *et al.* Enhanced electron extraction using SnO2 for high-efficiency planar-structure HC(NH2)2 PbI3-based perovskite solar cells. *Nat. Energy* **2**, 16177 (2016).
75. Anaraki, E. H. *et al.* Highly efficient and stable planar perovskite solar cells by solution-processed tin oxide. *Energy Environ. Sci.* **9**, 3128–3134 (2016).
76. Chen, Y. *et al.* SnO2-based electron transporting layer materials for perovskite solar cells: A review of recent progress. *J. Energy Chem.* **35**, 144–167 (2019).
77. Cheng, M. *et al.* Charge-transport layer engineering in perovskite solar cells. *Sci. Bull.* **65**, 1237–1241 (2020).
78. Dunlap-Shohl, W. A., Younts, R., Gautam, B., Gundogdu, K. & Mitzi, D. B. Effects of Cd diffusion and doping in high-performance perovskite solar cells using CdS as electron transport layer. *J. Phys. Chem. C* **120**, 16437–16445 (2016).
79. Dou, J., Shen, D., Li, Y., Abate, A. & Wei, M. Highly Efficient Perovskite Solar Cells Based on a Zn2SnO4 Compact Layer. *ACS Appl. Mater. Interfaces* **11**, 36553–36559 (2019).
80. Qin, M. *et al.* Perovskite Solar Cells Based on Low-Temperature Processed Indium Oxide Electron Selective Layers. *ACS Appl. Mater. Interfaces* **8**, 8460–8466 (2016).
81. Mahmood, K., Swain, B. S., Kirmani, A. R. & Amassian, A. Highly efficient perovskite solar cells based on a nanostructured WO3-TiO2 core-shell electron transporting material. *J. Mater. Chem. A* **3**, 9051–9057 (2015).
82. Rajagopal, A., Yao, K. & Jen, A. K. Y. Toward Perovskite Solar Cell Commercialization: A Perspective and Research Roadmap Based on Interfacial Engineering. *Adv. Mater.* **30**, 1800455 (2018).
83. Liang, P. W., Chueh, C. C., Williams, S. T. & Jen, A. K. Y. Roles of fullerene-based interlayers in enhancing the performance of organometal perovskite thin-film solar cells.

Adv. Energy Mater. **5**, 1402321 (2015).

84. Zhou, L. *et al.* Enhanced planar perovskite solar cell efficiency and stability using a perovskite/PCBM heterojunction formed in one step. *Nanoscale* **10**, 3053–3059 (2018).
85. Shao, Y., Yuan, Y. & Huang, J. Correlation of energy disorder and open-circuit voltage in hybrid perovskite solar cells. *Nat. Energy* **1**, 15001 (2016).
86. Wang, Z. *et al.* Efficient and Air-Stable Mixed-Cation Lead Mixed-Halide Perovskite Solar Cells with n-Doped Organic Electron Extraction Layers. *Adv. Mater.* **29**, 1604186 (2017).
87. Yoon, H., Kang, S. M., Lee, J. K. & Choi, M. Hysteresis-free low-temperature-processed planar perovskite solar cells with 19.1% efficiency. *Energy Environ. Sci.* **9**, 2262–2266 (2016).
88. Said, A. A., Xie, J. & Zhang, Q. Recent Progress in Organic Electron Transport Materials in Inverted Perovskite Solar Cells. *Small* **15**, 1900854 (2019).
89. Wang, D., Ye, T. & Zhang, Y. Recent advances of non-fullerene organic electron transport materials in perovskite solar cells. *J. Mater. Chem. A* **8**, 20819–20848 (2020).
90. Yan, C. *et al.* Non-fullerene acceptors for organic solar cells. *Nat. Rev. Mater.* **3**, 1–19 (2018).
91. Nowak-Król, A., Shoyama, K., Stolte, M. & Würthner, F. Naphthalene and perylene diimides - better alternatives to fullerenes for organic electronics? *Chem. Commun.* **54**, 13763–13772 (2018).
92. Karuppuswamy, P. *et al.* Solution-processable electron transport layer for efficient hybrid perovskite solar cells beyond fullerenes. *Sol. Energy Mater. Sol. Cells* **169**, 78–85 (2017).
93. Wu, J. L. *et al.* Simple mono-halogenated perylene diimides as non-fullerene electron transporting materials in inverted perovskite solar cells with ZnO nanoparticle cathode buffer layers. *J. Mater. Chem. A* **5**, 12811–12821 (2017).
94. Yang, L. *et al.* Restrained light-soaking and reduced hysteresis in perovskite solar cells employing a helical perylene diimide interfacial layer. *J. Mater. Chem. A* **6**, 10379–10387 (2018).
95. Wang, H. *et al.* Achieving efficient inverted perovskite solar cells with excellent electron transport and stability by employing a ladder-conjugated perylene diimide dimer. *J. Mater. Chem. A* **7**, 24191–24198 (2019).
96. Jung, S. K. *et al.* Homochiral Asymmetric-Shaped Electron-Transporting Materials for Efficient Non-Fullerene Perovskite Solar Cells. *ChemSusChem* **12**, 224–230 (2019).
97. Shao, J. *et al.* Acenaphthylene-imide based small molecules/TiO 2 bilayer as electron-transporting layer for solution-processing efficient perovskite solar cells. *Sci. China Mater.* **62**, 497–507 (2019).
98. Liu, W. *et al.* Molecular Aggregation of Naphthalene Diimide(NDI) Derivatives in Electron Transport Layers of Inverted Perovskite Solar Cells and Their Influence on the Device Performance. *Chem. - An Asian J.* **15**, 112–121 (2020).
99. Zhao, D., Zhu, Z., Kuo, M. Y., Chueh, C. C. & Jen, A. K. Y. Hexaazatrinaphthylene Derivatives: Efficient Electron-Transporting Materials with Tunable Energy Levels for Inverted Perovskite Solar Cells. *Angew. Chemie - Int. Ed.* **55**, 8999–9003 (2016).
100. Wang, N. *et al.* Improving Interfacial Charge Recombination in Planar Heterojunction Perovskite Photovoltaics with Small Molecule as Electron Transport Layer. *Adv. Energy Mater.* **7**, 1700522 (2017).
101. Liu, X. *et al.* Energy level-modulated non-fullerene small molecule acceptors for improved V OC and efficiency of inverted perovskite solar cells. *J. Mater. Chem. A* **7**, 3336–3343 (2019).
102. Wu, F. *et al.* Efficient small-molecule non-fullerene electron transporting materials for

high-performance inverted perovskite solar cells. *J. Mater. Chem. A* **6**, 4443–4448 (2018).

103. Urbani, M., De La Torre, G., Nazeeruddin, M. K. & Torres, T. Phthalocyanines and porphyrinoid analogues as hole-and electron-transporting materials for perovskite solar cells. *Chem. Soc. Rev.* **48**, 2738–2766 (2019).
104. Jin, F. *et al.* Hexadecafluorophthalocyaninatocopper as an electron conductor for high-efficiency fullerene-free planar perovskite solar cells. *Sol. Energy Mater. Sol. Cells* **157**, 510–516 (2016).
105. Xie, C. *et al.* Silicon phthalocyanine passivation for fullerene-free perovskite solar cells with efficient electron extraction. *Appl. Phys. Express* **12**, 064006 (2019).
106. Lessard, B. H. *et al.* The position and frequency of fluorine atoms changes the electron donor/acceptor properties of fluorophenoxy silicon phthalocyanines within organic photovoltaic devices. *J. Mater. Chem. A* **3**, 24512–24524 (2015).
107. Melville, O. A. *et al.* Ambipolarity and Air Stability of Silicon Phthalocyanine Organic Thin-Film Transistors. *Adv. Electron. Mater.* **5**, 1900087 (2019).
108. Singh, R. & Parashar, M. Origin of Hysteresis in Perovskite Solar Cells. in *Soft-Matter Thin Film Solar Cells: Physical Processes and Device Simulation* (AIP Publishing LLC, 2020).
109. Saive, R. S-Shaped Current-Voltage Characteristics in Solar Cells: A Review. *IEEE J. Photovoltaics* **9**, 1477–1484 (2019).
110. Lin, Z. *et al.* Interface studies of the planar heterojunction perovskite solar cells. *Sol. Energy Mater. Sol. Cells* **157**, 783–790 (2016).
111. Ge, R., Qin, F., Hu, L., Xiong, S. & Zhou, Y. High fill factor over 82% enabled by a biguanide doping electron transporting layer in planar perovskite solar cells. *Front. Optoelectron.* **11**, 360–366 (2018).
112. Hu, L. *et al.* An Amidine-Type n-Dopant for Solution-Processed Field-Effect Transistors and Perovskite Solar Cells. *Adv. Funct. Mater.* **27**, 1703254 (2017).
113. Chiang, S. E. *et al.* Origins of the s-shape characteristic in J-V curve of inverted-type perovskite solar cells. *Nanotechnology* **31**, 115403 (2020).
114. Chang, S. H. *et al.* Effects of the washing-enhanced nucleation process on the material properties and performance of perovskite solar cells. *J. Alloys Compd.* **808**, 151723 (2019).

Chapter 6: Conclusions and Recommendations for Future Work

6.1. Overall Conclusions

As the interest in OPV technologies increases, the development of novel low-cost, simple, and efficient active materials along with more scalable fabrication processes remain critical challenges. Silicon phthalocyanine derivatives are promising, inexpensive acceptor candidates which are easy to synthesize following a 2-step route while providing tunable chemical handles for the optimization of molecular properties and corresponding thin films. This thesis assessed the role of SiPcs as NFAs in LbL OPV devices, providing improved path towards scalable materials and processes for the development of high performance OPVs.

The evolution from the common blended BHJ structure to a LbL bilayer configuration starts with a review in **Chapter 2**. This review focuses on the organic semiconducting materials and the principal fabrication routes (all-solution, hybrid solution-vacuum and blade coating) used for the fabrication of bilayer LbL OPV devices where the donor and acceptor materials are sequentially deposited. Emphasis was placed on the advances in material structure and thin film morphology that led to significant *PCE* improvements, as well as on device engineering and thin film processing through systematic report of recurring processing conditions. Advantages of the LbL technique over the BHJ were summarized: increased control over active layer structure through the ability to independently optimize and characterize each sequential layer ; the ability to reach optimal morphology by inducing a favourable vertical gradient concentration enabling balance between dissociation and transportation of free charges generated; improved device reproducibility; increased thermal, mechanical and optical stability of resulting devices; comparable or greater *PCE*s depending on choice of donor/acceptor system; and increased *PCE* retention when transitioning from lab-scale to large-scale devices. Therefore, this review lays out the foundation for the justification of the continued exploration of the LbL technique over the BHJ technique.

In **Chapter 3**, a series of direct LbL OPV devices were fabricated using a hybrid solution-vacuum process. Two thermally deposited SiPc derivatives, $(246F)_2$-SiPc and $(345F)_2$-SiPc, were investigated as acceptor materials, on top of different spin coated donor polymers, P3HT and PCDTBT. Device engineering was undertaken and impact of the processing conditions on devices performances was assessed. While the spin rate of the donor had only a little effect, thickness of the acceptor revealed to be critical. Different thermal treatments were applied to the PCDTBT/(345F)$_2$-SiPc system and annealing of the bilayer at 150°C for 30min appeared to induce a 50% increase in *FF*, with a *PCE* of 1.52 ± 0.06%.

In **Chapter 4**, a series of direct LbL OPV devices were fabricated through spin coating using an all-solution process. (3BS)$_2$-SiPc was selected as the solution processable NFA and paired with two donor polymers, P3HT and PBDB-T. Device engineering included investigation of different hole transporting layers, solvent systems, spin rates, deposition kinetics and thermal treatments. The use of VOx instead of PEDOT:PSS as the HTL induced a favorable P3HT film morphology and resulted in increased *FF* and *Voc* values. For P3HT/(3BS)$_2$-SiPc devices *PCE*s up to 3.0% were achieved, and for PBDB-T/(3BS)$_2$-SiPc devices *PCE*s up to 3.3% were achieved with an impressive *Voc* up to 1.06 V, which is amongst the highest obtained for both PBDB-T-based and LbL OPV devices. In comparison to their BHJ counterparts, LbL devices performed similarly, with comparable EQE responses, absorption spectra, and vertical film composition.

In **Chapter 5** a thermally evaporated SiPc derivative, F$_{10}$-SiPc, was used as ETL in perovskite solar cells to extend the potential of SiPcs to other solar technologies. Primary studies showed that comparatively to the PC$_{61}$BM fullerene reference, SiPc-based PSCs seemed to achieve equivalent efficiencies with no S-shapes and improved interfaces.

Overall, this thesis contains the first reports demonstrating SiPc-based LbL OPV devices fabricated through either a hybrid solution-vacuum processing route or an all-solution processing route, and presents their first use as ETL in perovskite devices. These studies further established the potential of SiPcs as active materials for different solar technologies, and laid the groundwork for better scalable and commercially viable OPV devices.

6.2. Recommendation for Future Work

The main advantages of the LbL technique over BHJ technique arises from the formation of a vertical concentration gradient where the acceptor and donor materials are aggregated at their respective electrode while leaving an intermixed region in the middle of the film. As previously explained, this thin film morphology structure enables the efficient dissociation of the charges while leaving clear paths to the electrodes to avoid recombination. This configuration has often been reported to form with the all-solution LbL sequential deposition of the donor and acceptor materials. Unfortunately, we were not able to obtain this film structure in our studies, thus, future recommendations will involve the further investigation of device engineering in order to find experimental conditions that could lead to this particular type of morphology.

1) Improved vertical separation through device engineering: we could switch from a spin coating method to a blade coating method or other solution processing techniques. The differences in deposition kinetics and drying paths compared to spin coating could help the formation of such a morphology. Investigation of different solvent systems including green solvents, different drying times, deposition rate, thermal treatments should be done. Additionally, the choice of axial groups could be investigated as they dictate the interaction with the polymer film and therefore the penetration depth could be tuned through simple changes such as length of axial groups (**Figure 6.1**).

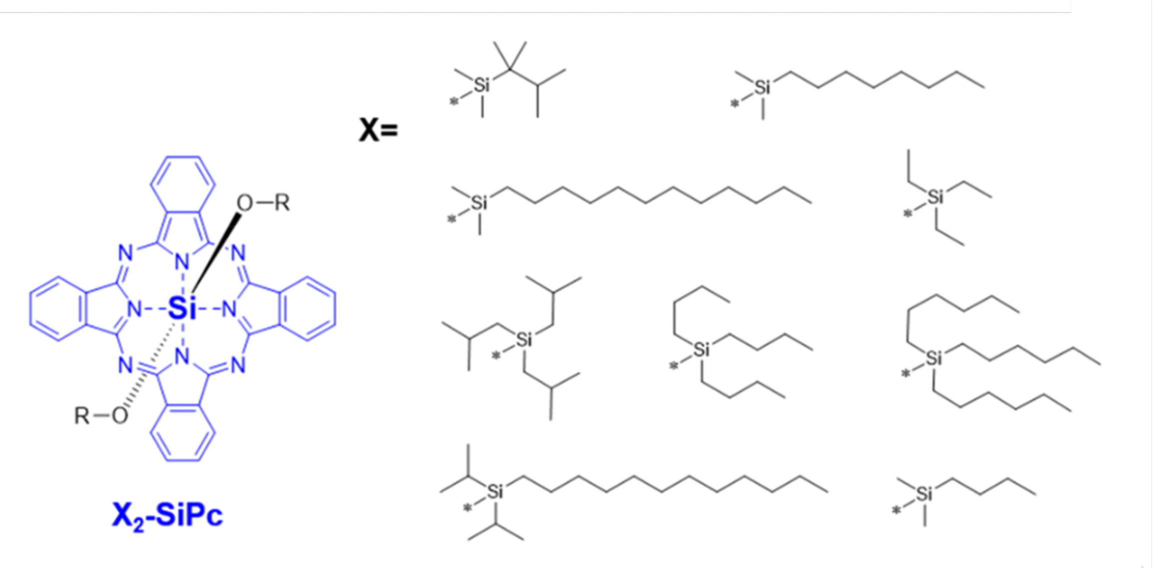

Figure 6.1. Examples of SiPc derivatives with varied axial groups lengths that have been synthetized in the lab[1] and that could be integrated into LbL OPV devices to tune the vertical separation gradient.

2) Improved current extraction through use of corresponding ETL: another way to improve device structure would be to thermally evaporate the same SiPc derivative used in the active layer on top of the LbL deposited active layer with limited vertical separation. For example, the use of an SiPc which can be both solution-processed and evaporated could lead to the same SiPc being blended into the polymer layer (LbL active layer) followed by the evaporation of this exact SiPc on top of the active layer as an ETL layer. This would lead to the SiPc NFA material intermixed with a polymer followed by a solid ETL layer of the same SiPc material with likely no resistance between the two layers (**Figure 6.2**). For example, bis(tri propyl silyl) SiPc ($(3PS)_2$-SiPc) has been shown to be soluble enough for solution processing but can also be sublimed and could be a promising candidates for this engineered structure.[2]

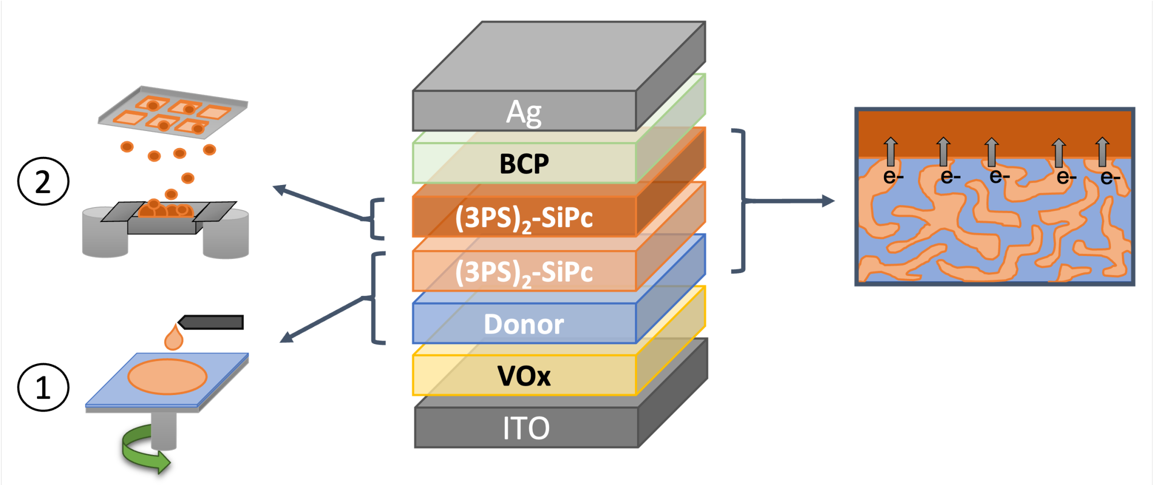

Figure 6.2. Schematic representation of the fabrication route and morphology of an LbL OPV device where the SiPc material is used both as the NFA in the active layer and as an intermediate ETL layer.

3) Improved matching with donor polymers through SiPc derivatives engineering: independently of the active layer morphology, global OPV devices performances could be increased by improved tuning of the SiPcs' HOMO/LUMO levels and band gap using their chemical versatility. The shallow energy levels of the soluble SiPc alkyl derivatives such as $(3BS)_2$-SiPc are not optimal for matching with a large range of top performing donor polymers, impeding the reach of high *PCE*s as well. For example, with donor polymers such as PTQ10 or PM6 whose HOMO are at -5.5 eV and -5.6 eV respectively (**Figure 6.3**),[3] $(3BS)_2$-SiPc's HOMO at -5.3 eV is too high and will not enable the efficient dissociation and extraction of holes. Incorporation of fluoro atoms have shown to help increase the HOMO level, as for $(345F)_2$-SiPc that reaches an HOMO level of -5.9 eV.[4] However, the band gap of $(345F)_2$-SiPc is increased at 1.9 eV, which is again not the best for an optimal solar spectrum coverage when wide band gap top performing donors are used. In order to complement the absorption range of these types of donors, SiPcs absorption needs to be further pushed in the NIR region of the solar spectrum by reduction of the band gap around 1.6 to 1.7 eV. Recently our lab synthetized new fluorinated SiPc derivatives, F_{10}-SiPc and F_2-F_{16}-SiPc, that achieved deeper HOMO/LUMO levels of -5.8 eV/-4.1 eV and -6.5 eV/-4.8 eV respectively (**Figure 6.3**), that would allow dissociation and extraction of charges.[5] Moreover band gaps of 1.7 eV enabled a thin-film UV-Vis absorption peak pushed to around 750 nm. These derivatives represents promising NFAs for OPV devices, however they can only be thermally evaporated. To fabricate all-solution LbL devices, soluble versions should be synthetized.

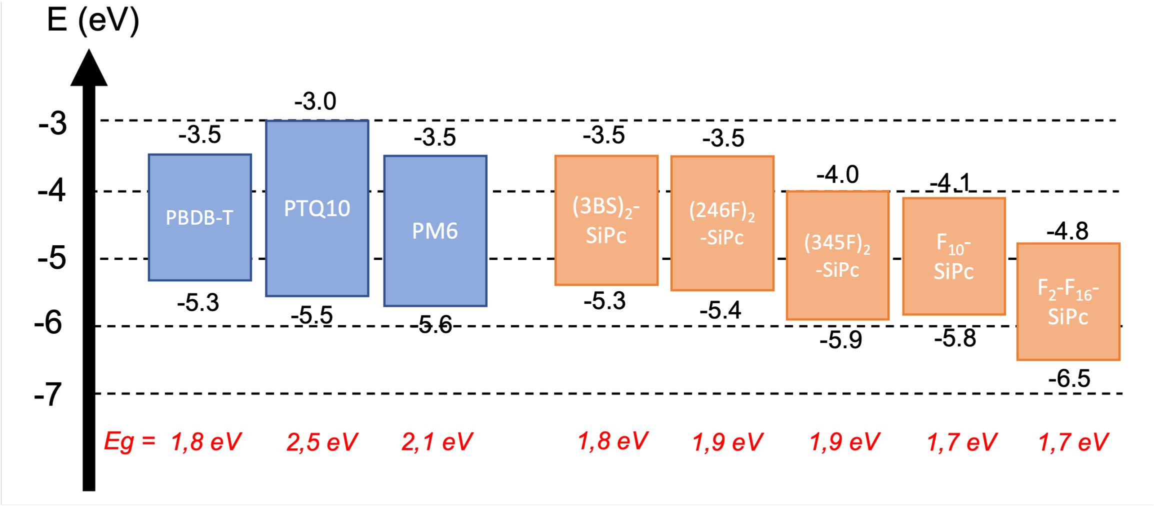

Figure 6.3. Summary of HOMO/LUMO energy levels and band gaps values for materials of interest.

6.3. References

1. Vebber, M. C., Grant, T. M., Brusso, J. L. & Lessard, B. H. Bis(trialkylsilyl oxide) Silicon Phthalocyanines: Understanding the Role of Solubility in Device Performance as Ternary Additives in Organic Photovoltaics. *Langmuir* **36**, 2612–2621 (2020).
2. Lessard, B. H. The Rise of Silicon Phthalocyanine : From Organic Photovoltaics to Organic Thin Film Transistors. *Appl. Mater. Interfaces* **13**, 31321–31330 (2021).
3. Faure, M. D. M. & Lessard, B. H. Layer-by-layer fabrication of organic photovoltaic devices: material selection and processing conditions. *J. Mater. Chem. C* **9**, 14–40 (2021).
4. Faure, M. D. M., Grant, T. M. & Lessard, B. H. Silicon Phthalocyanines as Acceptor Candidates in Mixed Solution/Evaporation Processed Planar Heterojunction Organic Photovoltaic Devices. *Coatings* **9**, 1–13 (2019).
5. Yutronkie, N. J., King, B., Melville, O. A., Lessard, B. H. & Brusso, J. L. Attaining air stability in high performing n-type phthalocyanine based organic semiconductors. *J. Mater. Chem. C* **9**, 10119–10126 (2021).

Appendix A: Supplementary Information for Chapter 3

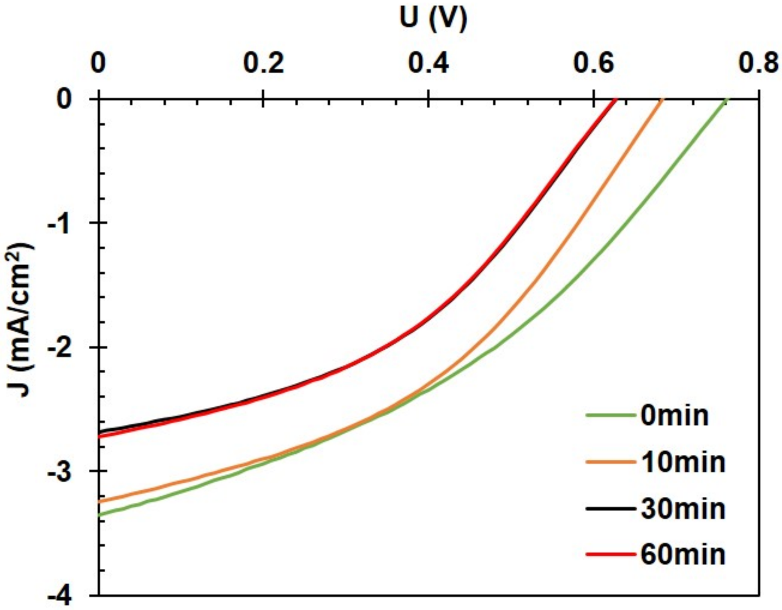

Figure S3.1. Characteristic current vs. voltage (J-V) for PHJ OPV devices where the active layer is PCDTBT/(345F)$_2$-SiPc (50 nm) and where the PCDTBT layer have been annealed at 150 ºC at 0 min, 10 min, 30 min and 60 min.

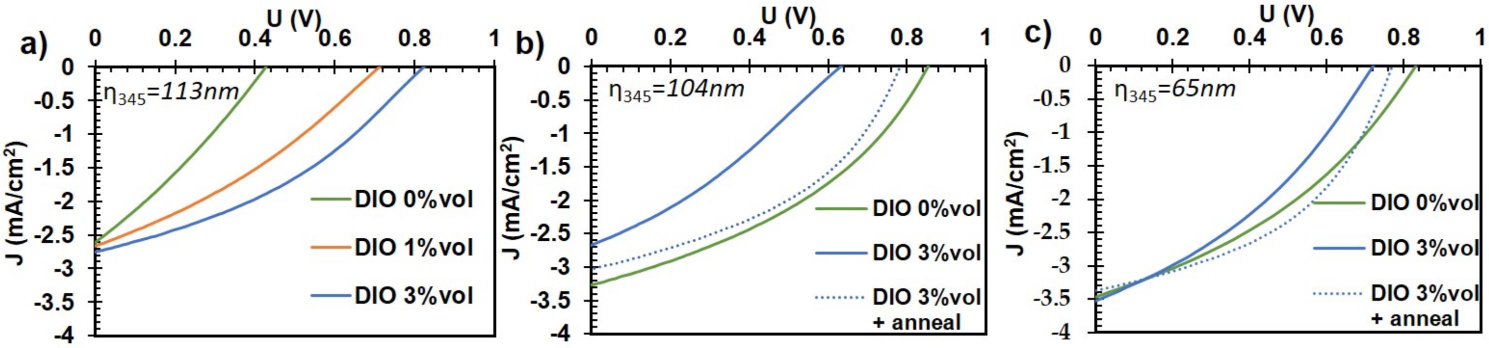

Figure S3.2. Characteristic current vs. voltage (J-V) for PHJ PCDTBT/(345F)$_2$-SiPc devices with a SiPc thickness of **(a)** 113nm with incorporated DIO in the PCDTBT layer at 0, 1 and 3 vol%, **(b)** 104nm and **(c)** 65nm where DIO have been incorporated in the PCDTBT layer at 0, 3 and 3 vol% followed by annealing at 100 ºC for 15min.

Appendix B: Supplementary Information for Chapter 4

Table S4.1: Optimization of experimental processing conditions for ITO/PEDOT:PSS/P3HT/(3BS)$_2$-SiPc/BCP/Ag LbL devices: J-V characteristics (best determined conditions are highlighted in bold and (3BS)$_2$-SiPc is referred to as 3BS). For spinning a / b / c: a is the rate in rpm, b is the dispensing kinetic (S for static, D for dynamic) and c is the volume in µL.

P3HT (15 mg/mL)			**3BS (15 mg/mL)**			**I-V parameters**			
Solvent	**Spinning** a / b / c	**Annealing**	**Solvent**	**Spinning** a / b / c	**Annealing**	V_{oc} (V)	J_{sc} (mA/cm^2)	FF	PCE (%)
DCB	2000 / S / 200	- 10 min 80°C 20 min 80°C 30 min 80°C	DCB	2000 / S / 400	-	NaN	NaN	NaN	NaN
DCB	1000 / S / 200	- 20 min 80°C - 20 min 80°C	DCB	3500 / S / var 3500 / S / var 3500 / D / var 3500 / D / var	-	NaN	NaN	NaN	NaN
CB	1000 / S / 200	- - 20 min 80°C	CB	3500 / S / var 3500 / D / var 3500 / D / var	-	NaN 0.60 ± 0.07 0.61 ± 0.04	NaN 6.0 ± 0.5 6.4 ± 0.4	NaN 0.40 ± 0.07 0.43 ± 0.06	NaN 1.5 ± 0.5 1.7 ± 0.4
CB	1000 / S / 200	20 min 80°C	CB	1000 / D / var 2000 / D / var 2000 / D / var	- - 10 min 150°C	0.52 ± 0.1 0.67 ± 0.06 0.68 ± 0.04	3.5 ± 2.0 5.6 ± 0.9 5.0 ± 0.3	0.33 ± 0.1 0.44 ± 0.08 0.46 ± 0.06	0.6 ± 0.4 1.7 ± 0.5 1.5 ± 0.2
CF	1000 / S / 200 1000 / S / 200 **1000 / D / 150** 1000 / D / 150	- - **-** -	**CB**	3500 / S / 200 3500 / D / var **3500 / D / 40** 3500 / D / var	- - **-** 10 min 100°C	0.48 ± 0.3 0.65 ± 0.02 **0.57 ± 0.03** 0.64 ± 0.03	4.0 ± 2.1 3.8 ± 0.8 **7.4 ± 0.3** 4.5 ± 1.3	0.34 ± 0.1 0.33 ± 0.01 **0.41 ± 0.02** 0.44 ± 0.05	1.0 ± 0.9 0.82 ± 0.2 **1.76 ± 0.19** 1.3 ± 0.5
CB	1000 / S / 200 1000 / S / 200 1000 / S / 200 1000 / D / 200 1000 / D / 200	- - 20 min 80°C - 20 min 80°C	TOL	3500 / S / 150 3500 / D / 150 3500 / D / 150 3500 / D / 150 3500 / D / 150	-	0.77 ± 0.01 0.71 ± 0.04 0.68 ± 0.07 0.67 ± 0.1 0.67 ± 0.05	6.1 ± 0.08 6.5 ± 0.5 5.1 ± 0.3 7.4 ± 0.2 6.7 ± 0.3	0.35 ± 0.01 0.33 ± 0.01 0.33 ± 0.01 0.37 ± 0.03 0.34 ± 0.01	1.7 ± 0.1 1.5 ± 0.2 1.1 ± 0.2 1.8 ± 0.4 1.6 ± 0.2
CF	1000 / S / 150	-	DCM:CB 100:0 60:40 20:80	3500 / D / 40	-	0.69 ± 0.05 0.75 ± 0.04 0.73 ± 0.09	0.46 ± 0.1 2.1 ± 0.2 4.5 ± 0.4	0.52 ± 0.06 0.33 ± 0.01 0.34 ± 0.02	0.17 ± 0.07 0.51 ± 0.04 1.1 ± 0.2
CF	1000 / S / 200 1000 / D / 150	-	CF	3500 / D / 40 3500 / D / 40	-	0.75 ± 0.01 0.64 ± 0.04	2.7 ± 0.3 6.9 ± 0.7	0.32 ± 0 0.39 ± 0.02	0.65 ± 0.07 1.7 ± 0.3

Table S4.2: Optimization of experimental processing conditions for ITO/VOx/P3HT/$(3BS)_2$-SiPc/BCP/Ag LbL devices: J-V characteristic (best determined conditions are highlighted in bold and $(3BS)_2$-SiPc is referred to as 3BS). For spinning a / b / c: a is the rate in rpm, b is the dispensing kinetic (S for static, D for dynamic) and c is the volume in µL.

P3HT (15 mg/mL)			**3BS (15 mg/mL)**			**I-V parameters**			
Solvent	**Spinning** a / b / c	**Annealing**	**Solvent**	**Spinning** a / b / c	**Annealing**	V_{oc} (V)	J_{sc} (mA/cm²)	FF	PCE (%)
CF	1000 / S / 150	-	TOL	3500 / S / 150	-	0.76 ± 0.02	0.51 ± 0.50	0.34 ± 0.01	0.14 ± 0.14
	1000 / S / 150	20 min 80°C		3500 / S / 150		0.78 ± 0.01	1.16 ± 0.41	0.34 ± 0.01	0.31 ± 0.12
	1000 / S / 150	-		3500 / D / 150		0.75 ± 0.02	0.28 ± 0.04	0.30 ± 0.01	0.06 ± 0.01
	1000 / S / 150	20 min 80°C		3500 / D / 150		0.74 ± 0.02	0.21 ± 0.02	0.29 ± 0.00	0.05 ± 0.00
	1000 / D / 150	-		3500 / S / 150		0.77 ± 0.02	4.87 ± 0.30	0.36 ± 0.01	1.34 ± 0.08
	1000 / D / 150	20 min 80°C		3500 / S / 150		0.77 ± 0.01	4.49 ± 0.49	0.36 ± 0.01	1.24 ± 0.14
	1000 / D / 150	-		3500 / D / 150		0.80 ± 0.01	2.92 ± 0.18	0.35 ± 0.01	0.82 ± 0.05
	1000 / D / 150	20 min 80°C		3500 / D / 150		0.79 ± 0.03	2.10 ± 0.33	0.35 ± 0.02	0.58 ± 0.12
CB	1000 / S / 150	-	TOL	3500 / S / 150	-	0.79 ± 0	7.99 ± 0.14	0.41 ± 0.01	2.56 ± 0.10
	1000 / S / 150	20 min 80°C		3500 / S / 150		0.78 ± 0.01	6.02 ± 1.07	0.38 ± 0.01	1.77 ± 0.34
	1000 / S / 150	20 min 80°C		3500 / D / 150		0.78 ± 0.02	5.41 ± 0.49	0.37 ± 0.02	1.59 ± 0.23
	1000 / D / 150	-		3500 / S / 150		0.75 ± 0.04	7.44 ± 0.45	0.40 ± 0.02	2.22 ± 0.18
	1000 / D / 150	20 min 80°C		3500 / S / 150		0.78 ± 0.01	7.63 ± 0.38	0.40 ± 0.01	2.40 ± 0.19
	1000 / D / 150	-		3500 / D / 150		0.79 ± 0.01	6.46 ± 0.47	0.39 ± 0	1.97 ± 0.15
	1000 / D / 150	20 min 80°C		3500 / D / 150		0.79 ± 0	6.57 ± 0.21	0.39 ± 0.01	2.03 ± 0.09
CF	1000 / S / 150	-	**CB**	3500 / S / 150	-	0.76 ± 0.02	6.18 ± 0.31	0.57 ± 0.01	2.64 ± 0.22
	1000 / S / 150	20 min 80°C		3500 / S / 40	-	0.79 ± 0.01	5.11 ± 0.88	0.41 ± 0.01	1.63 ± 0.27
	1000 / S / 150	-		3500 / D / 150	-	0.78 ± 0.01	4.21 ± 1.13	0.43 ± 0.05	1.42 ± 0.56
	1000 / S / 150	20 min 80°C		3500 / D / 40	-	0.79 ± 0	2.18 ± 0.32	0.35 ± 0	0.60 ± 0.08
	1000 / D / 150	-		3500 / S / 150	-	0.72 ± 0.02	1.64 ± 0.65	0.61 ± 0.03	0.73 ± 0.32
	1000 / D / 150	20 min 80°C		3500 / D / 20	-	0.77 ± 0.02	6.59 ± 1.10	0.48 ± 0.06	2.44 ± 0.58
	1000 / S / 150	-		3500 / D / 40	-	0.77 ± 0.01	2.53 ± 0.35	0.42 ± 0.01	0.83 ± 0.13
	1000 / S / 150	20 min 80°C		3500 / D / 40	-	0.78 ± 0.01	2.36 ± 0.59	0.40 ± 0.02	0.75 ± 0.21
	1000 / D / 150	**-**		**3500 / D / 40**	**-**	**0.76 ± 0.01**	**7.66 ± 0.25**	**0.46 ± 0.02**	**2.68 ± 0.15**
	1000 / D / 150	-		3500 / D / 40	10 min 150°C	0.76 ± 0.01	6.44 ± 0.19	0.54 ± 0.03	2.65 ± 0.08
	1000 / D / 150	40 min 80°C		3500 / D / 40	10 min 150°C	0.77 ± 0.01	5.76 ± 0.28	0.51 ± 0.03	2.27 ± 0.18
	1000 / D / 150	10 min 150°C		3500 / D / 40	10 min 150°C	0.76 ± 0.01	6.12 ± 0.18	0.56 ± 0.02	2.62 ± 0.05
CF	1000 / S / 150	-	DCM:CB 100:0	3500 / D / 40	-	NaN	NaN	NaN	NaN
			60:40			0.77 ± 0.01	0.99 ± 0.09	0.34 ± 0.01	0.26 ± 0.02
			20:80			0.77 ± 0	1.6 ± 0.45	0.35 ± 0.01	0.44 ± 0.13

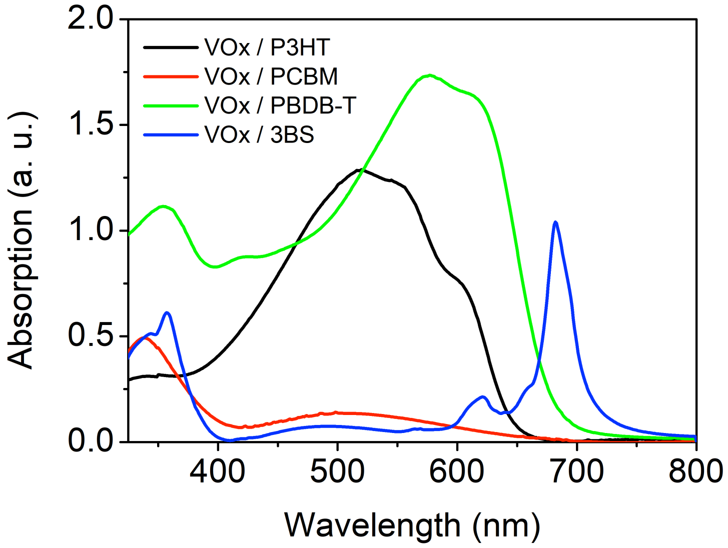

Figure S4.1: UV-Vis absorption spectra for P3HT, PCBM, PBDB-T, and $(3BS)_2$-SiPc films deposited on VOx. For convenience, $(3BS)_2$-SiPc is referred to as 3BS.

Table S4.3: Contact angle values (in °) of water or chloroform on ITO/PEDOT:PSS and ITO/VOx stacks.

	Contact angle (°) (averaged over 3 measurements)	
	Water	Chloroform
VOx	8	4
PEDOT:PSS	11	4

Table S4.4: Optimization of experimental processing conditions for ITO/VOx/PBDB-T/(3BS)$_2$-SiPc/BCP/Ag LbL devices: J-V characteristics (best determined conditions are highlighted in bold and (3BS)$_2$-SiPc is referred to as 3BS). For spinning a / b / c: a is the rate in rpm, b is the dispensing kinetic (S for static, D for dynamic) and c is the volume in µL.

PBDB-T			**3BS**			**I-V parameters**			
Solvent / Concentration (mg/mL)	**Spinning** a / b / c	**Annealing**	**Solvent / Concentration (mg/mL)**	**Spinning** a / b / c	**Annealing**	V_{oc} (V)	J_{sc} (mA/cm^2)	FF	PCE (%)
CF / 10	1000 / S / 200	-	CB / 10	3500 / D / 200	-	0.98 ± 0.1	0.57 ± 0.5	0.29 ± 0.01	0.97 ± 0.1
	1000 / D / 200			3500 / D / 200		0.98 ± 0.05	5.1 ± 0.4	0.32 ± 0.01	1.6 ± 0.2
	1000 / S / 200			3500 / S / 200		1.03 ± 0.04	4.7 ± 0.6	0.44 ± 0.02	2.2 ± 0.3
CF / 12	1000 / S / 200	**-**	**CB / 12**	3500 / S / 200	-	1.07 ± 0.01	6.1 ± 0.2	0.42 ± 0.01	2.7 ± 0.09
	1000 / S / 300			**3500 / S / 300**	**10 min 100°C**	**1.06 ± 0.0**	**6.15 ± 0.48**	**0.46 ± 0.01**	**3.02 ± 0.20**
	1000 / S / 300			3500 / S / 300	10 min 150°C	1.04 ± 0.01	6.0 ± 0.05	0.47 ± 0.01	2.9 ± 0.05 [d]
CF / 12	1000 / S / 200	-	CF / 12	3500 / S / 200	-	1.05 ± 0.02	3.0 ± 0.3	0.36 ± 0.01	1.1 ± 0.1
	1000 / D / 200			3500 / D / 200		1.05 ± 0.01	1.7 ± 0.2	0.28 ± 0.00	0.50 ± 0.06

[d] important number of short-circuited devices (6 devices over 10).